(56)

Measurements of Segmental Order Parameters and Torsional Angles in Solid State Nuclear Magnetic Resonance

by

John D. Gross

B.S. Chemistry

The University of the South

Submitted to the Department of Chemistry
in Partial Fulfillment of the Requirements for the Degree of
Doctor of Philosophy in Chemistry

at the

Massachusetts Institute of Technology

May 1998

Signature of Author: _____
Department of Chemistry
May 15, 1998

Certified by: _____
Robert G. Griffin
Professor of Chemistry
Thesis Supervisor

Accepted by: _____
Deitmar Seyferth
Professor of Chemistry
Chairman, Departmental Committee on Graduate Students

This Doctoral thesis has been examined by a Committee of the Department of Chemistry as follows:

Professor Keith A. Nelson _____
Chairman

Professor John S. Waugh _____

Professor Robert G. Griffin _____
Thesis Supervisor

Measurements of Segmental Order Parameters and Torsional Angles in Solid State Nuclear Magnetic Resonance

by
John D. Gross

Submitted to the Department of Chemistry May 15, 1998 in partial fulfillment of the requirements for the Degree of Doctor of Philosophy in Physical Chemistry

ABSTRACT

The dipolar interaction between nuclear spins is dependent on the internuclear distance and the orientation of the internuclear vector with respect to an applied magnetic field, thereby providing a valuable source of information on molecular geometry. Procedures for correlating the dipolar interactions generated by directly bonded spin pairs in the presence and absence of molecular motion are presented. In the former case, a correlation is established between the internuclear vector and a motional axis. In the latter case, correlations between dipolar spin pairs are observed. The use of the separated-local-field principle in conjunction with rapid MAS and dipolar recoupling allows multiple correlations to be extracted with high sensitivity and resolution.

In part one, procedures for the measurement of ^{13}C-^{1}H dipolar interactions under rapid MAS are presented. The magnitude and signs of motionally averaged ^{13}C-^{1}H dipolar interactions in fluid phase lipid bilayers may be extracted within the MAS framework with ^{13}C-^{1}H dipolar recoupling. Conversion of the measured values into ^{13}C-^{1}H order parameters and comparison with those obtained by ^{2}H NMR indicates that dipolar recoupling is a viable method for determining segmental order in fluid phase lipid bilayers without recourse to isotopic enrichment. Second, efficient methods are developed for the assignment of ^{1}H and ^{13}C chemical shifts in fluid phase bilayers in order to facilitate the analysis of the ^{13}C-^{1}H order parameters. Application of the methods to the trans membrane peptide, *gramicidin A* fails due to an anomolous broadening that occurs in the L_α phase at 25 °C. Numerical lineshape simulations indicate that the rate corresponding to a three-site jump is on the order of 10^5 s^{-1} at 25 °C. This is comparable to the rf field used for CW decoupling resulting in an interference between molecular motion and ^{1}H decoupling.

In part two, procedures for the measurement of molecular torsional angles are presented. Dipolar couplings between directly bonded spin pairs are correlated either through dipolar evolution of double- and zero-quantum coherence or correlated single-quantum coherences. Specifically, techniques for measuring the backbone torsion angles ϕ and ψ across HNCH and NCCN spin quartets are presented. For measurements of ϕ, ^{15}N-^{13}C double- and zero-quantum coherence is generated and allowed to evolve under the ^{15}N-^{1}H and ^{13}C-^{1}H dipolar interactions during a period of ^{1}H homonuclear dipolar decoupling prior to reconversion into observable ^{13}C magnetization. In the resulting 2D spectrum, rotational sideband manifolds reflecting the relative orientation of the ^{15}N-^{1}H and ^{13}C-^{1}H dipolar tensors are sorted by the ^{13}C isotropic shift. An increase in angular resolution is achieved by evolution of ^{15}N and ^{13}C antiphase magnetization under the ^{15}N-^{1}H and ^{13}C-^{1}H dipolar interactions in a separate-and-synchronous evolution scheme where the ^{15}N-^{1}H dipolar interaction is amplified by two. For measurements of ψ, $^{13}C_\alpha$-^{13}CO double quantum coherence is generated and allowed to evolve under the recoupled ^{15}N-$^{13}C_\alpha$ and ^{15}N-^{13}CO dipolar interactions prior to reconversion into observable magnetization.

Thesis Supervisor: Dr. R.G. Griffin
Title: Professor of Chemistry and Director of the Francis Bitter Magnet Laboratory

This thesis is dedicated to Merik

Table of Contents

Acknowledgments

A Ph.D. thesis is not completed in a vacuum. There are many people who have been instrumental in both encouragement and collaboration. First, my parents Ray and Barbara constantly supported and encouraged my pursuit of knowledge. My wife Merik supported me throughout college and graduate school in my sometimes single minded effort. My brother Danny and sister Ellen also deserve credit in encouraging me to go into science. Mary and Adam Cherry, Maria and Marion Spiers, and Mundi, Jimmy, James, and Rawlings Elam have helped me keep things in perspective. Finally, my friends Dennis Hall, Tim Warren, Tom Rutishauser, Alex Brodsky, Matt Ford, Mike "The professor" Rydock, Dror Warschawski, Jim Balcom, Jen Evans, and Allistair Lucks should be specifically acknowledged for making life in Cambridge a memorable experience.

Second, and just as important as the first, I would like to thank those with whom I have had the pleasure of collaborating. Phil Costa took me under his wing upon my joining the lab and taught me how to run the spectrometers (tricks included) in addition to many stimulating discussions about solid-state NMR. Dror Warschawski contributed many ideas on the lipid bilayer studies, led the work on gramicidin A, and provided a fresh perspective on NMR spectroscopy. Mei Hong contributed to an exciting collaboration in the area of torsion angle measurements. Also, Christian Freund, Volker Doetsch and Hans Wendt should be acknowledged for their contributions to the protein G project; Professors Gerhard Wagner and Tom Ellenberger are thanked for the use of their laboratories for protein biosynthesis and crystallography.

Finally, I would like to thank those with whom I have interacted very closely throughout my time at the Magnet Lab. Chad Rienstra advised me in the fine art of transmission line probe construction and designed the HCN probe used in many of these experiments. David Ruben designed the spectrometer hardware and software. Peter Allen and Ajay Thakkar assisted in electronics and general hardware matters. Chris Turner is acknowledged for insightful discussions on solution NMR. Boqin Sun, Andrew Bennett, David Rovnyak, Marc Baldus and Len Mueller are thanked for many rewarding discussions of spin dynamics and simulations thereof. Joanna Long contributed many insightful discussions and advice on lipid dynamics. My officemates, in particular Jingui Hu and K.V. Lakshmi, are thanked for the many conversations over the years. Last, but not least, Professor Robert Griffin encouraged me to pursue the areas presented in this thesis and created a stimulating research environment. Prior to coming to MIT, I asked a Griffin group alumnus about the research environment in Bob's group. He said that Bob always got the best people and that this lab would be an excellent place to learn NMR spectroscopy. I wholeheartedly agree.

1. Solid State NMR

1.1 Introduction

Solid-state nuclear magnetic resonance (NMR) has proven to be an invaluable tool for the study of both structure and dynamics of systems that are difficult to characterize by conventional techniques such as solution NMR or x-ray crystallography. Of particular interest are biological membranes, membrane proteins, and small membrane spanning peptides which are difficult to crystallize; furthermore, rotational correlation times of these systems are typically well in excess of 20 ns so that high-resolution liquid state NMR is precluded[1]. In addition, there are other systems that do not occur natrurally as solids - such as proteins or nucleic acids which are difficult to crystallize and unyielding to solution NMR - that would be ideally suited for NMR studies in the solid state. Although these systems occur naturally in the liquid state, they may be prepared as lyophilized powders or frozen solutions so that solid-state NMR studies may be performed. Finally, an additional advantage of solid-state NMR is the ability to perform time-resolved spectroscopy[2-5]. This approach has been applied to the study of enzyme catalysis or signal transduction where enzyme-substrate complexes are trapped by rapid freezing along different stages of the reaction coordinate so that mechanistic details such as conformational changes may be probed.

Because of this enormous potential, solid-state NMR is being developed as a method for probing structure and dynamics in biological molecules which are of considerable complexity. Ideally, resolution of each atomic site is desired so that very local information may be built up into a structural (or a dynamical) model. However, in randomly oriented solids, the lineshapes of the individual sites are broadened by interactions such as the dipolar coupling[6] and chemical shift which contain an anisotropic dependence on orientation with respect to the magnetic field. Such a broadening renders the spectra of biomolecules containing thousands of sites difficult to disentangle. However, pioneering work by groups at MIT and others in the development of techniques such as cross-polarization[7] with the application of magic-angle spinning (MAS)[8, 9] and high power proton decoupling[10-13] have allowed high resolution isotropic chemical shift spectra rivaling the quality of those obtained in liquids to be recorded with optimal sensitivity.

This is due to the fact that MAS is capable of averaging the anisotropic interactions (2nd rank tensors) to zero leaving behind only the isotropic components. Indeed, the exact conditions for such averaging were presented in a very elegant fashion with the development and application of coherent averaging theory by J. S. Waugh and co-workers at MIT[14, 15]. Coherent averaging theory has proven to be a very general approach for analyzing and designing NMR experiments in both liquid and solid state NMR. In liquids, it has enjoyed success in establishing criteria for efficient decoupling and led to the design of very powerful decoupling[12, 16, 17] and isotropic mixing sequences[18]. In solids it has proven indispensable for the understanding of both hetero[12, 13] and homonuclear dipolar decoupling[14, 19, 20] sequences in addition to MAS[15, 17], and recently, the combined effects of MAS and rf pulses have been analyzed in detail[21]. Although MAS is capable of averaging the anisotropic interactions, rf schemes may be designed to selectively interfere with this process so that specific anisotropic interactions may be introduced. This approach, referred to as "recoupling", along with application of two dimensional NMR allows a specific anisotropic interaction, such as the dipolar coupling, to be measured with the site resolution provided by the isotropic shift[21, 22].

Over the past 20 years, many advances toward structure determination by solid-state NMR in the CP/MAS framework have been made. With dipolar recoupling it is possible to accurately measure distances between pairs of like and unlike spin 1/2 nuclei in either a broadband [23-30] or spectrally selective [17, 31 , 32] fashion. Furthermore, these techniques, when used with dipolar mixing schemes for polarization or coherence transfer, allow high resolution multidimensional chemical shift correlation experiments, analogous to those used in liquid state spectroscopy, to be performed allowing for the complete assignment of biological macromolecules in the solid state[33]. Despite these advances, there are complications when trying to measure many distances at once. Specifically, the non-commutation of the dipolar interaction between homonuclear spin pairs leads to an attenuation of the weak-and therefore interesting-interactions by the uninformative, strong dipolar interactions between directly bonded nuclei[34]. This dipolar truncation effect has motivated the development of alternative techniques for determining structure.

In one approach, correlations between strong heteronuclear dipolar interactions are established as a method of measuring torsion angles in uniformally ^{15}N, ^{13}C labelled samples[35-39]. Dipolar interactions between like spins are kept at bay by either homonuclear decoupling or fast MAS. These methods are a promising means to determine local structure. In addition, it is unclear what the optimum methods are for measuring chemical shifts and determining structure with the MAS framework in systems which contain some degree of molecular motion, such as lipid bilayers or small membrane peptide/lipid bilayer systems.

This thesis addresses methods for measuring bond order parameters and chemical shifts in model biological membranes and techniques for measuring molecular torsion angles in rigid solids. Measurements of segmental order and torsion angles provide very local information that in some cases may provide a more accurate conformational model than internuclear distances. An outline of the material covered is as follows.

The remainder of Chapter one constitutes an introduction to nuclear spin interactions and solid-state NMR spectroscopy. An introduction to nuclear spin dynamics is presented along with examples of solid state spectra under MAS in both rigid and semi-rigid solids. The physical basis of the techniques for measuring segmental order parameters and molecular torsion angles is introduced.

In Chapter two, methods for determining ^{1}H and ^{13}C chemical shifts in fluid phase lipid bilayers are presented. It is demonstrated that, contrary to rigid solids, high resolution ^{1}H spectra may be obtained in lipid bilayers due to the effects fast limit axial diffusion on the MAS dynamics. It is shown that in the absence of high power ^{1}H decoupling, resolved heteronuclear J coupling are observed and may be used for coherence transfer using a rotor synchronized refocused INEPT sequence. The effectiveness of the rotor-synchronized INEPT scheme is demonstrated by rotor-synchronized ^{1}H-^{13}C HSQC experiments on uniform ^{13}C labeled lipid bilayers. Furthermore methods for correlating ^{13}C chemical shift using the TOCSY scheme employed in liquid state NMR are also presented. These techniques, taken together, could allow the complete assignment

of ^{13}C and ^{1}H resonances in lipid bilayers. In addition, the benefits and limitations of using heteronuclear J couplings for coherence transfer in semi-rigid and rigid solids is discussed.

In Chapter three, two-dimensional magic-angle spinning (2D MAS) NMR experiments designed to measure the magnitudes and signs of ^{13}C-^{1}H dipolar interactions in fluid phase lipid bilayers are presented. MAS is employed throughout the experiments while dipolar recoupling is achieved (by radio frequency irradiation) during the evolution period. Multiple ^{13}C-^{1}H dipolar couplings are measured for a natural abundance sample of L_α phase dimyristoylphosphatidylcholine (DMPC). The magnitudes of ^{13}C-^{1}H dipolar interactions are determined by fitting numerical simulations of recoupled powder lineshapes with experimental data while the signs of these interactions are obtained by monitoring the build-up of antiphase magnetization by ^{13}C detection. A comparison of the order parameters obtained by ^{13}C-^{1}H dipolar recoupling with those previously obtained for DMPC by ^{2}H NMR indicates that dipolar recoupling is a viable method for determining segmental order in fluid phase lipid bilayers without recourse to isotopic enrichment. Measurement of the signs of ^{13}C-^{1}H dipolar couplings provides additional structural information that is unavailable through ^{2}H NMR. The results obtained for DMPC suggest that the accuracy of the dipolar recoupling experiments presented in this work is competitive with that of previous techniques which require switched-angle spinning for the measurement of the magnitudes and signs of ^{13}C-^{1}H dipolar interactions in lipid bilayers.

Attempts to obtain ^{1}H decoupled ^{13}C spectra of the transmembrane peptide gramicidin A (gA) embedded in model lipid bilayers are complicated by the very short transverse relaxation rate of the peptide resonances, and this effect is explored in detail in Chapter 4. Experimentally, it is found that the ^{13}C linewidths of uniformly ^{15}N,^{13}C Gly in gramicidin A ($NCCH_2$-Gly gA) in hydrated DMPC lipid bilayers exhibits a dramatic dependence on temperature. As temperature is decreased from 60 °C, the ^{13}C linewidths broaden and reach a maximum broadening at room temperature while a further reduction of temperature results in line narrowing. ^{2}H substitution at the C_α site eliminates the effect suggesting that there is an interference between some molecular motion of gA with proton decoupling. Numerical lineshape simulations employing a simple

dynamical modal of a three site hop for the CH_2 group of in $NCCH_2$-Gly gA along with MAS and CW ^1H decoupling corroborate such an interference effect.

In Chapter 5 a method for determining the torsion angle ϕ in peptides, using magic-angle-spinning solid-state NMR spectroscopy is described. The angle ϕ is obtained from the relative orientations of the $N\text{-}H^N$ and $C^\alpha\text{-}H^\alpha$ bonds, which are manifest in the rotational sideband spectrum of the sum and difference of the two corresponding dipolar couplings. The technique exploits $^{15}N\text{-}^{13}C$ double-quantum and zero-quantum coherences, which evolve simultaneously under the N-H and C-H dipolar interactions. The magnitudes of these dipolar couplings scaled by the proton homonuclear decoupling sequence are directly extracted from control experiments that correlate the dipolar interactions with the isotropic chemical shifts. Applied to ^{15}N-labeled *N*-acetyl-*D,L*-valine, the experiment yielded ϕ=-135°, which agrees well with the X-ray crystal structure. Simulations indicate that the accuracy of the measured ϕ angle is within ±10° when the $N\text{-}H^N$ and $C^\alpha\text{-}H^\alpha$ bonds are approximately antiparallel and ±20° when they are roughly parallel. The technique is sufficiently sensitive to be applied to small peptides that are labeled only in ^{15}N. Its multiple-quantum nature also allows it to be applied to larger peptides that are uniformly and randomly labeled in both ^{15}N and ^{13}C. Most importantly, the technique allows the simultaneous determination of ϕ angles in multiple residues, if C^α chemical shifts are resolved.

In Chapter 6, a technique for amplifying the apparent magnitudes of $^{13}C\text{-}^1H$ and $^{15}N\text{-}^1H$ dipolar interactions in magic-angle spinning experiments is described. This coupling amplification method is incorporated into the experiment presented in Chapter 5 that determines the peptide torsion angle ϕ through the relative orientation of the $C^\alpha\text{-}H^\alpha$ and $N\text{-}H^N$ bonds. It is shown both experimentally and theoretically that the angular resolution of the measurement is enhanced significantly by the selective doubling of the $N\text{-}H^N$ coupling. By inserting rotor-synchronized 180° pulses in the evolution period of a 2D dipolar-chemical shift experiment, heteronuclear dipolar couplings are doubled or quadrupled relative to the spinning speed. The increased number of dipolar sidebands is desirable for retaining structural information in the indirectly detected dipolar dimension while resolving inequivalent sites in the isotropic chemical shift dimension at relatively

high spinning speeds. This coupling amplification method is incorporated into an experiment that determines the peptide torsion angle ϕ through the relative orientation of the C^{α}-H^{α} and N-H^{N} bonds. It is shown both experimentally and theoretically that the angular resolution of the measurement is enhanced significantly by the selective doubling of the N-H^{N} coupling.

In Chapter 7, a solid-state NMR experiment is presented for measuring Ψ torsion angles in (^{15}N-$^{13}C_{\alpha}$-$^{13}C_{=O}$-^{15}N)-labeled peptides. Creation of $^{13}C_{\alpha}$-$^{13}C_{=O}$ double-quantum coherence (DQC) is followed by selective evolution under ^{15}N-^{13}C dipolar interactions. The time-course of $^{13}C_{\alpha}$-$^{13}C_{=O}$ DQC dephasing is sensitive to the Ψ torsion angle, particularly for values associated with ß-sheet secondary structure (120°-180°). We apply the technique to glycylglycine•HCl and extract a value for Ψ that matches the diffraction-determined value (Ψ=162.1°) with a precision of ±5°. In contrast to the experiments presented in Chapters 5 and 6, this method of determining torsion angle can be implemented at spinning speeds that exceed the magnitudes of ^{13}C chemical anisotropy thereby increasing sensitivity and resolution.

In Chapter 8, new solid-state NMR methods for measuring the magnitude of the chemical shift anisotropy (CSA) and/or the heteronuclear dipolar coupling in the presence of homonuclear dipolar coupled spin networks under magic-angle spinning (MAS) are described. The techniques employ $2\pi/5$ phase shifts of a frequency switched Lee-Goldburg irradiation scheme which recouples the CSA and/or the heteronuclear dipolar coupling while simultaneously decoupling the homonuclear dipolar interactions. The techniques are sensitive to the magnitude of the CSA and its asymmetry and may be implemented under conditions where the MAS rate exceeds the size of the anisotropic interactions. These approaches could find use in measurements of the magnitudes and relative orientations of CSA and/or heteronuclear dipolar couplings to extract torsion angles in uniformly labeled systems.

Finally, in Chapter 9, initial investigations of a 56 amino acid protein (protein G) are carried out in order to test the structural methodology presented previously. Resolution is paramount for successful measurement of chemical shifts, distances and torsion angles in multiply labeled samples. Extensive use of various isotopic labeling and sample preparation schemes have

been employed to obtain optimal resolution. It is found that either slowly or quickly freezing protein solutions prior to lyophilization results in poor resolution in ^{15}N and ^{13}C one- and two-dimensional spectra. In contrast, crystals of protein G yield high-resolution ^{15}N spectra rivaling the quality of those obtained in liquids. The results of these preliminary investigations will play a crucial role in subsequent efforts to obtain the full three-dimensional structure of protein G by solid-state NMR.

1.2 Introduction to Nuclear Spin Dynamics

1.2.1 The Hamiltonian

The Hamiltonian corresponding to a system of like nuclei (I) may be written:

$$H_{Total} = H_Z + H_{Int} \tag{1.1}$$

where H_Z corresponds to the sum of the Zeeman interactions with:

$$H_Z = \omega_0^I I_Z \tag{1.2}$$

where $\omega_0^i = -\gamma_i B_0$ is the Larmor frequency of the nucleus I or S and H_{Int} corresponds to the internal interactions with

$$H_{Int} = \sum_Q H^Q \tag{1.3}$$

where Q represents the type of nuclear spin interaction consisting of either the chemical shift, dipolar or quadrupolar interaction. The internal interactions may be represented as products of two independent irreducible tensor operators $T_{\lambda\mu}$ and $R_{\lambda\mu}$ which correspond to interactions in spin and ordinary space respectively. Formally, this is written[40]:

$$H^Q = \sum_{\lambda=0}^{2} \sum_{\mu=-\lambda}^{\lambda} (-1)^\mu T^Q_{\lambda,\mu} R^Q_{\lambda,-\mu} \tag{1.4}$$

The separation between spin and ordinary space is convenient for treating magnetic resonance since rotations of the spin operators $T^Q_{\lambda\mu}$ effected by radio frequency irradiation (in the appropriate interaction frame) or sample rotation are effected independently of one another (See below). The

irreducible spherical tensor operators may be written in terms of the angular momentum operators. The rank one tensors are written as:

$$T_{00} = V \cdot U \tag{1.5a}$$

$$T_{10} = V_Z \tag{1.5b}$$

and

$$T_{1\pm1} = \mp 2^{-1/2} V^{\pm} \tag{1.5c}$$

while the rank two tensors are:

$$T_{20} = 6^{-1/2}(3V_Z U_Z - V \cdot U) \quad , \tag{1.5d}$$

$$T_{2\pm1} = \mp 2^{-1}(V^{\pm} U_Z + V_Z U^{\pm}) \quad , \tag{1.5e}$$

$$T_{2\pm2} = 2^{-1} V^{\pm} U^{\pm} \quad . \tag{1.5f}$$

Rotations of the $T^Q_{\lambda\mu}$ are characterized by the transformation law[41]:

$$R(\Omega)\, T^Q_{\lambda\mu} R^{+}(\Omega) = \sum_{\mu'=-\lambda}^{\lambda} D^{(\lambda)}_{\mu'\mu}(\Omega)\, T^Q_{\lambda\mu'} \tag{1.6}$$

with

$$R(\alpha,\beta,\gamma) = R_Z(\alpha)\, R_Y(\beta)\, R_Z(\gamma) \tag{1.7}$$

and

$$R_n(\phi) = e^{-i\, I \cdot n\, \phi} \tag{1.8}$$

In principle, irreducible spherical tensor operators as defined in Eqs. 1.5a-f can be constructed from any two vector operators V and U. For NMR, these operators represent the coupling of two interactions. For example, V is a spin angular momentum operator while U may be either the static magnetic field with components $(0,0,B_0)$ for the case of the chemical shift interaction, or another spin operator for the case of the dipolar interaction. V and U are the same operator for the case of the quadrupolar interaction.

Considering only the chemical shift and dipolar interactions the spatial components, $R^{Q}_{\lambda\mu}$, are written[40]:

$$R^{Q,L}_{\lambda\mu} = \sum_{\mu'=-\lambda}^{\lambda} \rho^{Q}_{\lambda\mu'} D^{(\lambda)}_{\mu'\mu} (\Omega_{PL}) \qquad (1.9)$$

with $D^{(\lambda)} (\Omega_{PL})$ as a Wigner rotation matrix for a tensor of rank λ and the relevant components, $\rho_{\lambda\mu}$:

$$\rho^{Q}_{00} = C^{Q}_{0}, \qquad (1.10a)$$

$$\rho^{Q}_{20} = \sqrt{\frac{3}{2}} C^{Q}_{1} \quad , \qquad (1.10b)$$

$$\rho^{Q}_{2\pm1} = 0 \qquad (1.10c)$$

and

$$\rho^{Q}_{2\pm2} = -\frac{1}{2} C^{Q}_{1} \eta^{Q} \qquad (1.10d)$$

where the C^{Q}_{0}, C^{Q}_{1}, and η^{Q} are the isotropic component, the anisotropy and the asymmetry parameter respectively. For the chemical shift (Q = I or S), $C^{I}_{0} = -\gamma_{I} \delta^{I}_{0}$ and with the isotropic shift chemical shift defined $\delta^{I}_{0} = \frac{1}{3} Tr(\tilde{\sigma})$ where $\tilde{\sigma}$ is the chemical shift tensor while $C^{I}_{1} = -\gamma_{I} \delta^{I}_{1}$. The I spin chemical shift anisotropy is defined $\delta^{I}_{1} = \sigma_{iso} - \sigma_{ZZ}$ where $\sigma_{iso} - \sigma_{ZZ}$ represents the deviation of the largest principle component of the chemical shift tensor (σ_{ZZ}) from the isotropic shift while the asymmetry parameter is defined $\eta^{I} = (\sigma_{YY} - \sigma_{XX})/ \delta^{I}_{1}$. For the dipolar coupling, Q= II , $C^{ij}_{0} = 2\pi J_{ij}$ and $C^{ij} = -2\, b_{ij}$ where J_{ij} is the scalar coupling and $b_{ij} = \frac{\mu_0}{4\pi} \frac{\gamma_i \gamma_j}{r^3_{ij}} \hbar$ is the dipolar coupling constant between the spins i and j. The asymmetry parameter , η^{ij} , is zero for the dipolar interaction due uniaxial symmetry. Equation 1.9 illustrates that the magnitude of the anisotropic interactions depends on the relative orientation of the interaction tensor with respect to the laboratory frame with Z_L axis defined by the direction of the static magnetic field B_0. The definitions of the Euler angles ,Ω_{PR} , is given in Figure 1.1[40].

Figure 1.1 Schematic representation of convention for the Euler angles $\{\alpha,\beta,\gamma\}$ that rotate the X,Y,Z system into the x,y,z frame. The first rotation is about the Z axis by α to the node line k. The second rotation is about the node line k by β, the angle between Z and z. Finally, γ is rotation about the z axis.

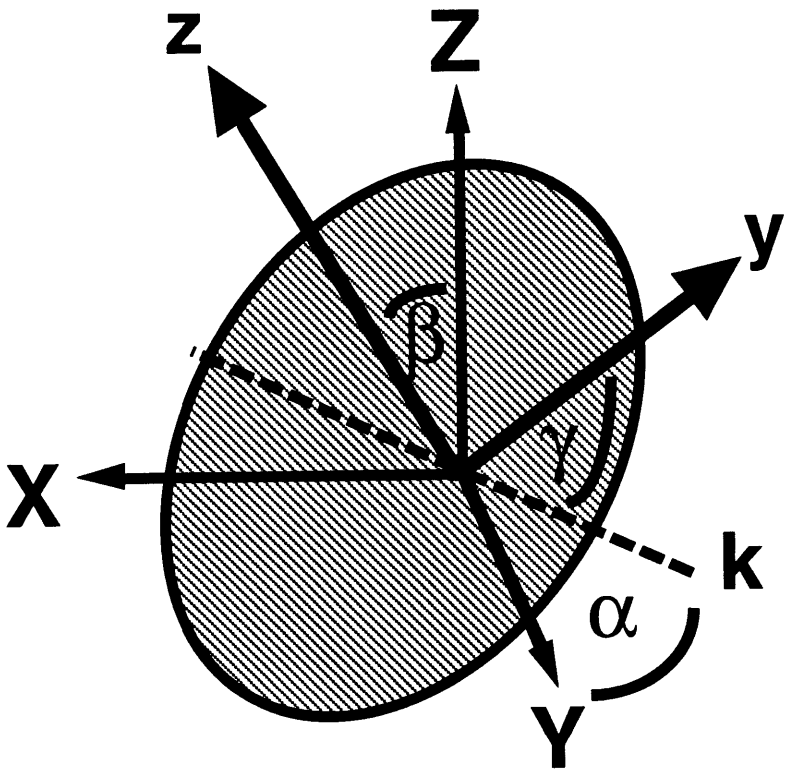

Figure 1.1

As noted in Eq.1.4, each interaction is decomposed into an rotational invariant or isotropic part (λ=0) and anisotropic components characterized as a rank 1 (λ=1,antisymmetric) and rank 2 (λ=2,symmetric) tensor. The antisymmetric component will be assumed to be zero. Although this component may take on a value, it is usually negligible and such considerations are beyond the scope of this thesis As indicated by Eqs 1.5a-e, the Hamiltonian may be written in terms of spherical tensor operators or products of angular momentum operators. In this thesis, the choice of notation will be based on convenience.

1.2.2 Average Hamiltonian Theory

Observables are calculated from a statistical ensemble of nuclear spins through the Liouville-von Neumann (LVN) equation[41]:

$$\frac{d}{dt}\rho(t) = -i[H(t),\rho(t)] \tag{1.11}$$

with the formal solution as:

$$\rho(t) = U(t,0)\ \rho(0)\ U^{-1}(t,0) \tag{1.12}$$

and the evolution operator

$$U(t,0) = \hat{T}\ \exp\{-i\int_0^t dt'\ H(t')\} \tag{1.13}$$

The expectation value of an observable A may then be calculated by projection - in the sense of the trace - onto the density matrix through:

$$\langle A\rangle = \ Tr\{\ A\ \rho(t)\ \} \tag{1.14}$$

The Dyson time-ordering operator $\hat{T}$ requires stepwise propagation to evaluate the evolution operator. Explicit evaluation is complicated by a time-dependent Hamiltonian that does not commute with itself at different times. In this case the dynamics may be calculated by numerical integration or through Average Hamiltonian Theory (AHT). With the latter approach, the evolution operator under a time-dependent periodic Hamiltonian with period τ_C is replaced by:

$$U(n\tau_c,0) = \ \hat{T}\ \exp\{-i\int_0^{\tau_c} dt'\ H(t')\}\ =\ \exp\{-i\ \bar{H}\ \tau_c\} \tag{1.14}$$

with the time-independent effective Hamiltonian given by the series:

$$\bar{H} = \overline{H^{(0)}} + \overline{H^{(1)}} + \overline{H^{(2)}} + \ldots \tag{1.15}$$

where:

$$\overline{H^{(0)}} = \frac{1}{\tau_c}\int_0^{\tau_c} dt\, H(t) \quad , \tag{1.16a}$$

$$\overline{H^{(1)}} = \frac{-i}{2\tau_c}\int_0^{\tau_c} dt \int_0^{t} dt' \,[\, H(t) \,,\, H(t') \,], \tag{1.16b}$$

and

$$\overline{H^{(2)}} = \frac{1}{6\tau_c}\int_0^{\tau_c} dt \int_0^{t} dt' \int_0^{t'} dt'' [H(t''), [\, H(t') \,,\, H(t) \,]] + [H(t), [\, H(t') \,,\, H(t'') \,]] \tag{1.16c}$$

Convergence of the series is ensured only if $|\bar{H}|\ \tau_C << 1$ in which case the first few terms constitute a valid approximation[14, 42-44]

1.2.2.1- Interaction Frames

Considerable insight into nuclear spin dynamics may be obtained by a judicious choice of an "interaction representation" in conjunction with AHT. In many cases the Hamiltonian may be partitioned:

$$H(t) = H_0(t) + H_1(t) \tag{1.17}$$

Using the transformation

$$\tilde{H}_1(t) = U_I^{-1}\, H_1\, U_I + U_I^{-1}\, H_0\, U_I - i\, U_I^{-1}\dot{U}_I \tag{1.18}$$

with

$$U_I(t,0) = \hat{T}\, \exp\{-i\int_0^{t} dt'\, V(t')\} \tag{1.19}$$

yields

$$\rho(t) = U_I(t,0)\, U_1(t,0)\rho(0)\, U_1^{-1}(t,0)U_I^{-1}(t,0) \qquad (1.20)$$

with

$$U_1(t,0) = \hat{T}\exp\{-i\int_0^t dt'\, \tilde{H}_1(t')\} \qquad (1.21)$$

as a solution to the LVN equation. If both $H_0(t)$ and $H_1(t)$ are periodic modulo τ_C, and if $U_I(n\tau_C,0) = 1$ then Eq. 1.20 simplifies to:

$$\rho(n\tau_C) = U_1(n\tau_C,0)\rho(0)\, U_1^{-1}(n\tau_C,0). \qquad (1.22)$$

In this case the evolution due to the large interactions in H_0 is considered to be cyclic: sampling over cycles then allows one to observe the effects of the small interactions contained in H_1. The utility of this result will become apparent by considering several examples (see below). The results that follow will be employed throughout the entirety of this thesis.

1.2.2.1.1 Example-High Field "Truncation"

If the total Hamiltonian given by Eq 1.1 is partitioned so that H_0 and H_1 (of Eq. 1.17) correspond to the Zeeman and internal interactions ,respectively and V (of Eq 1.19) is chosen to be $\omega_0^I I_z$ then

$$U_I(t,0) = \exp\{-i\,\omega_0 t\, I_z\}\,. \qquad (1.23)$$

Since V commutes with H_0, Eq 1.18 reduces to

$$\tilde{H}_1(t) = U_I^{-1}(t,0)\, H_1\, U_I(t,0) \qquad (1.24)$$

$$= R(\alpha=\omega_0 t,0,0)\, H_1\, R^{+}(\alpha=\omega_0 t,0,0) \qquad (1.25)$$

$$= \sum_Q \sum_{\lambda=0}^{2} \sum_{\mu=-\lambda}^{\lambda} (-1)^{\mu}\exp\{-i\mu\omega_0 t\}\, T^Q_{\lambda\mu}\, R^Q_{\lambda\mu}$$

by application of Eqs 1.6 and 1.7. Defining $\tau_C = 2\pi/\omega_0$,

$$U_I(n\tau_C,0) = \exp\{-i\,2\pi\, I_z\} = \hat{1} \qquad (1.26)$$

and

$$\tilde{H}_1(t) \cong \bar{\tilde{H}}_1^{(0)} = \sum_Q \sum_{\lambda=0}^{2} T_{\lambda 0}^Q R_{\lambda 0}^Q \tag{1.27}$$

Equation 1.27 may be cast into the familiar form:

$$H = H_I + H_{II} \tag{1.28}$$

with the chemical shifts

$$H_I = \sum_i \omega_i^I I_{iZ} \tag{1.29}$$

and dipolar couplings

$$H_{II} = \sum_{i<j} \omega_{ij}^{II} (3I_{jZ}I_{kZ} - I_j \cdot I_k) \tag{1.30}$$

and the spatial components written as a sum of isotropic and anisotropic terms where:

$$\omega^Q = \tilde{\rho}_{00}^Q + \sum_{k=-2}^{2} \tilde{\rho}_{2k}^Q D_{k0}^{(2)} (\Omega_{PL}) \tag{1.31}$$

where the Euler angles Ω_{PL} $\{\alpha_{PL},\beta_{PL},\gamma_{PL}\}$ map the interaction tensor from principle axis to laboratory frame and $\rho_{\lambda\mu}^Q$ is redefined so that $\tilde{\rho}_{00}^i = B_0\rho_{0(}^i$ and $\tilde{\rho}_{2k}^i = 6^{-1/2}2B_0\rho_{2k}^i$ for the chemical shift while $\tilde{\rho}_{00}^{ij} = \rho_{00}^{ij}$ and $\tilde{\rho}_{2k}^{ij} = 6^{-1/2}\rho_{2k}^{ij}$ for the dipolar coupling.

Inspection of Eq. 1.25 reveals that in the high-field limit, any terms which do not commute with the Zeeman interaction become time-dependent upon transferring to the interaction frame. These non-secular terms are effectively eliminated provided that the Larmor frequency ω_0 is large relative to the internal interactions. In the work presented here, ω_0 is 400 MHz while the largest internal interactions are on the order of tens of kHz[45]. In this limit, the zeroeth order average (consisting of only secular terms) is an excellent approximation and is often referred to as the high-field truncated Hamiltonian. In this example, transferring to the interaction frame defined by the Zeeman interaction of the I spin provides insight into which spin components govern evolution through the LVN equation (1.11) at high-fields. Other interaction frames that will prove convenient in analyzing the response of the spin system to radio frequency irradiation are discussed in Appendix A.

More generally, the above procedure may be performed for a system of abundant spins (I) dipolar coupled to rare spins (S) by transferring to a frame rotating at $\omega_0^I I_z + \omega_0^S S_z$ .and in this case the total Hamiltonian becomes:

$$H = H_I + H_S + H_{IS} + H_{II} \qquad (1.32)$$

with H_I and H_{II} as defined above and H_S defined as H_I with substitution of S for I and the truncated heteronuclear dipolar interaction as:

$$H_{IS} = \sum_{i<j} \omega_{ij}^{IS} 2I_{jZ}S_{kZ} \quad . \qquad (1.33)$$

1.3 Powder Spectra

1.3.1 Single Quantum Excitation

The energy level diagram for a single spin 1/2 nucleus, I, is provided in figure 1.2a. Each state is associated with the Zeeman quantum numbers of -1/2 or +1/2 (from now on depicted - or + respectively) and for the chemical shift, the resulting two energy levels (in the rotating frame) are shifted by $\omega^I/2$. A $(\pi/2)_y$ pulse rotates the equilibrium density operator, proportional to I_Z in the high-temperature limit, into I_X which is referred to as single quantum coherence, depicted by the curly arrow in Figure 1.2. A coherence is a superposition of eigenstates, and in this case a superposition between |-)+|+). Since the difference between Zeeman quantum number involved in the superposition is 1, this superposition is referred to as a single quantum coherence. It is important to note that only single-quantum coherence can be detected. The observation of other coherences, say double quantum, requires indirect observation through the single-quantum coherence via 2D spectroscopy, for example[1].

Figure 1.2 Energy level picture corresponding to a single-quantum transition of spin S alone (a) or dipolar coupled (b) to spin I. In (a), the S spin levels are shifted by half of the chemical shift $\omega^I/2$ while in b -where the S spin shift is neglected- the corresponding levels are shifted by half the dipolar coupling, $\omega^{IS}/2$. The curly lines with arrows denote a the superposition of spin states , single quantum coherence, formed by a $\pi/2$ pulse. In (b), the S spin transitions increase (decrease) when the I spin state is +(-) due to the increase (decrease) in the local field generated by the dipolar interaction giving rise to a "doublet".

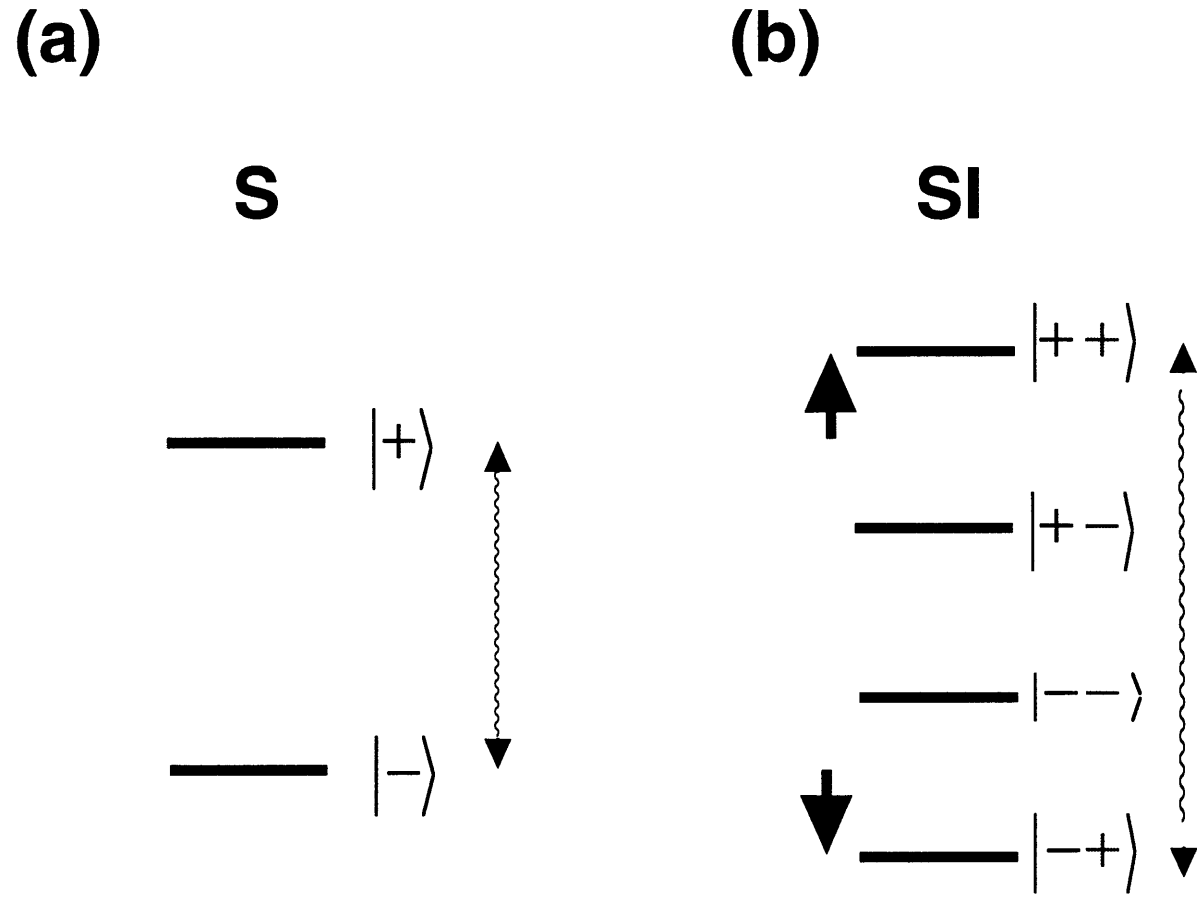

Levels shift by:

$$\frac{\omega^{I}}{2} \qquad \frac{\omega^{IS}}{2}$$

Figure 1.2

With the exact form of the nuclear spin interactions defined, one may proceed to calculate the frequency spectrum of the S spin. For example, for a single spin 1/2 nucleus, the spectrum obtained upon single-quantum excitation is given energy difference between the two spin states as:

$$\omega^I = \omega_0^I\delta_0^I + \omega_0^I\delta_1^I\{\frac{1}{2}(3\cos^2\beta_{PL}-1) - \frac{1}{2}\eta^I\cos2\alpha_{PL}\sin^2\beta_{PL}\} \tag{1.34}$$

and for randomly oriented (powder) solid the resulting spectrum is broadened. (See Figure 1.3) The width off the chemical shift powder pattern depends on the size of the anisotropy, δ_1^I (See Eq 1.10) which is determined by the local electronic environment. The magnitude of the shift tensor is completely characterized by the three principle values which are revealed as singularities in the powder lineshape. Conventionally these components are labeled by the absolute deviation from the isotropic shift with $|\sigma_{iso}-\sigma_{zz}| > |\sigma_{iso}-\sigma_{yy}| > |\sigma_{iso}-\sigma_{xx}|$[40]. By inspection of Eq. 1.34, one can verify that one when the chemical shift tensor has the orientations $\{\alpha_{PL}, \beta_{PL}\}$ of {0,0}, {0,90}, and {90,90} that either σ_{zz}, σ_{xx}, and σ_{yy} are parallel to the static magnetic field as depicted in Figure 1.3. The dependence on electronic environment and orientation render the chemical shift an excellent probe of local structure.

If S is coupled to a different spin 1/2 nucleus, I the dipolar coupling one observes that two S spin single quantum transitions are allowed as depicted in Figure 1.2b. The transitions are shifted by $\omega_{IS}/2$. For example, when the I spin is in the |+) state, one observes a energy difference between the S single-quantum transition as ω_{IS}. This increase in energy is indicated by the arrows in Figure 1.2b. Correspondingly, one also observes a decrease in energy for the S spin SQT corresponding to the I spin state |-). These shifts, resulting from the dipolar interaction are written:

$$\omega^{IS} = \pm [2\pi J_{IS} - b_{IS}(3\cos^2\beta_{PL}-1)/2] \tag{1.35}$$

The corresponding S spin spectrum (neglecting the chemical shift) is depicted in Figure 1.4.

Figure 1.3 Chemical shift spectrum of a randomly oriented solid. The size of the shift depends on the orientation of the shift tensor with respect to the applied magnetic field, B_0 yielding the broad lineshape. The three orientations corresponding to alignment of each of the principle components of the shift tensor parallel to the applied field correspond to the singularities in the powder pattern.

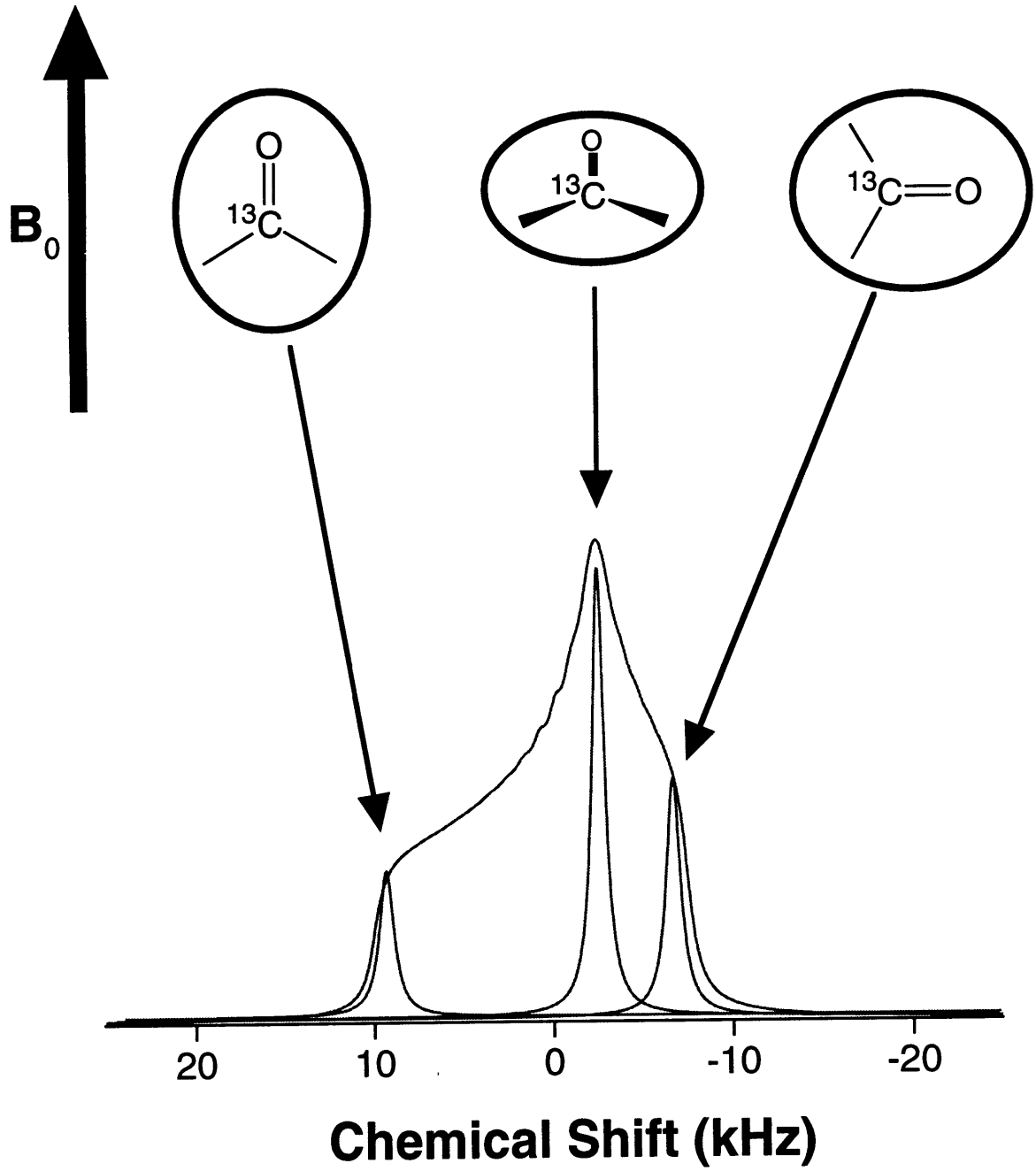

Figure 1.3

Figure 1.4 Spectrum resulting from two, unlike, dipolar coupled spin 1/2 nuclei. The size of the dipolar coupling depends on the inverse cube of the internuclear distance and the orientation of the the dipolar tensor (unique axis directed along the internuclear vector) relative to the applied field B_0. The parallel and perpendicular orientations correspond to the singularities which are positioned at the values of b_{IS} and $b_{IS}/2$.

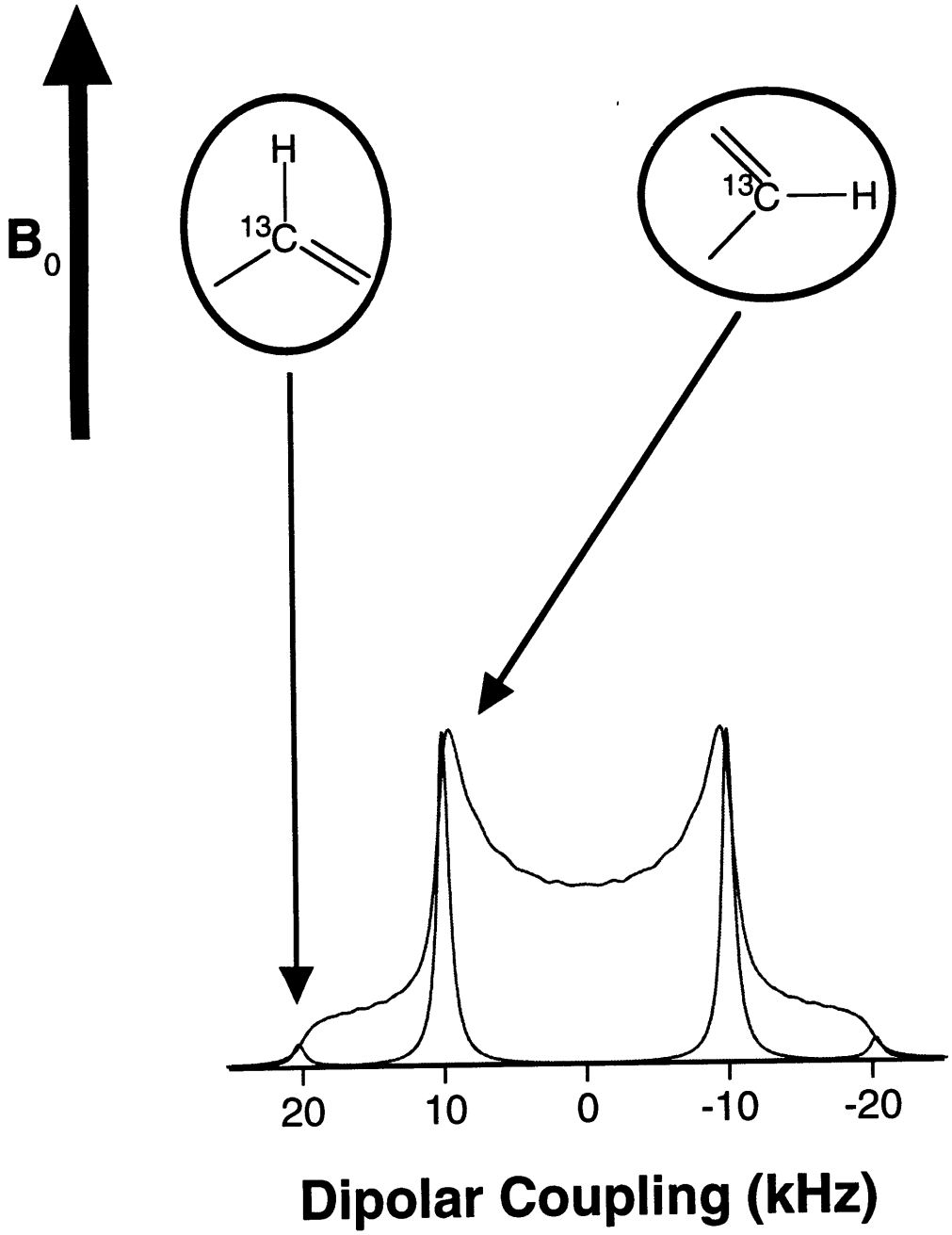

Figure 1.4

The singularities observed correspond to orientations of the unique component of the dipolar tensor - oriented along the internuclear vector- that are parallel and perpendicular to the applied magnetic field direction. From Eq 1.35 one observes that the dipolar interaction depends on the internuclear distance between the two nuclei in addition to the orientation of the dipolar tensor.

1.3.2 Double Quantum Excitation

Double-quantum transitions (DQT)[46], although not directly observable, provide an excellent probe for the relative orientation of tensors[35-39, 47-49]. Depicted in Figure 1.5a is the DQT corresponding to two like spins S_a and S_b. If S_a is dipolar coupled to I_a and S_b to I_b, neglecting the chemical shift interaction, one observes that the DQT depicted in Figure 1.5a breaks into four transitions as shown in Figure 1.5b. In the former case, the DQT oscillate at the some of the chemical shift. In the latter case - assuming that the chemical shift can be turned off by refocusing- one observes that the energy of the DQTs goes as either the sum or difference in the I_a-S_a and I_b-S_b dipolar couplings. Physically, this is due to the fact that the local fields generated from the IS dipolar interaction depend on the I spin state. If the spin states of I_a and I_b are both $|+\rangle$, the energy is increased (or decreased) by the sum of the I_a-S_a and I_b-S_b dipolar couplings while if the spin states are antiparallel, the energy is increased (or decreased) by the difference in the I_a-S_a and I_b-S_b dipolar couplings.

Figure 1.5 Energy level picture of double-quantum coherence of two spin 1/2 nuclei S_a and S_b alone (a) and dipolar coupled to unlike spin 1/2 nuclei I_a and I_b(b). In this example, the I_a-S_b (I_b-S_a) dipolar couplings are assumed zero. In (a), the energy level difference between the double quantum states appears as the sum of the chemical shifts, $\omega^{S_a} + \omega^{S_b}$. In (b)-where the chemical shift are neglected-the dipolar fields generated by the I spins shift the S spin generate 4 double quantum transitions (only two transitions depicted) that correspond to $\pm\omega_\Sigma$ and $\pm\omega_\Delta$, the sum and difference of the dipolar couplings $\omega^{I_a S_a}$, $\omega^{I_b S_b}$.

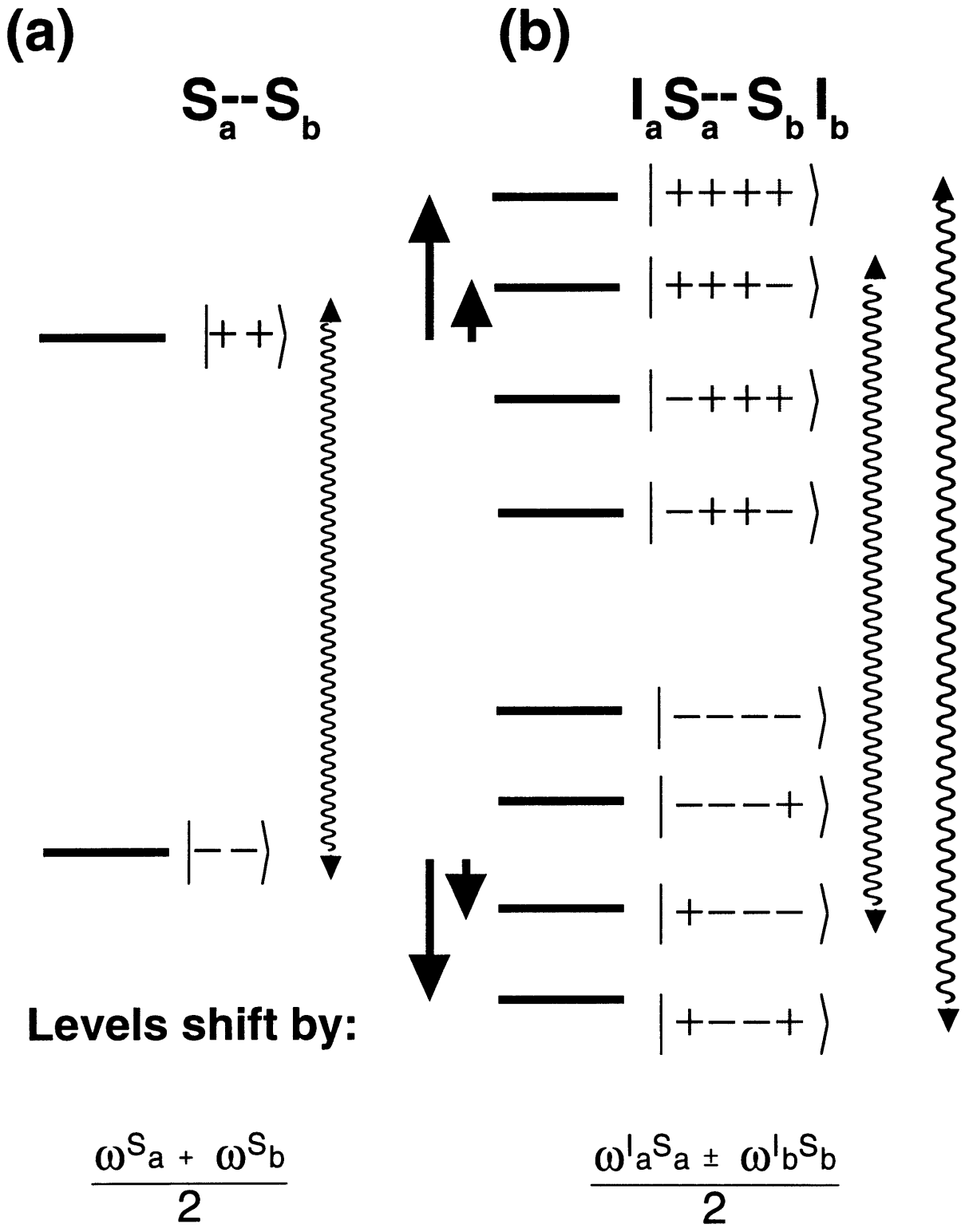
(a)
S_a--S_b
$|++\rangle$
$|--\rangle$
(b)
I_aS_a--S_bI_b
$|++++\rangle$
$|+++-\rangle$
$|-+++\rangle$
$|-++-\rangle$
$|----\rangle$
$|---+\rangle$
$|+---\rangle$
$|+--+\rangle$
Levels shift by:
$\frac{\omega^{S_a} + \omega^{S_b}}{2}$
$\frac{\omega^{I_a S_a} \pm \omega^{I_b S_b}}{2}$

Figure 1.5

This dependence allows the S_a-S_b DQT to be exploited for the measurement of the relative orientation of dipolar tensors. For example, consider a spin system comprised of HCCH nuclei that are directly bonded. Depicted in Figure 1.6a, are two molecular orientations with respect to the applied magnetic field containing two different torsion angles about the C-C bond. The corresponding "stick" spectra for the orientations on the left and right of Figure 1.6a are given on the left and right of Figure 1.6b. Note that distances between H_a-C_a and H_b-C_b are fixed by bond lengths and that the HC dipolar tensors are oriented parallel to the HC bond. On the left of Figure 6.1a, The H_a-C_a dipolar coupling is different than the H_b-C_b coupling due to the different orientations of the tensors with respect to the applied field. C_a-C_b double quantum evolution under these dipolar interaction results in the stick spectrum with the sum and difference dipolar interaction given by ω_Σ and ω_Δ. If the torsion angle in Figure 6.1a is changed to be trans, one observes the dipolar couplings H_a-C_a and H_b-C_b are identical, irrespective of molecular orientation, since the H_a-C_a and H_b-C_b tensors are parallel. Thus, the difference frequency, ω_Δ , is always zero resulting in the stick spectrum on the left of Figure 1.6b. Hence the C_a-C_b DQ spectra depend on the relative orientation of dipolar tensors and in this case, the torsion angle across the HCCH spin system. Figure 1.7 shows the the powder C_a-C_b DQ spectrum of the above HCCH spin system for the cis and trans geometries depicted in Figure 1.6. As expected the trans orientation generates a large feature centered at zero due to the cancellation of dipolar fields that occurs irrespective of molecular orientation. In addition, expansion of the vertical axis demonstrates the sum frequency mimics a dipolar coupling with twice the value for an CH pair. Deviation from the trans geometry reduces this cancellation effect resulting in corresponding changes in the powder lineshape. Methods for observing DQ transitions indirectly we be discussed in more detail in the latter part of this thesis.

Figure 1.6 Schematic representation of two HCCH spin systems with Cis and Trans torsion angles (a) with corresponding stick spectra in (b) resulting from C_a-C_b double quantum evolution under the CH dipolar couplings in the absence of C_a-C_b chemical shifts. A spectral variation results for the molecular orientations depicted in (a) due to the different relative orientations of the H_a-C_a and C_b-H_b dipolar tensors. Specifically, in the left of (a) the Ha-Ca dipolar coupling is different than the H_b-C_b dipolar coupling due to their different orientations with respect to the applied field B_0. The double quantum spectrum results in splitting given by the difference (ω_Δ) and sum (ω_Σ) of these interactions. In contrast, for the orientation depicted in the left of (a), the dipolar couplings are of equal size since the tensors are parallel - and therefore have the same orientation with respect to the applied field B_0- resulting difference frequency of zero giving rise to a pronounced central peak in the corresponding spectrum in (b).

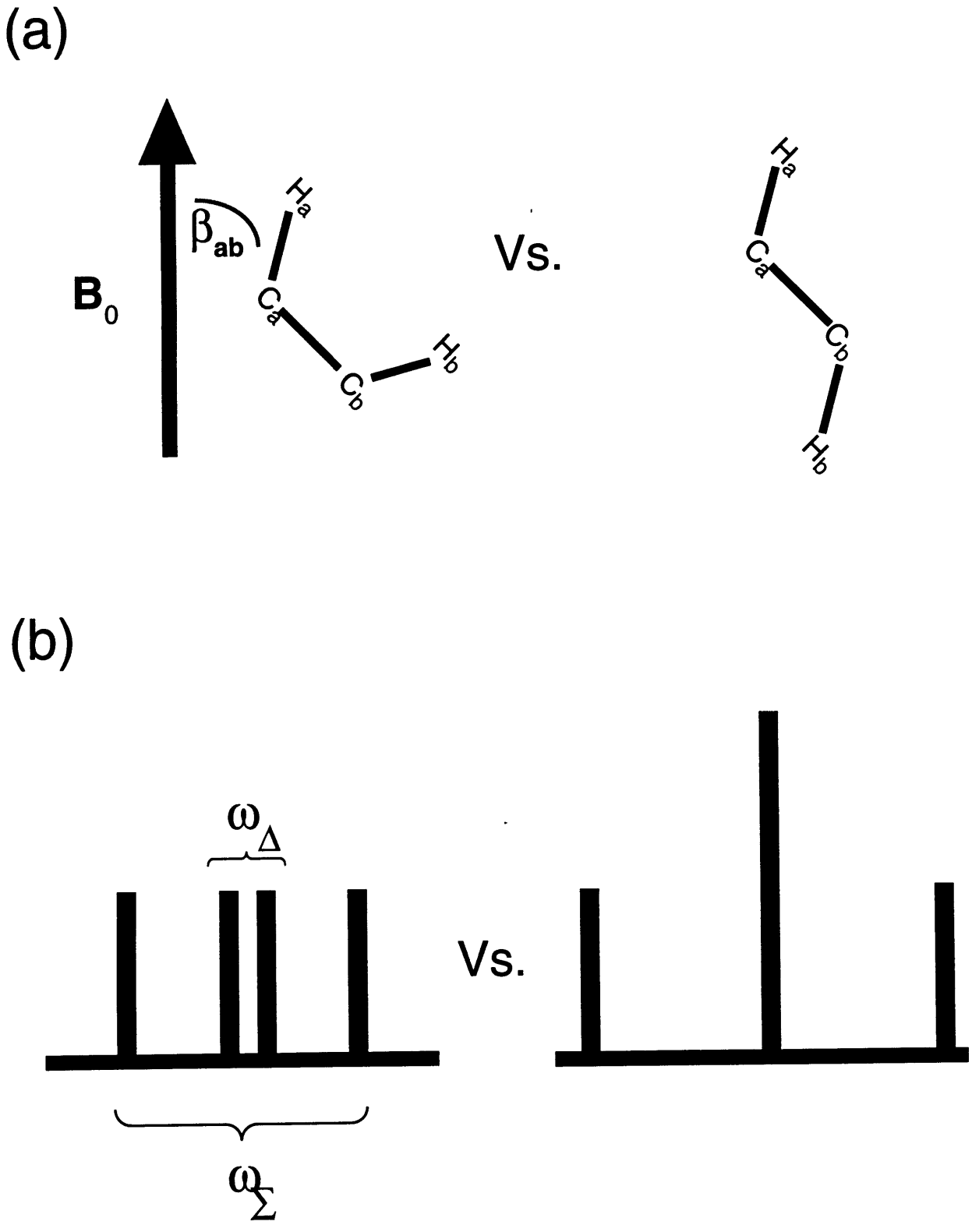
(a)
B_0
β_{ab}
H_a
C_a
C_b
H_b
Vs.
H_a
C_a
C_b
H_b
(b)
ω_Δ
ω_Σ
Vs.

Figure 1.6

Figure 1.7 C_a-C_b double quantum powder spectra corresponding to the HCCH spin system in the Cis (a) and Trans (b) orientation depicted in Figure 1.6a. The central peak in the Trans spectrum corresponds to the fact that for this torsion angle, ω_Δ zero irrespective of molecular orientation since the H_a-C_a and H_b-C_b tensors are parallel and therefore always make the same angle with respect to the magnetic field. Note that in this case, perfect cancellation can occur only if the C_a-H_a and C_b-H_b internuclear distances are equal. An expansion of the vertical axis of (b) results illustrates that for the Trans orientation, a Pake pattern with an effective dipolar coupling of ω_Σ results from the ω_Σ transitions. In this case, where the CH dipolar coupling constant is taken to be 20 kHz, the effective coupling ω_Σ is 40 kHz.

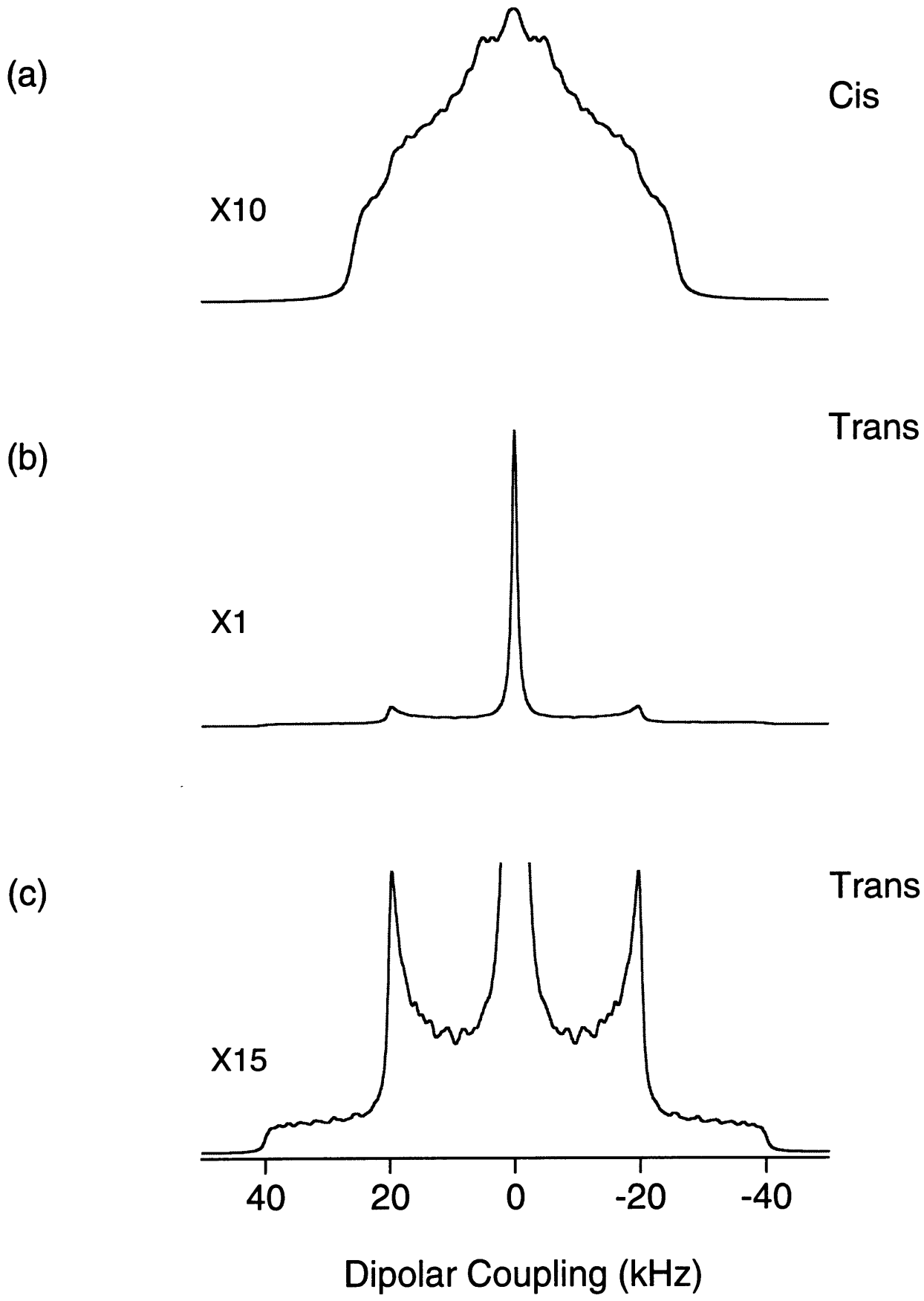
(a)
Cis
X10
(b)
Trans
X1
(c)
Trans
X15
40
20
0
-20
-40
Dipolar Coupling (kHz)

Figure 1.7

1.4 Introduction to Magic Angle Spinning (MAS)

In randomly oriented solids, a gain in resolution may be obtained by spinning the sample about an axis inclined at the magic-angle (54.74°) with respect to the direction of the static magnetic field, B_0[8, 9, 15]. In this case, sample spinning imparts a periodic time dependence on the Hamiltonian 1.32 through modulation of the anisotropic interactions :

$$\omega^Q(t) = \sum_{k=-2}^{2} \sum_{m=-2}^{2} \tilde{\rho}^Q_{2k} D^{(2)}_{km}(\Omega_{PR}) D^{(2)}_{m0}(\Omega_{RL}) = \sum_{m=-2}^{2} \omega^Q_m(\Omega_{PR}) \exp(im\omega_r t) \tag{1.32}$$

The Fourier component, $\omega^Q_m(\Omega_{PR})$ [17]is written:

$$\omega^Q_m(\Omega_{PR}) = \tilde{\rho}^Q_{00}\delta_{m,0} + \sum_{k=-2}^{2} \tilde{\rho}^Q_{2k} D^{(2)}_{k-m}(\Omega_{PR}) d^{(2)}_{-m0}(\beta_{RL}) \tag{1.33}$$

and contains the orientation dependence thereof through the Euler angles $\Omega_{PR} = \{\alpha_{PR}, \beta_{PR}, \gamma_{PR}\}$ that map the interaction tensor from its PAS to the rotor fixed frame. Depicted in Figure 1.8 is a series of simulated spectra of an isolated carbonyl group (CO) of glycine. Without MAS, a powder pattern results due to the large chemical shift anisotropy (CSA) of the CO moiety. (See Figure 1.8a, left). Upon the introduction of MAS, this broad powder lineshape breaks into rotational sidebands which are spaced at the spin rate $\omega_r/2\pi$. As the spin rate increases, the centerband increases with intensity along with a reduction in intensity of the rotational sidebands. In the limit of fast spinning relative to the size of the CSA, the rotational sidebands vanish leaving behind the centerband which reports on the value of the isotropic shift. In Figure 1.8, right a similar behavior is observed for the heteronuclear dipolar coupling.

Figure 1.8 The effect of MAS on the chemical shift and dipolar (heteronuclear) interactions. As the spinning speed increases from zero to 12 kHz the respective powder patterns are broken up into rotational sidebands separated by the spin rate, $\omega_r/2\pi$, until the limit where the spinning speed exceeds the magnitude of the anisotropic interactions is reached. As the spinning is increased, the reduced sideband intensity is folded into the centerband giving rise to the most intense signal in the fast spinning limit.

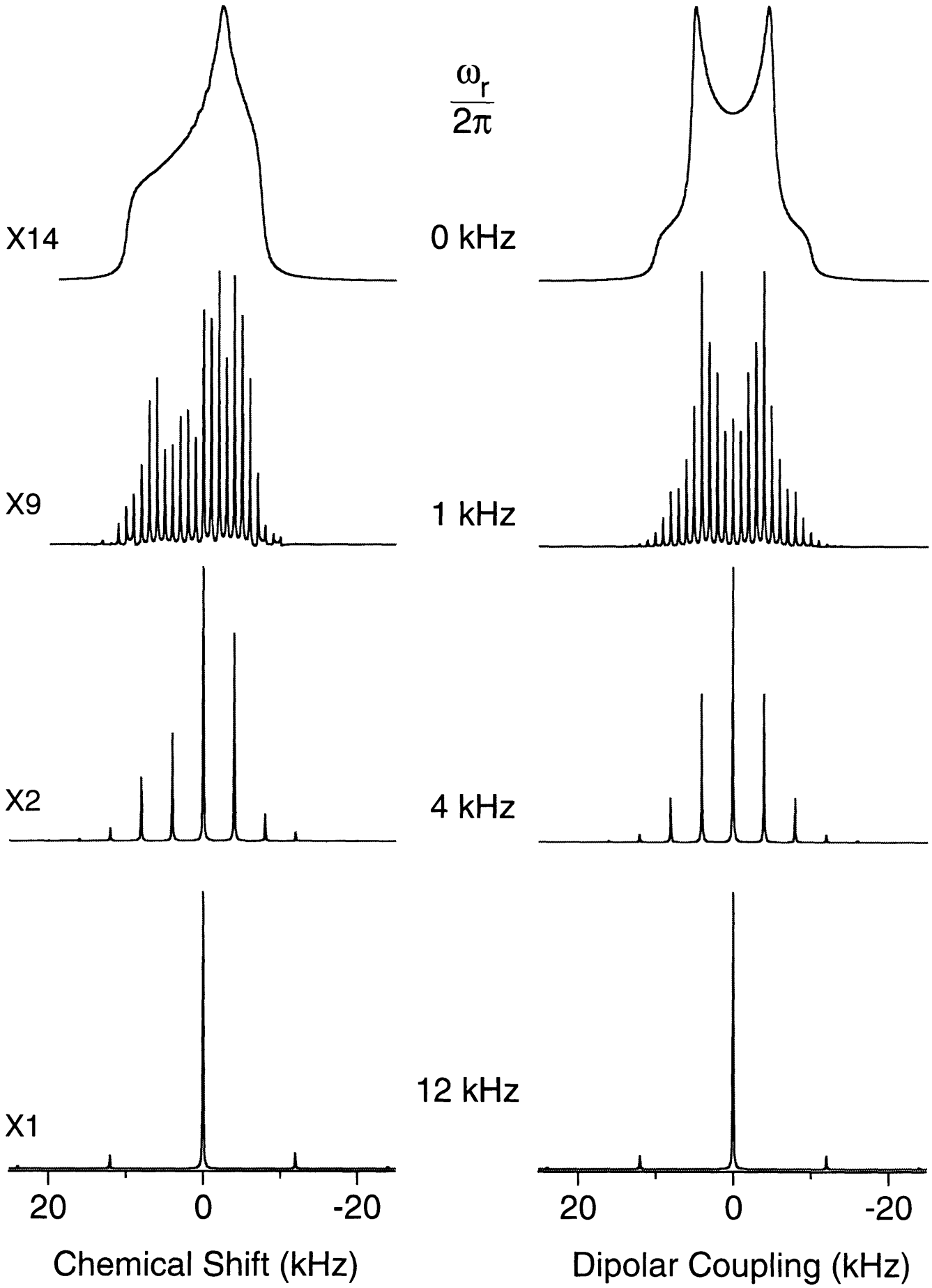
$\frac{\omega_r}{2\pi}$
X14
0 kHz
X9
1 kHz
X2
4 kHz
X1
12 kHz
20
0
-20
Chemical Shift (kHz)
20
0
-20
Dipolar Coupling (kHz)

Figure 1.8

Since both the chemical shift and heteronuclear dipolar interactions commute with themselves at different times, the evolution may be written:

$$\langle S^+\rangle(t) = \exp\{-i\Phi_S(t,0)\} \tag{1.34a}$$

$$\langle S^+\rangle(t) = \cos\{\Phi_{IS}(t,0)\} \tag{1.34b}$$

where the dynamic phase[17] defined:

$$\Phi_Q(t_b,t_a) = \exp\{-i\int_{t_a}^{t_b} dt\ \omega^Q(t)\} \tag{1.35}$$

$$= \tilde{\rho}_{00}^{Q}\,(t_b - t_a) + \sum_{m\neq 0} \frac{\omega_m^Q\,(\Omega_{PR})}{im\omega_r}\{\exp(im\omega_r t_b) - \exp(im\omega_r t_b)\}\ .$$

Analytical expressions for the sideband intensities are complex but may be obtained in a closed form solution by expanding Eq. 1.34 as an infinite series of Bessel functions of the first kind[50]. Nevertheless, from the dynamic phase, Eq 1.35, it is obvious that in the high spinning limit, where $\omega_r >> b_{IS}, \delta_1^{I,S}$ that only the centerband - determined by the isotropic part of Eq. 1.35 remains.

In contrast, MAS has little or no effect on the ^{1}H linewidth which is dominated by strong homonuclear dipolar interactions[14]. The ability of MAS to average the CSA over the homonuclear dipolar interactions stems from the unique nature of the homonuclear dipolar coupling. (See II) The critical distinction is that for the case of the CO CSA, the Hamiltonian commutes with itself at different times[15]. Therefore, calculating the zeroth-order Average Hamiltonion with τ_c is $2\pi/\omega_r$ we have the CSA vanishes. However, the homonuclear dipolar interaction does not commute with itself at different times rendering MAS ineffective at averaging the dipolar interactions. In the parlance of Maricq and Waugh a periodic Hamiltonian H(t) is homogeneous if $[H(t),H(t')] \neq 0$[15]. The homogeneous Hamiltonian is complicated by the fact that its eigenvalues and eigenstates are changing with time, whereas for an inhomogeneous Hamiltonian, only the eigenvalues change with time. For example, in the case of two like spin 1/2 nuclei under MAS, the Hamiltonian $H(t) = H_I(t) + H_{II}(t)$ is such that $[H(t),H(t')] \neq 0$[15]. The homogeneous nature of the this two spin system manifest as a broadening of spectral features which is maximized on "rotational resonance" where $(\omega_\Delta^{iso} - n\omega_r) = 0$ where ω_Δ^{iso} is the

difference in isotropic shift between the two spins and n is an integer. This effect has been studied in detail by several authors[8, 15, 17, 51]. In the high-speed spinning limit where

$$\frac{\left|\omega_n^{II}\right|}{\left|(\omega_\Delta^{iso} - n\omega_r)\right|} << 0 \qquad (1.36)$$

with ω_{II}^n as the dipolar Fourier defined in Eq. (1.33), the broadening is proportional to:

$$\sum_{n\neq 0} \frac{\omega_{\Delta,n}^{aniso}\,\omega_{-n}^{II}}{n\omega_r} \qquad (1.37a)$$

for n=0[15] where $\omega_{\Delta,n}^{aniso} = \omega_n^{I_i} - \omega_n^{I_j}$ is the Fourier component associated with the difference in the anisotropic part of the I_i and I_j spin chemical shifts. For n>0[17]:

$$\sum_{n\neq 0} \frac{\left|\omega_n^{II}\right|^2\,\omega_\Delta^{iso}}{2\,n^2\omega_r^2} \quad . \qquad (1.37b)$$

The broadening for the case of multiple spins is exacerbated by the fact that $[H_{II}(t),H_{II}(t')] \neq 0$ [14].

1.5 Spatial Dynamics

The fast limit for an internal interaction Q is defined as (12)[52]:

$$\omega^Q\tau_c << 1 \qquad (1.38)$$

where λ denotes either the quadrupolar, dipolar, or chemical shift interaction. In the fast limit, for discrete hopping the motionally averaged Hamiltonian is[53, 54]

$$\langle H^Q\rangle = \sum_{j=1}^{N} P_{eq,j}(\alpha,\beta,\gamma)\, H_j^Q(\alpha,\beta,\gamma) \qquad (1.39)$$

where Peq,j is the equilibrium occupancy probability and H_j^Q is the Hamiltonian for the jth site.

Since motion modulates only the spatial part of H^Q, calculating the motionally averaged Hamiltonian amounts to finding the motionally averaged tensor:

$$\left\langle \widetilde{\omega_C^Q} \right\rangle = \widetilde{\rho^Q} \left\langle D^{(2)}(\Omega_{PC}) \right\rangle \tag{1.40}$$

where $D^{(2)}(\Omega_{PC})$ is the Wigner Rotation matrix that transforms the 2nd rank spherical tensor $\widetilde{\rho^Q}$ from its principle axis system to the common or molecular frame C[40]. Separate and uncorrelated motions may be represented by successive transformations of averaged rotations in the J and C frame[53, 54]:

$$\left\langle D^{(2)}(\Omega_{PC}) \right\rangle = \left\langle D^{(2)}(\Omega_{PJ}) \right\rangle \left\langle D^{(2)}(\Omega_{JC}) \right\rangle. \tag{1.41}$$

1.5.1 Example-Fast Limit Axial Diffusion

Consider a molecule, like a lipid in a lipid bilayer or a helical transmembrane peptide, that undergoes fast limit reorientation about the molecular long axis. Assuming that the correlation time of this process is orders of magnitude shorter than the inverse of the MAS rate, the mth Fourier component under MAS may be written:

$$\left\langle \omega_m^Q (\Omega_{PR}) \right\rangle = \tilde{p}_{00}^Q \delta_{m,0} + \sum_{l=-2}^{2} \sum_{k=-2}^{2} \tilde{p}_{2k}^Q \left\langle D_{kl}^{(2)} (\Omega_{PD}) \right\rangle D_{l-m}^{(2)} (\Omega_{DR}) d_{-m0}^{(2)} (\beta_{RL}) \tag{1.42}$$

where

$$\left\langle D_{kl}^{(2)} (\Omega_{PD}) \right\rangle = e^{-ik\alpha_{PD}} d_{kl}^{(2)}(\beta_{PD}) x \frac{1}{2\pi} \int_0^{2\pi} d\gamma_{PD} \exp\{-il\gamma_{PD}\}$$
$$= e^{-ik\alpha_{PD}} d_{kl}^{(2)}(\beta_{PD}) \delta_{l,0} \ . \tag{1.43}$$

With Eq 1.43 Eq. 1.42 is written:

$$\left\langle \omega_m^Q (\Omega_{PR}) \right\rangle = \tilde{p}_{00}^Q \delta_{m,0} + \left\langle \tilde{p}_{20}^Q \right\rangle D_{0-m}^{(2)} (\Omega_{DR}) d_{-m0}^{(2)} (\beta_{RL}) \tag{1.44}$$

where

$$\left\langle \tilde{p}_{20}^Q \right\rangle = \sum_{k=-2}^{2} \tilde{p}_{2k}^Q d_{k0}^{(2)}(\beta_{PD}) e^{-ik\alpha_{PD}} \tag{1.45}$$

is an axially symmetric tensor with the unique axis aligned parallel to the Z-axis of the Diffusion frame. (The axial diffusion axis). For example, the motionally averaged dipolar tensor is written:

$$\langle \tilde{\rho}^{IS}_{20} \rangle = [(3\cos^2\beta_{PD} - 1)/2]\tilde{\rho}^{IS}_{20} \qquad (1.46)$$

In the case of fast-limit axial diffusion alone, the motionally averaged dipolar interaction contains structural information. Figure 1.9 depicts a series of MAS spectra where a CH moiety is under going fast limit axial diffusion and the dependence on β_{PD}.

Figure 1.9 A dipolar powder spectra with a MAS rate of 1kHz corresponding to: an immobile CH group (a) and the result of fast-limit axial diffusion with orientations, θ, of the CH tensor relative to the diffusion axis (Z_C) of 90,45, and 54.74 ° in (b), (c), and (c) respectively indicating the $P_2(\cos(\theta))$ dependence of the motional averaged interaction.

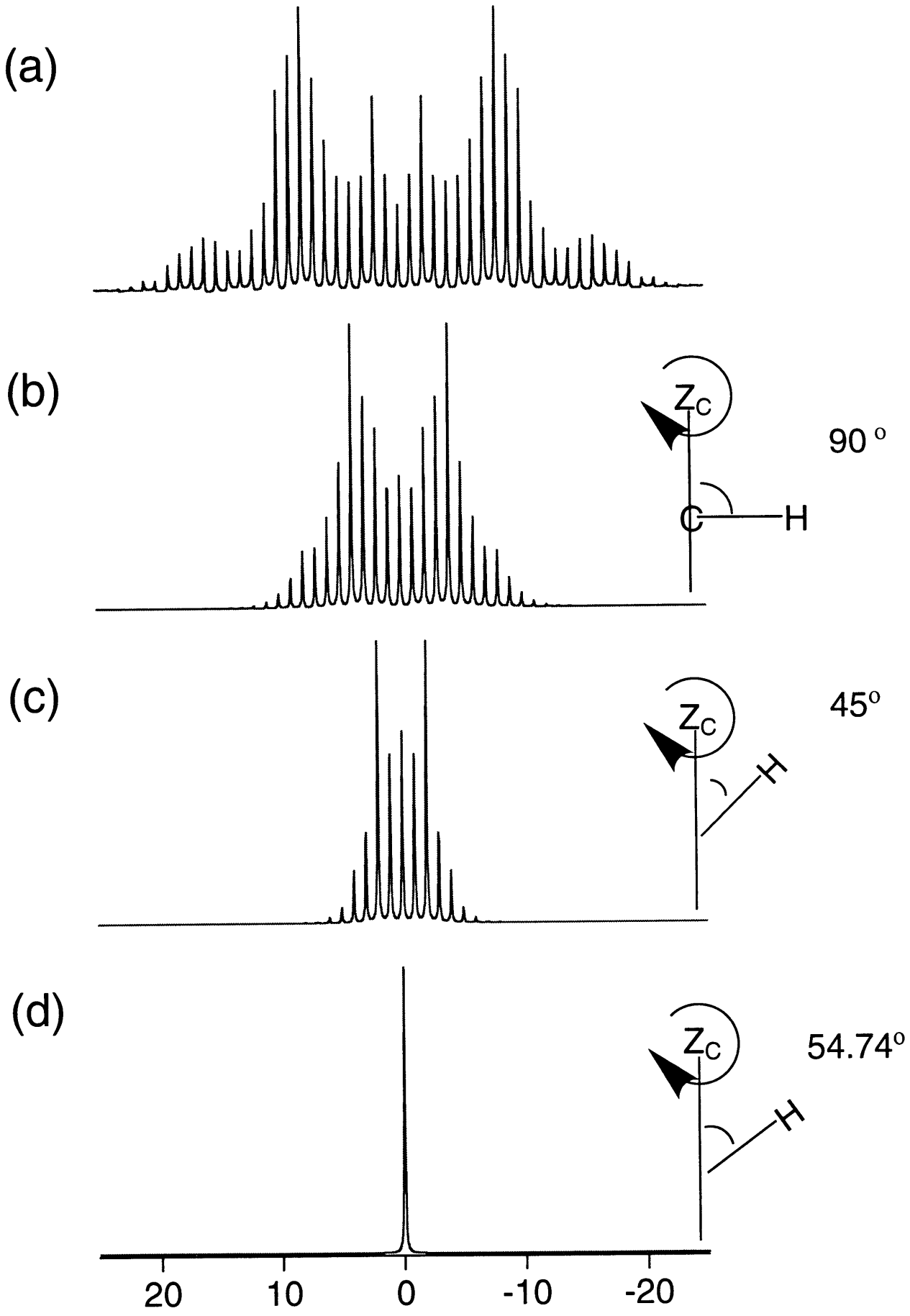

Figure 1.9

Clearly, for a directly bonded CH group where the bond length, and therefore magnitude of the static dipolar interaction, is known, one is able to extract the orientation of the CH dipolar tensor relative to the motional axis through β_{PD}.

References for Chapter 1

[1] R. R. Ernst, G. Bodenhausen and A. Wokaun, Principles of Nuclear Magnetic Resonance in One and Two Dimensions, (Clarendon Press, Oxford, 1987).

[2] J. M. Griffiths, K. V. Lakshmi, A. E. Bennett, J. Raap, C. M. Vanderwielen, J. Lugtenburg, J. Herzfeld and R. G. Griffin, J. Am. Chem. Soc. 116 (1994) 10178.

[3] A. E. MacDermott, F. Creuzet, R. Gebhard, K. Vanderhoef, M. H. Levitt, J. Herzfeld, J. Lugtenburg and R. G. Griffin, Biochemistry 33 (1994) 6129.

[4] Y. Li, R. J. Appleyard, W. A. Shuttleworth and J. N. S. Evans, J. Am. Chem. Soc. 116 (1994) 10799.

[5] D. R. Studelska, L. M. McDowell, M. P. Espe, C. A. Klug and J. Schaefer, Biochemistry 36 (1997) 15555.

[6] G. E. Pake, J. Chem. Phys. 16 (1948) 327.

[7] A. Pines, M. G. Gibby and J. S. Waugh, J. Chem. Phys. 59 (1973) 569.

[8] E. R. Andrew, A. Bradbury and R. G. Eades, Nature (London) 182 (1958)

[9] I. J. Lowe, Phys. Rev. Lett. 2 (1959) 285.

[10] A. L. Bloom and J. N. Shoolery, Phys. Rev. 97 (1955) 1261.

[11] V. Royden, Phys. Rev. 96 (1954) 543.

[12] J. S. Waugh, J. Magn. Reson. 50 (1982) 30.

[13] A. E. Bennett, C. M. Rienstra, M. Auger, K. V. Lakshmi and R. G. Griffin, J. Chem. Phys. 103 (1995) 6951.

[14] U. Haeberlen and J. S. Waugh, Phys. Rev. 175 (1968) 453.

[15] M. Maricq and J. S. Waugh, J. Chem. Phys. 70 (1979) 3300.

[16] A. J. Shaka and J. Keeler, Prog. in NMR Spectroscopy 19 (1987) 47.

[17] M. H. Levitt, D. P. Raleigh, F. Creuzet and R. G. Griffin, J. Chem. Phys. 92 (1990) 6347.

[18] S. P. Rucker and A. J. Shaka, Mol. Phys. 68 (1989) 509.

[19] J. S. Waugh, L. M. Huber and U. Haeberlen, Phys. Rev. Lett. 20 (1968) 180.

[20] U. Haeberlen, High Resolution NMR in Solids: Selective Averaging, (Academic Press, New York, 1976).

[21] A. E. Bennett, R. G. Griffin and S. Vega, in: Vol. 33, ed. 1994) p. 1

[22] J. M. Griffiths and R. G. Griffin, Anal. Chim. Acta 283 (1993) 1081.

[23] R. Tycko and G. Dabbagh, Chem. Phys. Lett. 173 (1990) 5.

[24] T. Gullion and J. Schaefer, J. Magn. Reson. 81 (1989) 196.

[25] A. W. Hing, S. Vega and J. Schaefer, J. Magn. Reson. 96 (1990) 205.

[26] A. E. Bennett, J. H. Ok, R. G. Griffin and S. Vega, J. Chem. Phys. 92 (1992) 8624.

[27] B. Q. Sun, P. R. Costa, D. Kocisko, P. T. Lansbury and R. G. Griffin, J. Chem. Phys. 102 (1995) 702.

[28] D. M. Gregory, D. J. Mitchell, J. A. Stringer, S. Kiihne, J. C. Shiels, J. Callahan, M. A. Mehta and G. P. Drobny, Chem. Phys. Lett. 246 (1995) 654.

[29] Y. K. Lee, N. D. Kurur, M. Helmle, O. G. Johannessen, N. C. Nielsen and M. H. Levitt, Chem. Phys. Lett. 242 (1995) 304.

[30] M. Baldus, R. J. Iuliucci and B. H. Meier, J. Am. Chem. Soc. 119 (1997) 1121.

[31] A. E. Bennett, L. R. Becerra and R. G. Griffin, J. Chem. Phys. 100 (1994) 812.

[32] P. R. Costa, B. Q. Sun and R. G. Griffin, J. Am. Chem. Soc. 119 (1997) 95.

[33] B. Q. Sun, C. M. Rienstra, P. R. Costa, J. R. Williamson and R. G. Griffin, J. Am. Chem. Soc. 119 (1997) 8540.

[34] P. R. Costa, Thesis, Ph.D., Massachusetts Institute of Technology (1996).

[35] X. Feng, Y. K. Lee, D. Sandstrom, M. Eden, H. Maisel, A. Sebald and M. H. Levitt, Chem. Phys. Lett. 257 (1996) 314.

[36] M. Hong, J. D. Gross and R. G. Griffin, J. Phys. Chem. 101 (1997) 5869.

[37] M. Hong, J. D. Gross, C. M. Rienstra, R. G. Griffin, K. K. Kumashiro and K. Schmidt-Rohr, J. Magn. Reson. 129 (1997) 85.

[38] P. R. Costa, J. D. Gross, M. Hong and R. G. Griffin, Chem. Phys. Lett 280 (1997) 95.

[39] X. Feng, M. Eden, A. Brinkmann, H. Luthman, L. Eriksson, A. Graslund, O. N. Antzutkin and M. H. Levitt, J. Am. Chem. Soc. 119 (1997) 12006.

[40] H. W. Spiess, in: Vol. 15, ed. 1978) p. 55

[41] J. J. Sakurai and S. F. Tuan, Modern Quantum Mechanics, (Benjamin/Cummings Publishing, Menlo Park, 1985).

[42] W. Magnus, Pure Math. 7 (1954) 649.

[43] P. Pechukas and J. C. Light, J. Chem. Phys. 44 (1966) 3897.

[44] W. A. B. Evans, Ann. Phys. 48 (1968) 72.

[45] This holds true for diamagnetic solids with the exception the quadrupolar interaction.

[46] A. Wokaun and R. R. Ernst, Mol. Phys. 38 (1979) 1579.

[47] K. Schmidt-Rohr, Macromolecules 29 (1996) 3975.

[48] K. Schmidt-Rohr, J. Am. Chem. Soc. 118 (1996) 7601.

[49] D. M. Gregory, M. A. Mehta, J. C. Shiels and G. P. Drobny, J. Chem. Phys. 107 (1997) 28.

[50] J. Herzfeld and A. E. Berger, J. Chem. Phys. 73 (1980)

[51] D. P. Raleigh, M. H. Levitt and R. G. Griffin, Chem. Phys. Lett. 146 (1988) 189.

[52] A. Abragam, The Principles of Nuclear Magnetism, (Oxford University Press, London, 1961).

[53] D. A. Torchia and A. Szabo, J. Magn. Reson. 49 (1982) 107.

[54] D. A. Torchia and A. Szabo, J. Magn. Reson. 64 (1985) 135.

2. Multidimensional NMR in Lipid Systems. Coherence Transfer Through J Couplings under MAS

2.1 Introduction

Lipids are amphipathic molecules that may adopt a variety of arrangements when hydrated. One such arrangement is a bilayer where the hydrophilic lipid head groups are exposed to water and the hydrophobic tails are buried within the bilayer interior. Cell membranes are composed of a lipid bilayer which is the solvent for membrane proteins, peptides, and glycoconjugates, and act as a complex interface for cell-cell recognition, signal transduction, and many enzymatic reactions. Such membranes are often described in beginning cell biology text as a random two dimensional fluid where the lipid bilayer provides a matrix for surrounding proteins. However, the distribution of lipids in membranes is far from random. For example, membrane asymmetry is necessary for the proper functioning of enzymes, and lipid composition effects membrane fluidity. In addition it is thought that the lateral distribution of lipids in a bilayer, whether a random mixture or non-random clusters, has an effect on the activity of certain membrane enzymes [1].

Lipids bilayers may occupy two types of phases: the gel phases, such as L_β and $L_{\beta'}$ and the liquid crystalline phases, such as L_α and H_{II}. Liquid crystalline phases are usually characterized by the disorder in the acyl chains that is concomitant with the gel-liquid crystalline phase transition. The gel phase has a high population of all-trans conformers, so bilayers are generally thicker than the fluid phase. The high level of gauche conformers in the fluid phase reduces chain packing, and consequently, long range order is reduced. In addition, the axial diffusion and gauche-trans isomerization correlation times decrease upon chain melting from 10^{-5} s in the Gel phase to shorter than 10^{-8} s in the liquid crystalline phase [2]. Much of the connection between disorder, molecular dynamics, and motional rates with particular bilayer phases has been established by ^2H NMR [2-4]. An advantage of ^2H NMR is that the quadrupolar interaction is larger than all other internal interactions which simplifies interpretation of powder spectra. For example, the rigid lattice quadrupolar coupling, e2qQ/h, is ~ 168 kHz for a C-^2H bond, the maximum dipolar coupling found in a geminal methylene ^2H-^2H pair is only 1 kHz, and at B_0 = 9.4 T, the range of chemical shifts is under 1.5 kHz. In addition, the orientation dependence of quadrupolar coupling makes it a good reporter of motion on time scales ranging

from 10^{-3} to 10^{-10} s. However, ^2H has a natural abundance of .016%, so ^2H spectroscopy isotopic enrichment. The poor chemical shift dispersion of ^2H poses a severe obsticle probing multiple sites. in order a complete picture of the dynamics. Therefore spectroscopy is typically performed on many samples, each with only one or two ^2H labels, to facilitate analysis.

In the following two chapters, an alternative approach to probing segmental order is explored. The ^{13}C-^1H dipolar coupling of a directly bonded CH group provides the same information as the ^2H quadrupole tensor in a similar environments since both the quadropole and dipole tensors are axially symmetric and directed along the intervening CH bond. Measurements of residual ^{13}C-^1H dipolar couplings may be performed with the site resolution provided by the ^{13}C isotropic chemical shift as presented in Chapter 3. Therefore, if the ^{13}C-^1H dipolar couplings for each CH (or CH_2) site may measured provided that the ^{13}C chemical shift assignments are known. In this chapter, techniques for obtaining ^{13}C chemical shift asigments in lipid bilayers are presented.

Multidimensional chemical shift correlation spectroscopy is a standard analytical tool for unraveling complicated NMR spectra of biomolecules in solution. These techniques are useful for establishing connectivity relationships and resonance assignments which are subsequently required for interpretation of NOESY spectra that contain information related to internuclear distances [5]. In general, chemical shift correlations are established by coherence transfer between nuclear spins which may proceed through either dipolar (through space) or scalar J (through bond) couplings. However, in isotropic liquids, molecular tumbling averages spatially dependent interactions such as dipolar couplings and chemical shift anisotropies (CSAs) to zero, leaving behind the rotationally invariant scalar couplings and isotropic chemical shifts.

The situation in rigid solids is quite different. CSAs and dipolar couplings are not averaged due to the absence of molecular motions, and these orientation dependent interactions give rise to characteristic powder lineshapes. Nevertheless, high resolution liquid-like spectra are obtained routinely by application of Magic Angle Spinning (MAS) which averages inhomogeneous interactions such as CSA, heteronuclear, and, in certain cases, homonuclear dipolar couplings [6].

Recently, there has been a resurgence of interest in chemical shift correlation spectroscopy in rigid solid and semisolid materials. Most schemes employ MAS along with a mixing period where dipolar couplings are partially restored [7-10]. Such mixing schemes have reduced transfer efficiency due to the orientation dependence of the recoupled dipolar interaction; therefore, transfer through the isotropic J coupling could potentially offer improved signal strengths. However, coherence transfer through J couplings in MAS of rigid solids is precluded in most biomolecules since the magnitude of the J coupling is smaller than the homogeneous linewidth. In addition, ^{13}C-^{1}H transfer is complicated by ^{1}H-^{1}H interactions that render the proton reservoir at least partially homogeneous [6].

In contrast to rigid solids, lipid/water systems in the L_α and H_{II} phases- present in biological membranes under physiological conditions- undergo high frequency motions such as gauche-trans isomerization and lateral and axial diffusion which attenuate both inter and intramolecular dipolar interactions [11, 12]. Furthermore, as illustrated by Forbes et. al., fast limit axial diffusion renders the proton reservoir inhomogeneous , thus MAS of lipid/water systems in the liquid crystalline phase attenuates residual anisotropic interactions thereby producing high resolution ^{1}H spectra [13]. (See Appendix B) This fact plus the observation that lipid systems yield ^{13}C spectra with linewidths of a few hertz [14] permits observation of both J_{CH} and J_{CC} in spinning samples.

In what follows, a discussion of fast limit motion and the effects on ^{1}H MAS dynamics is presented. Then, the possibilities of combining pulse schemes routinely employed in solution state NMR with MAS to obtain information about intermolecular interactions are presented. It is found that solution state coherence transfer schemes along with MAS provide high-resolution multidimensional ^{13}C-^{1}H and ^{13}C-^{13}C chemical shift connectivity relationships and resonance assignments. Such assignments will facilitate the assignment of ^{13}C-^{1}H segmental order parameters as discussed in Chapter 3.

2.2. Motional Averaging and Attenuation of Anisotropic Interactions

2.2.1 Fast Motions

In L_a phase multilamellar vesicles, lipids undergo fast reorientation about their molecular long axis in addition to rapid gauche-trans isomerization. Axial diffusion rates vary from 10^8 s^{-1} for phospholipids to 10^9 s^{-1} for galactolipids while the rates of gauche-trans rearrangement of methylene groups in acyl chains vary between 10^{10} and 10^{12} s^{-1} [15, 16]. These motions are fast on ^1H time scale (~10^{-5} s.) and cause considerable attenuation of anisotropic interactions. One can calculate the motionally averaged couplings for fast axial diffusion and gauche-trans isomerization by using the fast limit theory outlined above. By modeling gauche-trans isomerization as a three site hop where the equilibrium populations of gauche-sites are equal and by superimposing fast continuous axial diffusion one finds that methylene group ^2H quadrupole couplings, ^1H-^{13}C dipolar couplings and ^1H CSA(assuming η=0) get scaled by $-P_t/2$ where P_t trans population. Likewise, geminal ^1H-^1H couplings get scaled by $-(3P_t+1)/8$. Experimentally it is found that P_t ranges from .3 to .6 which implies that directly bonded ^1H-^{13}C dipolar couplings may be scaled from their rigid lattice value of 20 kHz to ~ 3 kHz while geminal ^1H-^1H dipolar coupling may get scaled from ~ 20 kHz to 5 kHz. The considerable attenuation of ^1H-^1H dipolar dipolar interactions along with the symmetry properties of rapid axial motion on the MAS Hamiltonian (as discussed in Appendix B) renders the ^1H reservoir inhomogeneous under experimentally realizable magic angle spinning speeds.

2.2.2 Slow Motions

Lateral diffusion takes place in the plane perpendicular to the bilayer normal. One might argue that all axially symmetric anisotropic interactions may be averaged to zero by lateral diffusion in spherical vesicles since their size goes as $(3\cos^2\beta-1)/2$ where β is the angle between the bilayer normal and the static magnetic field which may change from 0 to 2π; however, the correlation time for lateral diffusion goes as $R^2/6D$ where D is the lateral diffusion constant and R is the vesicle radius [4]. The multilameller vesicles used in all of the following NMR experiments have radii of 1000 angstroms or more while lateral diffusion coefficients may be as high as 10^{-11} m^2 s^{-1}. So

the lateral correlation time is of order 10^{-3} s which is insufficient to motionally average ^{1}H-^{1}H or ^{1}H-^{13}C couplings.

2.3 Experimental

For the following, all spectra were recorded at room temperature on a home-built solid-state spectrometer operating at 397.7 MHz for ^{1}H and 100.0 MHz for ^{13}C. The MAS probe was also home-built and utilized rotors and stators purchased from Doty Scientific, Inc. (Columbia, South Carolina). Typical ^{1}H and ^{13}C pulse lengths were 4.5 and 5 us, respectively. Natural abundance monogalactosyldiacyldiglyceride (MGDG) (primarily 1,2-di[(9Z,12Z,15Z)octadec-9,12,15-trienoyl]-3-beta-D-galactopyranosyl-sn-glycerol) was purchased from Lipid Products (South Nutfield, Surrey, U.K.) and used without further purification. Uniformly ^{13}C labelled MGDG (U-(^{13}C)-MGDG) was isolated from a crude lipid mixture that was extracted with acetone/chloroform/methanol (2/1/1) from *Spirulina Maxima* grown on ^{13}C sodium carbonate as the sole carbon source. The U-(^{13}C)-MGDG fraction was separated using chromatography on silica gel columns eluted with 9:1 (chloroform/acetone) and purified by TLC on silica gel plates. ^{13}C enrichment was estimated at 98% using mass spectrophotometry. The sample is a mixture containing different levels of saturation in the acyl chains which are 16 and 18 carbons in length as revealed by TLC. The 16 carbon chain is roughly 84% saturated and 16% delta 7. The 18 carbon chain is 77% delta 6:9:12, 10% delta 9:12, 10% delta 9 and 3% saturated.

2.4 Results and Discussion

Figure 2.1a is a static ^{1}H spectrum of a natural abundance mixture of MGDG as a 1:1 w/w ratio dispersion in D_2O at room temperature. MGDG is thought to be in the H_{II} phase at ~ 22 °C under these conditions [17]. Figure 2.1b is the same sample spinning at 6.6 kHz about the magic angle and shows resolved isotropic chemical shifts consistent with spectra obtained by Adebodun, et. al.[18].

Figure 2.1 ^1H Bloch decay of natural abundance MGDG/D_2O mixture described in text. (a) Static and (b) MAS with $\omega_r/2\pi$ = 6.6 kHz.

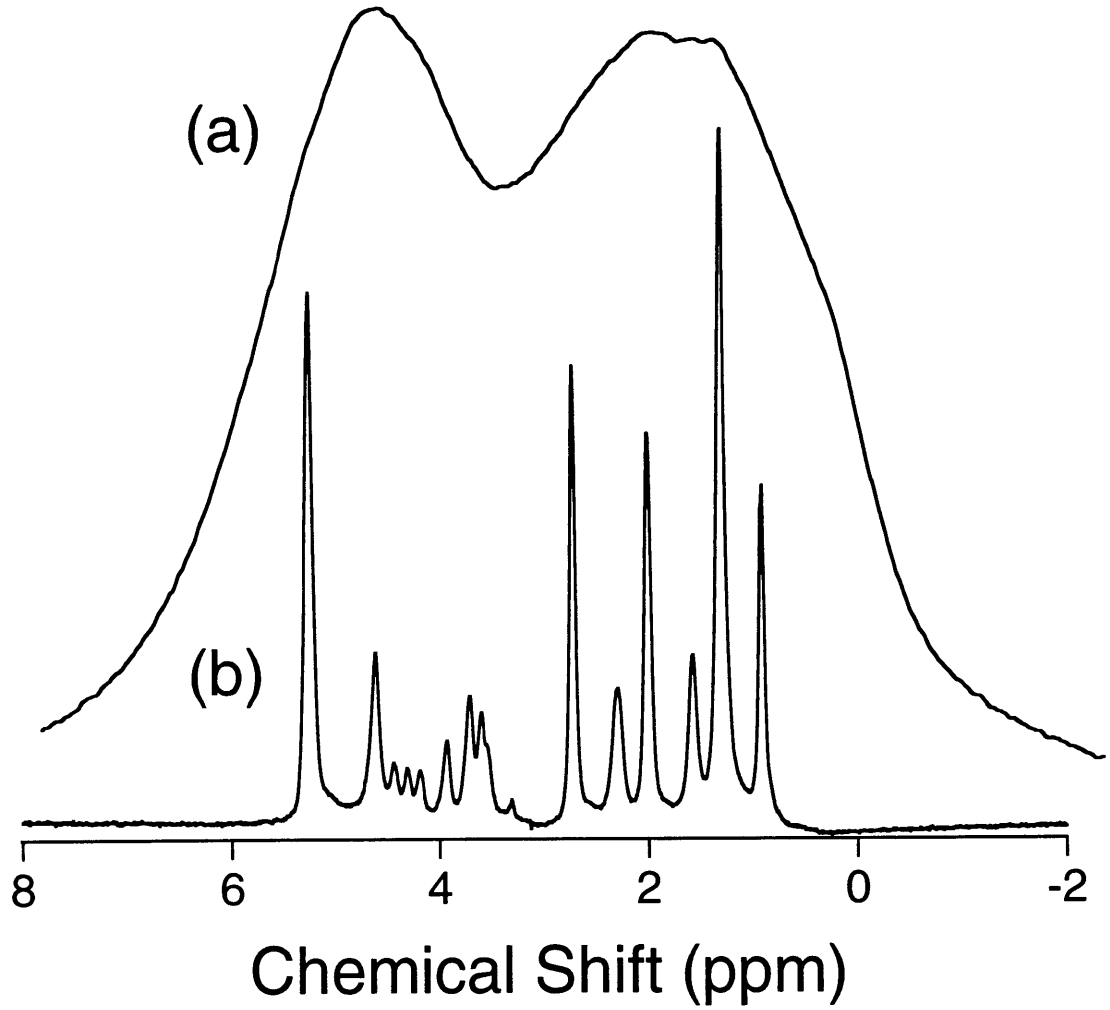

Figure 2.1

Figure 2.2a is a ^{13}C (^{1}H decoupled) MAS spectrum of U-(^{13}C)-MGDG as a 1:1 w/w ratio dispersion in D_2O spinning at 5 kHz at room temperature. Figure 2.2 is the same as 2a but without ^{1}H decoupling. Here, one is able to observe resolvable heteronuclear J couplings which may be used for heteronuclear coherence transfer. That the heteronuclear J couplings are observable is consistent with the fact that the proton reservoir is inhomogeneous and that ^{13}C-^{1}H dipole couplings are motionally averaged while any residual couplings are attenuated by MAS.

Figure 2.2 ^{13}C MAS Bloch decay of U-(^{13}C)-MGDG/D_2O mixture described in text with $\omega_r/2\pi$ = 5.3 kHz. (a) With and (b) without ^1H decoupling. (c)^1H-^{13}C MAS/Refocussed-INEPT with CW ^1H decoupling on U-(^{13}C)-MGDG/D_2O mixture described in text with a spinning speed of 5.3 kHz. The pulse sequence employed was $90_x(^1H)$-δ_1-$180_x(^1H,^{13}C)$-δ_1-$90_y(^1H)$,$90_x(^{13}C)$-δ_2-$180_x(^1H,^{13}C)$-δ_2-acquire. The first delay, δ_1, is 1.85 ms while δ_2 is 1.11 ms. (d) Expansion of terminal methyl region in 2b.

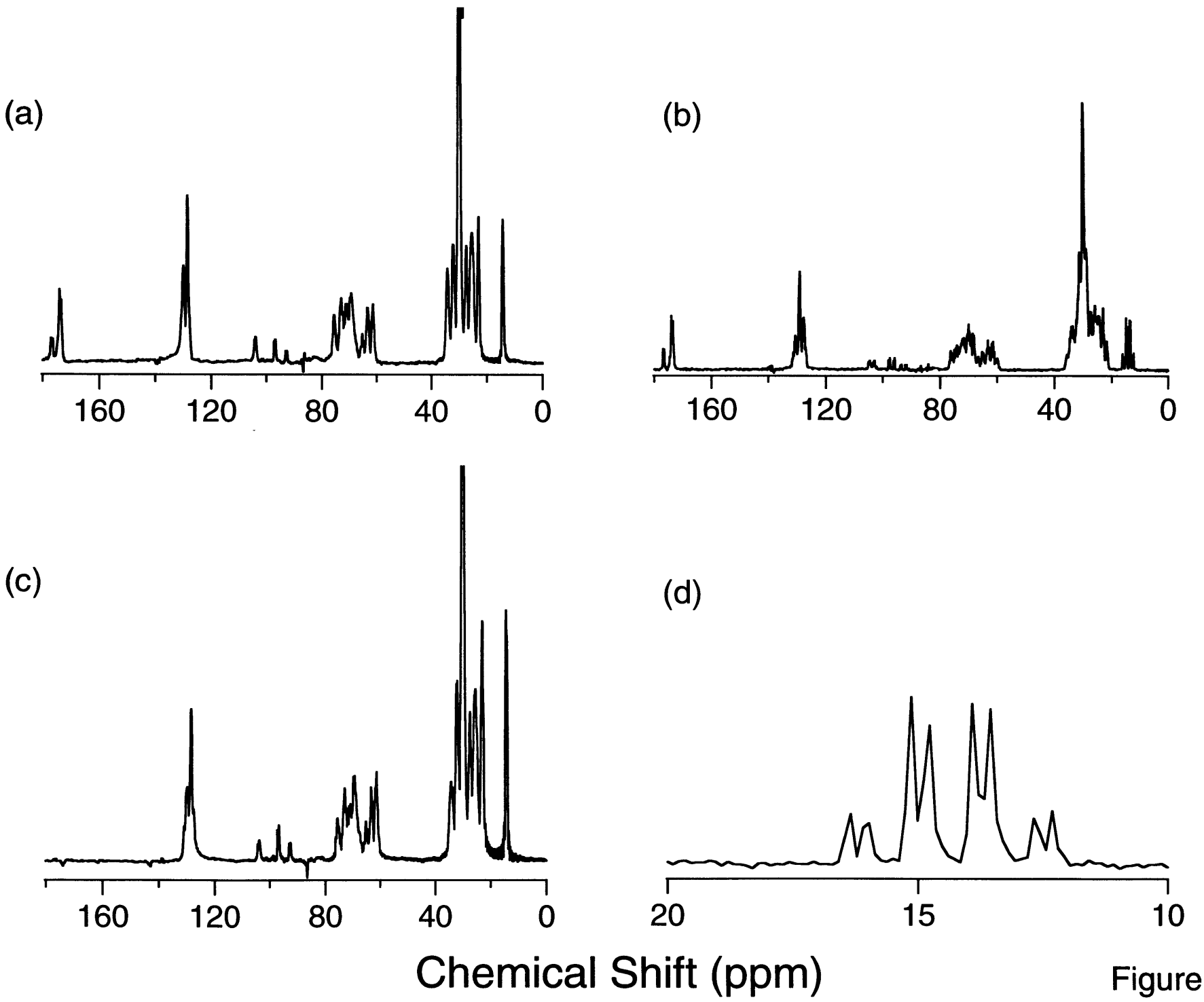
(a)
160
120
80
40
0
(b)
160
120
80
40
0
(c)
160
120
80
40
0
(d)
20
15
10
Chemical Shift (ppm)

Figure 2.2

Figure 2.2c is a Refocussed-INEPT [19] spectrum of the U-(^{13}C)-MGDG/D_2O mixture under the same experimental conditions as in figure 2.2a. The spectra in Figures 2.2a and 2.2c have the same intensity scale. As in solution NMR, INEPT style transfers from ^{1}H to ^{13}C increase the overall sensitivity for ^{13}C detection. These results imply that 2D heteronuclear ^{13}C-^{1}H NMR experiments such as HMQC [20] and HSQC [21] are feasible in lipid/water systems in the liquid crystalline phases. Figure 2.3 is a ^{13}C detected heteronuclear chemical shift correlation spectrum of the U-(^{13}C)-MGDG/D_20 mixture.

Figure 2.3 MAS/^{13}C detected 2D ^{1}H-^{13}C chemical shift correlation on U-(^{13}C)-MGDG/D_2O mixture described in text with a spinning speed of 5 kHz. The pulse sequence employed was $90_x(^{1}H)$-$t_1/2$-$180_x(^{13}C)$-$t_1/2$-δ_1-$180_x(^{1}H,^{13}C)$-δ_1-$90_y(^{1}H)$,$90_x(^{13}C)$-δ_2-$180_x(^{1}H,^{13}C)$-δ_2-acquire (t_2). Timings are the same as Refocussed-INEPT. Data were acquired using the method of States, et. al. [22]. Sixteen transients were collected for each t_1 point with a recycle delay of 3s. The 2D matrix of 128x1024 points was zero-filled to 512x2048. 5 and 15 Hz of line broadening were applied in F_1 and F_2, respectively.

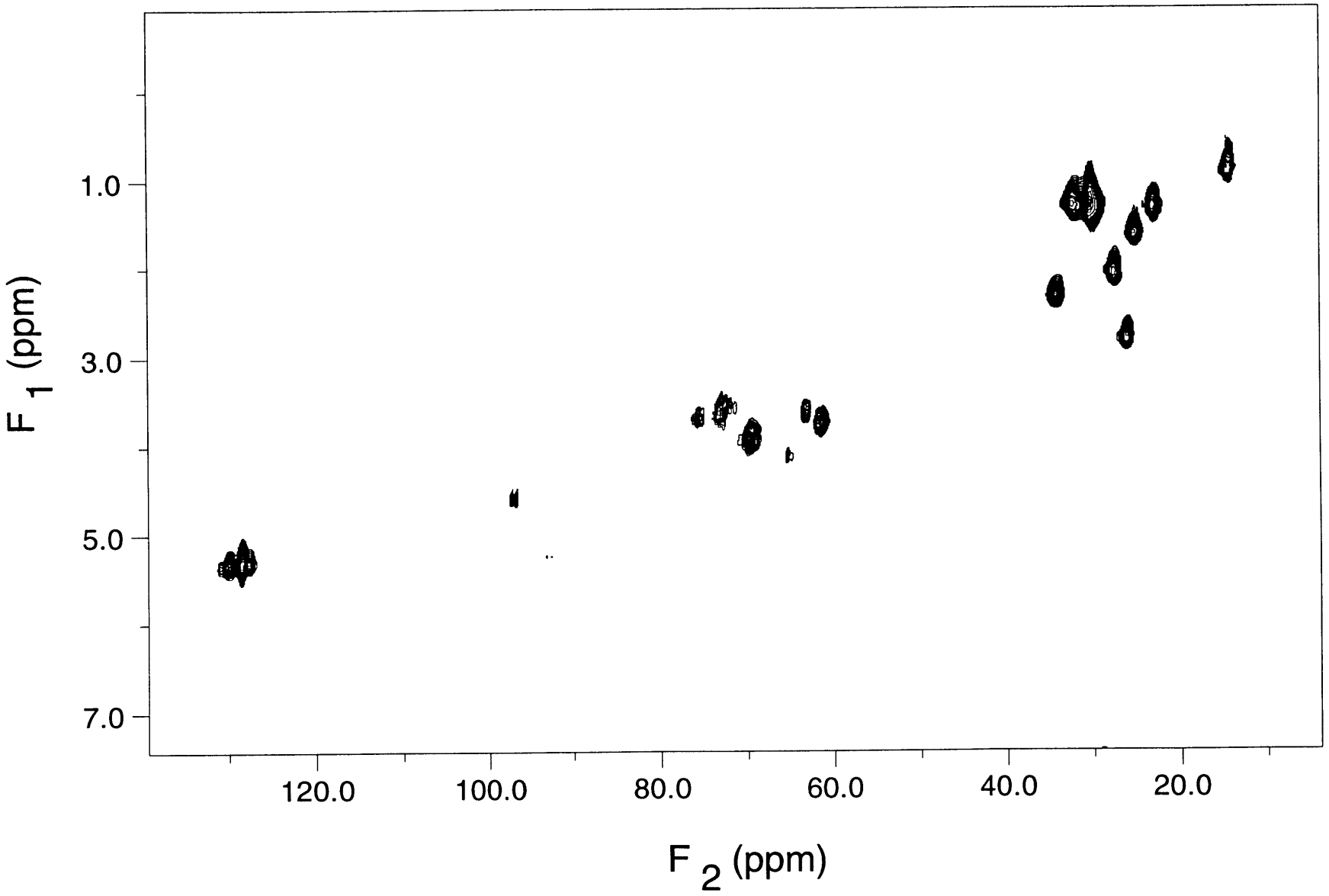

Figure 2.3

Finally, the expansion of the aliphatic region depicted in Figure 2.2d shows resolvable J_{CC} couplings. Since these couplings are often between 35 and 45 Hz while the homogeneous ^{13}C line widths are often less than 10 Hz, it is possible to perform ^{13}C-^{13}C homonuclear chemical shift correlation using J_{CC}. Figure 2.4 is a ^{13}C-^{13}C TOCSY[23] spectrum of the U-(^{13}C)-MGDG/D_2O mixture. The acyl chains, glycerol backbone, and galactosyl group show up as independent spin systems, and preliminary assignments have been made. Additional experiemnts such as 3D HCCH-TOCSY [24] and 3D CCH-TOCSY- REV-INEPT [25] may be employed to completely assign the U-(^{13}C)-MGDG/D_2O mixture.

Figure 2.4 MAS 2D ^{13}C-^{13}C TOCSY on U-(^{13}C)-MGDG/D_2O mixture described in text with a spinning speed of 5kHz: (a) Full spectrum, (b) xpansion of aliphatic region, (c) expansion of glycerol/galactosyl region. The MLEV-17 mixing scheme of Bax, et. al. was employed[26]. The total mixing time was 20 ms while trim pulses were 2.5 ms. The ^{13}C carrier was placed in the middle of the ^{13}C spectrum and an rf field strength of 40 kHz was employed to minimize offset effects. Proton decoupling during the evolution period was achieved by placing a 180° pulse on the ^{1}H channel in the middle of t_1. CW proton decoupling was applied during detection. Sixteen transients were collected for each t_1 point, and a recycle delay of 3s was employed. Data were acquired using the method of States, et. al. [22]. The 2D matrix of 256x1024 points was zero-filled to 1024x2048.

(a)

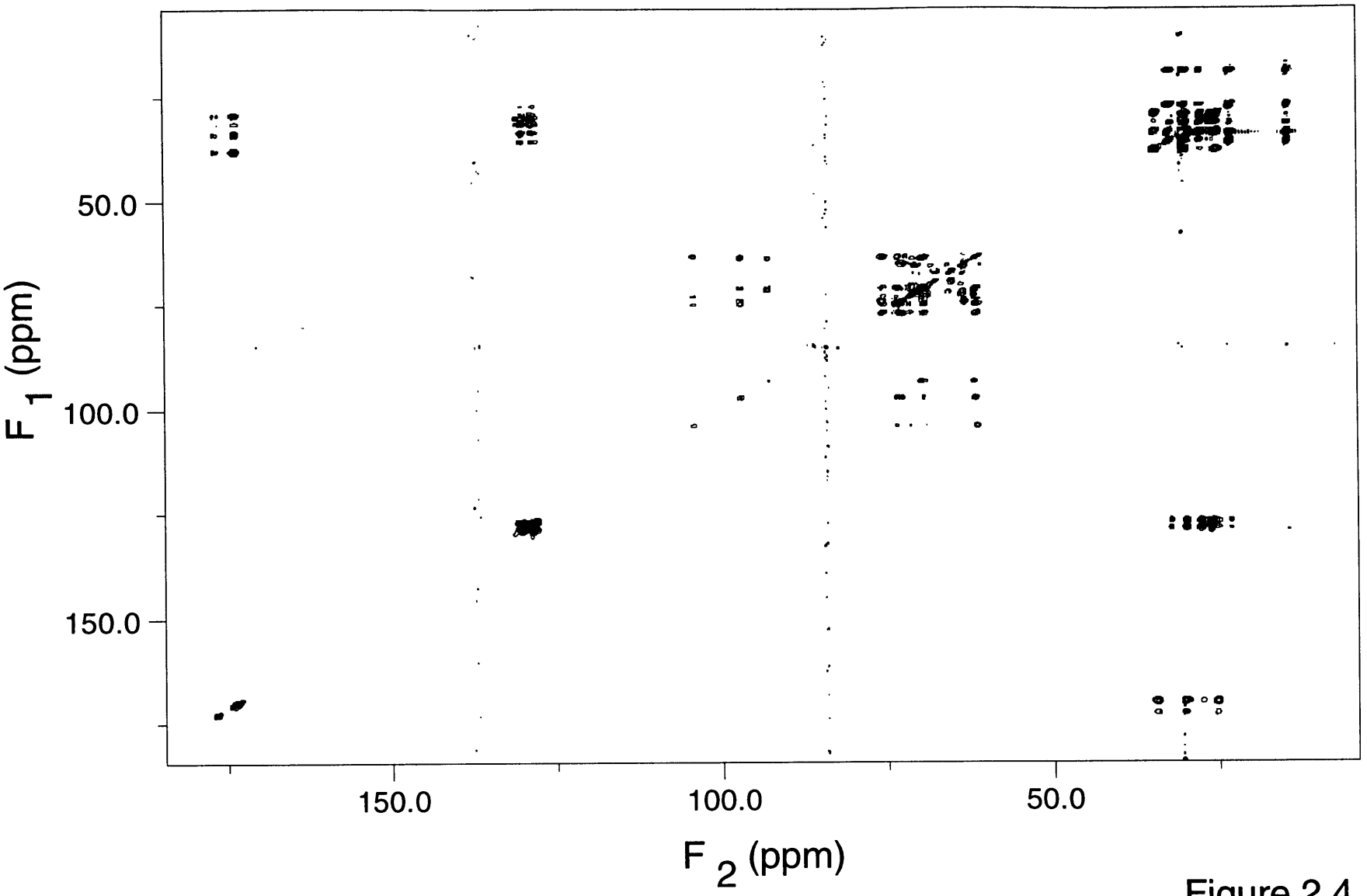

Figure 2.4

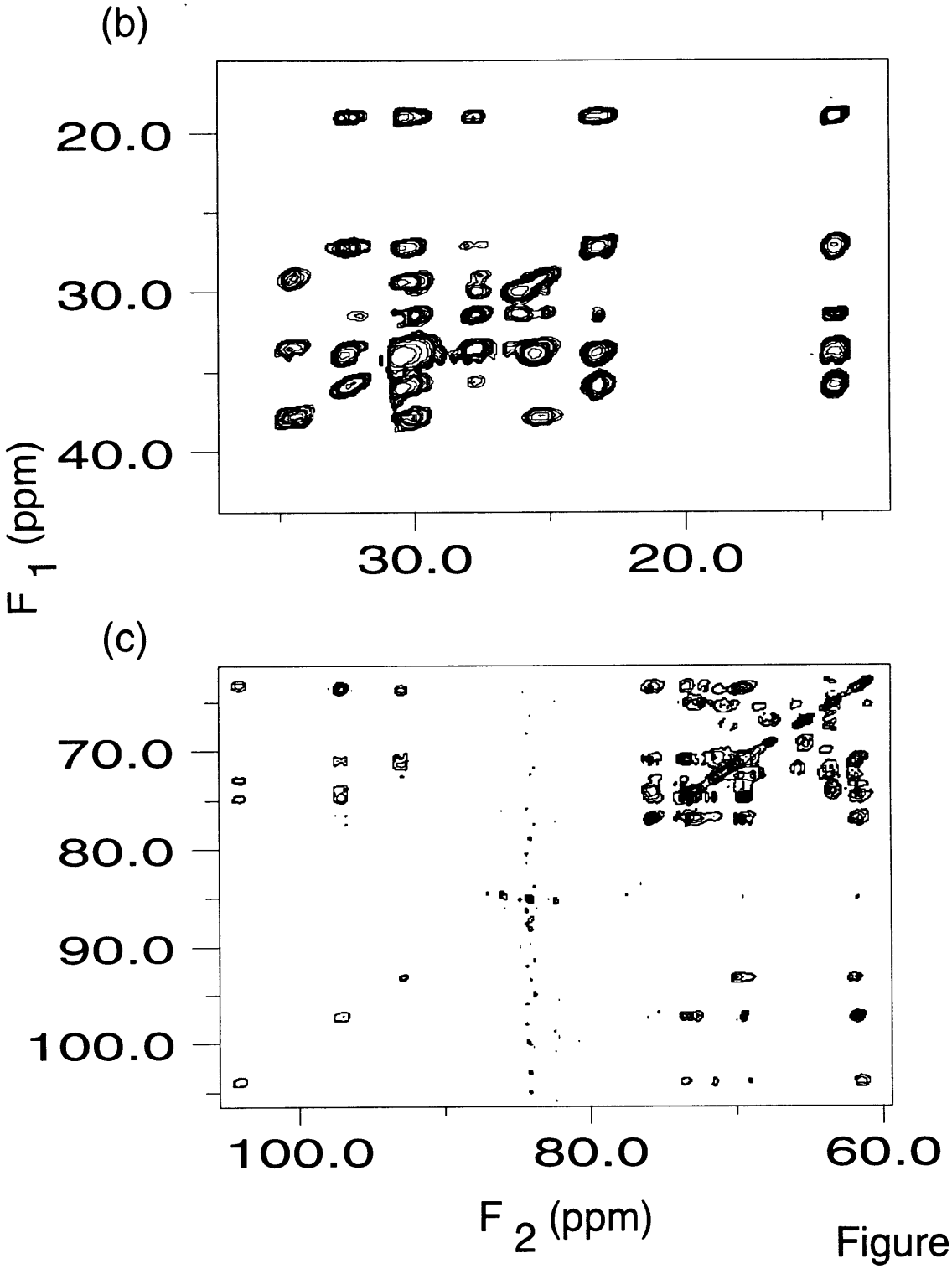
(b)
20.0
30.0
40.0
F 1 (ppm)
30.0
20.0
(c)
70.0
80.0
90.0
100.0
100.0
80.0
60.0
F 2 (ppm)

Figure 2.4

2.5 Conclusion

These results demonstrate the feasibility of obtaining high resolution multidimensional chemical shift correlation spectra in lipid/water systems by employing coherence transfer schemes routinely performed in solution NMR experiments together with MAS. In addition, these results have implications for CP/MAS[27] in lipid/water systems. It is well known that ^{1}H-^{13}C CP/MAS intensities become extremely sensitive to Hartmann-Hahn mismatch when spinning speeds exceed the strength of the relevant dipolar couplings [7]. This dependence of Hartmann-Hahn match on spinning speed for lipid/water systems in the liquid crystalline phase can be especially acute since dipolar couplings are reduced significantly by motional averaging. Therefore, optimal CP intensities may be difficult to achieve and maintain for long times even at moderate spinning speeds. Typically the problem of CP at high spinning speeds is circumvented by any of a wealth of new phase switched and amplitude modulated techniques [28-30]. INEPT provides an alternative for polarization transfer in lipid/water systems.

We have shown that MAS combined with multidimensional chemical shift correlation techniques are useful for obtaining high resolution spectra of lipids in their biologically relevant state. Individual components of membranes may be traced out using the connectivity information provided by these experiments. It is possible that chemical shift correlation, in conjunction with dipolar mixing, will provide a probe for studies of lipid structure and membrane organization.

Acknowledgments for Chapter 2 This chapter is excerpted from an article that appeared in J. Magn Reson. B 106 (2) 187-190 1995. The work was done in collaboration with P.R. Costa, J.-P. Dubacq, D. E. Warschawski#, P.-N. Lirsac, and P.F. Devaux.

References for Chapter 2

[1] J. M. Smaby, J. M. Muderhwa and H. L. Brockman, Biochemistry 33 (1994) 1915.

[2] J. H. Davis, Biochim. Biophys. Acta 737 (1983) 117.

[3] R. G. Griffin, Methods Enzym. 72 (1981) 108.

[4] M. Bloom, E. Evans and O. Mouritsen, Q. Rev. Biophys. 24 (1991) 293.

[5] J. Jeener, B. H. Meier, P. Bachman and R. R. Ernst, J. Chem. Phys. 71 (1979) 4546.

[6] M. M. Maricq and J. S. Waugh, J. Chem. Phys. 70 (1979) 3300.

[7] E. O. Stejskal, J. Schaefer and R. A. McKay, J. Mag. Reson. 57 (1984) 471.

[8] R. Tycko and G. Dabbagh, Chem. Phys. Letters 173 (1990) 461.

[9] A. W. Hing, S. Vega and J. Schaefer, J. Magn. Reson. 96 (1992) 205.

[10] A. E. Bennett, J. H. Ok, S. Vega and R. G. Griffin, J. Chem. Phys. 96 (1992) 8624.

[11] M. Bloom, E. E. Burnell, S. B. W. Roeder and M. I. Valic, J. Chem. Phys. 66 (1977) 3012.

[12] M. Bloom, E. E. Burnell, A. L. Mackay, C. P. Nichol, M. I. Valic and G. Weeks, Biochemistry 17 (1978) 5750.

[13] J. Forbes, J. Bowers, L. Moran, X. Shan and E. Oldfield, J. Chem. Soc., Faraday Trans. 84 (1988) 3821.

[14] R. A. Haberkorn, J. Herzfeld and R. G. Griffin, J. Am. Chem. Soc. 100 (1978) 1296.

[15] J. B. Speyer, R. T. Weber, S. K. D. Gupta and R. G. Griffin, Biochemistry 28 (1989) 9569.

[16] C. Morrison and M. Bloom, J. Chem. Phys. 101 (1994) 749.

[17] G. G. Shipley, J. P. Green and B. W. Nichols, Biochim. Biophys. Acta 311 (1973) 531.

[18] F. Adebodun, J. Chung, B. Montez, E. Oldfield and X. Shan, Biochemistry 31 (1992) 4502.

[19] D. P. Burum and R. R. Ernst, J. Magn. Reson. 39 (1980) 163.

[20] M. F. Summers, L. G. Marzilli and A. Bax, J. Am. Chem. Soc. 108 (1986) 4285.

[21] G. Bodenhausen and D. J. Ruben, Chem. Phys. Letters 69 (1980) 185.

[22] D. J. States, R. A. Haberkorn and D. J. Ruben, J. Magn. Reson. 48 (1982) 286.

[23] I. Braunschweiler and R. R. Ernst, J. Magn. Reson. 53 (1983) 521.

[24] A. Bax, G. M. Clore and A. M. Gronenborn, J. Magn. Reson. 88 (1990) 425.

[25] S. W. Fesik, H. L. Eaton, E. T. Olejniczak, E. R. P. Zuiderweg, L. P. McIntosh and F. W. Dahlquist, J. Am. Chem. Soc. 112 (1990) 886.

[26] A. Bax and D. G. Davis, J. Magn. Reson. 65 (1985) 355.

[27] J. Schaefer and E. O. Stejskal, J. Am. Chem. Soc. 98 (1976) 1031.

[28] X. Wu and K. W. Zilm, J. Magn. Reson. A 104 (1993) 154.

[29] O. B. Peerson, X. Wu, I. Kustanovich and S. O. Smith, J. Magn. Reson. A 104 (1993) 334.

[30] B. Q. Sun, P. R. Costa and R. G. Griffin, J. Magn. Reson. A in press.

3. Dipolar Recoupling in MAS NMR as a Probe for Segmental Order in Lipid Bilayers

3.1 Introduction

Over the last two decades, ^2H NMR has been an important method for investigating the structure and dynamics of liquid crystalline systems such as lipid bilayers[1-3]. The ^2H quadrupolar coupling provides an excellent probe of C-^2H (CD) segmental order since the quadrupolar tensor is, in general, axially symmetric, with the unique axis directed along the CD bond[4]. In randomly oriented samples containing a specifically labeled CD segment, the quadrupolar coupling is obtained by measuring the width of a Pake doublet. A departure from the 250 kHz rigid lattice width is indicative of motions (*vide infra*), and the powder lineshape contains information regarding the average orientation of the CD segment with respect to the motional axis[1,3]. Furthermore, ^2H Pake patterns provide a useful mapping of orientation dependent relaxation. Simulations of both T_1[5-7] and T_2 [2,8-10] anisotropy have yielded excellent models of lipid dynamics in both gel and fluid phases.

A major shortcoming of ^2H NMR is the requisite isotopic enrichment, due to a prohibitively low natural abundance (0.01%), for the measurement of spectra. Therefore, there has been an increased interest in obtaining similar information from directly bonded ^{13}C-^1H dipolar couplings[11-16] since the spatial dependence of the ^{13}C-^1H dipolar tensor is formally identical to that of the ^2H electric field gradient tensor and it is possible to record natural abundance ^{13}C spectra in concentrated samples such as liquid crystals. In contrast to ^2H NMR, where the quadrupolar coupling dominates other spin interactions such as dipolar couplings and chemical shifts, interpretation of ^{13}C-^1H dipolar splittings may be complicated by chemical shift anisotropy (CSA) and dipolar interactions among abundant spins. In addition, multiple ^{13}C-^1H dipolar couplings found in more complicated systems make ^{13}C spectra difficult to disentangle. The latter complication is partially solved by separated-local-field spectroscopy on static samples where dipolar interactions and chemical shifts are separated into orthogonal frequency domains in a 2D experiment. There, each magnetically distinct site, defined by a unique chemical shift, reports on the individual dipolar fields[17], and multiple ^{13}C-^1H couplings are resolved by their associated ^{13}C chemical shift.

The first separated-local-field experiments were performed with static single crystalline solids, but unfortunately, powder samples generate additional broadening that reduces sensitivity with a concomitant loss of resolution[17]. The advent of cross polarization with magic-angle spinning (CP/MAS)[18] and high power proton decoupling has dramatically increased the sensitivity and resolution in spectra of rare nuclei such as ^{13}C. Indeed, isotropic chemical shift spectra rivaling the quality of resolution obtained in liquids may be recorded for solids but at the sacrifice of orientation dependent information. It was precisely within this framework that Munowitz and coworkers proposed the idea of selectively re-introducing anisotropic interactions during MAS[11]. The dipolar-chemical shift correlation (DIPSHIFT) experiment is a MAS analog of the separated-local-fields experiment of Hester et al[17]. A notable increase in sensitivity and resolution is achieved since the powder patterns present in the evolution and detection period are replaced with rotational sidebands. Analysis of the dipolar sideband intensities yields the magnitude of ^{13}C-^{1}H dipolar couplings provided that the sample spinning speed is less than the ^{13}C-^{1}H dipolar interactions[19], a condition that is generally satisfied for directly bonded ^{13}C-^{1}H couplings in rigid solids. However, in weakly coupled spin pairs, such as ^{13}C-^{13}C and ^{13}C-^{15}N, it is difficult to obtain significant sideband intensity at typical spinning speeds. Methods that increase the number of spinning sidebands by magnifying the effective dipolar interactions during the dipolar evolution period[20-22] require slow spinning and, in general, the CSAs of multiple sites may overlap, thereby complicating spectral analysis. Alternatively, methods that involve the dephasing of rotational echoes, such as rotational echo double resonance (REDOR)[23], are not restricted by slow spinning and have consequently found wide use in measuring the magnitudes and signs[24] of weak couplings among rare spin nuclei. In the opposite regime, where dipolar couplings become large relative to experimentally realizable spinning speeds, the REDOR experiment becomes difficult to implement since the spectral window that accommodates dipolar powder patterns is limited by the spinning speed[23]

Unlike in rigid solids, directly bonded ^{13}C-^{1}H dipolar couplings in liquid crystalline systems such as lipid bilayers may range from the order of 1 to 10 kHz. Such motionally averaged

dipolar interactions are in the intermediate range with respect to spinning speeds typically employed. Although the larger couplings within this range could be measured with the DIPSHIFT[11] type of experiment while the weaker couplings could be measured with REDOR[23] or frequency selective dipolar recoupling (FDR)[25], clearly it would be beneficial to measure a range of dipolar couplings within one experiment. Techniques that allow scaling control of anisotropic interactions while preserving the recoupled powder lineshape relative to the shape of the static line are a desirable means to this end. Uniform scaling of recoupled interactions may be achieved by switching either the angle of rotation[13,26] or the spinning speed[27,28], between dipolar evolution and detection periods; however, these techniques require specialized hardware and are difficult to implement.

We present here recoupling techniques for the measurement of both the magnitudes and signs of motionally averaged ^{13}C-^{1}H interactions found in liquid crystalline systems. The approach utilizes MAS at a constant speed throughout the experiment while a series of rotor-synchronized π pulses is applied for ^{13}C-^{1}H dipolar recoupling during the evolution period. Spacing between π pulses may be varied in order to control scaling of the recoupled Pake patterns, insuring the simultaneous measurement of a wide range of couplings with an orientation dependence of the recoupled dipolar interactions that is identical to that of static samples. The methods introduced here are therefore π pulse analogs of the switched-angle spinning experiments previously proposed for the measurement of the magnitudes[13,16] and signs[29,30] of ^{13}C-^{1}H dipolar interactions. Accordingly, these experiments are referred to as DROSS (Dipolar Recoupling On-axis with Scaling and Shape preservation) and S-DROSS (Sign-DROSS) for the measurement of the magnitudes and signs of dipolar interactions. Their applicability is restricted to a class of systems where fast limit molecular motion enables ^{1}H-^{1}H dipolar couplings to be effectively averaged by MAS. However, this class includes a large number of chemically, physically, and biologically important systems such as model membranes and other liquid crystals which have heretofore relied almost exclusively on ^{2}H labeling for the study of segmental order.

3.2 Theory

3.2.1 Fast Limit Motional Averaging and the effects on MAS Dynamics

There are considerable large amplitude molecular motions in fluid phase lipid bilayers. It is well known that both gauche-trans isomerization and axial diffusion are rapid relative to ^1H-^1H and ^{13}C-^1H dipolar time scales, and consequently these anisotropic interactions are attenuated relative to their rigid lattice values[31,32]. Rapid axial motion, as demonstrated by Oldfield et al.[33], Forbes et al.[34], and recently discussed in detail by Davis[35], enables MAS to effectively average ^1H homonuclear dipolar couplings(See Appendix B). This is a remarkable result which indicates that high resolution ^1H spectra may be obtained with MAS since the broadening off of rotational-resonance[36,37] is negligible in fluid phase lipid bilayers even at moderate spinning speeds[35]. In the language of Maricq and Waugh, the total Hamiltonian may be viewed as inhomogeneous under these conditions[36]. Therefore, ^{13}C-^1H dipolar couplings may be treated as independent spin pairs, and the relevant rotating frame Hamiltonian for a rare spin 1/2 nucleus, S, in the presence of abundant spin 1/2 nuclei, I, under MAS reduces to:

$$H(t) = \langle \omega_I(t) \rangle I_z + \langle \omega_S(t) \rangle S_z + \langle \omega_{IS}(t) \rangle 2I_z S_z \quad . \qquad (3.1)$$

where the expressions $\omega_I(t)$, $\omega_S(t)$, and $\omega_{IS}(t)$ correspond to the I spin chemical shift, the S spin chemical shift, and heteronuclear couplings between spins I and S under MAS[36]. The brackets < > indicate motional averaging over time scales that are the short relative to MAS period[38].

3.2.2 Pulse sequences for measuring the magnitudes and the signs of CH dipolar couplings

The pulse sequences for measuring the magnitude and the sign of CH dipolar couplings are depicted in Figure 3.1a and b. Dipolar recoupling is achieved through an adaptation of the rotor-synchronized CSA recoupling sequence suggested by Tycko et al (see Figure 3.1c)[39].

Figure 3.1 Pulse sequences for measuring the magnitudes and signs of dipolar interactions under MAS and 4-π pulse recoupling scheme: (a) 2D DROSS, (b) S-DROSS, and (c) 4-π pulse recoupling scheme. Selected values of the scaling factors χ and ε with the corresponding pulse spacings given by $\omega_r\tau_1/2\pi$ and $\omega_r\tau_2/2\pi$ are tabulated in Ref. 39. Delays δ_1 and δ_2 are integer multiples of the rotor period and are either set equal to values of $1/4J_{CH}$ and $1/8J_{CH}$ or optimized empirically. Phase cycling for 2D DROSS (a): ϕ_1 = (xxyy), $\phi_2 = \phi_4$ =(x$\bar{x}$y$\bar{y}$), ϕ_3 = (yy$\bar{x}\bar{x}$)($\bar{y}\bar{y}$xx), ϕ_5 = (yy$\bar{x}\bar{x}$) , ϕ_6 = (x$\bar{x}$y$\bar{y}$)($\bar{x}$xy$\bar{y}$) for S-DROSS (b): ϕ_1 = (xxyy)($\bar{x}\bar{x}\bar{y}\bar{y}$), ϕ_2 = (xy$\bar{x}\bar{y}$), ϕ_3 = (xy$\bar{x}\bar{y}$), ϕ_4 = (x$\bar{x}y\bar{y}$), ϕ_5 = (y$\bar{y}\bar{x}$x), ϕ_6 = (x$\bar{x}y\bar{y}$)($\bar{x}x\bar{y}$y).

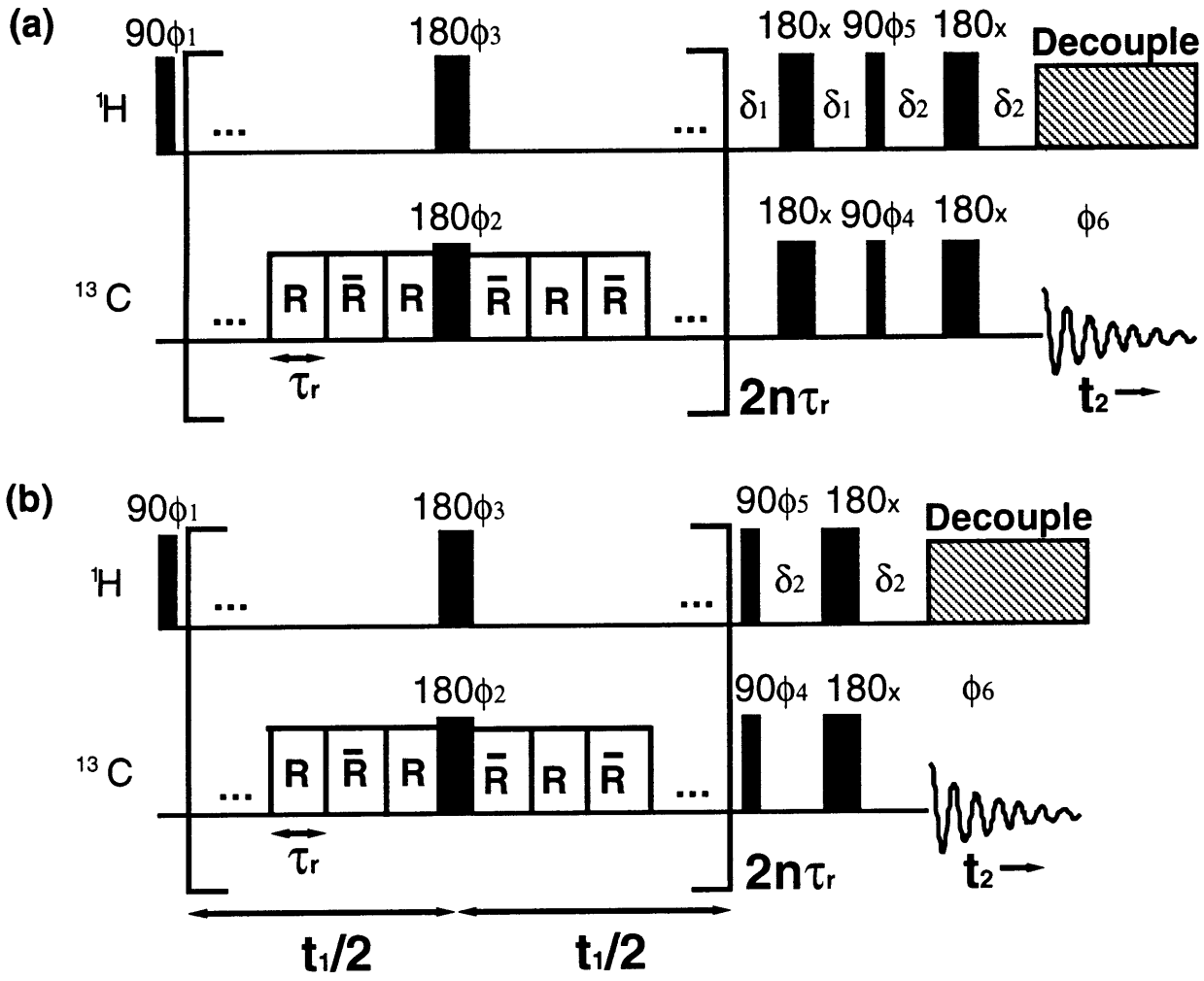
(a)
90φ1
180φ3
180x 90φ5 180x
Decouple
¹H
δ1 δ1 δ2 δ2
180φ2
180x 90φ4 180x
φ6
¹³C
R R̄ R R̄ R R̄
τr
2nτr
t2
(b)
90φ1
180φ3
90φ5 180x
Decouple
¹H
δ2 δ2
180φ2
90φ4 180x
φ6
¹³C
R R̄ R R̄ R R̄
τr
2nτr
t2
t1/2
t1/2
(c)
180φ2 180φ2 180φ2 180φ2
R ≡
-τ2 -τ1 0 τ1 τ2
τr

Figure 3.1

In both sequences, the heteronuclear dipolar interactions and S spin CSA are recoupled during both halves of the evolution period. However, the simultaneous π pulses on ^1H and ^{13}C, applied at the center of the evolution period, ensure that the chemical shifts are refocused over the duration of t_1. Therefore, evolution of initial transverse magnetization is governed by the effective Hamiltonian:

$$H^{eff} = \overline{\langle \omega_D \rangle} 2I_z S_z \tag{3.2}$$

where

$$\overline{\langle \omega_D \rangle} = \varepsilon \pi J_{CH} + \chi \langle b_{CH} \rangle \frac{1}{2}(3\cos^2\beta - 1) \tag{3.3}$$

with β as the angle between the bilayer normal and the direction of the static magnetic field and

$$\langle b_{CH} \rangle = - b_{CH} S_{CH} \tag{3.4}$$

as the motionally averaged heteronuclear dipolar coupling where

$$S_{CH} = \frac{1}{2}\langle 3 \cos^2\theta - 1 \rangle \tag{3.5}$$

is the ^{13}C-^1H dipolar order parameter, $b_{CH} = \left(\frac{\mu_0}{4\pi}\right)\frac{\gamma_C \gamma_H \hbar}{r_{CH}^3}$ is the rigid lattice dipolar coupling, and θ is the average angle between the internuclear vector and motional axis. The spacings τ_1 and τ_2 corresponding to several values of the scale factors χ and ε (ranging from 0 - 0.393 and 0.797 - 0 respectively) are tabulated in Ref. 39.

In principle, the DROSS experiments could be implemented with the 4-π pulse sequence applied to either ^{13}C or the ^1H nuclei; however, it is found experimentally that the later case yields distorted lineshapes. Numerical lineshape simulations that include the effect of finite π pulses and homonuclear dipolar couplings between protons indicate decreasing lineshape distortions with increasing power. In the limit of δ-function π pulses ideal Pake patterns are recovered. The effect is unobservable when ^1H dipolar couplings are neglected. In contrast, the effects of finite pulses

on the rare spins are minimal for the r.f. field strengths and resonance offsets employed in this work. Therefore, the 4-π pulse recoupling scheme is applied to the ^{13}C nuclei.

In addition, the techniques presented here could be performed by employing either ^{13}C or ^{1}H transverse magnetization as an initial condition for the evolution period. Although the former case would not require coherence transfer from ^{1}H to ^{13}C, evolution of ^{13}C magnetization under recoupled ^{13}C-^{1}H dipolar couplings would complicate spectral lineshapes. In analogy to the J_{CH} coupling in liquids, a CH group yields a doublet while CH_2 and CH_3 moieties generate ^{13}C-^{1}H dipolar "triplets" and "quartets". In contrast, an initial condition of ^{1}H transverse magnetization generates doublets irrespective of ^{1}H multiplicity since each ^{1}H in the CH_n group is coupled to only one ^{13}C thereby simplifying spectral analysis. Accordingly, ^{1}H transverse magnetization is allowed to evolve under the recoupled ^{13}C-^{1}H dipolar interaction in both experiments.

In the 2D DROSS experiment, after a time t_1, the resulting proton magnetization is transferred in an orientation-independent fashion via J_{CH} to the directly bonded ^{13}C with a rotor-synchronized refocused-INEPT[40,41]. The resulting ^{13}C magnetization, $S_x\cos(\overline{\langle\omega_D\rangle}\, t_1)$, then evolves under MAS with proton decoupling. A two dimensional Fourier transform generates a 2D DROSS spectrum where scaled, recoupled powder lineshapes are separated by the corresponding ^{13}C chemical shifts.

For the case of S-DROSS, omission of the first refocusing period, $2\delta_1=1/2J_{CH}$, found in the DROSS sequence insures that the simultaneous $\pi/2$ pulses select and transfer proton antiphase magnetization, $2I_yS_z$, carrying the $\sin(\overline{\langle\omega_D\rangle}\, t_1)$ term to net ^{13}C magnetization on the directly bonded carbon during the subsequent delay. Just as in the switched-angle spinning version of the experiment[29,30], the sign of the $\sin(\overline{\langle\omega_D\rangle}\, t_1)$ term, resulting from a ^{13}C-^{1}H dipolar coupling during the evolution time t_1, determines the sign of the corresponding ^{13}C resonance. That is, for short evolution times relative to the inverse of the recoupled dipolar coupling, the sign of the resulting ^{13}C resonance is determined by $\chi<\pm\omega_D>t_1$, provided that $|\chi<\pm\omega_D>| >> \varepsilon\pi J_{CH}$. A series of one-dimensional spectra are collected for different values of t_1 so that the initial build-up rate of

^1H antiphase magnetization may be monitored. Alternatively, the signs may be extracted from the polarity of antiphase Pake doublets resulting from a 2D implementation.

3.3 Materials and Methods

3.3.1 Sample Preparation

Dimyristoylphosphatidylcholine (DMPC) was purchased from Avanti Polar Lipids (Alabaster, AL) as a solution in chloroform and used without further purification. Samples were prepared by evaporating chloroform under a gentle stream of N_2 followed by mechanical vacuum pumping overnight. Dispersions of DMPC in D_2O with 1:1 ratio by weight were subjected to three freeze-thaw cycles before performing NMR experiments.

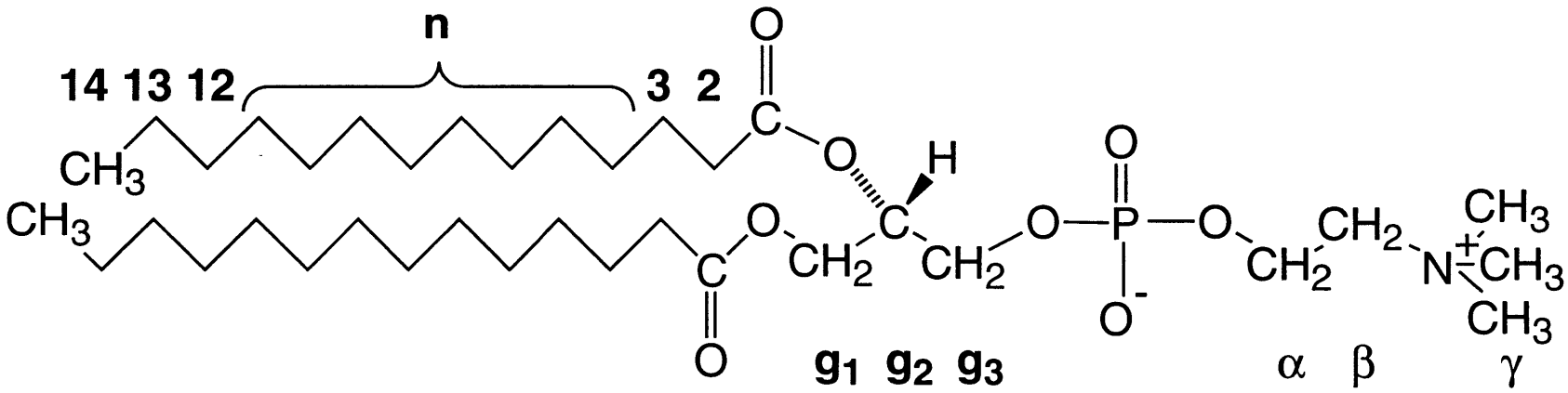

Figure 3.2 Schematic representation of DMPC

3.3.2 NMR Methods

All NMR experiments were performed on a custom designed spectrometer operating at a proton frequency of 397.9 MHz. Spectra were recorded with a custom designed double tuned probe equipped with a 5mm high-speed spinning assembly procured from Doty Scientific, Inc (Columbia, S.C.). Spinning speeds were 8.0 kHz and controlled to within 2 Hz with a Doty spinning speed controller while the sample temperature was maintained at 30°C throughout the experiment. Typical $\pi/2$ pulse lengths were 4.0 and 4.4 μs for ^1H and ^{13}C respectively. Proton decoupling during the acquisition period was achieved using the two-pulse phase modulation scheme[42] with an r.f. field strength of 50 kHz, a pulse length of 10.4 μs, and a phase angle ϕ of 10°. The 2D experiments were acquired with 512 scans per t_1 point and a recycle delay of 3 s. Quadrature detection during the evolution period was omitted due to the symmetry of the dipolar interaction. The data matrices ,originally 32 x 1024 points, were zero filled to 128 x 2048 points. Data were processed with a sinebell window function in t_2 and 50-100 Hz Gaussian multiplication in t_1 prior to Fourier transformation.

3.3.3 Numerical Lineshape Simulations

In order to extract information on orientational order from the spectra, it is necessary to simulate the recoupled powder lineshapes. Accordingly, the spin dynamics of an isolated CH or CH_2 segment during MAS and the 4-π pulse recoupling sequence, including finite pulse effects, were evaluated by numerical integration of the propagator. For simplicity, the coherence transfer from ^1H to ^{13}C is neglected so that only the propagator for the evolution period is calculated. The amplitude modulated ^1H magnetization is then Fourier transformed to generate powder lineshapes. The principal values for the ^1H and ^{13}C chemical shift tensors in polyethylene[43,44] were employed in the simulations. In general it was found that $\geq$ 5000 orientations were needed for convergence of the powder average.

The simultaneous π pulses in the center of the evolution period complicate the numerical evaluation of the propagator. For exact calculations including these pulses, the amplitude of ^1H

transverse magnetization would be found by forming the propagator for each value of t_1 which would be time consuming. A significant increase in computational speed is realized if the simultaneous π pulses are neglected, and the resulting periodicity of the 4-π pulse scheme is fully exploited. For the radio frequency power levels and resonance offsets employed, there is excellent agreement between exact (involving simultaneous π pulses) and approximate (neglecting simultaneous π pulses and setting ^{1}H resonance offsets and CSAs to zero) simulations where the propagator is calculated only once. Therefore, such approximate simulations are employed in this work unless mentioned otherwise.

3.4 Results and Discussion

A 2D DROSS spectrum of DMPC at 30 °C is depicted in Figure 3.1 for $\chi = 0.393$ and $\varepsilon = 0.0$. Pake doublets are obtained since the 4-π pulse scheme of Tycko et. al.[39] preserves the recoupled powder lineshape: the angular dependence of the recoupled dipolar interaction is identical to that for static samples. Moreover, the 2D DROSS experiment may be employed with smaller values of χ if additional scaling is required[39]. In analogy with off magic-angle spinning (where the angle between the spinner axis and the static magnetic field, Θ, may be varied to generate a desired scaling of the recoupled interactions by $P_2(\cos\Theta)$[13]), the pulse spacings τ_1 and τ_2 may be varied to give a specified scaling of χ without deviating from the magic-angle[39].

Figure 3.3 2D ^{13}C-^{1}H DROSS spectrum of DMPC: (a) Acyl chain region (b) head group and glycerol region. The values of $\omega_r\tau_1/2\pi$ and $\omega_r\tau_2/2\pi$ chosen were 70.9° and 160.9° which correspond to χ = 0.393 and ε = 0.0. The delays δ_1 and δ_2 where set to 1.5 and 1.0 ms, respectively. The powder lineshapes corresponding to C_{14} and γ contain artifacts arising from data truncation during the evolution period.

(a)

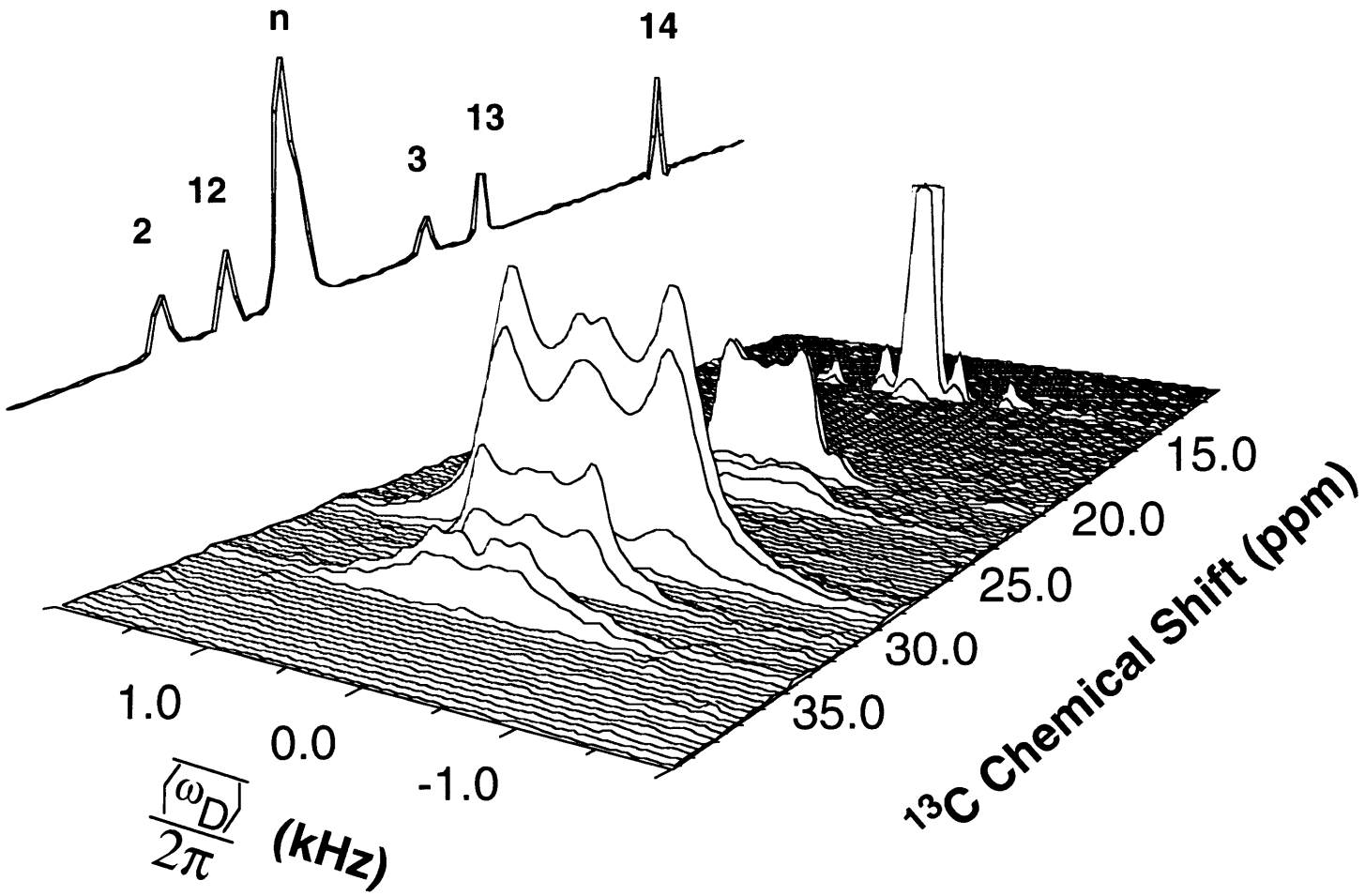
n
14
13
3
12
2
1.0
0.0
-1.0
$\frac{\langle\omega_D\rangle}{2\pi}$ (kHz)
35.0
30.0
25.0
20.0
15.0
^{13}C Chemical Shift (ppm)

Figure 3.3

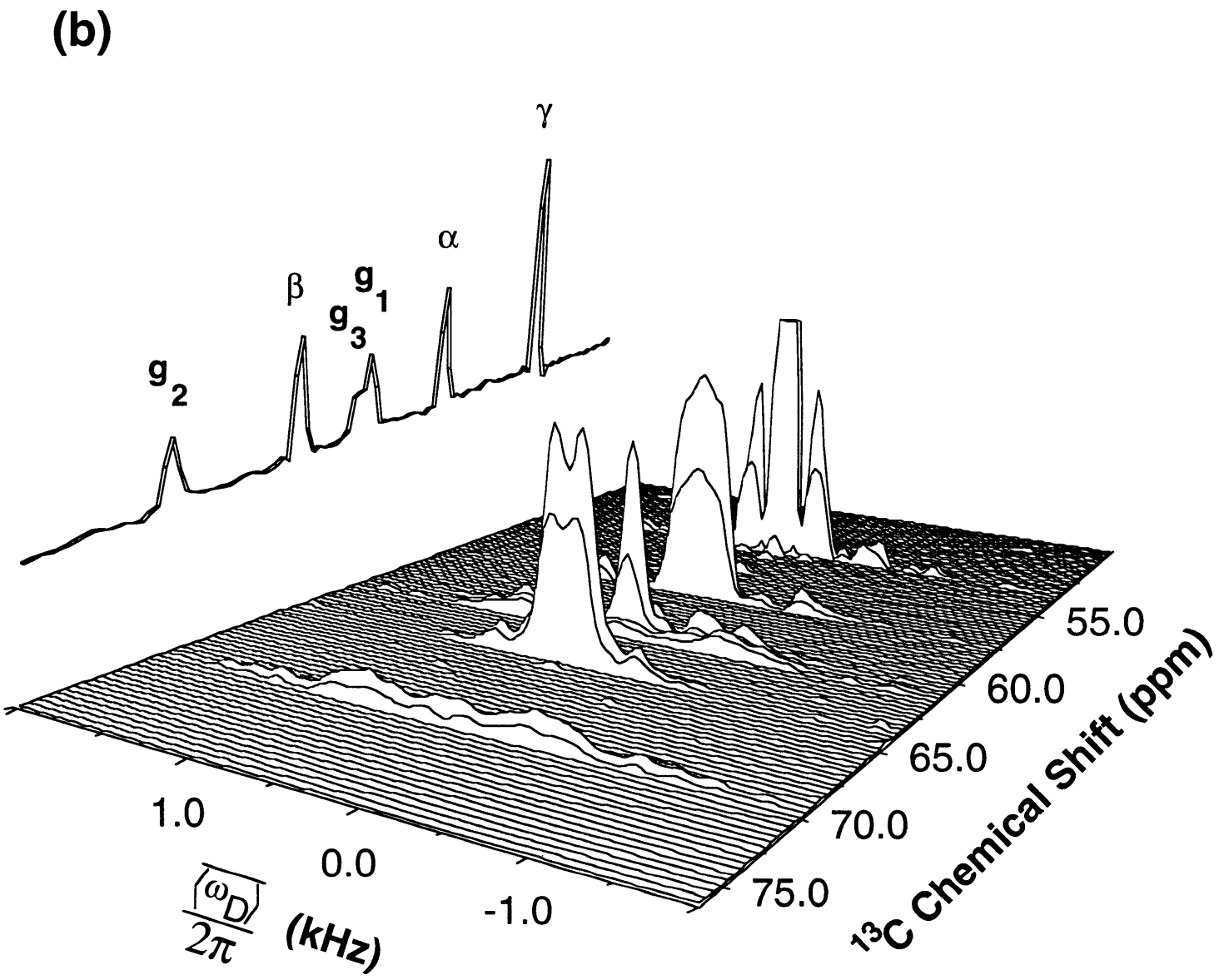
(b)
γ
α
β
g1
g3
g2
1.0
0.0
-1.0
⟨ωD⟩/2π (kHz)
55.0
60.0
65.0
70.0
75.0
13C Chemical Shift (ppm)

Figure 3.3

The CH_2 and CH_3 groups found in DMPC contain at least two ^{13}C-^{1}H dipolar couplings which *a priori* need not be identical. However, from ^{2}H NMR on specifically labelled CD_2 and CD_3 lipid bilayers it is well known that fast limit gauche-trans isomerization and axial diffusion renders the CD tensors, and therefore CH dipolar tensors, identical so that only one splitting is observed for most sites. The powder patterns found in Figure 3.3 mirror the lineshapes observed in ^{2}H NMR with the exception of the small central splittings which are attributed to long-range ^{13}C-^{1}H dipolar couplings. For example, the top row of Figure 3.4a depicts several recoupled dipolar powder patterns taken from the g_2, C_{12}, and α positions of the 2D DROSS spectrum. The C_{12} and α positions, which are CH_2 groups, both contain only two splittings with the larger splitting corresponding to the value given by ^{2}H NMR for the motionally equivalent CH sites. Similar results are obtained for the C_{13} and β sites (data not shown). As expected, the g_2 site contains only one large splitting since it is a CH group. In contrast, methylene segments closer to the bilayer interface, such as the glycerol backbone and the upper region of the acyl chains, are more motionally restricted and are known to contain inequivalent sites. For example, one of the CH segments in the g_1 CH_2 group is dynamically averaged so that the angle between the motional axis and the internuclear vector is close to the magic-angle. ^{2}H NMR with a specifically labelled CH_2 group at g_1 results in a intense and narrow lineshape superposed with broad Pake pattern[45]. Likewise, this inequivalence is observed in the 2D DROSS "slice" taken at the g_1 resonance (see Figure 3.4b). In this case the origin of the additional splitting, not predicted by ^{2}H NMR, is unkown. Moreover, it is known from ^{2}H NMR that the C_2 segment exhibits three splittings: the sn-2 chain contains two inequivalent CD segments while those found on the chain attached at the g_1 position are degenerate[46]. These inequivalences are also observed in the 2D DROSS experiment. The observed lineshapes depicted in Figure 3.4 are fitted excellently using the motionally averaged ^{13}C-^{1}H dipolar couplings corresponding to the order parameters given by ^{2}H NMR while the additional splittings are simulated under the assumption of long-range dipolar interactions.

Figure 3.4 Selected ^{13}C-^{1}H dipolar slices from 2D DROSS spectrum: (top) compared with numerical simulations (bottom) for g_2, C_{12}, and α (a) and g_1, C_2, and C_3 (b). The dipolar couplings that generated the best fit between simulation and experimental data are selected for the calculation of the ^{13}C-^{1}H segmental order parameter S_{CH}, as described in the text. In (a) input values for $<b_{CH}>$ are: g_2: 4.1 kHz, C_{12}: 2.2 and 0.7 kHz, and α: 0.9 and 0.2 kHz. ^{1}H resonance offsets for g_2, C_{12}, and α were 0.88, -0.70 and 0.48 kHz while those for ^{13}C were 1.90, -2.90 and 0.75 kHz respectively. In (b) input values for $<b_{CH}>$ are: g_1: 0.2, 2.8 and 4.2 kHz, C_2: 0.8, 1.9, 2.8 and 4.4 kHz, and C_3: 0.7, 2.6 and 3.8 kHz. ^{1}H resonance offsets for g_1, C_2 and C_3 were 0.44, -0.30 and -0.64 kHz while those for ^{13}C were 1.10, -2.00, and -2.70 kHz. Values for ^{13}C CSA tensor corresponding to δ_{11}, δ_{22}, and δ_{33} were taken to be 50, 37 and 13 ppm respectively while the ^{1}H CSA was taken to be zero. The timings for τ_1 and τ_2 were those given in Figure 3.3 for $\chi = 0.393$ and $\varepsilon = 0.0$.

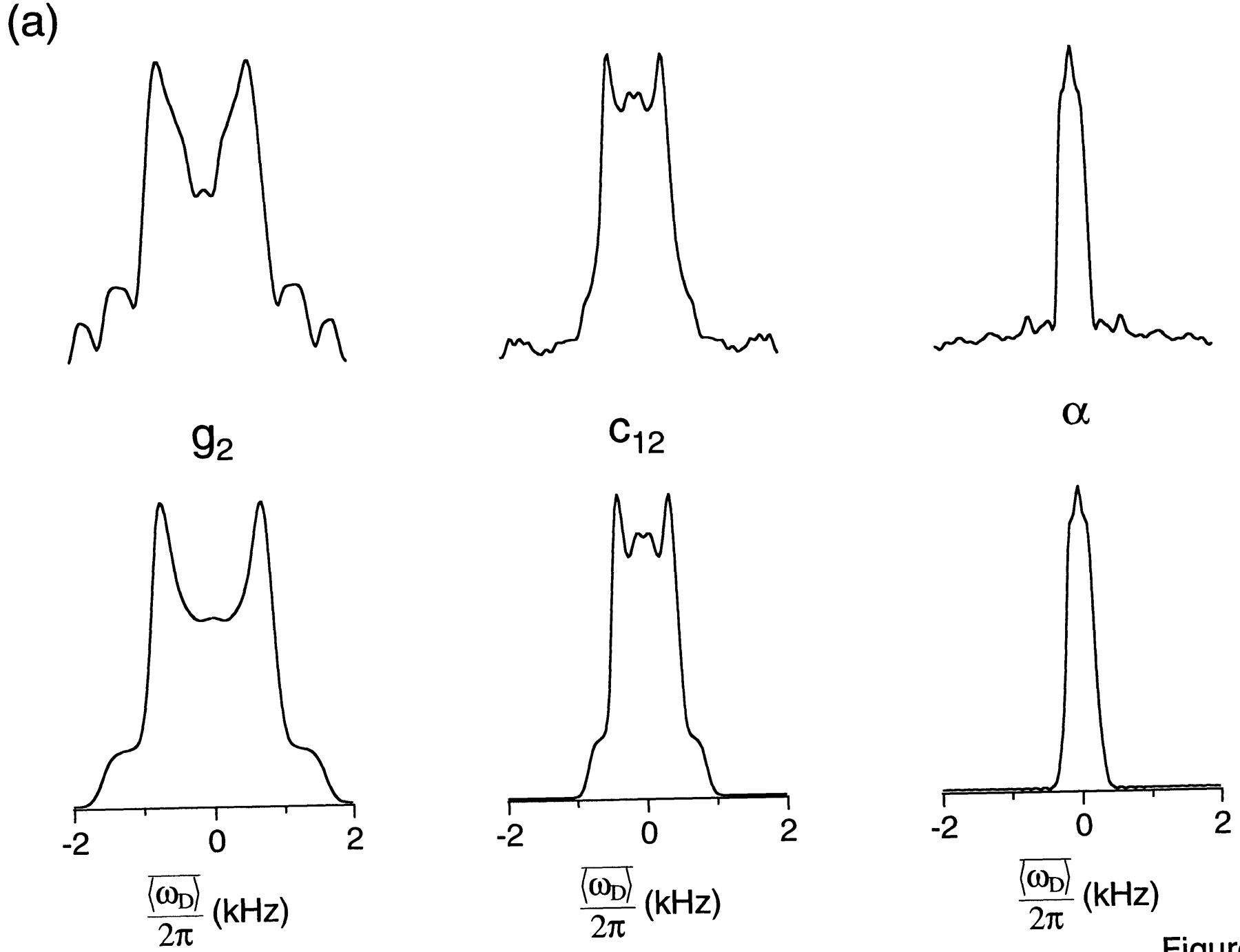

Figure 3.4

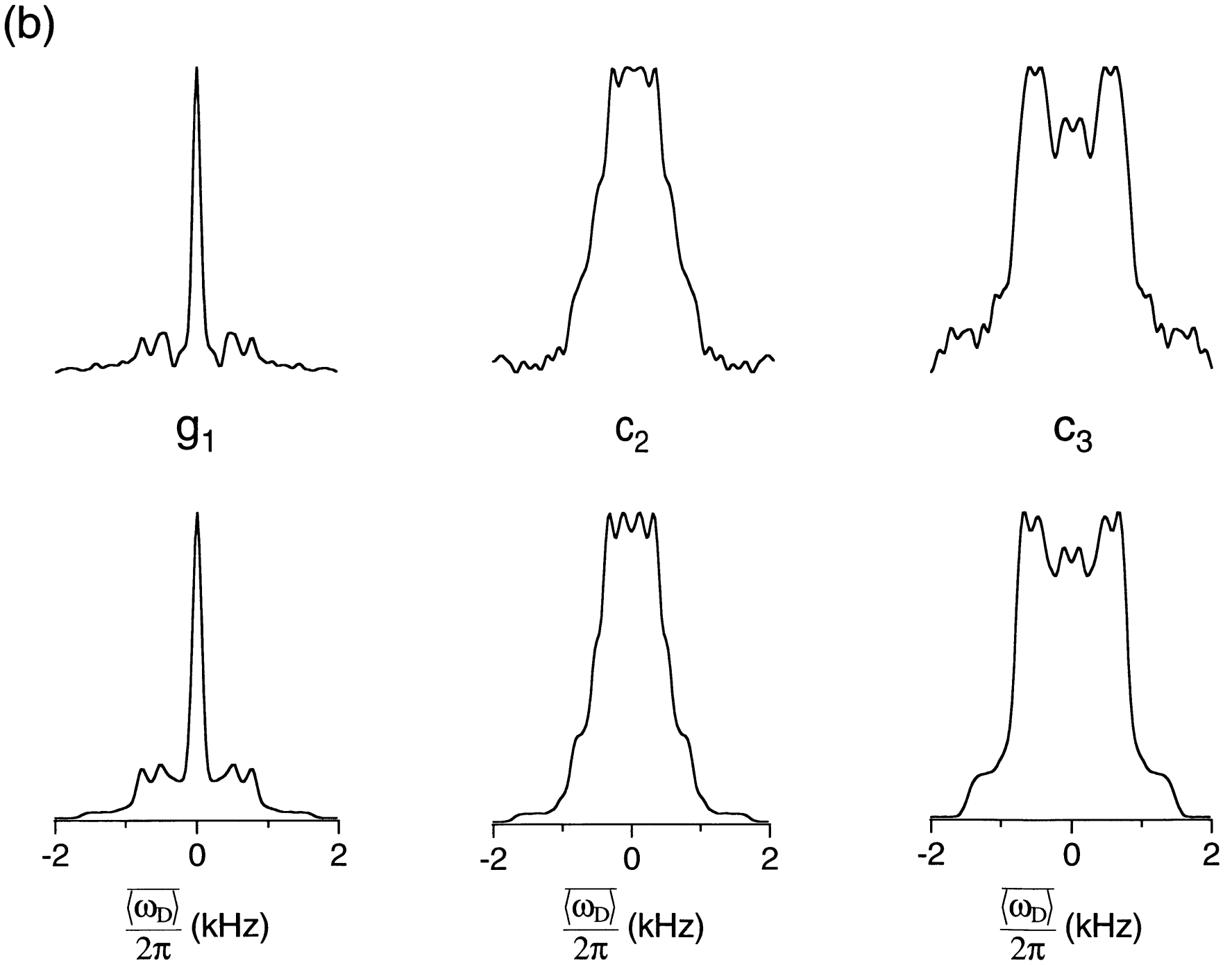

Figure 3.4

Long-range couplings which are not predicted by ^{2}H NMR are found in the 2D DROSS experiment due to the fact that the quadrupolar coupling reports on local order whereas ^{13}C-^{1}H dipolar couplings may report on larger spatial scales. For example, the small central splittings, observable in most of the recoupled dipolar lineshapes, are attributed to dipolar interactions between ^{13}C and a remote ^{1}H and are not due to pulse imperfections. Figure 3.5a illustrates numerical lineshape simulations of the scaled Pake pattern obtained for two motionally equivalent CH segments of the CH_2 group found at the C_{12} position of DMPC under conditions of δ-function pulses (ideal recoupling) superimposed with the lineshape obtained with the finite pulse lengths employed in this study. Note that the lineshapes are identical. The central splitting found in the experimental lineshape is fitted nicely by weighting and coadding the results of Figure 3.5a with the simulation of a long- range ^{13}C-^{1}H dipolar coupling between C_{12} and a remote proton (See Figure 3.5b). There is excellent agreement between the composite lineshape and experimental results (See Figures 3.5c and d).

Figure 3.5 Numerical lineshape simulations of DROSS recoupling for the C_{12} site using spectral parameters found in Figure 3.4 except the CH_2 group was simulated with a motionally averaged ^1H-^1H dipolar coupling of 5.0 kHz. (a) Solid line: finite π pulse widths of 8.8 μs. Dashed line: δ-function π pulses. (b) Overlay of finite pulse simulations for C_{12} and a weighted long-range dipolar coupling with $<b_{CH}>$ of 2.2 and 0.7 kHz respectively. (c) Experimentally obtained lineshape for C_{12}. (d) Addition of spectra found in (b).

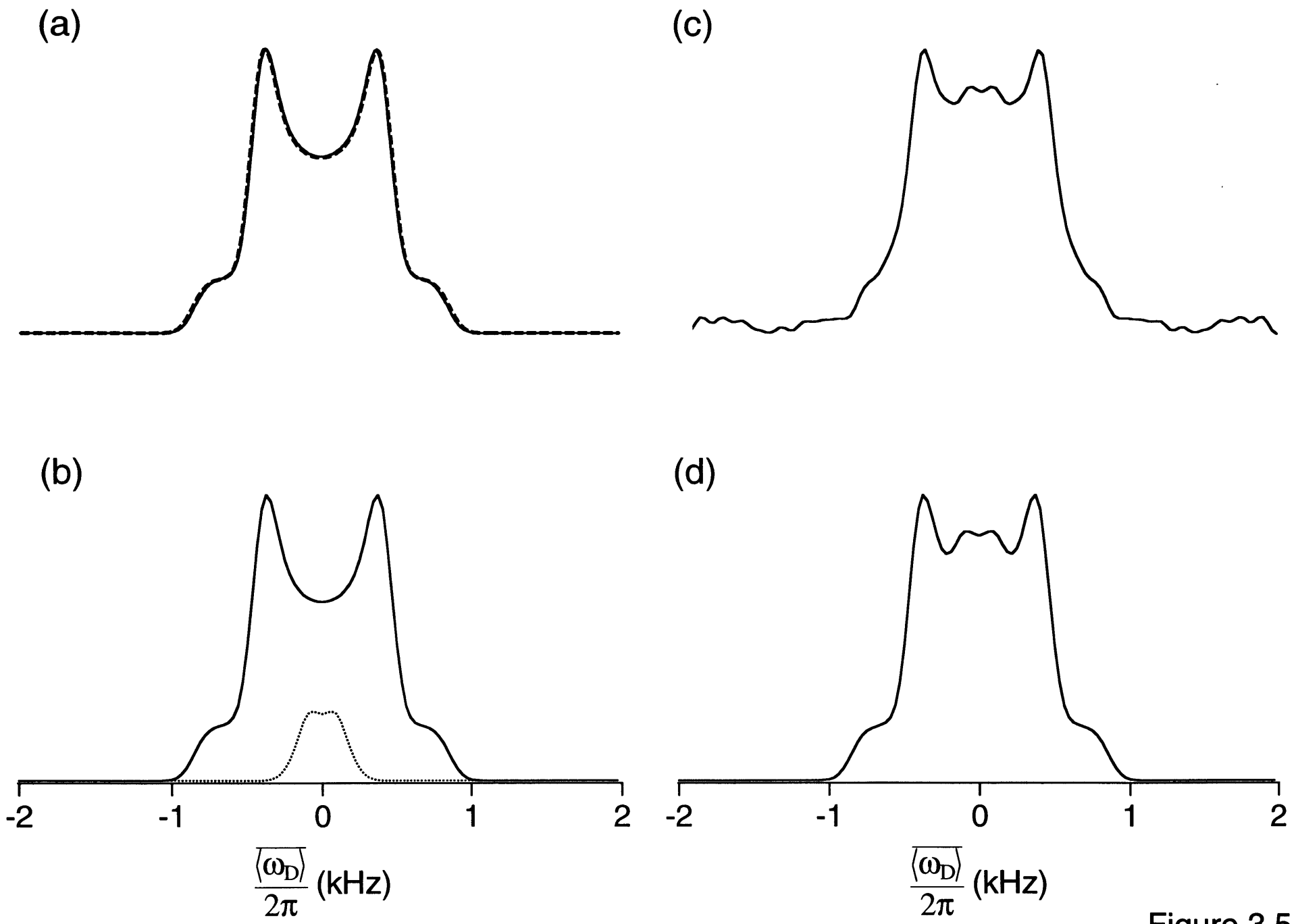

Figure 3.5

Similar long-range splittings have been observed in switched-angle spinning experiments that allow evolution of ^1H transverse magnetization under recoupled ^{13}C-^1H dipolar interactions followed by CP to ^{13}C for detection[29]. It is known that in these experiments there is a increase in intensity of the central splitting with increasing CP contact time. For the case of 2D DROSS where rotor-synchronized refocused-INEPT achieves the coherence transfer between ^1H and ^{13}C, variation of the transfer delays δ_1 and δ_2 produces a variation of the central splitting intensity corroborating the aforementioned results (data not shown). Presumably, the ^1H magnetization of a remote spin evolves under a long range dipolar coupling and is transferred via long range heteronuclear J coupling to ^{13}C. Long range dipolar couplings have been employed to yield additional constraints for average conformation in lipid bilayers[47]. Therefore, methods that assign these interactions to a specific ^1H would be useful and may include either selective excitation or the addition of a third dimension to the 2D DROSS experiment allowing for ^1H chemical shift evolution.

Lineshapes corresponding to directly bonded CH pairs are also simulated by weighting and coadding powder patterns obtained from individual simulations following the procedure outlined in Figure 3.5. The addition of lineshapes is justified within the approximation of δ-function pulses and an effectively inhomogeneous Hamiltonian while the weighting factors are chosen to fit the intensities corresponding to the relative transfer effeciency through rotor-synchronized refocused-INEPT. This procedure is particularly convenient for the simulation of inequivalent couplings found at CH_2 segments such as C_2. The ^{13}C-^1H dipolar coupling that produces the best fit between simulated and experimentally determined powder patterns is divided by the corresponding rigid lattice dipolar coupling to obtain S_{CH}. The value for the rigid lattice dipolar coupling between a directly bonded CH pair is chosen to be 20.2 kHz which is smaller than the value of 22.7 kHz given by an internuclear distance of 1.11 Å from neutron diffraction data[48]. This choice is justified by measurements of dipolar couplings in small molecules in the solid state, such as calcium formate, which indicate such a departure and are consistent with vibrational averaging of the dipolar interactions[11]. The apparent discrepancy between internuclear distances obtained by

neutron diffraction and solid state NMR is attributed to different time scales of measurement and has been discussed previously[49]. Interestingly, both experimental[12] and theoretical[50] studies on larger molecules such as polymers and long chain hydrocarbons have indicated a more severe vibrational averaging of ^{13}C-^{1}H dipolar interactions in the solid state which is attributed to the increased number of wagging or librational modes. Nevertheless, comparison of S_{CH}, obtained from directly bonded ^{13}C-^{1}H dipolar couplings, with the ^{2}H order parameter S_{CD} indicates good agreement between results obtained from the 2D DROSS technique and ^{2}H NMR (see Table 1). Values of S_{CH} obtained from switched-angle spinning experiments are tabulated for a comparison of the relative accuracy of the techniques.

Table 3.1: Comparison of S_{CH} with S_{CD} for DMPC at 30°C.

a) S_{CH} is defined as the ratio of the motionally averaged dipolar splitting, $\langle b_{CH} \rangle$, divided by the rigid lattice value taken to be 20.2 kHz for a directly bonded ^{13}C - ^{1}H pair.

b) S_{CH} for egg yolk lecithin taken from Hong, M.; Schmidt-Rohr, K.; Pines, A. *J. Am. Chem. Soc.* **1995**, 117, 3310-3311 where the rigid lattice dipolar coupling is taken to be 22.7 kHz for a directly bonded ^{13}C-^{1}H pair.

c) S_{CD} is defined as the ratio of the motionally averaged quadrupolar splitting $\langle \Delta\nu_Q \rangle$, divided by the rigid lattice value taken to be 127 kHz.

d) Interpolated between 23°C and 40°C from values given in Trouard, T.P. ; Alam, T. M. ; Zajicek, J. ; Brown, M.F. *Chem. Phys. Lett.* **1992**, 189, 67 and Meier, P.; Ohmes, E.; Kothe, G. *J. Chem. Phys.* **1986**,85, 3598.

e) Oldfield, E.; Meadows, M.; Jacobs, R. *Biochemistry* **1978**, 17, 2727.

f) Seelig, A. and Seelig, J. *Biochemistry* **1974**, 13,4839

g) Gally, H. U.; Pluschke, G; Overath, P; Seelig, J. *Biochemistry* **1981**, 20, 1826.

h) Gally, H. U.; Niederberger, W.; Seelig, J. *Biochemistry* **1975**, 14, 3647.

Table 3.1: Comparison of S_{CH} with S_{CD} for DMPC at 30°C.

Carbon Position	S_{CH} (± 0.02)[a]	S_{CH} [b]	$\|S_{CD}\|$[c]
13	-0.09	ND	0.10[d]
12	-0.11	ND	0.14[e]
3	-0.13	ND	0.18[f]
	-0.19	-0.22 ± 0.03	0.21[f]
2	-0.09	ND	0.09[f]
	-0.14	-0.12 ± 0.03	0.15[f]
	-0.21	-0.21 ± 0.03	0.21[f]
g_1	0.00	ND	0.00[g]
	-0.15	-0.12 ± 0.04	0.16[g]
g_2	-0.20	-0.16 ± 0.04	0.19[g]
g_3	-0.23	-0.19 ± 0.03	0.21[g]
a	+0.04	+0.04 ± 0.02	0.05[h]
b	-0.03	-0.04 ± 0.02	0.04[h]

Considerations affecting the overall sensitivity of the experiment include the coherence transfer from ^1H to ^{13}C. It is well known that ^1H-^{13}C CP/MAS intensities become sensitive to Hartmann-Hahn mismatch when spinning speeds exceed the strength of the relevant dipolar couplings[51]. Experiments in our lab on fluid phase lipids indicate that ^1H-^{13}C CP/MAS intensities are sensitive to Hartmann-Hahn mismatch even at moderate spinning speeds. This is due to the fact that dipolar couplings in fluid phase lipids are reduced significantly by motional averaging and that the Hamiltonian is rendered inhomogeneous due to fast limit axial diffusion, so that optimal CP intensities are difficult to achieve and maintain for long times. Typically this problem is rectified by employing any of a wealth of the new phase-switched and amplitude-modulated techniques[52-56]; however, for inhomogeneous systems, these schemes generate an orientation dependent polarization transfer which may complicate the interpretation of powder lineshapes. Consequently, we have chosen rotor-synchronized refocused-INEPT in order to insure an orientation independent transfer through the scalar coupling so that powder lineshapes are determined solely by the evolution under H^{eff} (see equation 3.2) during t_1. The utility of an orientation independent transfer is exhibited by the sharp CH lineshape visible for the g_1 site-expected from ^2H NMR and arising from a bond oriented at the magic-angle-which was lost in previously published spectra for which CP was used(See Figure 3.4b)[29,57]. This approach is well suited for fluid phase lipids since the ^1H and ^{13}C linewidths are less than J_{CH}. For systems where transverse relaxation rates are rapid relative to J_{CH}, the sensitivity of the 2D DROSS experiment will be compromised since the time scale of the refocused-INEPT transfer is approximately $1/2J_{CH}$[40]. In this case, CP transfer schemes may offer a sensitivity advantage, and dipolar couplings may be extracted by incorporating the particular CP transfer scheme into the lineshape simulations.

Figure 3.6 depicts the normalized ^{13}C resonance intensity as a function of evolution period, t_1, along with the corresponding Fourier transform for selected ^{13}C resonances in DMPC obtained with the S-DROSS sequence where $\chi = 0.393$ and $\varepsilon = 0$. The fact that values of τ_1 and τ_2 may be chosen so that $\varepsilon = 0$ presents two advantages over experiments which require switched-angle

spinning[29,30], one being the ability to determine the sign of the dipolar interaction independently from the ratio $\chi\langle\pm\omega_D\rangle / \pi J_{CH}$ and the other being the ability to do so unambiguously with only one set of scale factors. These advantages stem from the fact that, in the switched-angle spinning experiment, the sign of the dipolar interaction in given by the sign of $\langle\pm\omega_D\rangle\ P_2(\cos\Theta) + \pi J_{CH}$ while in the case of S-DROSS the sign is given by $\chi\langle\pm\omega_D\rangle\ + \varepsilon\pi J_{CH}$.

Figure 3.6 S-DROSS experimental data and numerical lineshape simulations for β, α, and C_2 sites depicted in (a) - (c) respectively. From left to right, the build-up of ^1H antiphase magnetization monitored by ^{13}C detection is depicted followed by the corresponding Fourier transform and numerical lineshape simulations. Input parameters for the simulations: (a) $\langle b_{CH} \rangle$ = +0.6 kHz with ^1H and ^{13}C resonance offsets of 0.22 and 2.20 kHz; (b) $\langle b_{CH} \rangle$ = -0.9 kHz with ^1H and ^{13}C resonance offsets of 0.47 and 1.60 kHz; and (c) $\langle b_{CH} \rangle$ = +1.9, +2.8 and +4.4 kHz with ^1H and ^{13}C resonance offsets of -0.30 and -1.00 kHz. The timings for τ_1 and τ_2 were those given in Figure 3.2 for χ = 0.393 and ε = 0.0.

(a)

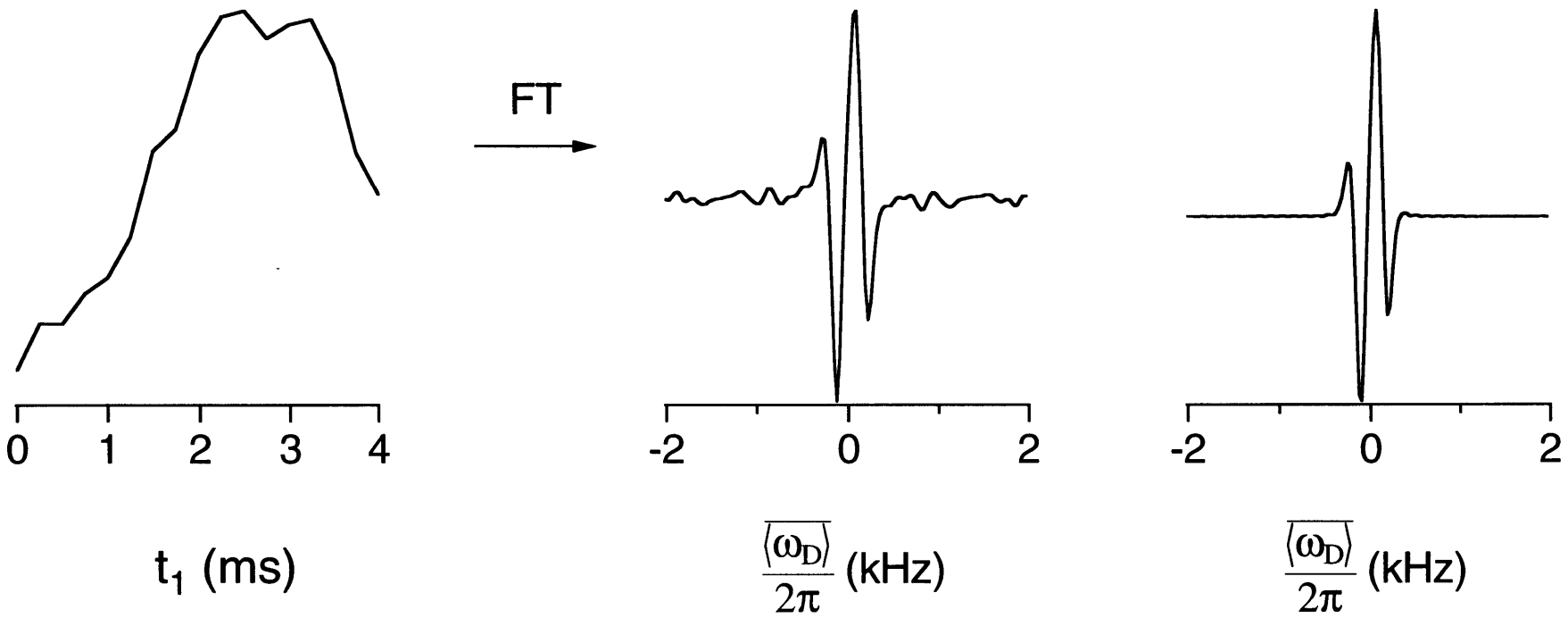

Figure 3.6

(b)

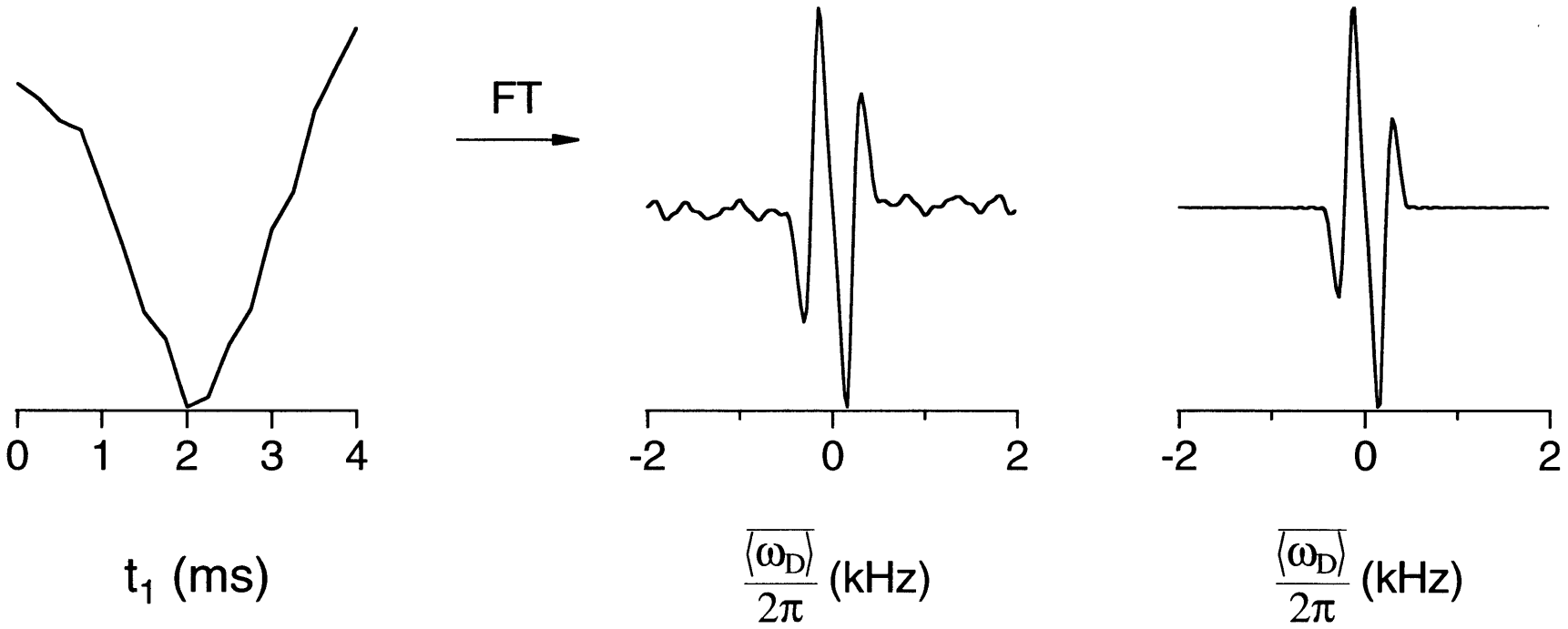

Figure 3.6

(c)

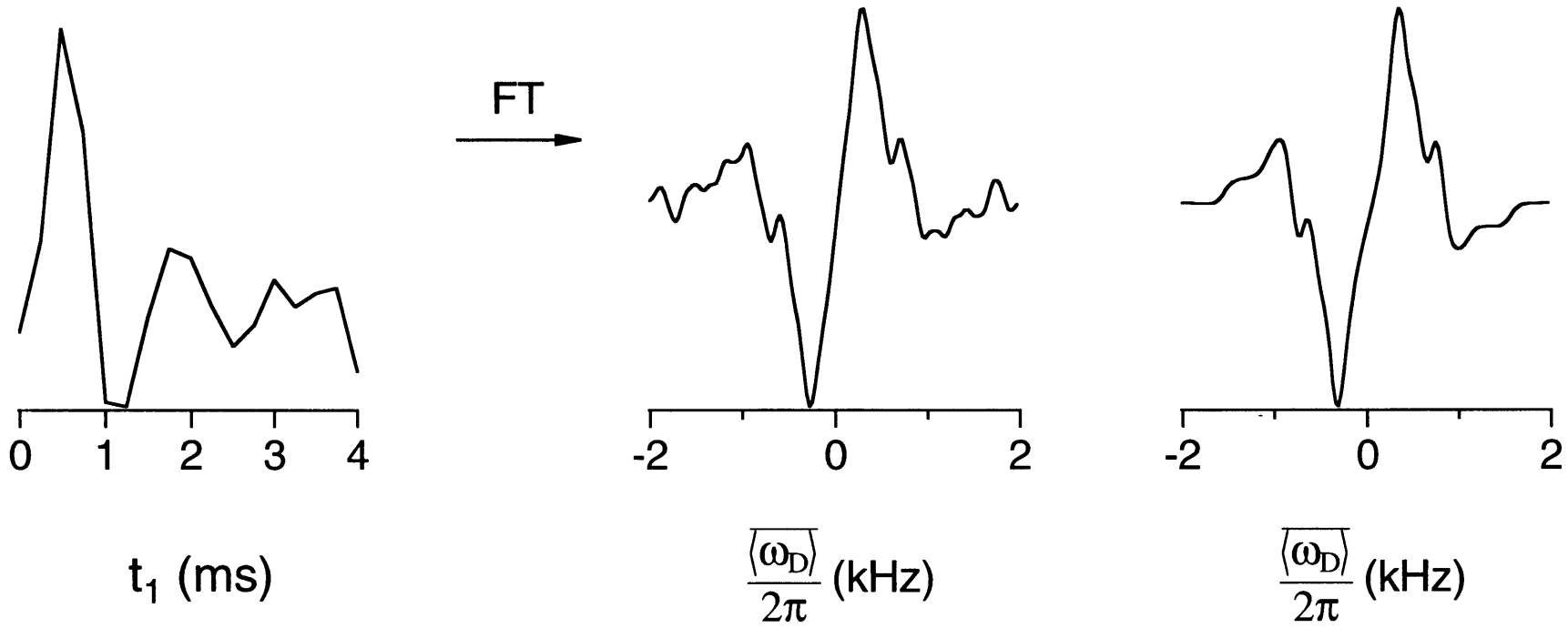
FT
0
1
2
3
4
-2
0
2
-2
0
2
t_1 (ms)
$\frac{\langle\omega_D\rangle}{2\pi}$ (kHz)
$\frac{\langle\omega_D\rangle}{2\pi}$ (kHz)

Figure 3.6

For ^{13}C sites containing degenerate ^{13}C-^{1}H dipolar couplings, the sign of the dipolar coupling is easily obtained from the initial build-up rate of antiphase magnetization provided that $|\chi<\pm\omega_D>| >> \varepsilon\pi J_{CH}$ as is the case here since ε=0. For example, the build-up curves for β and α positions indicate positive and negative dipolar couplings respectively. The negative dipolar coupling, or positive order parameter, found at the α position is consistent with the fact that the choline head group makes an unusual bend at the phosphate junction[47,58]. In contrast, segments that contain non-degenerate ^{13}C-^{1}H dipolar couplings may complicate the time-domain analysis. In this case, Fourier transformation of the data would clarify the results as inequivalent couplings would manifest as separate antiphase Pake doublets with sign differences given by opposite polarity since a positive dipolar coupling gives rise to a +-+- intensity pattern while the negative coupling yields a -+-+ pattern (see Figures 3.6a and b). Just as in the DROSS experiment, non-degenerate ^{13}C-^{1}H dipolar couplings may be simulated as a superposition of Pake patterns. In Figure 3.6c, all of the inequivalent couplings found at C_2 are found to be positive using this approach. A summary of the signs of ^{13}C-^{1}H dipolar interactions measured with S-DROSS utilizing either the time or frequency domain analysis are given in Table 1 and are in agreement with previous studies[29,57].

The magnitudes and signs of ^{13}C-^{1}H dipolar couplings determined in this study are useful for determining average molecular conformation. In the order matrix approach, each CH segment generally requires at least five anisotropies to be measured so that the complete orientation of the segmental order tensor may be specified [59]. The elements of the complete order matrix furnish angular distribution functions that yield the average orientation of a CH segment with respect to the director axis[60-62]. Alternatively, methods that involve the fitting of motionally averaged powder lineshapes with either assumed or known dynamical models may provide more insight between fast limit molecular dynamics and motionally averaged tensors[6]. Other approaches, utilizing motionally averaged dipolar couplings and J couplings in conjunction with molecular dynamics simulations are also a promising means for determining average molecular structure[63].

3.5 Conclusion;

We have presented an alternative method for the measurement of the magnitudes and signs of ^{13}C-^{1}H dipolar couplings in liquid crystalline systems such as lipid bilayers. It is possible to obtain information regarding the average orientation of CH bond segments without recourse to isotopic enrichment. Implementation of the proposed experiments is straightforward in that they do not require specialized hardware for angle switching between the evolution and detection periods. The techniques are applicable for systems where molecular motions render the ^{1}H spin dynamics effectively inhomogeneous at experimentally realizable spinning speeds.

We anticipate that, in the future, the information provided by dipolar recoupling, combined with MAS techniques which simultaneously correlate chemical shifts and long-range scalar couplings, will provide important constraints for determining the average molecular conformation in lipid bilayers. In addition, it may be possible to incorporate an inversion recovery period in the 2D DROSS experiment as a probe for anisotropic ^{13}C spin lattice relaxation. Presumably, recoupled dipolar powder patterns would serve as a reporter of orientation dependent relaxation which would present the exciting possibility of directly probing the rates of dynamic processes through dipolar recoupling.

Acknowledgments for Chapter 3

This chapter is excerpted from a manuscript that appeared in J Am Chem Soc 119: (4) 796-802 Jan 29 1997. The work was done in collaboration with Dror E. Warschawski.

References for Chapter 3

[1] Seelig, J.; Seelig, A.; Q. Rev. Biophys. 1980, 13, 19-61.

[2] Davis, J. H.; Biochim. Biophys. Acta 1983, 737, 117-171.

[3] Spiess, H. W.; Adv. Polym. Sci 1985, 66, 23.

[4] Oldfield, E.; Chapman, D.; Derbyshire, W.; FEBS Lett. 1971, 16, 103-104.

[5] Siminovitch, D. J.; Olejniczak, E. T.; Ruocco, M. J.; Gupta, S. K. D.; Griffin, R. G.; Chem. Phys. Lett. 1985, 119, 251.

[6] Wittebort, R. J.; Olejniczak, E. T.; Griffin, R. G.; J. Chem. Phys. 1987, 86, 5411-5420.

[7] Speyer, J. B.; Weber, R. T.; Gupta, S. K. D.; Griffin, R. G.; Biochemistry 1989, 28, 9569-9574.

[8] Spiess, H. W.; Sillescu, H.; J. Magn. Reson. 1981, 42, 381-389.

[9] Blume, A.; Griffin, R. G.; Biochemistry 1982, 24, 6230 - 6242.

[10] Mayer, C.; Muller, K.; Weisz, K.; Kothe, G.; Liq. Crys. 1988, 3, 797 - 806.

[11] Munowitz, M.; Griffin, R. G.; Bodenhausen, G.; Huang, T. H.; J. Am. Chem. Soc. 1981, 103, 2529.

[12] Schaefer, J.; Stejskal, E. O.; McKay, R. A.; Dixon, W. T.; J. Magn. Reson. 1983, 52, 123-129.

[13] Terao, T.; Miura, H.; Saika, A.; J. Chem. Phys. 1986, 85, 3816-3826.

[14] Kolbert, A. C.; Levitt, M. H.; Griffin, R. G.; J. Magn. Reson. 1989, 85, 42-49.

[15] Sanders, C. R.; Prestegard, J. H.; J. Am. Chem. Soc. 1991, 113, 1987-1996.

[16] Nakai, T.; Terao, T.; Magn. Reson. Chem. 1992, 30, 42-44.

[17] Hester, K.; Ackerman, J. L.; Neff, B. L.; Waugh, J. S.; Phys. Rev. Lett. 1976, 36, 1081-1083.

[18] Schaefer, J.; Stejskal, E. O.; J. Am. Chem. Soc. 1976, 98, 1031.

[19] Munowitz, M. G.; Griffin, R. G.; J. Chem. Phys. 1982, 76, 2848.

[20 Gullion, T.; Poliks, M. D.; Schaefer, J.; J. Magn. Reson. 1988, 80, 553-558.

[21] Bork, V.; Gullion, T.; Hing, A.; Schaeffer, J.; J. Magn. Reson. 1990, 88, 523-532.

[22] Kolbert, A. C.; Griffin, R. G.; J. Magn. Reson. 1991, 93, 242-255.

[23] Gullion, T.; Schaefer, J.; J. Magn. Reson. 1989, 81, 196-200.

[24] Hing, A. W.; Schaefer, J.; Biochemistry 1993, 32, 7593-7604.

[25] Bennett, A. E.; Becerra, L. R.; Griffin, R. G.; J. Chem. Phys. 1994, 100, 812-814.

[26] Bax, A.; Szeverenyi, N. M.; Maciel, G. E.; J. Magn. Reson. 1983, 55, 494-497.

[27] Zeigler, R. C.; Wind, R. A.; Maciel, G. E.; J. Magn. Reson. 1988, 79, 299-306.

[28] Kolbert, A. C.; Groot, H. J. M. D.; Griffin, R. G.; J. Magn. Reson. 1989, 85, 60-68.

[29] Hong, M.; Schmidt-Rohr, K.; Pines, A.; J. Am. Chem. Soc. 1995, 117, 3310-3311.

[30] Hong, M.; Schmidt-Rohr, K.; J. Magn. Res. B 1995, 109, 284-290.

[31] Bloom, M.; Burnell, E. E.; Roeder, S. B. W.; Valic, M. I.; J. Chem. Phys. 1977, 66, 3012-3020.

[32] Bloom, M.; Burnell, E. E.; Mackay, A. L.; Nichol, C. P.; Valic, M. I.; Weeks, G.; Biochemistry 1978, 17, 5750-5762.

[33] Oldfield, E.; Meadows, M.; Rice, D.; Jacobs, R.; Biochemistry 1978, 17, 2727-2740.

[34] Forbes, J.; Bowers, J.; Moran, L.; Shan, X.; Oldfield, E.; J. Chem. Soc., Faraday Trans. 1988, 84, 3821-3849.

[35] Davis, J. H.; Auger, M.; Hodges, R. S.; Biophys. J. 1995, 69, 1917-1932.

[36] Maricq, M. M.; Waugh, J. S.; J. Chem. Phys. 1979, 70, 3300-3316.

[37] Levitt, M. H.; Raleigh, D. P.; Creuzet, F.; Griffin, R. G.; J. Chem. Phys. 1990, 92, 6347-6364.

[38] Torchia, D. A.; Szabo, A.; J. Magn. Reson. 1982, 49, 107-121.

[39] Tycko, R.; Dabbagh, G.; Mirau, P. A.; J. Magn. Reson. 1989, 85, 265-274.

[40] Burum, D. P.; Ernst, R. R.; J. Magn. Reson. 1980, 39, 163-168.

[41] Gross, J. D.; Costa, P. R.; Dubacq, J.-P.; Warschawski, D. E.; Lirsac, P.-N.; Devaux, P. F.; Griffin, R. G.; J. Magn. Reson. B 1995, 106, 187-190.

[42] Bennett, A. E.; Rienstra, C. M.; Auger, M.; Lakshmi, K. V.; Griffin, R. G.; J. Chem. Phys. 1995, 103, 6951-6958.

[43] Burum, D. R.; Rhim, W.-K.; J. Chem. Phys. 1979, 71, 944.

[44] Nakai, T.; Ashida, J.; Terao, T.; J. Chem. Phys. 1988, 88, 6049.

[45] Gally, H. U.; Pluschke, G.; Overath, P.; Seelig, J.; Biochemistry 1981, 20, 1826-1831.

[46] Seelig, A.; Seelig, J.; Biochim. Biophys. Acta. 1975, 406, 1-5.

[47] Hong, M.; Schmidt-Rohr, K.; Zimmermann, H.; Biochemistry 1996, 35, 8335-8341.

[48] Al-Karaghouli, A. R.; Koetzle, T. F.; Acta Crystallogr. 1975, B31, 2461 - 2465.

[49] Roberts, J. E.; Harbison, G. S.; Munowitz, M. G.; Herzfeld, J.; Griffin, R. G.; J. Am. Chem. Soc. 1987, 109, 4163-4169.

[50] Henry, E. R.; Szabo, A.; J. Chem. Phys. 1985, 82, 4753-4761.

[51] Stejskal, E. O.; Schaefer, J.; Waugh, J. S.; J. Magn. Reson. 1977, 28, 105-112.

[52] Wu, X.; Zilm, K. W.; J. Magn. Reson. A 1993, 104, 154-165.

[53] Peerson, O. B.; Wu, X.; Kustanovich, I.; Smith, S. O.; J. Magn. Reson. A 1993, 104, 334-339.

[54] Hediger, S.; Meier, B. H.; Ernst, R. R.; Chem. Phys. Lett. 1993, 213, 627-635.

[55] Metz, G.; Wu, X.; Smith, S. O.; J. Magn. Reson. 1994, A110, 219-227.

[56] Sun, B. Q.; Costa, P. R.; Griffin, R. G.; J. Magn. Reson. A 112, 283-288.

[57] Hong, M.; Schmidt-Rohr, K.; Nanz, D.; Biophysical Journal 1995, 69, 1939-1950.

[58] Bueldt, G.; Gally, H. U.; Seelig, J.; Zaccai, G.; Nature 1978, 271, 182-184.

[59] Saupe, A.; Z. Naturf. 1964, 19a, 161-171.

[60] Hentschel, R.; Schlitter, J.; Sillescu, H.; Spiess, H. W.; J. Chem. Phys. 1978, 68, 56.

[61] Torchia, D. A.; Szabo, A.; J. Magn. Reson. 1985, 64, 135 - 141.

[62] Schmidt-Rohr, K.; Hong, M.; J. Phys. Chem. 1996, 100, 3861 - 3866.

[63] Howard, K. P.; Prestegard, J. H.; J. Am. Chem. Soc. 1995, 117, 5031 - 5040.

4. Effects of Membrane Peptide Dynamics on High-Resolution Magic-Angle Spinning NMR

4.1 Introduction

In the past fifteen years, interferences between molecular dynamics and coherent manipulation of nuclear magnetization in solid-state nuclear magnetic resonance (NMR) experiments such as spin decoupling, cross-polarization or magic-angle spinning (MAS) have been identified and studied carefully[1-5]. Recent experiments performed in our laboratory on model compounds have provided insight into the nature of a perturbation responsible for the broadening of ^{13}C and ^{15}N signals, namely the interference of some molecular motion with ^{1}H-decoupling[6, 7]. The same effect is demonstrated here for the first time in the case of a membrane peptide, *gramicidin A* (gA), in an hydrated lipid bilayer. A comparison of the experimental data with numerical lineshape simulations allows motional rates to be extracted illuminating the mechanism of the broadening and methods to circumvent the effect. Similar strategies could be useful for structural and dynamical studies of other membrane peptides in hydrated bilayers.

Gramicidin A (gA) is the major form of a linear peptide produced by the bacteria *Bacillus brevis*. It has a sequence of 15 alternating L- and D-amino acid residues and consists of a right-handed β-helix having 6.3 residues per turn that dimerizes, N-terminus to N-terminus, to form a monovalent cation selective channel in model membranes. The development of synthetic procedures which provide large quantities of this peptide and its relatively small size make gA an ideal candidate for spectroscopic studies of ion channels and membrane peptides. Accordingly significant attention has been given to the study of both the structure and dynamics of gA.

High-resolution structures of membrane peptides have been obtained in the case of single crystals or solutions of peptides in organic solvents or micellar systems, with NMR or X-ray diffraction; however, these environments are known to be different from a hydrated lipid bilayer and may induce changes in conformation[8]. Solid-state NMR is an ideal tool for the study of membrane peptides in their natural environment: hydrated bilayers in the liquid-crystalline L_α phase. Accordingly spectroscopic studies of oriented hydrated lipid bilayers have provided the structure of gA in its native state[9]. However, it would be convenient to use MAS NMR which does not require macroscopic sample orientation and has proven to be very powerful in

determining molecular conformation[10, 11]. Attempts to obtain high-resolution MAS NMR spectra of peptides and proteins in liquid-crystalline membranes were unsuccessful because of problems associated with the dynamics of the molecules[12-15]. Subsequent studies have circumvented these issues by performing experiments at very low temperatures, where motion is quenched. Unfortunately, information regarding structure and dynamics under physiological conditions is lost. Several authors have observed carbonyl (^{13}CO) resonances of gA amino acids[15-18] and these results provide some conformational and dynamical information. However it is desirable to address the more general case of signals corresponding to the many protonated carbons, during MAS and ^{1}H-decoupling.

4.2 Classical Relaxation Theory

The interference between CW proton decoupling and molecular motions was first observed by VanderHart[2]. Rothwell and Waugh subsequently provided a theoretical description that is based on classical relaxation theory[3]. The total Hamiltonian consist of both Zeeman terms for the unlike I and S spins and a heteronuclear IS dipolar coupling under CW irradiation of the I spins. The S spin T_2 may be calculated for the case of irradiation of I spins by considering motions which are slow relative to the Larmor frequencies but fast relative to the spinning speed. Invoking the standard secular and high-temperature approximations, the result is written:

$$\frac{1}{T_2} = \frac{2}{3}\omega_D^2 I(I+1) J_0^{IS}(\omega_1) \tag{4.1}$$

where

$$J_0^{IS}(\omega_1) = 2\int_0^{\infty} dt\, C_0^{IS}(t) \cos(\omega t) \tag{4.2}$$

and the effect of MAS has been neglicted. The autocorrelation function,

$$C_0^{IS}(t) = \langle R_{2m}^{IS*}(0) R_{2m}^{IS}(t) \rangle / \tilde{\rho}_{20}^{IS} \tag{4.3}$$

depends on the stochastic modulation of the spatial components R as defined in Chapter 1.

For isotropic rotational diffusion,

$$C_0^{iso}(t) = \frac{1}{5} e^{-t/\tau_c} \tag{4.4}$$

and immediately, one finds

$$\frac{1}{T_2} = \frac{4}{15}\omega_D^2 I(I+1)\frac{\tau_c}{1+(\omega_1\tau_c)^2} \tag{4.5}$$

which contains the essence of the effect as first described by Rothwell and Waugh[3]. For short correlation times where $\omega_1\tau_c<<1$- nature essentially eliminates the need for dipolar decoupling by the motional averaging of the dipolar interactions through isotropic diffusion . In the opposite regime where $\omega_1\tau_c>>1$- the linewidth is determined by the ratio of the dipolar coupling to the available decoupling field strength. In analogy to the T_1 minimum, when the correlation time is on the order of the inverse Larmor frequency, the T_2 here is minimized when the correlation time is on the same time scale as the inverse decoupling frequency. Physically, the line broadening occurs due to the interference between random molecular motion and the coherent averaging provided by proton decoupling as the time scales of the two modulations become similar (when $\omega_1\tau_c$ approaches unity). This dependence of the linewidth on the correlation time, τ_c, is depicted in Figure 4.1a for a 90 kHz decoupling field. Clearly, the effect changes the most rapidly about the interference maximum where the linewidth is the largest. In this case, the correlation time may be extracted but at the sake of resolution.

Figure 4.1 Display of full-width-half-maximum intensity ($1/\pi T_2$) as a function of $\log(\tau_c)$ with results from (a) classical relaxation theory for isotropic rotational diffusion and (b) three-site hop with classical theory (dashed line) and quantum mechanical treatment discussed in section 4.3 (solid line).

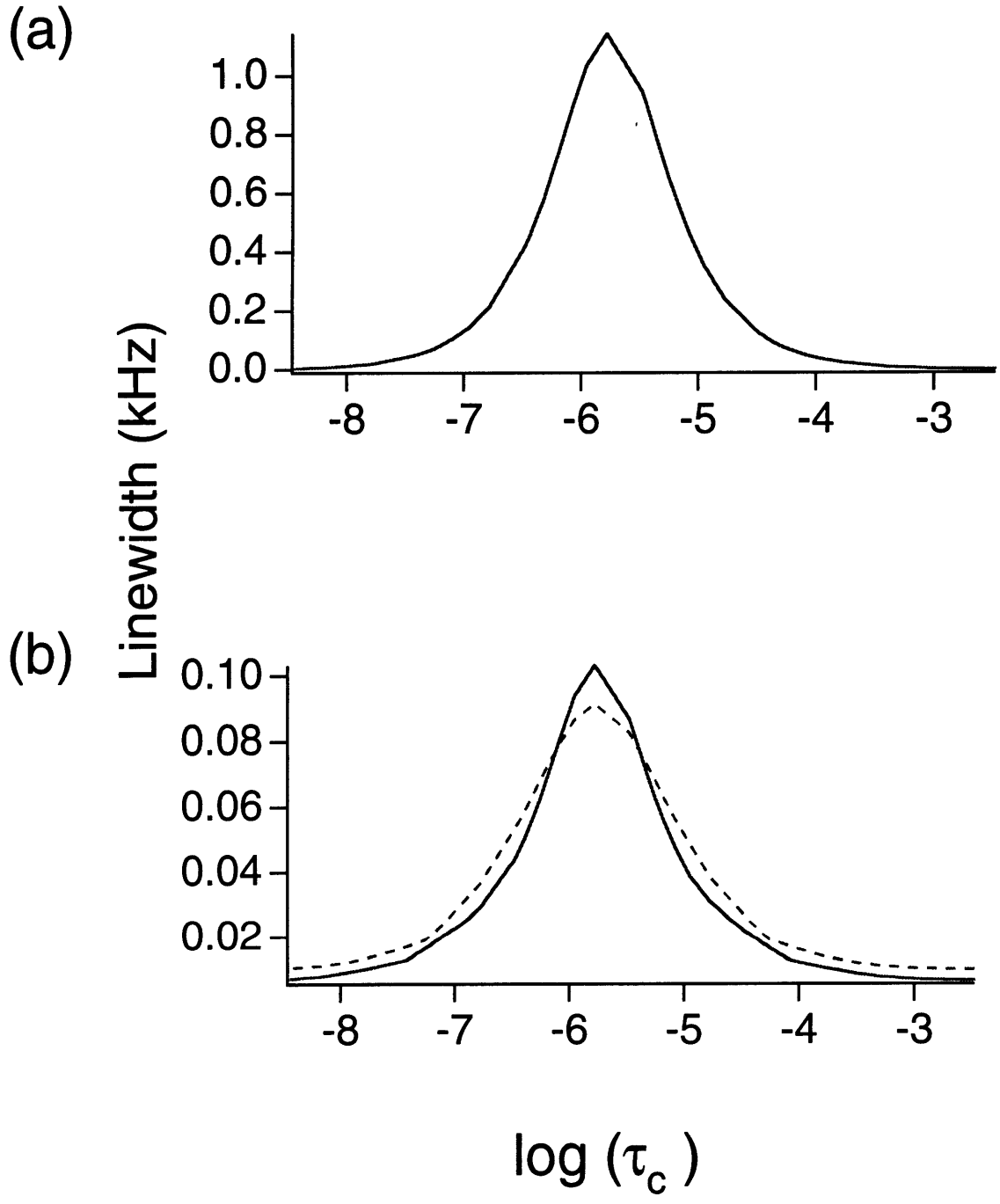
(a)
1.0
0.8
0.6
0.4
0.2
0.0
-8
-7
-6
-5
-4
-3
(b)
Linewidth (kHz)
0.10
0.08
0.06
0.04
0.02
-8
-7
-6
-5
-4
-3
log (τc)

Figure 4.1

The above expression for T_2 is inappropriate for treating anisotropic motion, the most common scenario encountered in the solid-state. However, correlation functions may be developed in order to test the agreement of the above theory with a given motional model which may then allow extraction of motional rates. In addition to physical insight, the advantage of such an analytic approach would be speed of computation. Generally, for the case of anisotropic motion, the Hamiltonian may be partitioned into a static, time independent part, and a time modulated part[19]. The effect of the time modulation is to induce relaxation. For a three-site hop as depicted in Figure 4.2a (assuming an isolated CH spin pair) the time independent part of the dipolar coupling may be written[20]

$$H^{IS}_{Stat} = \omega_D \, P_2(\cos(\beta_{PD}) \, P_2(\cos(\beta_{DL}) \tag{4.6}$$

while the correlation function is given by

$$C_0^{3SH}(t) = \frac{9}{32} [A_1B_1 + A_2B_2 - 8 \, A_3B_3\cos(3\alpha_{DL})]e^{-t/\tau_c} \tag{4.7}$$

with $\tau_c = (3k)^{-1}$ and the functions A and B written as:

$$\begin{aligned} A_1 &= \sin^2(2\beta_{PD}) & B_1 &= \sin^2(2\beta_{DL}) \\ A_2 &= \sin^4(\beta_{PD}) & B_2 &= \sin^4(\beta_{DL}) \\ A_3 &= \sin^3(\beta_{PD})\cos(\beta_{PD}) & B_3 &= \sin^3(\beta_{DL})\cos(\beta_{DL}) \end{aligned} \tag{4.8}$$

where β_{PD} is the angle between the CH bond and the Z axis of the diffusion frame and β_{DL} is the angle between the Z axis of the diffusion frame and B_0. Using Eqs 4.1,4.2, and 4.7 the rate becomes:

$$\frac{1}{T_2} = \frac{3}{8}\omega_D^2 I(I+1)\,[A_1B_1 + A_2B_2 - 8\,A_3B_3\cos(3\alpha_{DL})]\,\frac{\tau_c}{1+(\omega_1\tau_c)^2}\,. \tag{4.9}$$

Note that again, the essential physics are retained in the dependence on τ_c and ω_1 but that the interference effect is explicitly orientation dependent. For example, one observes that the rate goes to zero if the direction of the Z axis of the diffusion tensor is parallel to the Z axis of the lab frame. Physically this is due to the fact the the interference effect depends on a time modulated dipolar coupling. In this orientation, the effect of the three-site exchange is to rotate the dipolar coupling about B_0. In this case the dipolar coupling is not modulated due to rotational symmetry, the static part of the dipolar coupling is maximized and is may be eliminated by decoupling.

The excellant agreement between the quantum mechanical treatment (see below) and the classical approach is depicted in Figure 4.1b[21]. It should be noted that this result may be extended to free diffusion or wobble within a cone or both using the correlation functions given by Torchia and Szabo[20]. However, in order to extend this approach to CH_2 or CH_3 spin systems the cross-correlation effects between CH and HH dipolar tensors need to be taken into account.

Figure 4.2 Motional model for gramicidin A. A three-site hop (a) approximates the rotation of gramicidin A (a) about the helical long axis (b). P_1-P_3 are the equilibrium occupancy probabilities and k is the exchange rate.

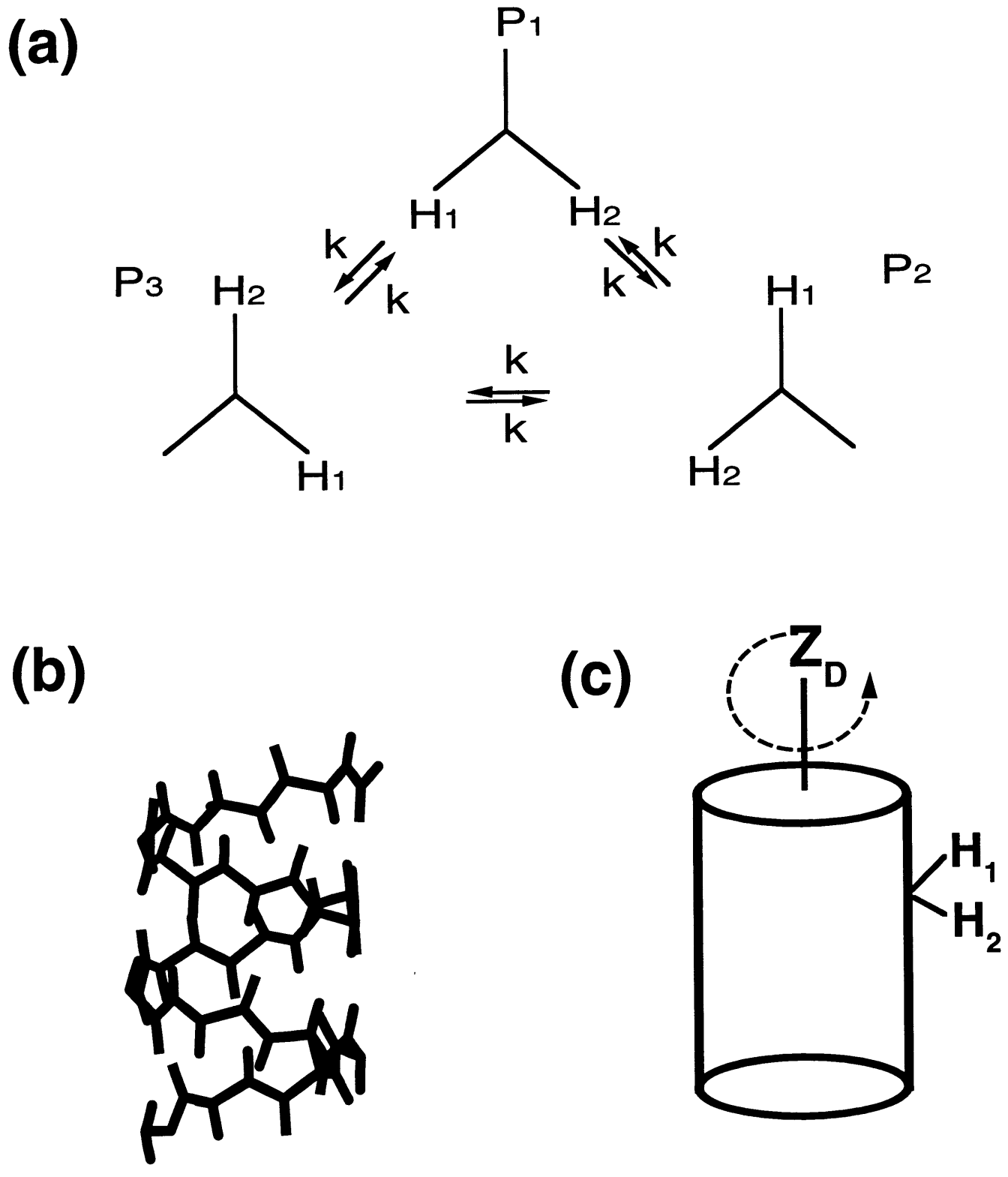

Figure 4.2

4.3 Numerical Lineshape Simulations

As an alternative to the classical approach outlined above, we employ a model that treats the molecular motion as a conformational exchange problem using a full quantum mechanical treatment in Liouville space[22]. It is assumed, to a first approximation, that the motion in gA can be represented as a three-site hop about the peptide long axis (See Figure 4.2). Second, the treatment is confined to an isolated CH_2 group. Finally, the dynamics are calculated in the rotating frame and the MAS is neglected. As in the classical approach, this is equivalent to considering motions which are slow on the timescale of the Larmor frequencies involved but fast relative to the timescale of sample rotation. Under these assumptions, the full Hamiltonian for the nth site is then written:

$$H^n = H_I^n + H_S^n + H_{IS}^n + H_{II}^n + H_{rf} \tag{4.10}$$

with

$$H_I^n = \omega_{I1}^n I_{1Z} + \omega_{I2}^n I_{2Z} \ , \tag{4.11}$$

$$H_S^n = \omega_S^n S_Z \ , \tag{4.12}$$

$$H_{IS}^n = \omega_{I1S}^n 2I_{1Z} S_Z + \omega_{I2S}^n 2I_{2Z} S_Z \ , \tag{4.13}$$

$$H_{II}^n = \omega_{II}^n (3I_{1Z} I_{2Z} - I_1 \cdot I_2) \tag{4.14}$$

and

$$H_{rf} = \omega_{rf}^I (I_{1X} + I_{2X}) \tag{4.15}$$

with

$$\omega_Q^n = \tilde{\rho}_{00}^Q + \sum_{k=-2}^{2} \tilde{\rho}_{2k}^Q D_{k0}^{(2)} (\Omega_{PL}^n) \tag{4.16}$$

where the $\tilde{\rho}_{2k}^Q$ are as defined in Chapter 1 (Eq. 1.31) and

$$D^{(2)} (\Omega_{PL}^n) = D^{(2)} (\Omega_{PC}) D^{(2)} (\Omega_{CM}) D^{(2)} (\Omega_{MD}^n) D^{(2)} (\Omega_{DL}) \tag{4.17}$$

A hierarchy of transformations is employed to rotate from the principle axis system (PAS) of the interaction Q to the lab frame which is indicated in Figure 4.3.

Figure 4.3 Scheme of rotations employed from the respective PAS of the chemical shifts and dipolar couplings to the laboratory frame. The interaction Q is transformed from its PAS to a common frame (C) where the relative orientations of the interactions are established. Then the common frame is transformed to the molecular frame (M) through the Euler angles Ω_{CM} which are given by structure of gA as determined by Ketchem *et al.*[9]. The rotation from molecular frame to the diffusion frame (D) depends on the exchange site occupied (n) generating the Hamiltonian, H^n. Finally, the diffusion frame is located to the lab frame (L)-the Z axis is defined by the direction of the applied field-where the S spin FID is evaluated.

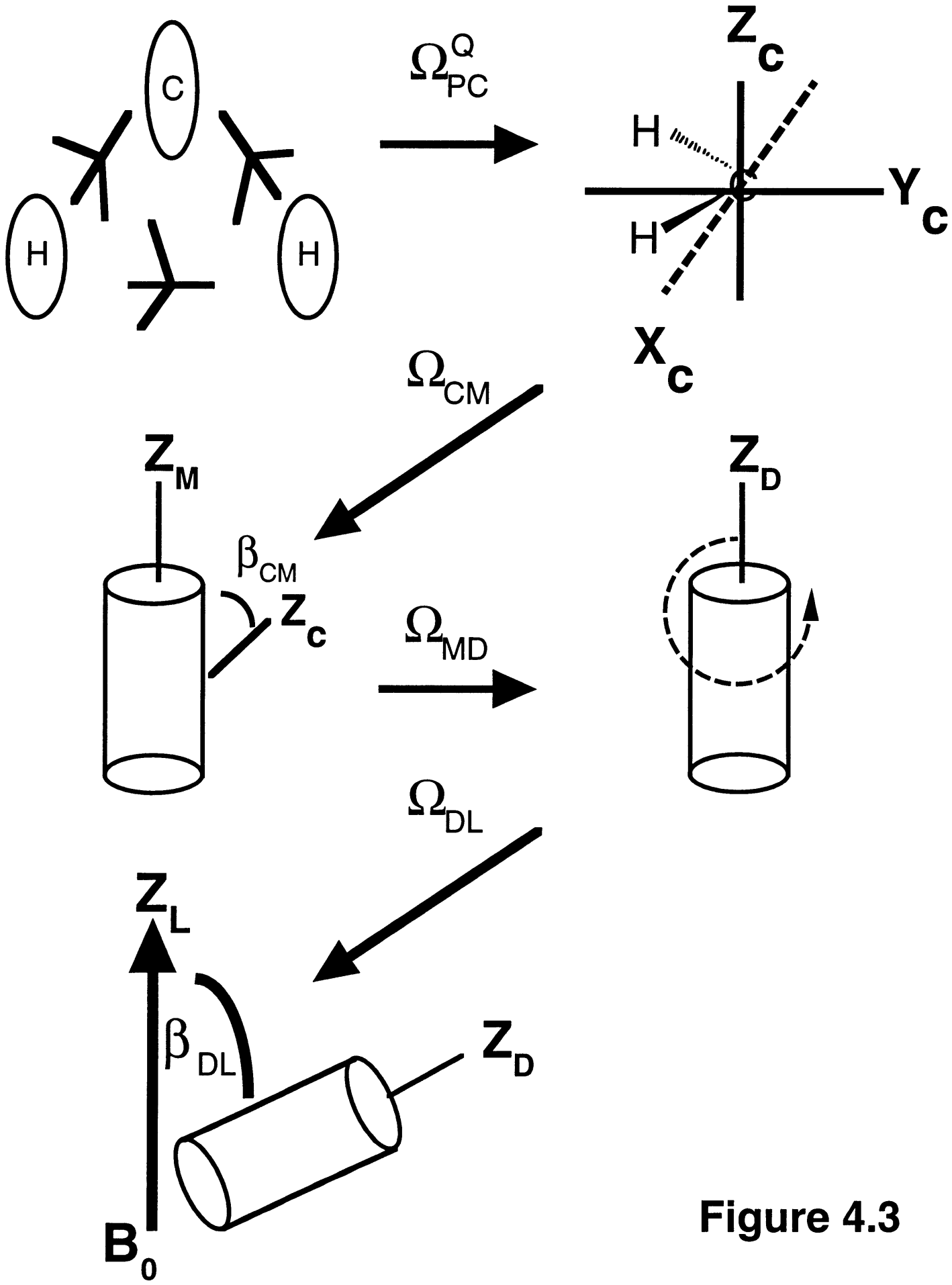
C
H
H
Ω^{Q}_{PC}
Z_c
H
H
Y_c
X_c
Ω_{CM}
Z_M
β_{CM}
Z_c
Ω_{MD}
Z_D
Ω_{DL}
Z_L
β_{DL}
Z_D
B_0

Figure 4.3

First, all interactions are rotated from their respective PAS to the common frame (C). Then the C frame is rotated into the molecular frame (M). The M frame is rotated into the diffusion frame (D) by the angles $\Omega_{MD}^{n} = \{\alpha_{MD}, \beta_{MD}, \gamma_{MD}^{n}\}$. The site index n corresponds to a $\gamma_{MD}^{n} = (2\pi n/3)$, an azimuthal rotation of the molecular frame M about the Z axis of the diffusion frame D. The diffusion frame is then transformed into the lab frame where the signals are evaluated.

The dynamics of the above spin system under three-site exchange are calculated in Liouville space using a formalism presented by Binsch[22]. In this framework, a system, with Hamiltonian H, of N nuclei exchanging between M magnetically inequivalent sites may be represented by a composite state vector in a composite Liouville space (L^c). We have dim (L^c)=dim (L^p)xM or dim $(H)^2$xM which for spin 1/2 is 2^{2NxM}. For the case considered here, N = 3 and M = 3 and the dimension of the problem is 192. Clearly, the dimension grows rapidly as the number of spins or the number of sites is increased. The state vectors in this composite Liouville space are formed from state vectors of the primitive Liouville space,L^p. For example, the operator S_x is written as a vector in the primitive Liouville space for the above SI_2 spin system as:

$$\hat{S}_x^P = \frac{1}{2}(\hat{S}_+^P + \hat{S}_-^P) \quad , \tag{4.18}$$

$$\hat{S}_+^P = |1,2\rangle + |3,4\rangle + |5,6\rangle + |7,8\rangle \tag{4.19}$$

and the superkets[23] defined

$$|i,j\rangle \Leftrightarrow |i\rangle\langle j| \tag{4.20}$$

where the states $|i\rangle$,$|j\rangle$ are defined by the Zeeman eigenbase as:

$$S_z |m_S, m_{I_1}, m_{I_2}\rangle = m_S |m_S, m_{I_1}, m_{I_2}\rangle \tag{4.21}$$

$$|1\rangle = |+\tfrac{1}{2},+\tfrac{1}{2},+\tfrac{1}{2}\rangle,\ |3\rangle = |+\tfrac{1}{2},+\tfrac{1}{2},-\tfrac{1}{2}\rangle,\ |5\rangle = |+\tfrac{1}{2},-\tfrac{1}{2},+\tfrac{1}{2}\rangle,\ |7\rangle = |+\tfrac{1}{2},-\tfrac{1}{2},-\tfrac{1}{2}\rangle$$

$$|2\rangle = |-\tfrac{1}{2},+\tfrac{1}{2},+\tfrac{1}{2}\rangle,\ |4\rangle = |-\tfrac{1}{2},+\tfrac{1}{2},-\tfrac{1}{2}\rangle,\ |6\rangle = |-\tfrac{1}{2},-\tfrac{1}{2},+\tfrac{1}{2}\rangle,\ |8\rangle = |-\tfrac{1}{2},-\tfrac{1}{2},-\tfrac{1}{2}\rangle \quad . \tag{4.22}$$

Figure 4.4 Schematic representation of an operator, A, from Hilbert space as a vector, $\hat{A}^p$, in Liouville space (L^p) where the |i,j> operator basis is defined as in Eq.4.20 and 4.21 (a). Extension of definition $\hat{A}^p$ to L^c (b) where $\hat{A}^{p,n}$ corresponds to the nth site and $\hat{A}^c$ is built up from the $\hat{A}^{p,n}$ corresponding to inequivalent sites (c).

(a)

$$\hat{A}^{p} = \begin{bmatrix} |1,1\rangle \\ |1,2\rangle \\ \vdots \\ |1,8\rangle \\ |2,1\rangle \\ |2,2\rangle \\ \vdots \\ |8,8\rangle \end{bmatrix}$$

(b)

$$\hat{A}^{p,n} = \begin{bmatrix} |1,1,n\rangle \\ |1,2,n\rangle \\ \vdots \\ |1,8,n\rangle \\ |2,1,n\rangle \\ |2,2,n\rangle \\ \vdots \\ |8,8,n\rangle \end{bmatrix}$$

(c)

$$\hat{A}^{c} = \begin{bmatrix} \hat{A}^{p,1} \\ \hat{A}^{p,2} \\ \hat{A}^{p,3} \end{bmatrix}$$

Figure 4.4

In a the composite Liouville space ,L^c, the state vector is written Sx

$$\hat{S}_X^C = \sum_{n=1}^{M} \frac{1}{2}(\hat{S}_+^{P,n} + \hat{S}_-^{P,n}) \tag{4.23}$$

with

$$\hat{S}_+^{P,n} = |1,2,n\rangle + |3,4,n\rangle + |5,6,n\rangle + |7,8,n\rangle \tag{4.24}$$

A schematic representation of how state vectors in the primitive Liouville space are built up from the superkets and how state vectors in composite Liouville space are built up from state vectors from the primitive Liouville space is depicted in Figure 4.4. Similarly, superoperators in L^c are built up from superoperators from L^p. For example, the Hamiltonian superoperator in L^c is written:

$$\hat{\hat{H}}^C = \sum_{1}^{M} \hat{\hat{H}}^{P,n} \tag{4.25}$$

Where the $\hat{\hat{H}}^{P,n}$ correspond to the different internal interactions experienced at sites 1 through M. The matrix representation of $\hat{\hat{H}}^{P,n}$ is written:

$$\langle i,j,q | \hat{\hat{H}}^{P,n} | k,m,r\rangle = \delta_{q,n}\delta_{r,n} \sum_{i,j}\sum_{k,m} (H^n_{i,j}\,\delta_{j,m} - \delta_{i,k}\,H^n_{m,j}) \tag{4.26}$$

and the schematic representation of $\hat{\hat{H}}^C$ is given in Figure 4.5. With this background, the dynamic equations governing the evolution in L^c are written in the familiar form:

$$\frac{\partial \hat{\rho}^c(t)}{\partial t} = \hat{\hat{W}}^c\,\hat{\rho}^c(t) \tag{4.27}$$

$$\hat{\hat{W}}^c = -i\,\hat{\hat{H}}^c + \hat{\hat{K}}^c \tag{4.28}$$

with $\hat{\tilde{H}}^{C}$ as defined above and $\hat{\tilde{K}}^{C}$ as depicted in Figure 4.5

Figure 4.5 Representation of the dynamic matrix, $\hat{\hat{W}}^c$ with $\hat{\hat{H}}^c$ and $\hat{\hat{K}}^c$ as the Hamiltonian and exchange superoperators respectively.

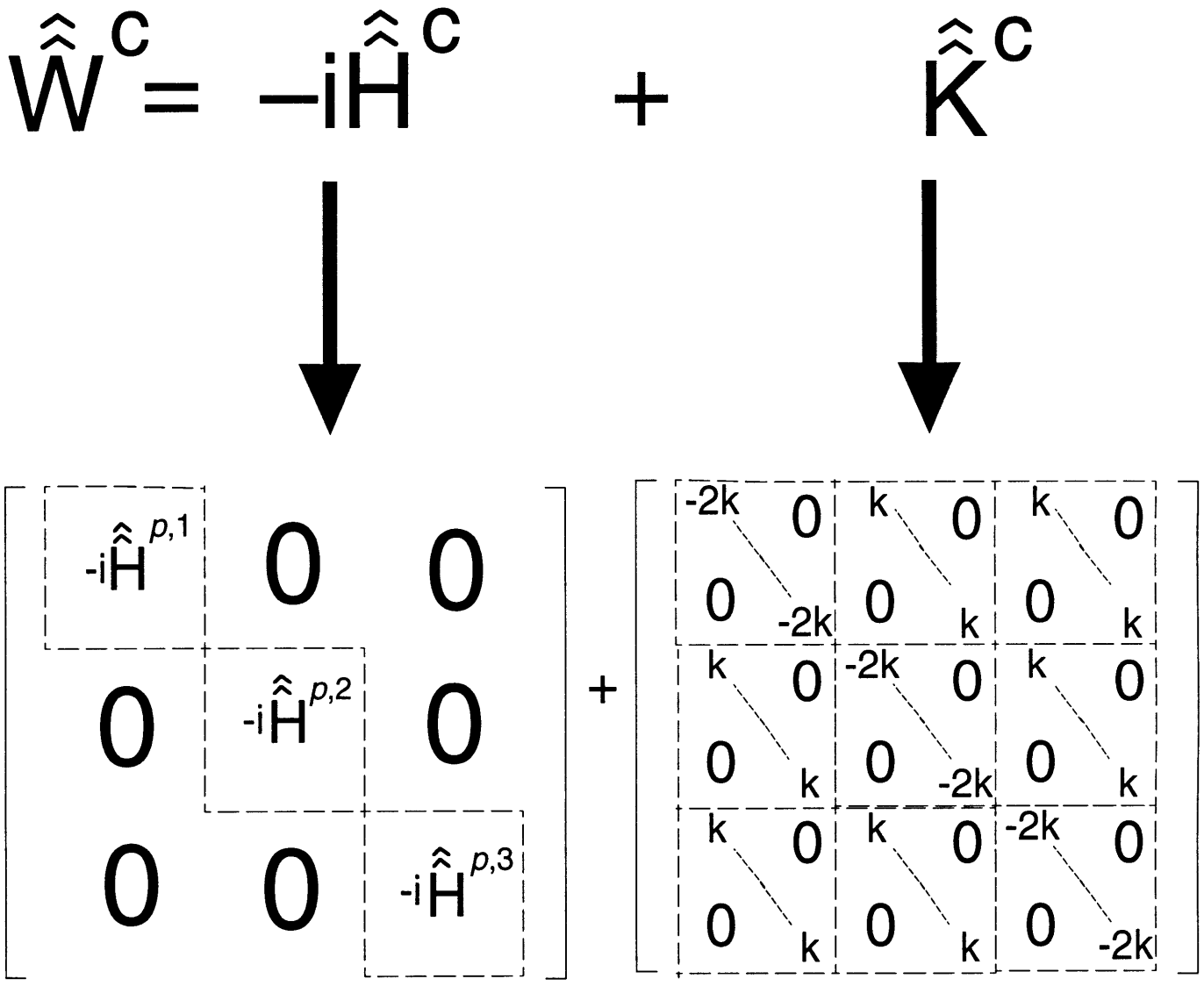
$\hat{\hat{W}}^c = -i\hat{\hat{H}}^c + \hat{\hat{K}}^c$
$-i\hat{\hat{H}}^{p,1}$
$-i\hat{\hat{H}}^{p,2}$
$-i\hat{\hat{H}}^{p,3}$
-2k
k
0

Figure 4.5

$$\hat{\rho}^c(t) = \hat{\hat{L}}^c(t,0)\,\hat{\rho}^c(0) \tag{4.29}$$

$$\hat{\hat{L}}^c(t,0) = \hat{\hat{T}}\exp\{\int_0^t dt'\,\hat{\hat{W}}^c(t')\} = \exp\{\hat{\hat{W}}^c t\} \tag{4.30}$$

The S spin free-induction decay is calculated:

$$\langle \hat{S}_+^c \rangle(t) = \hat{S}_-^c \bullet \hat{\rho}^c(t) \tag{4.31}$$

$$\hat{S}_-^c \bullet X \exp\{\Lambda t\}\, X^{-1}\, \hat{\rho}^c(0) \tag{4.32}$$

where X and Λ are the corresponding matrices of eigenvectors and eigenvalues of $\hat{\hat{W}}^c$ and

$$\rho(0) = \sum_{n=1}^{3} P_n^{eq}\, \hat{S}_X^{P,n} \tag{4.33}$$

with P_n^{eq} the probability of finding the nth conformation at equilibrium where

$$\sum_{n=1}^{3} P_n^{eq} = 1\ . \tag{4.34}$$

4.4 Experimental

(^{15}N,^{13}CO,$^{13}CH_2$-Gly_2; $^{15}N_1$-Trp_9) gA and (^{15}N,^{13}CO,$^{13}CD_2$-Gly_2) gA have been synthesized and purified to over 98% purity following the procedure of Fields *et al.*[24, 25] and will be designated as $NCCH_2$-Gly gA and $NCCD_2$-Gly gA respectively. Glycine was dideuterated at the alpha position following the procedure of Cable *et al* [26]. Each peptide was mixed together with DMPC, in a molar ratio of 10:1 lipid/peptide, in a solution of trifluoroethanol which was then removed by rotoevaporation followed by high-vacuum lyophilization overnight. After adding an equal weight of D_2O, the dispersion was kept frozen for 24 hours, incubated at 70°C for an additional 24 hours and subjected to several freeze-thaw cycles to ensure sample homogeneity.

Thin layer chromatography was performed on the samples before and after the NMR experiments. Only minor traces of lysolipids were found in samples that were heated for extended periods of time. Approximately 150 mg of sample, in a 5 mm high-speed Doty rotor, were run using a custom designed double resonance probe with a Doty spinning assembly. NMR experiments were performed on a custom designed spectrometer where ^{13}C frequency was 79.9 MHz and ^{1}H frequency was 317 MHz. Each experiment consists of a simple ^{13}C Bloch decay and CW decoupling at field strength of 90 kHz.

4.5 Results and Discussion

The ^{1}H-decoupled ^{13}C-MAS NMR spectra of $NCCH_2$-Gly gA/dimyristoyl phosphatidylcholine (DMPC)/D_2O are depicted in Figure 4.6. The resonances at 171 ppm and 45 ppm correspond to the ^{13}CO and the $^{13}CH_2$ of the labeled glycine in the peptide (Fig. 4.6). The temperature dependence of the $^{13}CH_2$-Gly linewidth is evident upon inspection of the figure. As the temperature is increased from -10°C , the lipid resonances narrow while the $^{13}CH_2$-Gly resonance broadens until it almost disappears in the noise at 25°C (Fig. 4.6c). With further increase in temperature to 40°C and 60°C, the $^{13}CH_2$-Gly resonance reappears and narrows again, although not as much as the lipid resonances (Fig. 4.6a-b). A similar effect was also observed for the $^{13}CH_3$-Ala resonances in $^{13}CH_3$-Ala gA (data not shown), but to a lesser extent due to a motionally averaged ^{13}C-^{1}H dipolar coupling generated by the fast three-fold rotation of the methyl group. In addition, we have incorporated dideuterated $NCCH_2$-Gly into gA to produce $NCCD_2$-Gly gA and we show the high-resolution ^{13}C-MAS NMR spectra of this compound at 25°C compared with the lower resolution obtained in the same conditions with $NCCH_2$-Gly gA in Figure 4.7. Clearly, the extent of broadening is reduced significantly upon deuterium substitution for the proton.

Figure 4.6 79.9 MHz ^{13}C-MAS-NMR spectra of $NCCH_2$-Gly gA/DMPC/D_2O with 90 kHz ^1H-decoupling at the indicated temperatures. At each temperature, careful optimization of the relaxation delay has been performed to avoid any loss of magnetization due to incomplete relaxation. a) T = 60°C, ω_r = 6.7 kHz, r. d. = 5 s, 2048 scans; b) T = 40°C, ω_r = 6.2 kHz, r. d. = 5 s, 1024 scans; c) T = 25°C, ω_r = 6.5 kHz, r. d. = 10 s, 2048 scans; d) T = 5°C, ω_r = 5.25 kHz, r. d. = 60 s, 1024 scans; e) T = -10°C, ω_r = 4.1 kHz, r. d. = 120 s, 960 scans.

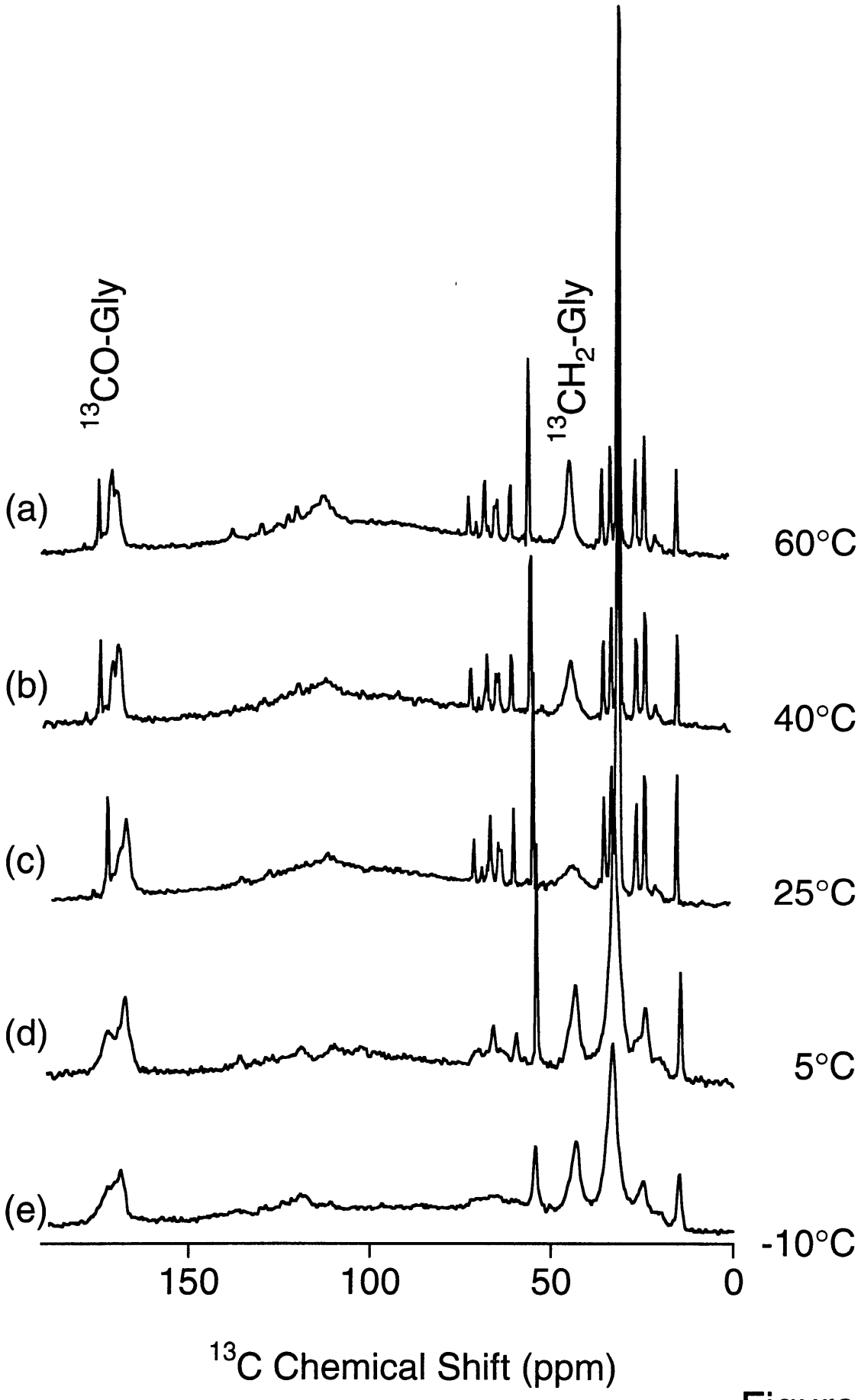
^{13}CO-Gly
^{13}CH$_2$-Gly
(a)
60°C
(b)
40°C
(c)
25°C
(d)
5°C
(e)
-10°C
150
100
50
0
^{13}C Chemical Shift (ppm)

Figure 4.6

Figure 4.7 79.9 MHz ^{13}C-MAS-NMR spectra of: a) $NCCD_2$-Gly gA/DMPC/D_2O with 90 kHz ^1H-decoupling. T = 25°C, ω_r = 4.7 kHz, r. d. = 15 s, 2048 scans; b) $NCCH_2$-Gly gA/DMPC/D_2O with 90 kHz ^1H-decoupling. T = 25°C, ω_r = 6.5 kHz, r. d. = 10 s, 2048 scans.

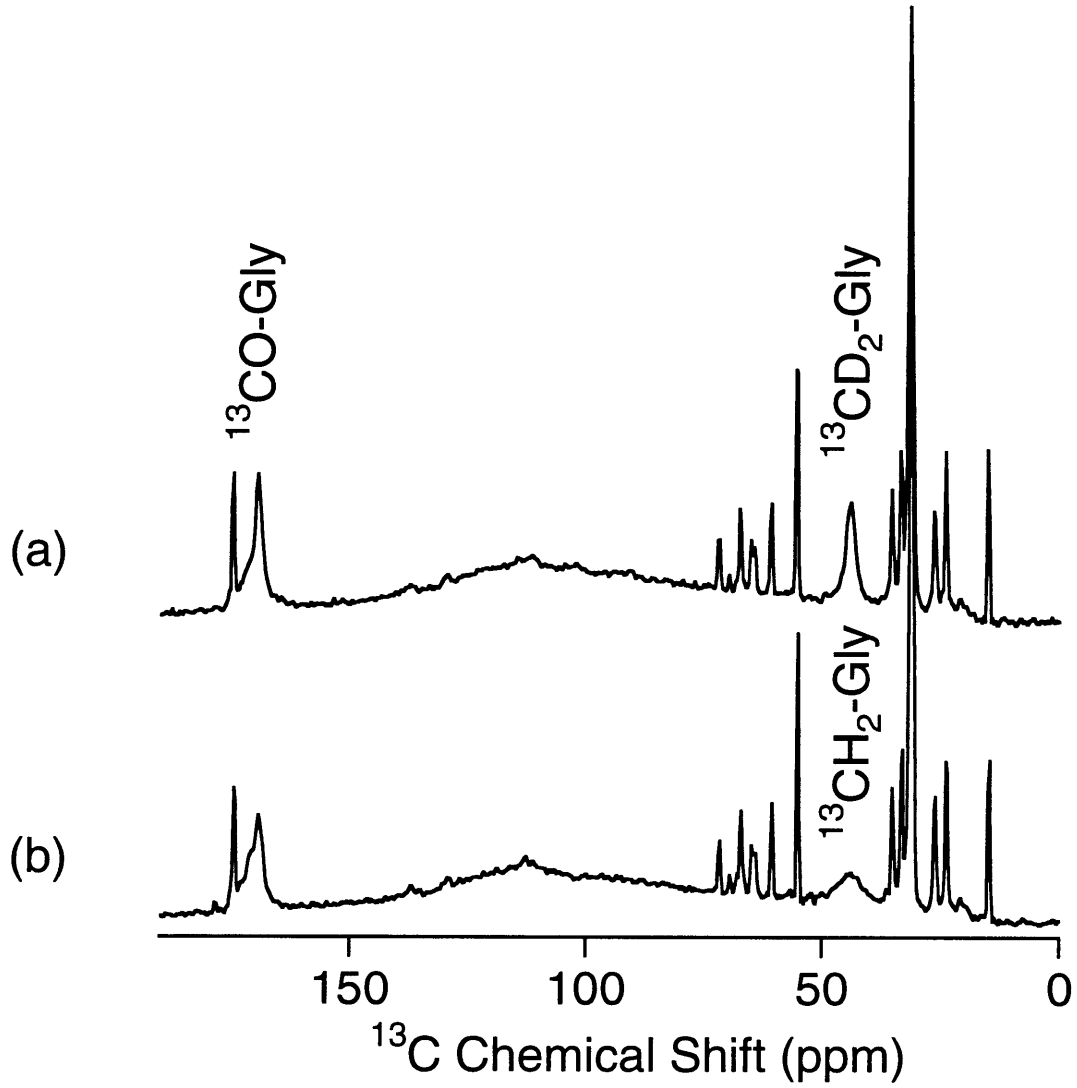
(a)
(b)
^{13}CO-Gly
^{13}CD$_2$-Gly
^{13}CH$_2$-Gly
150
100
50
0
^{13}C Chemical Shift (ppm)

Figure 4.7

Taken together, the spectra of Figure 4.6 and 4.7 suggest the occurrence of an interference between heteronuclear decoupling and incoherent molecular motion of the peptide, activated by a change in temperature. The following observations are crucial. First, the CH dipolar coupling is on the order of 20 kHz for a static CH bond, is generally suppressed by CW ^{1}H-decoupling at an rf field of 90 kHz. The approximately seven -fold reduction in dipolar coupling resulting from ^{2}H substitution and corresponding reduction of linebroadening indicate a dependence on the magnitude of the dipolar interaction. Second, the linebroadening is minimized both *below* and *above* a particular temperature regime. Finally, the variation of the $^{13}CH_2$-Gly resonance linewidth as function of 1/T mimics the inverse quadratic behavior predicted by Rothwell and Waugh[3] centered around the temperature of 25°C, where the broadening is maximal.

Numerical lineshape simulations using the dynamical model described in section 4.3 along with the experimental data over the temperature range from 25°C to 60°C are presented in Figure 4.8. Note that there is excellent agreement between the experimental and simulated lineshapes. Over this temperature range the correlation times vary from 2.5×10^{-7} to 3.3×10^{-6} s. In addition, the notion of interference between molecular motion and proton decoupling is supported by the fact the maximal line broadening occurs when τ_c is on the order of 10^{-6} s which is approximately the inverse of the decoupling field employed throughout the study (2π x 90 kHz). In addition, the effect of interference with the coherent averaging provided by MAS (2π x 5 kHz) can be safely neglected over this temperature range enabling a considerable savings in the CPU time required for the simulations. However, for data at 5 and -10°C, the MAS must be included as the rates approach the spinning speed. In fact, interference of molecular motion with MAS may explain why the linewidth at -10 °C is broader than at 5 °C.

Figure 4.8 Fits of the experimental lineshapes corresponding to the C_α region of glycine in gA at the indicated temperature with numerical lineshape simulations with the corresponding exchange rate k. Simulation parameters are appropriate to CH_2 group except the I and S spin chemical shifts have been neglected. The magnitude of the CH dipolar interactions are taken to be 22.7 kHz while the HH dipolar of 20.69 kHz is employed. The Euler angles employed were $\Omega_{PC}^{CH,a} = \{0,90,324.75\}$ $\Omega_{PC}^{CH,b} = \{0,90,215.25\}$, $\Omega_{PC}^{HH} = \{0,90,0\}$ $\Omega_{CM} = \{50,55,0\}$, and $\Omega_{MD}^{n} = \{0,0,2\pi n/3\}$ while $\omega_1/2\pi =$ 90 kHz.

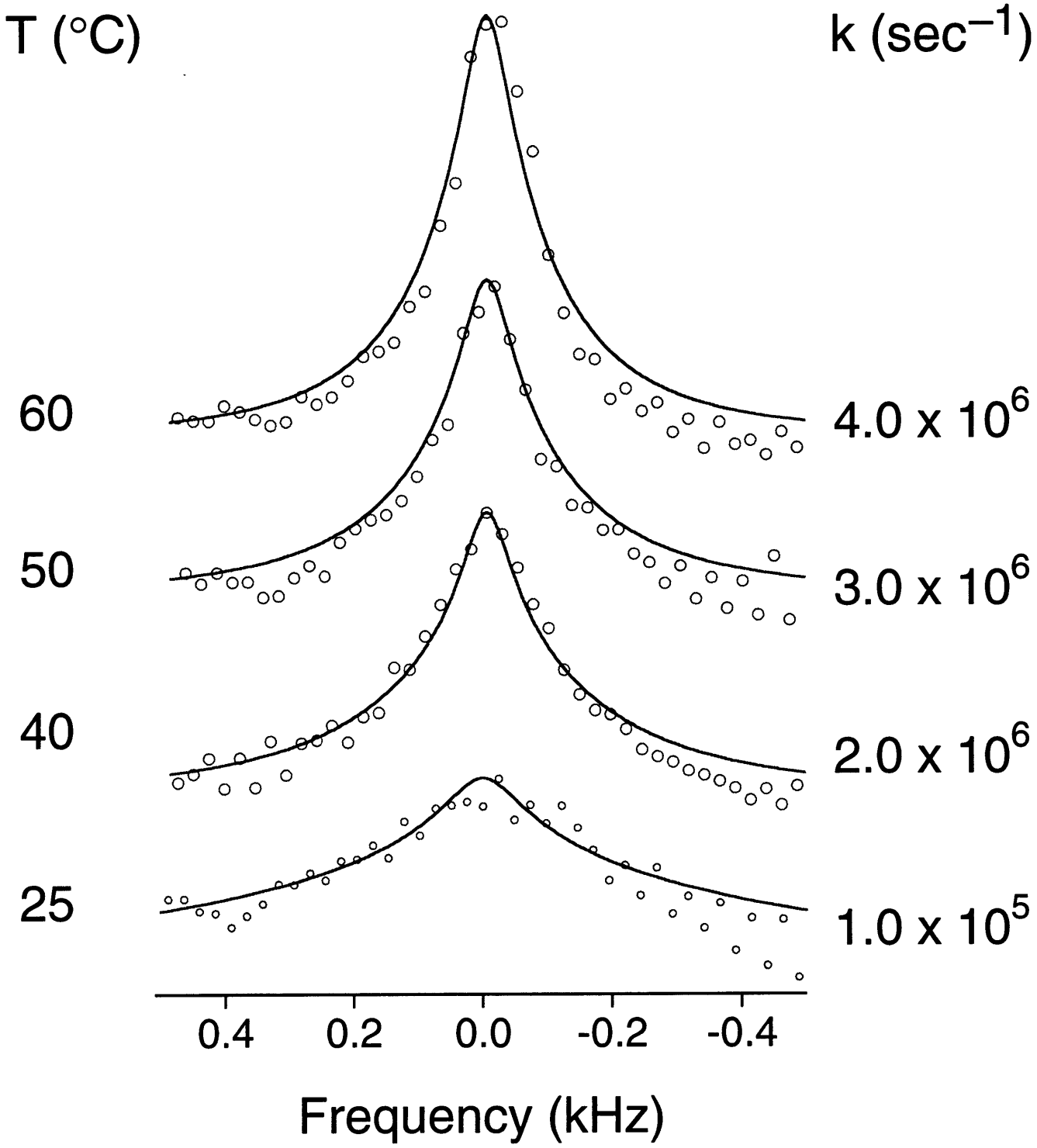
T (°C)
k (sec^{-1})
60
4.0 x 10^6
50
3.0 x 10^6
40
2.0 x 10^6
25
1.0 x 10^5
0.4
0.2
0.0
-0.2
-0.4
Frequency (kHz)

Figure 4.8

It should be noted that the accuracy of the extracted rates depends on the deconvolution of homogeneous contributions from the linewidth. In model compounds, this has been achieved by either going to low temperatures where any motion is quenched or by the same procedure with ^2H substitution. However, the complexity of the hydrated gA/DMPC system makes this difficult as there may be a variable inhomogeneous contribution to the linewidth. For example, in pure lipid bilayers, the ^{13}C linewidths broaden upon reducing the temperature. This is most likely due to a combination of homogeneous and inhomogeneous contributions to the linewidth. First, as has been suggested in the literature, the linebroadening is a result of the correlation time for axial diffusion going from 10^{-8} to 10^{-6}s upon transition from the fluid to gel phase and in this regime decoupling is rendered inefficient[27]. However, by going to temperatures of about -100°C this effect may be partially circumvented. In addition, slowly freezing the samples results in a conformational distributions yielding dispersion of isotropic shifts. This dispersion of shifts manifest as a inhomogenous broadening. In principle, Hahn-Echo experiments may be performed to extract the homogenous linewidth assuming that the homogeneous broadening is the uniform across the different conformers. In addition, the relative amount of inhomogeneous broadening due to conformational dispersion may vary as the temperature is decreased below the freezing point. Therefore, for the present study, it is assumed that the homogeneous linewidth is completely determined by the three-site hope. In the temperature range of 25°C to 60°C the inhomogeneous contribution is expected to be small and estimated to be 50 Hz.

At first glance, one might attempt to circumvent the interference between molecular motion and proton decoupling by changing the decoupling field. Depicted in Figure 4.9 is a plot of the linewidth as a function of the correlation time, τ_c, at decoupling field strengths of 45, 90, and 180 kHz. Assuming $\log(\tau_c) = -5.75$, decreasing the decoupling field from 90 to 45 kHz significantly increases the linewidth from roughly 300 to 600 Hz. This is due to the fact that a 45 kHz field is not significantly far enough from the maximal interference regime and that the static part of the dipolar coupling (unmodulated by motion) is inadequately decoupled. In contrast, an increase in the decoupling field from 90 to 180 kHz reduces the line broadening by approximately 300 to 150

Hz. Unfortunately, increasing the decoupling field by yet another factor of two is currently limited by technology. However, for a CH group, the broadening is less severe. Here a reduction in linewidth from 120,90, and 60 Hz is observed corresponding to decoupling field strengths of 45,90, and 180 kHz respectively. An alternative to to employing higher decoupling fields is to attempt to adjust the T_2 minimum by varying the nature of the lipid bilayer (shorter chain or unsaturated lipids have a lower transition temperature) or by adding cholesterol to the membrane. However, a more obvious solution is to perform deuterium substitution as in Figure 4.7 in conjunction with ^2H decoupling to remove the scalar interactions. Yet another way to circumvent the effect is to orient the sample so that the motional axis is parallel to the static field. In this case the dipolar coupling is not modulated by motion and complete decoupling may be achieved. Depicted in Figure 4.10 is the orientation dependence of the interference effect where the linewidth is plotted against the angle that the Z axis of diffusion frame makes with the Z axis of the lab frame. In Figure 4.10a, the orientation dependence of the interference of CH group undergoing a three-site hop with proton decoupling is plotted for the classical theory using Eq. 4.9 and for the numerical simulations. The curves are in excellent agreement consistent with the results depicted in Figure 4.1b. Figures 4.10c and d illustrate the effect for CH_2 groups with and without the homonuclear coupling between protons. Clearly the the broadening is a function of multiplicity in addition to the relative angles that the dipolar tensors make with respect to the diffusion frame. In all cases, the broadening goes to zero for $\beta_{DL}=0$ explaining the success of NMR investigations of samples aligned in this orientation[9].

Figure 4.9 Linewidth ($1/\pi T_2$) vs $\log(\tau_c)$ for CH_2 (a) and CH group (b) undergoing three-site hop with at 45, 90, and 180 kHz CW decoupling indicated with the solid, short dash, and long dash respectively. Note the different scales.

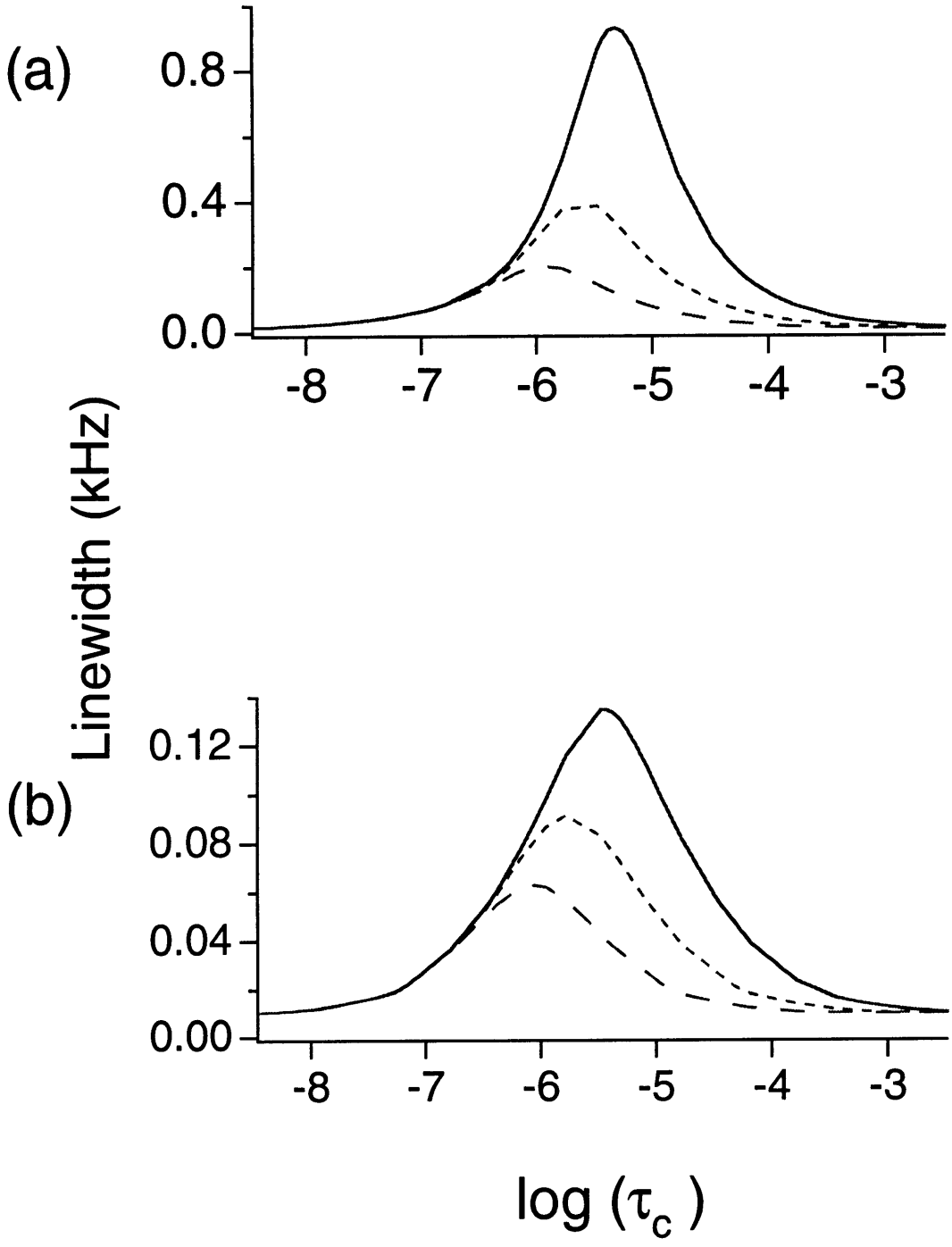

Figure 4.9

Figure 4.10 Linewidth ($1/\pi T_2$) vs β_{DL}, the angle between the Z axis of the diffusion frame and lab frame. CH group undergoing three-site hop: classical (dashed line) vs. quantum mechanical (solid line) treatment (a) and for 45 (solid line),90(short dash), and 180 (long dash) kHz decoupling fields (b). Anguler parameters: $\Omega_{PC}^{CH_1} = \{0,54.74,0\}$, $\Omega_{CM} = \{0,0,0\}$, and $\Omega_{MD}^{n} = \{0,0,2\pi n/3\}$. CH_2 group undergoing three-site hop with (c) and without (d) HH dipolar coupling for 45 (solid line),90(short dash), and 180 (long dash) kHz decoupling fields (b). Euler angles same are identical to those used in figure 4.8. All simulations perfromed with $\omega_1/2\pi = 90$ kHz and $\omega_1\tau_C = 1$.

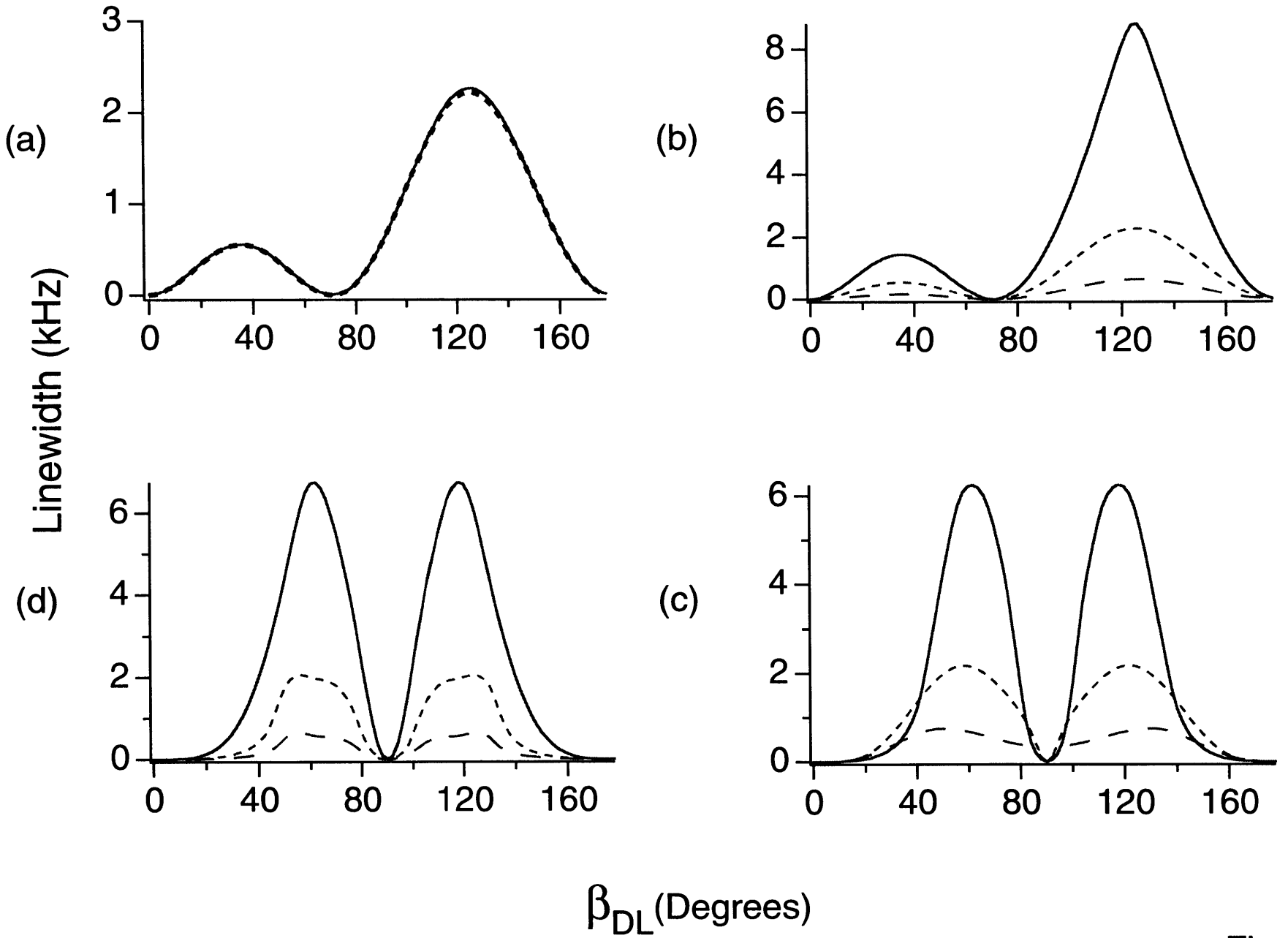
(a)
(b)
(c)
(d)
Linewidth (kHz)
β_{DL}(Degrees)
0
40
80
120
160
0
1
2
3
0
2
4
6
8
0
2
4
6

Figure 4.10

The fact that the interference effect is maximized around 25°C is not surprising since the temperature at which the sample changes phase from gel to liquid-crystalline L_α phase is around 20°C[28], modifying the bilayer viscosity, the peptide environment and degrees of motional freedom. Motional models that could account for such an effect have been discussed in previous studies of gA performed at temperatures exceeding 30°C: (1) fast axial diffusion ($7x10^{-9}$s) and intermediate rate wobbling ($6x10^{-6}$s), a model proposed by Prosser and Davis for gA in dilauroyl phosphatidylcholine at 65°C[29] or (2) intermediate rate axial diffusion (10^{-5}s - 10^{-7}s), the most common hypothesis found in the literature[16, 30-40]. The use of ^2H relaxation measurements on specifically labeled samples could confirm or reject certain models. Alternatively, experiments including selective ^{13}C labeling at addition sites on the helix would allow the application of classical relaxation theory in conjunction with various motional models to further delineate the details of the motion in gA through the decoupling interference effect.

4.6 Conclusion

We have demonstrated that there is an interference between axial motion of gramacidin A in hydrated lipid bilayers and proton decoupling that leads to a temperature dependent linebroadening in the ^{13}C spectra. Simulation of this effect confirms that the time scale (defined by τ_c) of the motion is on the order of 10^{-6} s at 25 °C, in agreement with previously reported values for axial diffusion. We have demonstrated that the broadening is orientation dependent and is particulary severe for CH_2 groups. Knowledge of the broadening effect in MAS NMR at room temperature, and of ways to circumvent it, will allow sensitivity optimized ^{13}C-MAS NMR spectra of peptides in hydrated lipid bilayers to be obtained at any temperature. Similar results are expected in ^{15}N-NMR spectra but to an even lesser degree due to the reduced value of the NH dipolar coupling constant. In the future we plan to refine the analytic theory to handle CH_2 groups and to include the effects of MAS so that more accurate rates may be extracted in a time efficient fashion. In addition, attempts to further optimize the ^{13}C linewidths with ^2H substitution and the effect of ^2H decoupling should be further explored.

Acknowledgments for Chapter 4

This work was done in collaboration with D. E. Warschawski.

References for Chapter 4

[1] D. Suwelack, W. P. Rothwell and J. S. Waugh, J. Chem. Phys. 73 (1980) 2559.

[2] D. L. VanderHart, W. L. Earl and A. N. Garroway, J. Magn. Reson. 44 (1981) 361.

[3] W. P. Rothwell and J. S. Waugh, J. Chem. Phys. 74 (1981) 2721.

[4] A. Schmidt, S. O. Smith, D. P. Raleigh, J. E. Roberts, R. G. Griffin and S. Vega, J. Chem. Phys. 85 (1986) 4248.

[5] L. Frydman and B. Frydman, J. Chem. Phys. 92 (1990) 1620.

[6] J. R. Long, B.-Q. Sun, A. Bowen and R. G. Griffin, J. Am. Chem. Soc. 116 (1994) 11950.

[7] D. C. Maus, V. Copié, B.-Q. Sun, J. M. Griffiths, R. G. Griffin, S. Luo, R. R. Schrock, A. H. Liu, S. W. Seidel, W. M. Davis and A. Grohmann, J. Am. Chem. Soc. 118 (1996) 5665.

[8] W. Hu, K.-C. Lee and T. A. Cross, Biochemistry 32 (1993) 7035.

[9] R. R. Ketchem, W. Hu and T. A. Cross, Science 261 (1993) 1457.

[10] J. M. Griffiths and R. G. Griffin, Anal. Chim. Acta 283 (1993) 1081.

[11] A. E. Bennett, R. G. Griffin and S. Vega, NMR Basic Principles and Progress 33 (1994) 1.

[12] M. D. Sefcik, J. Schaefer, E. O. Stejskal, J. F. Ellena, S. W. Dodd and M. F. Brown, Biochem. Biophy. Res. Commun. 114 (1983) 1048.

[13] B. A. Lewis, G. S. Harbison, J. Herzfeld and R. G. Griffin, Biochemistry 24 (1985) 4671.

[14] S. O. Smith, I. Palings, V. Copié, D. P. Raleigh, J. Courtin, J. A. Pardoen, J. Lugtenburg, R. A. Mathies and R. G. Griffin, Biochemistry 26 (1987) 1606.

[15] C. W. B. Lee, Characterization of New Lipid Phases by Solid State NMR, Ph. D., Massachusetts Institute of Technology (1990).

[16] R. Smith and B. A. Cornell, Biophys. J. 49 (1986) 117.

[17] C. Wang, Q. Teng and T. A. Cross, Biophys. J. 61 (1992) 1550.

[18] A. W. Hing and J. Schaefer, Biochemistry 32 (1993) 7593.

[19] A. Abragam, The Principles of Nuclear Magnetism, (Oxford University Press, London, 1961).

[20] D. A. Torchia and A. Szabo, J. Magn. Reson. 49 (1982) 107.

[21] Inspection of Figure 4.10a indicates that the powder averaged result should be identical. The discrepancy between the two treatments is due to the different number of crystallites employed in the powder average.

[22] G. Binsch, J. Am. Chem. Soc. 96 (1969) 1304.

[23] J. Jeener, Adv. Mag. Reson. 10 (1982) 1.

[24] G. B. Fields, C. G. Fields, J. Petefish, H. E. Van Wart and T. A. Cross, Proc. Natl. Acad. Sci., USA 85 (1988) 1384.

[25] C. G. Fields, G. B. Fields, R. L. Noble and T. A. Cross, Int. J. Peptide Protein Res. 33 (1989) 298.

[26] K. M. Cable, R. B. Herbert and J. Mann, J. Chem. Soc. Perkin Trans. I 1987 (1987) 1593.

[27] F. Adebodun, J. Chung, B. Montez, E. Oldfield and X. Shan, Biochemistry 31 (1992) 4502.

[28] L. K. Nicholson, F. Moll, T. E. Mixon, P. V. LoGrasso, J. C. Lay and T. A. Cross, Biochemistry 26 (1987) 6621.

[29] R. S. Prosser and J. H. Davis, Biophys. J. 66 (1994) 1429.

[30] R. J. Cherry, Biochim. Biophys. Acta 559 (1979) 289.

[31] K. P. Datema, K. P. Pauls and M. Bloom, Biochemistry 25 (1986) 3796.

[32] B. A. Cornell, F. Separovic, A. J. Baldassi and R. Smith, Biophys. J. 53 (1988) 67.

[33] J. H. Davis, Biochemistry 27 (1988) 428.

[34] A. W. Hing, S. P. Adams, D. F. Silbert and R. E. Norberg, Biochemistry 29 (1990) 4156.

[35] A. W. Hing, S. P. Adams, D. F. Silbert and R. E. Norberg, Biochemistry 29 (1990) 4144.

[36] R. S. Prosser, J. H. Davis, F. W. Dahlquist and M. A. Lindorfer, Biochemistry 30 (1991) 4687.

[37] Q. Teng, R. E. Koeppe II and S. F. Scarlata, Biochemistry 30 (1991) 7984.

[38] J. A. Killian, M. J. Taylor and R. E. Koeppe II, Biochemistry 31 (1992) 11283.

[39] K.-C. Lee, W. Hu and T. A. Cross, Biophys. J. 65 (1993) 1162.

[40] W. Hu, N. D. Lazo and T. A. Cross, Biochemistry 34 (1995) 14138.

5. Site-Resolved Determination of Peptide Torsion Angle ϕ from the Relative Orientations of Backbone N-H and C-H Bonds by Solid-State NMR

5.1 Introduction

The study of the three-dimensional structures of biomolecules in the solid state by nuclear magnetic resonance (NMR) spectroscopy has primarily relied on the measurement of internuclear distances through dipolar couplings. In order to resolve different chemical moieties in the NMR spectra, these distance measurements generally require magic-angle spinning (MAS) or macroscopically oriented samples. In the limit $\omega_r >> |H_D|$, where ω_r is the spinning speed and $|H_D|$ is the size of the dipolar Hamiltonian, the anisotropic dipolar interactions are efficiently attenuated unless specific radiofrequency (rf) pulses or spinning speeds are used to interfere with rotational averaging and thus "recouple" the spins of interest. Accordingly, a number of homonuclear[1-5] and heteronuclear[6-8] dipolar recoupling techniques have been proposed to selectively recouple the dipolar interaction of an isolated spin pair. However, efforts in achieving such broadband dipolar recoupling, which is crucial for obtaining multiple distances simultaneously, have met significant challenges because weak, long-range dipolar interactions containing the distance parameters of interest are masked by strong, short-range couplings[5,9].

Alternatively, biomolecular structures may be studied through the measurement of torsion angles, which constrain molecular conformations via the relative orientations of adjacent segments. For example, the secondary structures of proteins are characterized by backbone torsion angles ϕ and ψ, which are mapped in a Ramachandran plot[10]. For molecules undergoing fast isotropic motions in solutions, torsion angles can be determined from three-bond scalar couplings using the empirical Karplus equations[11,12]. For rigid and semi-rigid solids, in which anisotropic spin interactions are not averaged by motions, torsion angles can be extracted by correlating the orientations of two segment-fixed NMR interaction tensors, such as the chemical shift and the dipolar coupling, across the torsional axis.

This approach to determining molecular structures in the solid state has recently been pursued in several laboratories[13-17]. For example, by correlating two C-H dipolar couplings across a C-C bond, the cis and trans conformations of a H-C=C-H moiety in two aliphatic dicarboxylates were distinguished[13]. Also, by correlating the chemical shift anisotropy of the

carbonyl carbon with the C-H coupling of the neighboring α carbon in an amino acid, the angle ψ was determined[14]. These experiments have been carried out under either static or MAS conditions. However, to obtain torsion angles in large biomolecules, the required spectral sensitivity and the ability to achieve site resolution, which is prerequisite for extracting multiple torsion angles at once, make MAS the method of choice. A relatively common feature in the torsion angle techniques developed so far is the incorporation of two ^{13}C labels to enhance the spectral sensitivity and to create ^{13}C double-quantum coherence. Double-quantum coherence not only allows the two NMR interaction frequencies to be measured concurrently, but also suppresses signals of isolated spins, thus simplifying the spectra. However, it is worth mentioning that without double-quantum coherence the torsion angle ψ in an amino acid has also been determined successfully[18].

To determine a torsion angle from the relative orientations of two NMR tensors, the orientation of each tensor in a common reference frame must be known. While the dipolar interaction tensor has a well defined cylindrical symmetry (i.e. asymmetry parameter η=0) with its unique axis along the internuclear vector, the orientation of the chemical shift tensor with respect to the molecular segment is usually not known *a priori* and needs to be measured separately. Therefore, it is simpler to measure the torsion angle from the orientations of two dipolar coupling tensors across the intervening bond. For example, the peptide torsion ϕ=C(O)-N-C^{α}-C(O) can be obtained from the relative orientations of the N-H^N and C^{α}-H^{α} dipolar tensors, whose unique axes are along the respective bonds. The corresponding torsion angle H^N-N-C^{α}-H^{α}, termed ϕ_H in the following, is directly related to the conventional ϕ according to $\phi_H=\phi-60^{\circ}$ for the commonly occurring L-amino acids, and $\phi_H=\phi+60^{\circ}$ for D-amino acids. The relation between ϕ and ϕ_H is illustrated in a Newman projection in Fig. 5.1.

Figure 5.1 Newman projection of a L-amino acid, viewed from the N-C^{α} vector into the plane of the paper. The backbone torsion angle ϕ is defined as $C(O)_{i-1}$-N-C^{α}-$C(O)_i$ where i is the residue (R) number, and is negative as drawn here. The corresponding NMR-measurable ϕ_H (H^N-N-C^{α}-H^{α}) is related to ϕ as $\phi_H=\phi-60^{\circ}$. For the mirror image of this molecule, a D-amino acid, the relation $\phi_H=\phi+60^{\circ}$ holds true. The trans conformation of the angle ϕ_H corresponds to 180°, while the cis conformation corresponds to 0°.

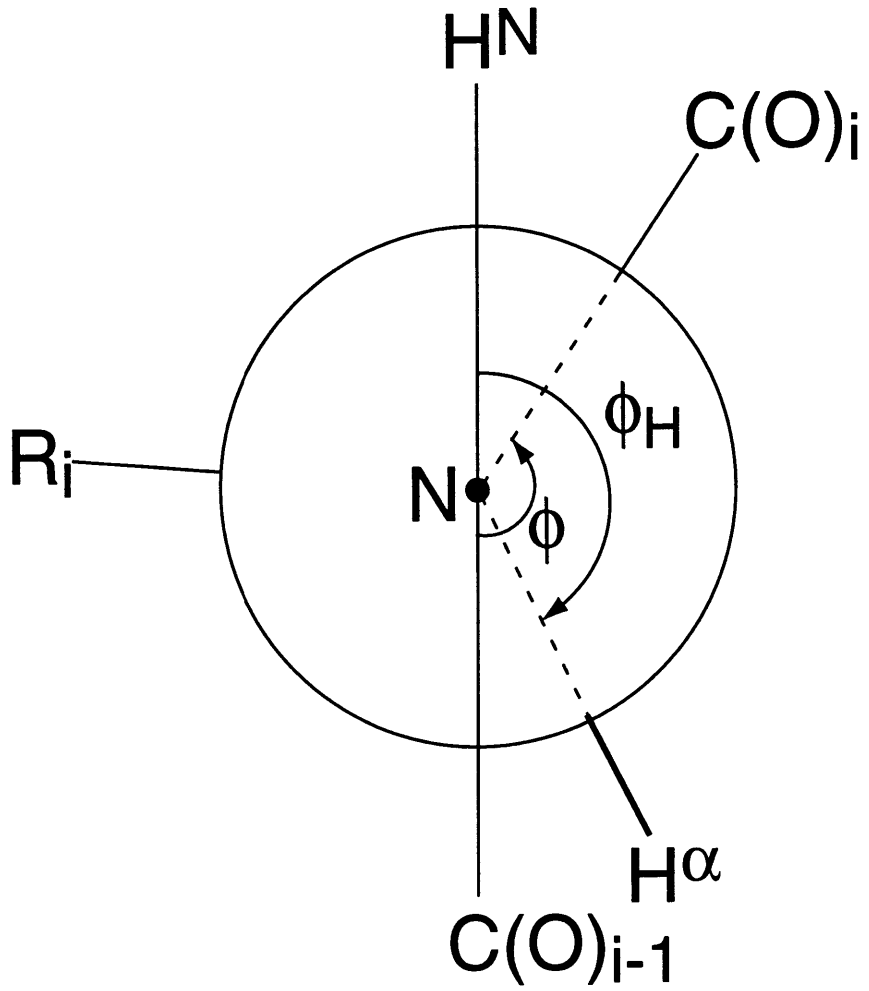

Figure 5.1

Here, we demonstrate the measurement of ϕ in ^{15}N-labeled *N*-acetyl-*D,L*-valine (NAV) by a two-dimensional (2D) MAS technique that correlates the C^{α}-H^{α} and N-H^{N} bond orientations. The technique is a variation of the H-C=C-H experiment mentioned above[13], but involves the evolution of heteronuclear (^{15}N-^{13}C) double and zero-quantum coherences instead of the homonuclear (^{13}C-^{13}C) double-quantum coherence. In accordance with the convention in solution-state NMR spectroscopy, we refer to this combination of ^{15}N-^{13}C double and zero-quantum coherences as heteronuclear multiple-quantum coherences[19-21]. We show that the N-C dipolar interaction can be recoupled under MAS with high efficiency, so that sensitive NMR spectra can be obtained even for this ^{13}C natural abundance sample. The one-bond C-H and N-H couplings, which are input parameters for the simulations of the ϕ-dependent heteronuclear multiple-quantum (HMQ) spectra, can be directly determined by single-quantum ^{13}C and ^{15}N dipolar-shift correlation experiments. Most importantly, the technique yields ϕ angles in a site-resolved fashion, thus making it possible to determine multiple ϕ angles at once in conveniently labeled peptides and proteins.

5.2 Experimental

All experiments were performed on a custom-designed spectrometer operating at 397.8 MHz for ^{1}H, 100.0 MHz for ^{13}C, and 40.3 MHz for ^{15}N nuclei. A custom-designed triple-resonance transmission-line probe with a 4 mm Chemagnetics (Fort Collins, CO) MAS spinning module was used. The transmission-line design enables high rf powers to be attained on all three channels without arcing. Proton rf fields of about 100 kHz were used for excitation and CW decoupling. The ^{1}H 90° pulse length for MREV-8 multiple-pulse decoupling was 3 μs. During the evolution period, the semi-windowless version of MREV-8 was employed and incremented in half cycles, typically 18 μs, in order to increase the spectral width of the indirect dimension. ^{13}C and ^{15}N 90° pulse lengths were 4 μs and 6.2 μs, respectively. The spinning speeds were controlled to ±2 Hz by a Doty (Columbia, SC) spinning speed controller. For the torsion angle and the ^{13}C DIPSHIFT experiments, $\omega_r/2\pi$=2525 Hz, while for the ^{15}N DIPSHIFT measurement,

$\omega_r/2\pi$=2137 Hz. For directly bonded N-C spin pairs, the HMQ excitation and reconversion times corresponded to two rotor periods, and were not further optimized by varying the spinning speed. The recycle delay was 2.5 s for all experiments. The cross polarization contact time was 2 ms.

Uniformly ^{15}N-labeled *N*-acetyl-*D,L*-valine in powder form was purchased from the Cambridge Isotope Laboratories, Inc. (Andover, MA), and was recrystallized in aqueous solution to reduce chemical shift dispersions due to conformational heterogeneity. The resulting C^{α} linewidth in the MAS spectra was about 0.6 ppm.

5.3 Theory N-H^N and C^{α}-H^{α} Tensor Correlation

The pulse sequence for determining the H^N-N-C^{α}-H^{α} torsion angle under MAS is shown in Fig. 5.2a. First, transverse ^{13}C magnetization is created by cross polarization from ^{1}H and evolves under the influence of the recoupled ^{15}N-^{13}C dipolar interaction for a period of τ. The N-C dipolar recoupling is achieved by rotor-synchronized ^{15}N and ^{13}C 180° pulses, with the ^{15}N pulses at the center and the ^{13}C pulses at the end of each rotor cycle[6,22,23]. These 180° pulses perturb rotational averaging of the anisotropic dipolar interaction so that antiphase magnetization C_yN_z, where C and N refer to ^{13}C and ^{15}N spins, respectively, is created. A ^{15}N 90° pulse converts C_yN_z into a combination of double and zero-quantum coherences, C_yN_x. Next, a semi-windowless MREV-8 pulse train is applied on the ^{1}H channel to attenuate the homonuclear ^{1}H interactions. The MREV-8 sequence is incremented and defines the evolution period t_1, which has a maximum length of one rotor period. At the end of this rotor period, a pair of 180° pulses are applied on the ^{15}N and ^{13}C channels, followed by an additional rotor cycle with continuous proton decoupling. Since the 180° pulses are situated at the center of this constant time period (τ_{const}), ^{15}N and ^{13}C isotropic chemical shifts are refocused. In addition, the N-C dipolar coupling and the ^{15}N and ^{13}C anisotropic chemical shift interactions are completely averaged after whole rotor periods by MAS. Thus, the effective Hamiltonians governing the evolution of the N-C multiple-quantum coherences during τ_{const} are the C-H and N-H dipolar couplings. Neglecting the long-range couplings, they can be written as

$$\overline{H}(t) = \kappa\left[\omega_{CH}(t)2C_z^{\alpha}H_z^{\alpha} + \omega_{NH}(t)2N_zH_z^{N}\right], \tag{5.1}$$

where the coefficient κ is the dipolar coupling scaling factor due to the homonuclear decoupling sequence.

After τ_{const}, a second ^{15}N 90° pulse and N-C recoupling period reconvert the N-C multiple-quantum coherences into observable ^{13}C magnetization, which is then detected during t_2 under continuous proton decoupling. Double Fourier transformation of the resulting 2D time signal yields N-C multiple-quantum dipolar sideband patterns in the ω_1 dimension, separated according to the ^{13}C isotropic chemical shifts in the ω_2 dimension.

The transformations of the spin density operators under the pulse sequence of Fig. 5.2a are outlined as

$$\begin{aligned}
&C_x \xrightarrow{\tau} C_yN_zf(\tau) \xrightarrow{90°_y\ ^{15}N} C_yN_xf(\tau)\\
&\xrightarrow{t_1} C_yN_xf(\tau)\cos\left(\Psi_{CH}(t_1)\right)\cos\left(\Psi_{NH}(t_1)\right)\\
&\xrightarrow{90°_{-y}\ ^{15}N} C_yN_zf(\tau)\cos\left(\Psi_{CH}(t_1)\right)\cos\left(\Psi_{NH}(t_1)\right)\\
&\xrightarrow{\tau} -C_xf^2(\tau)\cos\left(\Psi_{CH}(t_1)\right)\cos\left(\Psi_{NH}(t_1)\right),
\end{aligned} \tag{5.2}$$

where only observable magnetization derived from the HMQ coherences is considered. Here, $\Psi_Q(t_1)$ (Q=CH, NH) are the MAS phase angle accumulated during t_1 due to the C-H and N-H dipolar interactions,

$$\psi_Q(t_1) = \int_0^{t_1} dt\ \omega_Q(t)\ . \tag{5.3}$$

The function $f(\tau)$ describes the excitation of the HMQ coherences and equals $\sin\left(\overline{\omega}_D\tau\right)$, where $\overline{\omega}_D$ is the average N-C coupling under the pulse sequence used here[24m25]. The amplitude

modulation $\cos(\Psi_{CH}(t_1))\cos(\Psi_{NH}(t_1))$ of the observed ^{13}C magnetization in Eq. (5.2) can be rewritten as

$$\cos\left[\frac{\Psi_{CH}(t_1)+\Psi_{NH}(t_1)}{2}\right]+\cos\left[\frac{\Psi_{CH}(t_1)-\Psi_{NH}(t_1)}{2}\right]. \qquad (5.4)$$

We now show that these sum and difference dipolar phases depend on the relative orientations of the two dipolar coupling tensors, whose unique axes are along the C^{α}-H^{α} and N-H^N bonds, and therefore reflect the torsion angle ϕ_H=H^N-N-C^{α}-H^{α}. The time-dependent dipolar coupling $\omega_{\lambda}(t)$ that determines the dynamic phase $\Psi_{\lambda}(t_1)$ can be expressed as a Fourier series (as in Chapter 1):

$$\omega_Q(t) = \sum_{m=-2}^{2} \omega_Q^m \exp\{im\omega_r t\} , \qquad (5.5)$$

where $\omega_Q^m(\Omega_{PR})$ are time-independent frequencies calculated from the following coordinate transformations,

$$\omega_Q^m(\Omega_{PR}) = C^Q \{\sum_{m'=-2}^{2} D^{(2)}_{0,m'}(\Omega^Q_{PM})\, D^{(2)}_{m',-m}(\Omega_{MR})\}\, d^{(2)}_{-m,0}(\beta_{RL}) \quad . \qquad (5.6)$$

Here C^Q represents the rigid-limit anisotropy of the dipolar interaction Q. The Wigner rotation matrices $D^{(2)}(\Omega_{PR})$=$D^{(2)}(\Omega_{PM})\cdot D^{(2)}(\Omega_{MR})$ effect coordinate transformations from the principal axis systems of the dipolar coupling tensors to the rotor frame with Euler angles Ω_{PR} = (α_{PR}, β_{PR}, γ_{PR})[27.28]. The reduced rotation matrix $d^{(2)}_{-m,0}(\beta_{RL})$ dictates the transformation from the rotor frame to the laboratory frame with $\beta_{RL}=\tan^{-1}\sqrt{2}$. The orientations of the C^{α}-H^{α} and N-H^N dipolar tensors are expressed in a common molecular frame M, which is defined such that the relative orientations of the two bonds with respect to the Z_M axis are easily determinable by inspection. Combining Eqs. (5.3-5.6), it can be seen that the sum and difference phases that

determine the HMQ spectra are intrinsically the sum and difference frequencies of two segment-fixed dipolar couplings, $\omega_{CH}^{m}\left(\Omega_{PM}^{CH}\right) \pm \omega_{NH}^{m}\left(\Omega_{PM}^{NH}\right)$, and the segment-fixed Euler angles Ω_{PM} contain information on the torsion angle ϕ_H or ϕ.

Figure 5.2 (a). Pulse sequence for obtaining ^{15}N-^{13}C HMQ dipolar sideband spectra. The N-C dipolar interaction is recoupled under MAS by rotor-synchronized ^{15}N and ^{13}C 180° pulses during τ. The excited N-C double and zero-quantum coherences evolve during t_1 under C-H and N-H dipolar interactions, with ^{1}H homonuclear coupling removed by MREV-8 multiple-pulse decoupling. The evolution period has a maximum length of one rotor period, which is half of the constant time τ_{const}. A ^{13}C and ^{15}N 180° pulse is applied in the middle of τ_{const} to refocus ^{13}C and ^{15}N isotropic chemical shifts, respectively. The N-C HMQ coherences are then reconverted to single-quantum ^{13}C coherence for the detection of ^{13}C chemical shift during t_2. (b) DIPSHIFT pulse sequence for measuring C-H and N-H dipolar couplings separated by the ^{13}C and ^{15}N chemical shifts, respectively. The evolution period is similar to that of the previous experiment in order to extract the C-H and N-H couplings to simulate the ϕ-dependent HMQ spectra.

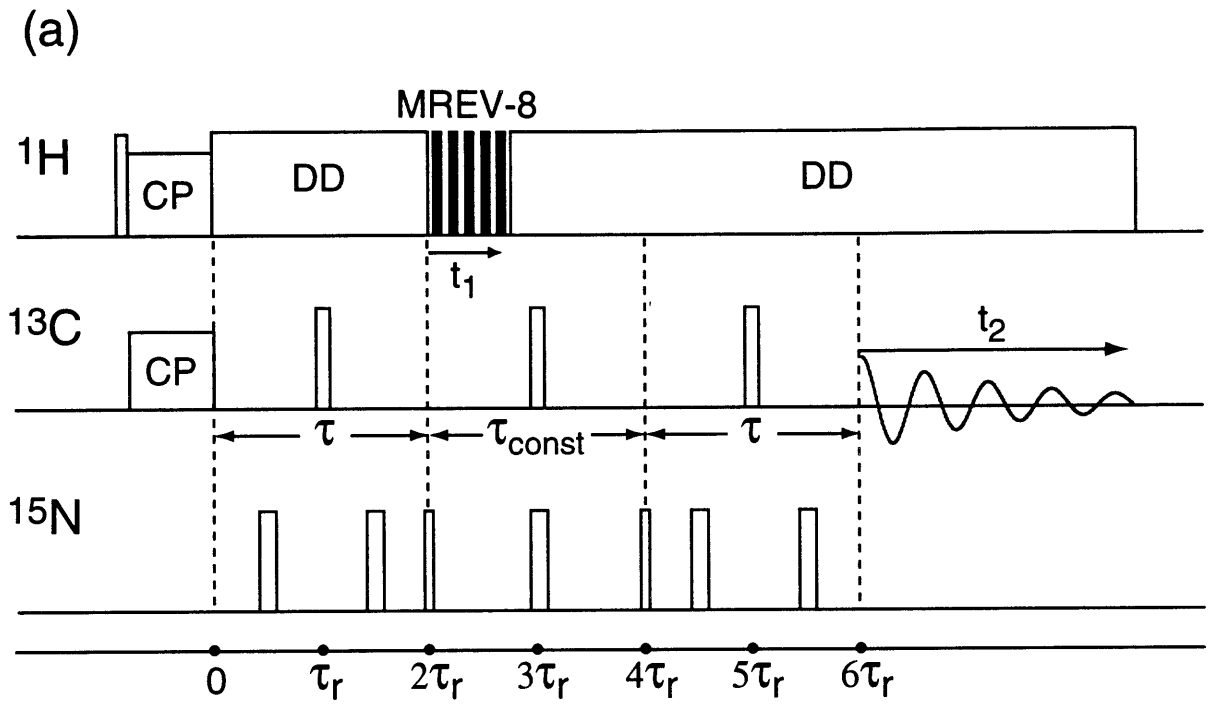
(a)
MREV-8
^{1}H
CP
DD
DD
t_1
^{13}C
CP
t_2
τ
τ_{const}
τ
^{15}N
0
τ_r
$2\tau_r$
$3\tau_r$
$4\tau_r$
$5\tau_r$
$6\tau_r$

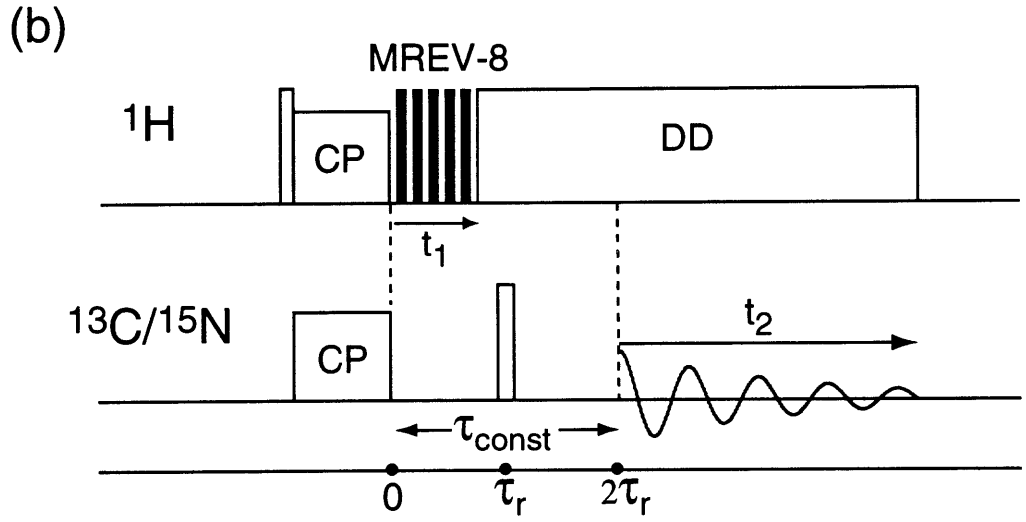
(b)
MREV-8
^{1}H
CP
DD
t_1
^{13}C/^{15}N
CP
t_2
τ_{const}
0
τ_r
$2\tau_r$

Figure 5.2

5.4 Numerical Simulations

The indirectly detected N-C multiple-quantum dipolar sideband spectrum is simulated by evaluating Eq. (5.4) over the course of the evolution period t_1. The N-C bond was chosen as the Z_M axis of the molecular frame, so that $\gamma_{PM}^{CH} - \gamma_{PM}^{NH} = \phi_H$, while β_{PM}^{CH} and β_{PM}^{NH} are simply the bond angles. Powder averaging was performed by Monte Carlo integration where the Euler angles Ω_{MR} that transform the molecular frame to the rotor frame are randomly generated according to a powder distribution. The time signals due to HMQ evolution are coadded and normalized by the number of crystallites. Input parameters for the simulation consist of the effective dipolar couplings $\kappa\delta_{CH}$ and $\kappa\delta_{NH}$, which are obtained from the ^{15}N and ^{13}C DIPSHIFT experiments described below, the Euler angles Ω_{PM} and Ω_{MR}, the spinning speed ω_r, the spectral width, and the number of crystallites employed in the powder average.

5.5 One-Bond N-H and C-H Dipolar Couplings

The simulation of the ϕ-dependent dipolar sideband spectrum requires C^{α}-H^{α} and N-H^N dipolar couplings as input parameters, thus the magnitudes of these couplings affect the accuracy of the ϕ measurement. The effective heteronuclear couplings in our experiments are the product of the rigid-limit anisotropies δ_λ and the scaling factor κ of the homonuclear decoupling sequence. Theoretically, κ=0.536 for semi-windowless MREV-8[29]. However, the actual κ value usually deviates from the theory due to experimental imperfections and is best obtained empirically under the same conditions as the torsion angle experiment. We determined the N-H^N and C^{α}-H^{α} couplings by a 2D MAS separated-local-field technique that separates dipolar rotational sideband patterns according to the isotropic chemical shifts of the ^{15}N or ^{13}C sites (DIPSHIFT)[30-32]. The resulting rotational sideband patterns in ω_1 are then simulated to yield the coupling strengths. As indicated in Fig. 5.2b, these DIPSHIFT experiments are executed in a constant-time fashion with a 180° refocusing pulse in order to be comparable to the torsion angle measurement. Since the performance of the multiple-pulse sequence that determines the scaling factor κ depends on the ratio of the multiple-pulse cycle time (τ_c) to the rotor period (τ_r), the MREV-8 pulse length and the

spinning speeds in the DIPSHIFT experiments were also very similar to those used in the torsion angle experiment.

5.6 Results and Discussion

Figure 5.3a is the ω_2 projection of the 2D N-C multiple-quantum spectrum of NAV. Compared to the ^{13}C CPMAS spectrum (Fig. 5.3b), only the C^{α} and the acetyl carbonyl resonances are observed, while other ^{13}C signals are efficiently suppressed by the short excitation time of the N-C HMQ filter. The relative signal-to-noise ratios of the two spectra indicate that the HMQ excitation efficiency is approximately 36%.

The t_1 modulation of the C^{α} peak is shown in Fig. 5.3c. The net signal decay after one rotor cycle (396 μs) is negligible: in general, we found that more than 80% of the initial signal intensity could be reproducibly refocused at the rotor echo. The time signal is quite symmetric with respect to the center of the rotor period, as expected for an ideal spin system evolving under MAS. The high echo intensity and the symmetry denote the excellent performance of the homonuclear decoupling sequence, since under ideal multiple-pulse decoupling, any intensity loss must result from true T_2 relaxation, which is not expected to be significant after about 400 μs (the ^1H homogeneous linewidth is likely to be smaller than 2.5 kHz). In our experiments, the MREV-8 performance is ensured by the short cycle time relative to the rotor period ($\tau_c=\tau_r/24$), since this minimizes undesirable interference effects between sample spinning and multiple-pulse decoupling.

In order to obtain ϕ-dependent spectra in the form of rotational sideband patterns, the t_1 modulation must be periodic. This was achieved by equalizing the echo intensity to the initial intensity (of the first t_1 point) by positive exponential multiplication $\exp(+t_1/T_2)$, then replicating the single-τ_r signal several times, followed by a negative exponential multiplication $\exp(-t_1/T_2)$ to restore the original decay[32,33]. Assuming equal linewidths for all dipolar sidebands, the periodicity of the MAS time signal dictates that the ϕ-dependent sideband spectra obtained in this way are the same as those resulting from the complete t_1 signal.

Figure 5.3 ^{15}N-^{13}C HMQ spectrum of NAV for determining the torsion angle ϕ_H. (a) ^{13}C MAS spectrum obtained with HMQ excitation and reconversion, but zero evolution time. 512 scans were added. The HMQ filter selects only the C^{α} and the acetyl carbonyl resonances, which are directly bonded to the ^{15}N atom. (b) ^{13}C CPMAS spectrum of NAV after 256 scans, exhibiting all ^{13}C chemical shift resonances. (c) Time evolution of the N-C^{α} double and zero-quantum coherences during one rotor period. The intensity unit is arbitrary. (d) Projected HMQ dipolar sideband spectrum of the C^{α} resonance, in which the highest intensity is observed at the centerband. (e) Simulation of the C^{α} spectrum is obtained with ϕ_H=165°. Other input parameters are: $\kappa\delta_{CH}$=10.9 kHz, $\kappa\delta_{NH}$=-5.2 kHz, ω_r=2.525 kHz, β_{PM}^{CH}=109.5°, β_{PM}^{NH}=60°, γ_{PM}^{CH}=0°, γ_{PM}^{NH}=165°, and 5000 crystallite orientations.

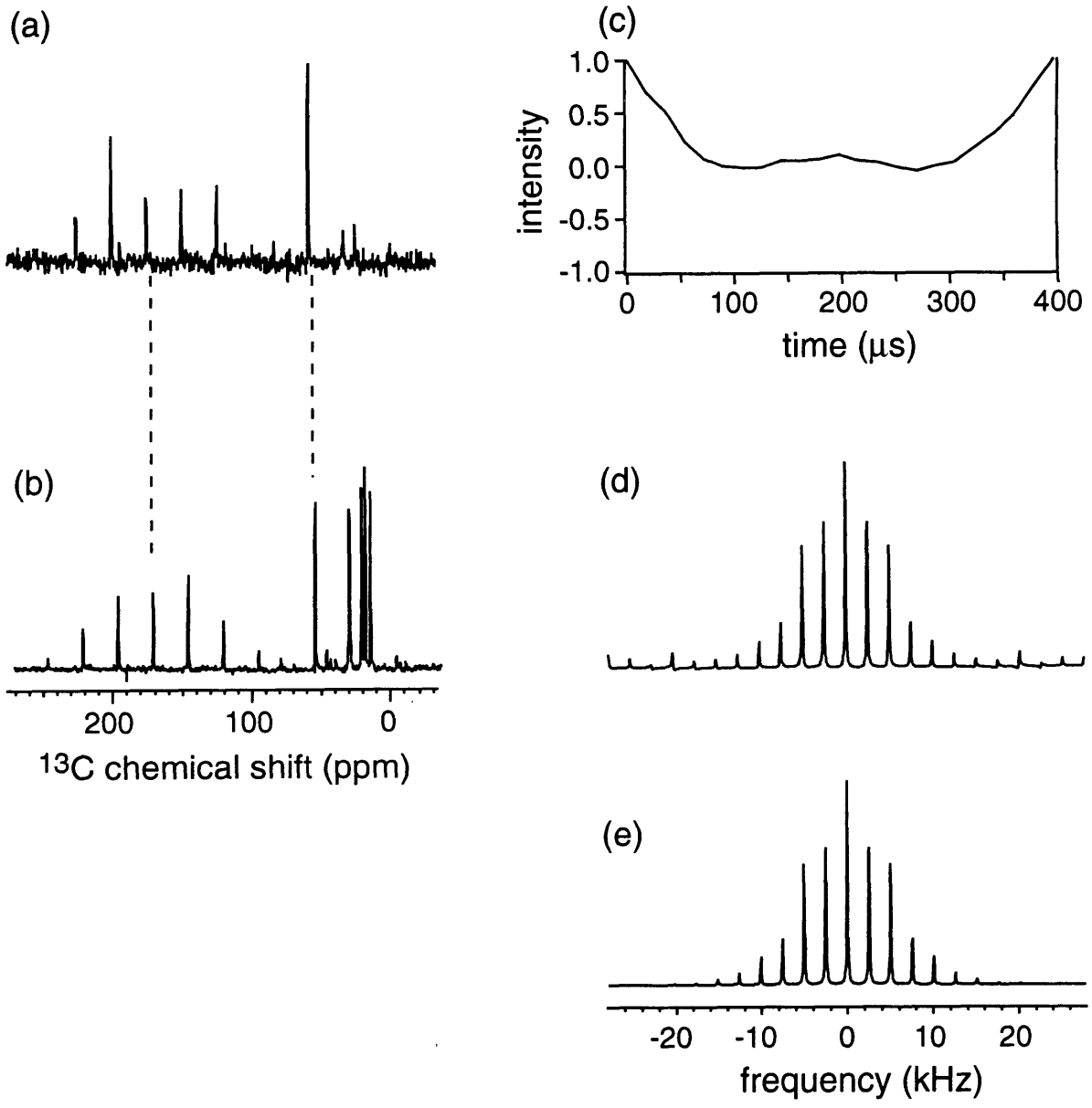
(a)
(b)
200
100
0
^{13}C chemical shift (ppm)
(c)
1.0
0.5
0.0
-0.5
-1.0
intensity
0
100
200
300
400
time (μs)
(d)
(e)
-20
-10
0
10
20
frequency (kHz)

Figure 5.3

Figure 5.3d shows the projection of the N-C multiple-quantum sideband spectrum of the C^{α} resonance. From 2D ^{13}C DIPSHIFT experiments, we found that a single ω_1 cross section at the maximum intensity of the C^{α} resonance produces inaccurate sideband intensity distributions as a result of inhomogeneous broadening of the C^{α} peak in the ω_2 dimension. Therefore, ω_1 slices within the C^{α} resonance linewidth were summed and used for extracting the ϕ angle. The projected spectrum is characterized by a high centerband intensity and lower but significant intensities up to the fourth order sidebands, with observable noise extending to the edges of the spectral window. The spectrum is simulated with $|\phi_H|=165^{\circ}$ (Fig. 5.3e), which corresponds to a backbone torsion angle $\phi=-135^{\circ}$ for the L-isomer and $+135^{\circ}$ for the D-isomer of NAV. This agrees remarkably well with the X-ray crystal structure (Fig. 5.4), in which C(O)-N-C^{α}-C(O) was determined to be -136.5°[34].

Figure. 5.4 X-ray crystal structure of *N*-Acetyl-*D,L*-valine, obtained from reference [34]. The C(O)-N-C^{α}-C(O) torsion angle was determined to be -136.5°.

N-Acetyl-*D,L*-valine

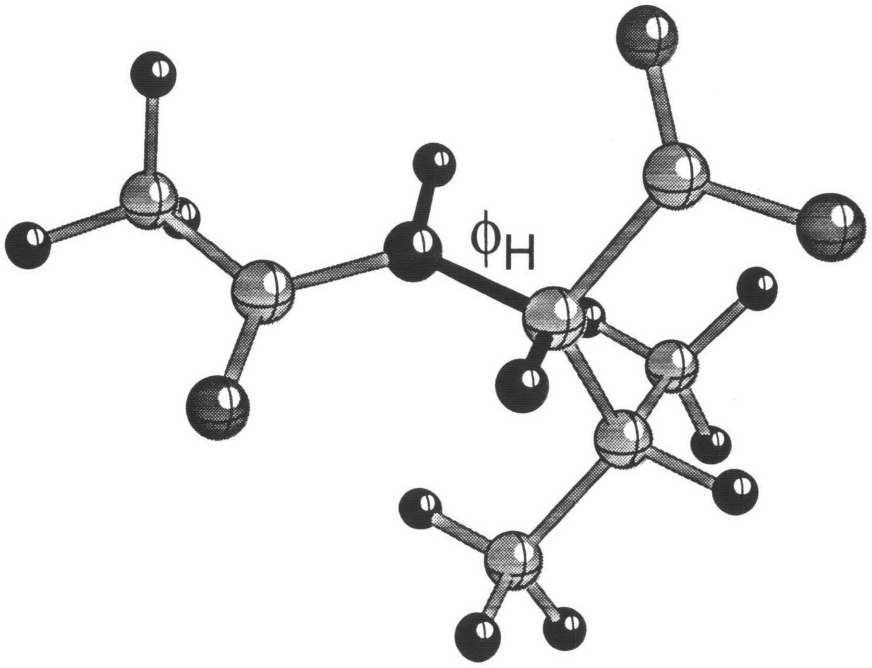

Figure 5.4

To demonstrate the resolution of the angle ϕ measured by this technique, we show some simulated N-C HMQ spectra as a function of ϕ_H in Fig. 5.5. The sideband patterns change more drastically around the trans conformation (ϕ_H=180°) than near the cis conformation (ϕ_H=0°). By simple inspection, the angular resolution is estimated to be less than ±10° for the former and ±20° for the latter. Typical protein secondary strucures with their corresponding ϕ_H angles are also indicated in the figure. It can be seen that the spectra of helical structures are clearly different from those of the β-sheets. It should be emphasized that these dipolar sideband patterns are dominated by the ϕ angle, and much less affected by other parameters such as the effective C-H and N-H dipolar couplings.

Figure 5.5 Simulation of N-C multiple-quantum dipolar sideband spectra as a function of ϕ_H. The spectra are unique in the range ϕ_H=[0, 180°], and have the highest angular resolution around ϕ_H=180°. Typical protein secondary structures are indicated at their expected spectra. Input parameters are: $\kappa\delta_{CH}$=10.9 kHz, $\kappa\delta_{NH}$=-5.2 kHz, τ_{DQ}=792 μs, ω_r=2.525 kHz, β_{PM}^{CH}=109.5°, β_{PM}^{NH}=60°, γ_{PM}^{CH}=0°, and $\gamma_{PM}^{NH}=\phi_H$, and 5000 crystallite orientations.

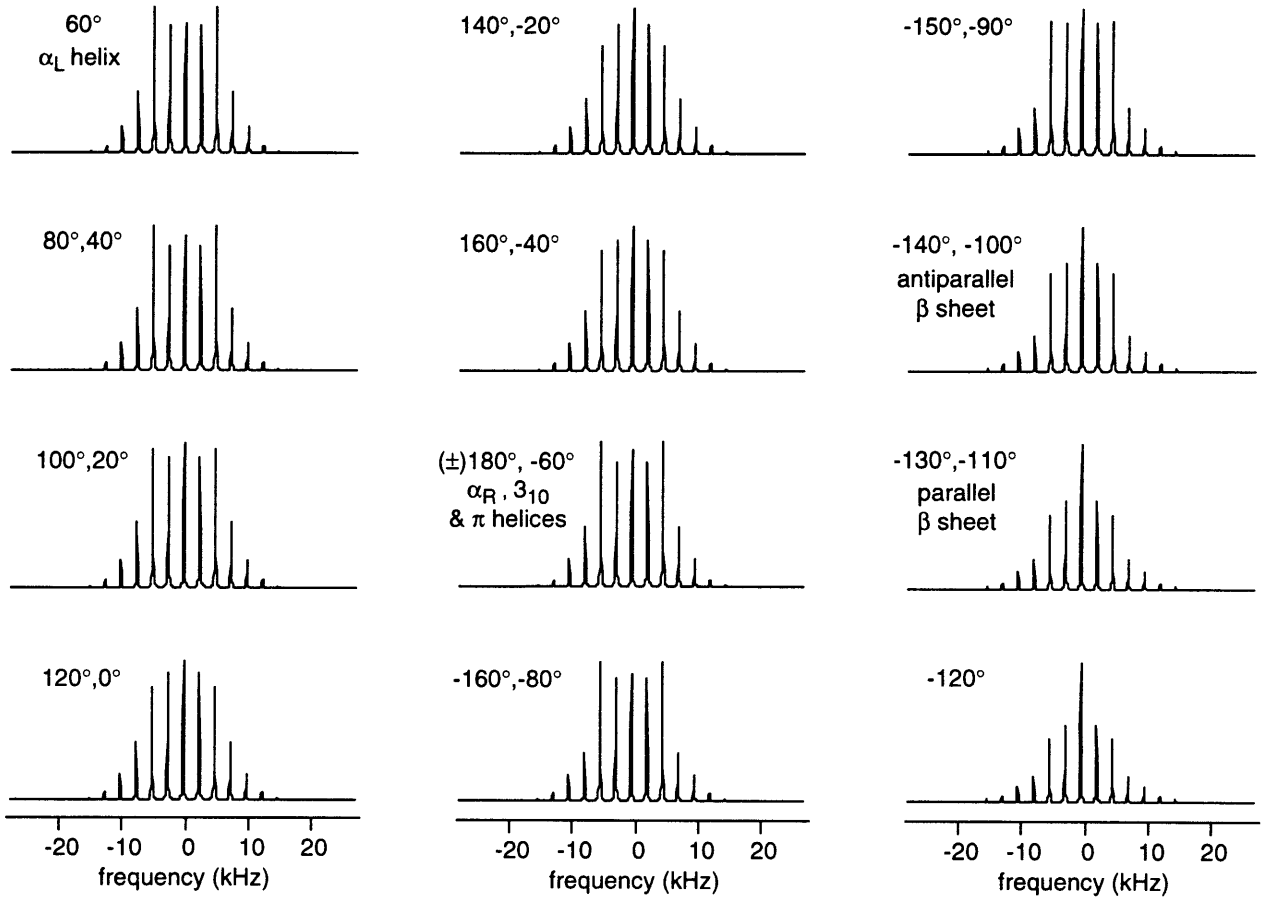
60°
α_L helix
140°,-20°
-150°,-90°
80°,40°
160°,-40°
-140°, -100°
antiparallel
β sheet
100°,20°
(±)180°, -60°
α_R , 3_{10}
& π helices
-130°,-110°
parallel
β sheet
120°,0°
-160°,-80°
-120°
-20 -10 0 10 20
frequency (kHz)
-20 -10 0 10 20
frequency (kHz)
-20 -10 0 10 20
frequency (kHz)

Figure 5.5

Due to the uniaxiality of the dipolar interaction, the HMQ dipolar sideband spectra for $\pm\phi_H$ are equivalent. Since ϕ_H in the commonly occurring L-amino acids is related to the backbone torsion ϕ according to $\phi_H=\phi-60^\circ$, this means that two ϕ angles (ϕ_1, ϕ_2) related by $\phi_1+\phi_2=120^\circ$ yield the same dipolar sideband spectra. Similarly, for D-amino acids, ϕ angles related by $\phi_1+\phi_2=-120^\circ$ produce identical spectra.

The C^α-H^α and N-H^N couplings used in the simulation of the ϕ-dependent spectra were determined by ^{13}C and ^{15}N DIPSHIFT experiments conducted with the pulse sequence of Fig. 5.2(b). The resulting C^α-H dipolar sideband spectrum can be simulated with an effective C^α-H^α coupling of 10.9 kHz, as shown in Fig. 5.6. This coupling strength is about 10% smaller than expected for a 1.1 Å C-H bond (δ_{CH}=-22.7 kHz) under a semi-windowless MREV-8 sequence (κ=0.536). Such a reduction of one-bond C-H couplings in rigid solids has been previously observed and discussed extensively[32,35-37]. It might be attributed to several factors, such as high frequency vibrations of the internuclear bond, imperfect homonuclear decoupling, and long-range C-H dipolar couplings. In our case, since the deviation of the effective coupling from the expected value is relatively small, we did not investigate the exact causes of the difference. Interestingly, in the simulation of the ^{13}C DIPSHIFT spectrum, we found it necessary to consider not only the directly bonded C^α-H^α coupling, but also long-range C^α-H^β and C^α-H^N couplings. Although these long-range couplings also contain information on torsion angles, namely, the H^α-C^α-C^β-H^β angle (from the C^α-H^β coupling) and the ϕ_H angle (from the C^α-H^N coupling), the DIPSHIFT sideband pattern is mainly influenced by the one-bond C^α-H^α coupling. Angles estimated from the X-ray structure of NAV were used as the Euler angles Ω_{PM} that describe the orientations of the C^α-H^β and C^α-H^N dipolar coupling tensors in the molecular frame.

Figure 5.6 (a) NAV C^{α}-H dipolar sideband pattern, taken from the 2D ^{13}C DIPSHIFT spectrum. ω_1 slices within the C^{α} resonance linewidth were summed up to compensate for inhomogeneous broadening. (b) Simulation yields a C^{α}-H^{α} coupling of 10.9 kHz. Two smaller couplings of 1.4 kHz approximating the effects of long-range C^{α}-H^{N} and C^{α}-H^{β} couplings were also used in the simulation.

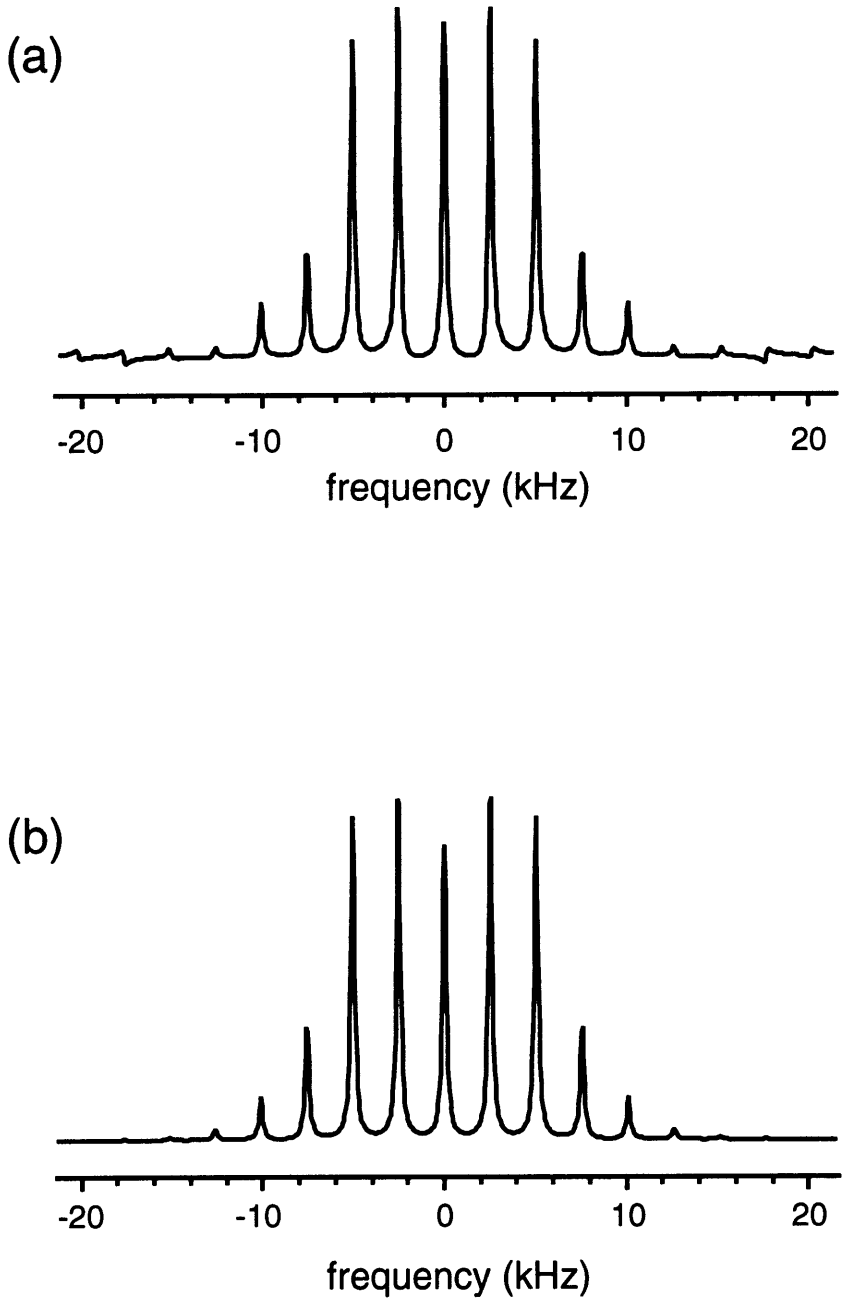

Figure 5.6

Finally, in the ^{15}N 2D DIPSHIFT spectrum, ^{15}N chemical shift sidebands were observed in the ω_2 dimension due to the large ^{15}N chemical shift anisotropy relative to the spinning speed. Thus, the N-H^N dipolar coupling spectrum was obtained by integrating the ω_1 cross sections at these sideband frequencies (data not shown). Simulation of the projected dipolar spectrum yields an effective N-H^N coupling of -5.2 kHz, which corresponds to a MREV-8 scaling factor of 0.48 if a N-H bond length of 1.049 Å is used[37]. The reduction in κ is similar to that observed in the ^{13}C DIPSHIFT experiment.

5.7 Conclusion

We described the determination of the torsion angle ϕ in solid peptides by a 2D MAS technique utilizing ^{15}N-^{13}C double and zero-quantum coherences. The ϕ angle is measured through the relative orientations of the N-H^N and C^α-H^α bonds, which are reflected in the sideband spectrum of the sum and difference of the C^α-H^α and N-H^N dipolar couplings. The N-C dipolar interaction is recoupled by rotor-synchronized 180° pulses and the multiple-quantum coherences can be excited with an efficiency of about 36% under optimum conditions. Applied to NAV, the experiment yielded a ϕ angle of ±135°, which agrees well with the X-ray crystal structure. Simulation indicates that this ϕ angle technique has a resolution of less than 10° when the N-H^N and C^α-H^α bonds are nearly antiparallel and 20° when they are nearly parallel. The accuracy of the experiment is improved by determining the effective C^α-H^α and N-H^N couplings with control DIPSHIFT experiments. These dipolar couplings not only serve as reliable input parameters for simulating the torsion angle spectrum, but also check the performance of the homonuclear decoupling sequence.

Since the ϕ-dependent sideband patterns are separated according to the ^{13}C isotropic chemical shifts, the technique allows the extraction of ϕ angles in multiple residues simultaneously, as long as the C^α isotropic shifts are resolved. In terms of spectral sensitivity, based on the amount of sample and the acquisition time used to obtain a NAV spectrum, we estimate that sufficiently sensitive spectra can be obtained for 40 mg of 100% ^{15}N-labeled peptides with repeat units of 6 residues in 2 days. The same spectral sensitivity can be achieved in 1 hours on a 20-

residue peptide if both ^{15}N and $^{13}C^{\alpha}$ are labeled at a level of 50%. In this light, the multiple-quantum nature of the technique is expected to alleviate the problem of many-spin couplings, which are encountered in distance measurements of highly labeled systems, so that ϕ angles in uniformly and fractionally ^{15}N and ^{13}C labeled samples can be determined. Finally, the angular resolution of the technique can be further enhanced by increasing the spectral variation with ϕ through the adjustment of the C-H and N-H coupling strengths. This may enable the distinction between similar secondary structures such as the α-helix and the 3_{10} helix, or the antiparallel and the parallel β-sheets. Efforts in these directions are currently pursued in this laboratory.

Acknowledgments for Chapter 5

This chapter is excerpted from a manuscript that appeared in J.Phys. Chem. B 101: (30) 5869-5874 Jul. 24 1997. The work was done in collaboration with Mei Hong.

References for Chapter 5

[1] Raleigh, D. P.; Levitt, M. H. and Griffin, R. G. *Chem. Phys. Lett.* **1988**, *146*, 71.

[2] Levitt, M. H.; Raleigh, D. P.; Creuzet, F. and Griffin, R. G. *J. Chem. Phys.* **1990**, *92*, 6347.

[3] Tycko, R. and Dabbagh, G. *Chem. Phys. Lett.* **1990**, *173*, 461.

[4] Bennett, A. E.; Ok, J. H.; Griffin, R. G. and Vega, S. *J. Chem. Phys.* **1992**, *96*, 8624.

[5] Sun, B.-Q.; Costa, P. R.; Kocisko, D.; Lansbury, P. T. J. and Griffin, R. G. *J. Chem. Phys.* **1995**, *102*, 702.

[6] Gullion, T. and Schaefer, J. *J. Magn. Reson.* **1989**, *81*, 196.

[7] Oas, T. G.; Griffin, R. G. and Levitt, M. H. *J. Chem. Phys.* **1988**, *89*, 692.

[8] Levitt, M. H.; Oas, T. G. and Griffin, R. G. *Isr. J. Chem.* **1988**, *28*, 271.

[9] Costa, P. R.; Sun, B. Q. and Griffin, R. G. *manuscript in preparation* **1997**,

[10] Creighton, T. E. *Proteins: Structures and molecular properties*, 2nd Ed.; W.H. Freeman and Co.: New York, 1993.

[11] Karplus, M. *J. Chem. Phys.* **1959**, *30*, 11.

[12] Wang, A. C. and Bax, A. *J. Am. Chem. Soc.* **1996**, *118*, 2483.

[13] Feng, X.; Lee, Y. K.; Sandstroem, D.; Eden, M.; Maisel, H.; Sebald, A. and Levitt, M. H. *Chem. Phys. Lett.* **1996**, *257*, 314.

[14] Schmidt-Rohr, K. *J. Am. Chem. Soc.* **1996**, *118*, 7601.

[15] Mehta, M. A.; Bower, P.; Gregory, D.; Zebroski, H. and Drobny, G. *37th Experimental NMR Conference*, Asilomar, CA. 1996.

[16] Gregory, D.; Mehta, M. A. and Drobny, G. *37th Experimental NMR Conference*, Asilomar, CA. 1996.

[17] Weliky, D. and Tycko, R. *J. Am. Chem. Soc.* **1996**, *118*, 8487.

[18] Ishii, Y.; Terao, T. and Kainosho, M. *Chem. Phys. Lett.* **1996**, *256*, 133.

[19] Mueller, L. *J. Am. Chem. Soc.* **1979**, *101*, 4481.

[20] Minoretti, A.; Aue, W. P.; Reinhold, M. and Ernst, R. R. *J. Magn. Reson.* **1980**, *40*, 175.

[21] Bax, A.; Griffey, R. H. and Hawkins, B. L. *J. Magn. Reson.* **1983**, *55*, 301.

[22] Pan, Y.; Gullion, T. and Schaefer, J. *J. Magn. Reson.* **1990**, *90*, 330.

[23] Christensen, A. M. and Schaefer, J. *Biochemistry* **1993**, *32*, 2868.

[24] Gullion, T. and Schaefer, J. *Advances in Magn. Reson.*; Warren, W. S., Ed.; Academic Press: San Diego, 1989; 57.

[25] Bennett, A. E.; Griffin, R. G. and Vega, S. *NMR Basic Principles and Progress*; Diehl, P.; Fluck, E. and Kosfeld, E., Ed.; Springer: Berlin, 1994; 1.

[26] Shirley, J. M. *Phys. Rev. B* **1965**, *138*, 979.

[27] Zare, R. N. *Angular Momentum*, Wiley: New York, 1957.

[28] Mehring, M. *High Resolution NMR in Solids*, Springer-Verlag: New York, 1983.

[29] Rhim, W.-K.; Elleman, D. D. and Vaughan, R. W. *J. Chem. Phys.* **1973**, *59*, 1740.

[30] Munowitz, M. G.; Griffin, R. G.; Bodenhausen, G. and Huang, T. H. *J. Am. Chem. Soc.* **1981**, *103*, 2529.

[31] Munowitz, M.; Aue, W. P. and Griffin, R. G. *J. Chem. Phys.* **1982**, *77*, 1686.

[32] Schaefer, J.; Mckay, R. A. and Stejskal, E. O. *J. Magn. Reson.* **1983**, *52*, 123.

[33] Schaefer, J.; Stejskal, E. O.; Mckay, R. A. and Dixon, W. T. *Macromolecules* **1984**, *17*, 1479.

[34] Carroll, P. J.; Stewart, P. L. and Opella, S. J. *Acta Cryst.* **1990**, *C46*, 243.

[35] Schaefer, J.; Stejskal, E. O. and Mckay, R. A. *J. Magn. Reson.* **1984**, *57*, 85.

[36] Webb, G. G. and Zilm, K. W. *J. Am. Chem. Soc.* **1989**, *111*, 2455.

[37] Roberts, J. E.; Harbison, G. S.; Munowitz, M. G.; Herzfeld, J. and Griffin, R. G. *J. Am. Chem. Soc.* **1987**, *109*, 4163.

6. Coupling Amplification in 2D MAS NMR and its Application to Torsion Angle Determination in Peptides

6.1 Introduction

Heteronuclear dipolar interactions have long been recognized as useful probes of bond lengths and orientations in solids. For example, ^{13}C-^{1}H and ^{15}N-^{1}H couplings detected under homonuclear proton decoupling were used for determining internuclear distances, for relating chemical shift tensors to bond directions, and for observing fast molecular motions [1-6]. Recently, they have found new uses in NMR experiments that permit measurement of torsion angles through the relative orientation of molecular segments [7-9]. Many of these experiments employ magic-angle spinning (MAS) to provide site resolution and spectral sensitivity. However, since MAS confines the spectral intensity to rotational sidebands, the information content of the spectra is optimized in the slow spinning regime. At spinning speeds $\omega_r/2\pi > b_{ij}/3$, where b_{ij} is the dipolar coupling strength, the dipolar spectrum is dominated by an uninformative centerband. For a one-bond N-H dipolar coupling measured with MREV-8 homonuclear decoupling, b_{ij} = -4.5 kHz and the centerband dominates for spinning speeds as low as $\omega_r/2\pi \approx 1.5$ kHz. While low spinning speeds are desirable for extracting structural information, the necessity to resolve different chemical moieties through isotropic chemical shifts results in an opposing constraint. Higher spinning speeds average the chemical shift anisotropy (δ) more completely and thus yield better resolved spectra. This conflict is exacerbated at higher magnetic field strengths, since shift anisotropies scale linearly with the field strength while the dipolar couplings are field-independent. Thus, the desirable spinning speed range $\delta << \omega_r << b_{ij}$ is reduced at the higher magnetic fields, making it more difficult to observe dipolar sideband spectra and sideband-free isotropic shift spectra simultaneously. Methods to suppress chemical shift sidebands such as TOSS and SELTICS [10-12] have the disadvantage of inducing signal losses. In addition to the chemical shift anisotropy, the homonuclear dipolar interaction among the low-γ spins has also become a source of line broadening in the chemical shift spectrum, as uniformly or fractionally labeled molecules are increasingly used for the study of biomolecular structures. Again, the most convenient way of minimizing this broadening is to employ higher spinning speeds.

In order to obtain informative dipolar sideband patterns in the ω_1 dimension and simple spectra in ω_2 of a 2D dipolar-chemical shift (DIPSHIFT) spectrum without changing the spinning speed, it is desirable to amplify the apparent dipolar coupling strengths in ω_1 by rotor-synchronized 180° pulses. These 180° pulses are employed such that they define the evolution period of a DIPSHIFT experiment in which a MREV-8 multiple pulse train is applied for a fixed number of rotor periods. As a result, the dipolar couplings of interest are amplified with respect to the spinning speed. The technique is based on a sequence first employed in REDOR experiments [13], and is closely related to earlier MAS experiments that achieve sideband enhancement [14-16].

As a practical example of the amplification of the X-^{1}H (e.g. X=^{13}C, ^{15}N) dipolar interaction under MAS, we show the result of increasing the number of dipolar sidebands in a recently introduced experiment (*8*) that correlates the relative orientation of the N-H^N and C$^\alpha$-H$^\alpha$ bonds in order to determine the peptide torsion angle ϕ. The relative orientation is observed in the sum and difference frequencies of the N-H and C-H dipolar couplings, which are measured under homonuclear decoupling of the protons. However, there were two restrictions in this NH/C$^\alpha$H experiment. First, it required low spinning speeds of about 2.5 kHz in order to generate a sufficient number of sidebands in the dipolar dimension. Secondly, the ϕ dependence of the spectra is small in certain angular regions, thus limiting the ability to distinguish similar secondary structures such as the right-handed α helix and the 3_{10} helix. We now show that not only can the spinning speed constraint be relaxed, but the spectral variation with ϕ can also be enhanced by doubling the effective N-H coupling while keeping the C-H coupling unchanged. In other words, both the spectral and the angular resolutions of the NH/C$^\alpha$H technique can be improved by coupling amplification.

6.2 Theory

6.2.1 Interaction "Doubling" under MAS

In a MAS rotor period unperturbed by rf pulses, the dynamic phase Φ acquired by a spin due to the interaction Q after time t_1 is

$$\Phi(t_b, t_a) = \int_{t_a}^{t_b} dt \sum_{m=-2}^{2} \omega_Q^m \exp\{i\, m\, \omega_r\, t\} \quad , \tag{6.1}$$

where the Fourier coefficent ω_Q^m is written

$$\omega_Q^m = b_{ij} d_{0m}^{(2)}(\beta_{PR}^Q) d_{m0}^{(2)}(\beta_{RL}) \exp(i\, m\, \gamma_{PR}^Q) \tag{6.2}$$

for Q = the NH or the CH dipolar interaction where $b_{ij} = -\left(\frac{\mu_0}{4\pi}\right)\frac{\gamma_j \gamma_k \hbar}{r_{jk}^3}$ is the dipolar coupling, $d_{\mu\,\mu'}^{(2)}$, is the reduced Wigner function, β_{PR} and γ_{PR} are the Euler angles that rotate the dipolar tensor into the rotor fixed frame, and β_{RL} is the inclination of the rotor (z-axis) with respect to the lab frame. Therefore, the dynamic phase (6.1) accumulated is proportional to the dipolar coupling b_{ij} as indicated by Eq. and 6.2.

After each full rotation period during which the spin interaction is active, the phase averages to zero

$$\Phi(t + \tau_r, t) = 0 \quad , \tag{6.3}$$

indicating refocusing of the interaction. A 180° pulse applied at time t_1 in the rotor period inverts the phase of the magnetization so that the overall phase (viewed in the toggling frame) at the end of the rotor cycle becomes

$$\begin{aligned} \tilde{\Phi}(\tau_r, 0) &= \Phi(t_1, 0) - \Phi(\tau_r, t_1) \\ &= \Phi(t_1, 0) + \Phi(t_1, \tau_r,) = 2\,\Phi(t_1, 0) \end{aligned} \tag{6.4}$$

The phase in Eq. (6.4) is twice that of the evolution in Eq. (6.1). Since $\Phi(t)$ is proportional to b_{ij}, this doubling of the dynamic phase can be viewed as an effective doubling of the dipolar coupling b_{ij} at the spinning speed ω_r. Alternatively, since

$$2\,\Phi(t_1, 0, \omega_r) = \Phi(2\,t_1, 0, \omega_r/2) \quad , \tag{6.5}$$

the doubling of the phase is also equivalent to an effective reduction of the spinning speed ω_r by half while the coupling strength b_{ij} remains constant.

The simple pulse sequence described above is applicable to NMR interactions that are linear in the spin to which the 180° pulse is applied. Thus, the anisotropic chemical shift and the heteronuclear dipolar couplings are suitable interactions to be manipulated. For X-^{1}H dipolar couplings, two versions of the experiment are possible. Both involve a constant-time evolution period of two rotor cycles, where on the ^{1}H channel homonuclear multiple-pulse decoupling is applied during the first rotor cycle and heteronuclear dipolar decoupling is applied during the second. In the first experimental version (Figure 6.1a), two 180° pulses are applied on the X spins at t_1 and τ_r+t_1. The X-^{1}H dipolar evolution is doubled by the first 180° pulse and unaffected by the second, while the X spin chemical shift is refocused by both 180° pulses upon completion of the two rotor periods. In the second version of the experiment (Figure 6.1b), a proton 180° pulse is applied at t_1, while a X spin 180° pulse is applied at τ_r to refocus the isotropic chemical shift. The X anisotropic chemical shift is removed by magic-angle spinning. Both versions of the experiment yield 2D DIPSHIFT spectra in which the dipolar dimension exhibits effectively doubled coupling strength.

The effects of the 180° pulses on the formation of the dipolar spin echoes in MAS experiments have been examined in detail previously [16,19-21]. There, 180° pulses were similarly employed on the protons or the rare spins to perturb the formation of rotational echoes, leading to enhanced chemical shift or dipolar sidebands. However, there are two important differences between these previous experiments and the current version. In the previous

experiments, the 180° pulses and the homonuclear decoupling pulses were not synchronized with the rotor cycle, and the evolution period was usually not part of a constant time. As a result, the experiments produced convolutions of spectral patterns with sideband intensities at both ω_r and $\omega_r/2$ [21], which are not rigorously identical to the spectra taken at $\omega_r/2$. In addition, the dipolar sidebands were usually mixed with the chemical shift sidebands due to the lack of synchronization and must be separated by skew projections. However, the separation is not possible in certain cases. The current experiment avoids these complications by limiting the dipolar evolution to an integer multiple of the rotor cycle, thus producing simple dipolar sideband spectra with the envelope identical to that of a sample spinning at $\omega_r/2$.

Figure 6.1 (a-b) Pulse sequences for doubling the effective X-^{1}H dipolar couplings under MAS. MREV-8 homonuclear decoupling is applied for an entire rotor period in both sequences. (a) Two X 180° pulses are applied at t_1 and $t_1+\tau_r$. (b) One ^{1}H 180° pulse at t_1 and one X 180° pulse at τ_r are used. (c) Pulse sequence for quadrupling the X-^{1}H dipolar interaction. The MREV-8 multiple pulse train is applied for two rotor cycles. A X 180° pulse is applied at time t_1 from the beginning of each rotor cycle. A 180° pulse at the end of the first rotor period ensures the proper addition of the dynamic phase associated with each rotor period. Two more rotor periods with the same X pulses but heteronuclear decoupling follow in order to refocus the X spin chemical shift. In all the sequences filled narrow rectangles represent 90° pulses while the unfilled broad rectangles indicate 180° pulses.

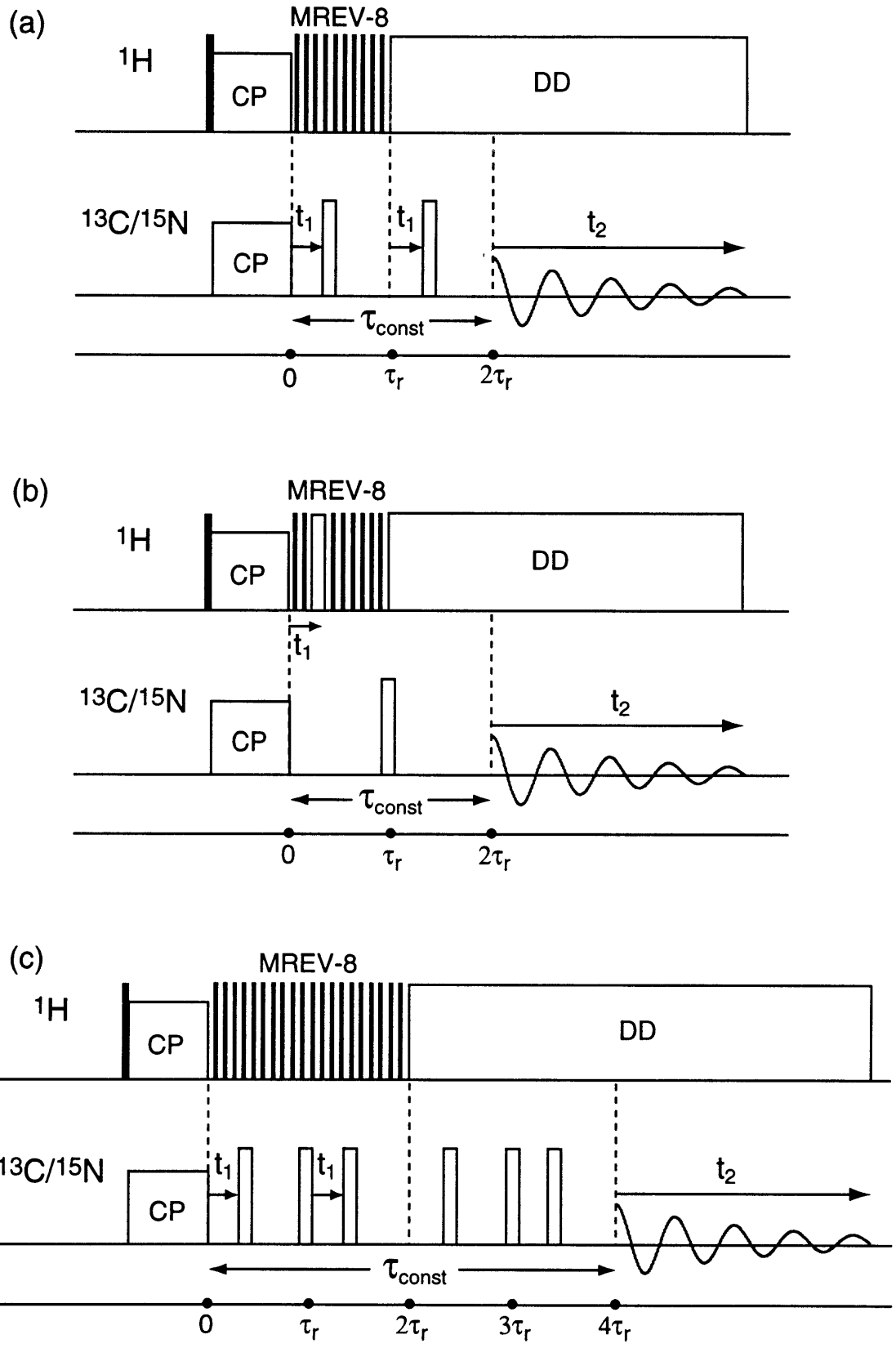
(a)
MREV-8
^{1}H
CP
DD
^{13}C/^{15}N
CP
t_1
t_1
t_2
τ_{const}
0
τ_r
$2\tau_r$
(b)
MREV-8
^{1}H
CP
DD
t_1
^{13}C/^{15}N
CP
t_2
τ_{const}
0
τ_r
$2\tau_r$
(c)
MREV-8
^{1}H
CP
DD
^{13}C/^{15}N
CP
t_1
t_1
t_2
τ_{const}
0
τ_r
$2\tau_r$
$3\tau_r$
$4\tau_r$

Figure 6.1

6.2.2 n-Fold Amplification of the Dipolar Evolution

The basic scheme of doubling the dynamic phase of an NMR interaction can be repeated n times to produce a 2n-fold increase in the phase, thus amplifying the interaction strength b_{ij} by the same factor. For example, to "quadruple" the X-^{1}H dipolar coupling, we can employ *two* rotor cycles of proton homonuclear decoupling and a X spin 180° pulse at time t_1 from the beginning of each rotor cycle (Figure 6.1c). Another X spin 180° pulse must be applied at the end of the first rotor cycle to ensure the addition of the phases associated with each rotor period. To refocus the X chemical shift anisotropy that is also amplified by this point, two more rotor cycles with heteronuclear dipolar decoupling and the same X pulses must be added. The resulting spectrum has sidebands spaced at the actual spinning speed but an intensity envelope identical to that taken at a quarter of the spinning speed. The extendability of this pulse sequence distinguishes it from methods that enhance the sidebands by dipolar decoupling for a fraction of the rotor cycle.[14,22].

Higher order amplification of b_{XH} is useful in applications where high spinning speeds are desirable, and is limited only by the attainable spectral bandwidth in the ω_1 dimension. For example, using semi-windowless MREV-8 [23] a t_1 increment equal to a quarter of the MREV-8 cycle, and high ^{1}H rf powers, it is possible to achieve a dwell time small enough to contain the quadrupled one-bond C-H dipolar coupling. Other homonuclear decoupling sequences with short cycle times such as the frequency-switched Lee-Goldberg sequence may also be employed [24,25]. The upper limit of the spinning speeds is about 10 kHz, above which interference effects between multiple-pulse decoupling and sample rotation become significant.

For simplicity, in the following we refer to the X-^{1}H coupling "doubled" and "quadrupled" DIPSHIFT experiments as $2\Phi_{XH}$- and $4\Phi_{XH}$-DIPSHIFT, respectively.

6.2.3 Selective Dipolar "Doubling" for Measuring the Torsion Angle ϕ

The coupling amplification method can be incorporated into the recently developed NH/$C^{\alpha}H$ experiment that determines the peptide torsion angle ϕ [8]. The new pulse sequence, shown in Figure 6.2, adopts the approach of separate but synchronous evolutions [26]. First, antiphase ^{13}C magnetization $C_{x,y}N_z$ is generated after recoupling the N-C dipolar interaction with a short period of REDOR sequence [27]. $C_{x,y}N_z$ is then allowed to evolve under the C-H dipolar interaction for a duration defined by the length of the MREV-8 train that decouples the proton homonuclear interaction. Next, two simultaneous 90° pulses on ^{13}C and ^{15}N are applied to transform the density operator to antiphase ^{15}N magnetization, $C_zN_{x,y}$, which evolves under the effectively doubled N-H coupling in the same fashion as in Figure 6.1a. The ^{15}N 180° pulses are moved synchronously with the increment of the MREV-8 train during the preceding C-H evolution period, so that the resulting ω_1 dimension of the 2D spectrum reflects both the N-H and C-H couplings. Finally, the ^{15}N antiphase magnetization is converted to observable ^{13}C magnetization by a combination of 90° pulses and a second REDOR period. The ^{13}C isotropic chemical shift is detected during the t_2 period.

Figure 6.2 Pulse sequence for determining the peptide backbone torsion angle ϕ using effectively doubled N-H dipolar coupling. The C-H and N-H dipolar interactions evolve in two separate periods synchronously in order to double the N-H dipolar phase selectively. The C-H coupling is measured by incrementing the MREV-8 multiple pulse train, while the N-H interaction is measured by moving the ^{15}N 180° pulse through a rotor period with constant MREV-8 decoupling. Antiphase magnetization of the forms C_xN_z and N_xC_z are created by refocusing the ^{13}C-^{15}N dipolar interaction and simultaneous 90° pulses. The filled rectangles indicate 90° pulses while the unfilled ones represent the 180° pulses. The phase cycles are θ_0=13, θ_1=11223344, θ_2=13243142, θ_3=13243142 31421324, receiver=31421324 13243142, where 1, 2, 3, 4 represent the four phases x, y, -x, -y, respectively.

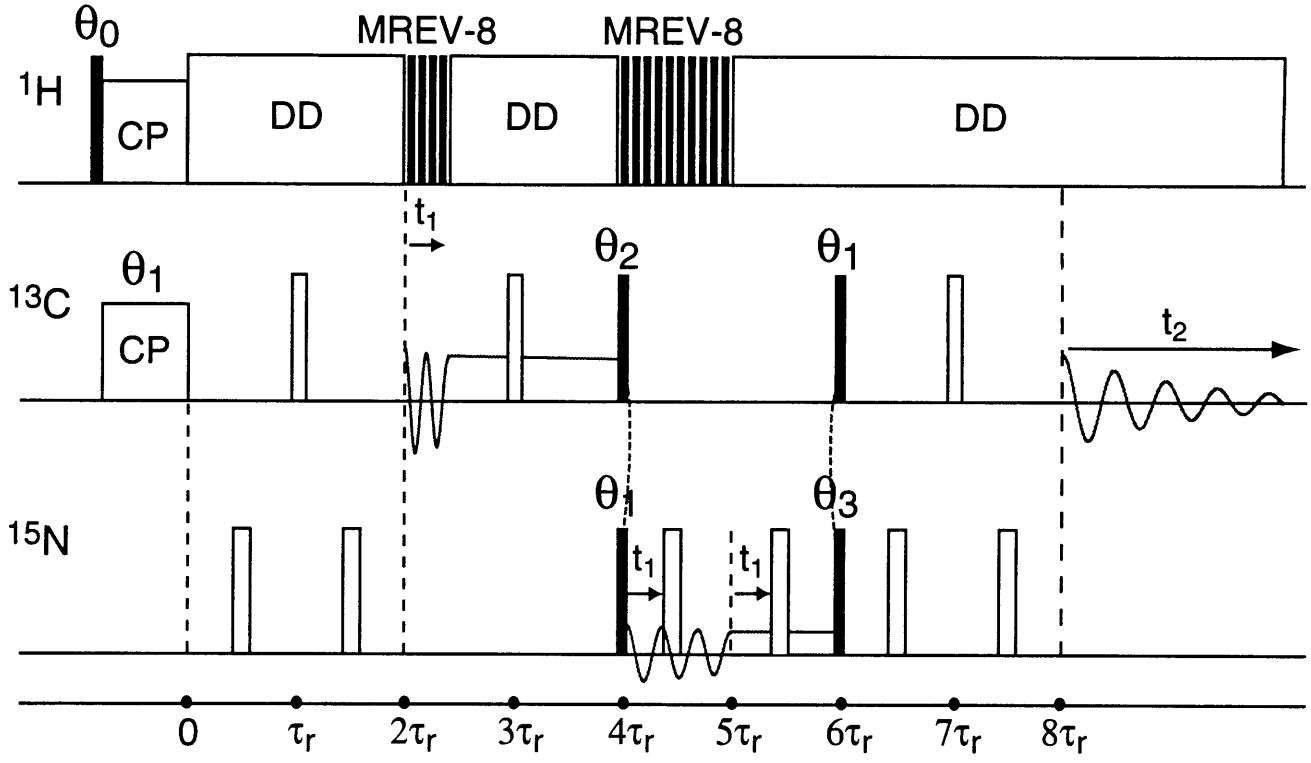
θ0
MREV-8
MREV-8
1H
CP
DD
DD
DD
t1
θ2
θ1
θ1
13C
CP
t2
θ1
θ3
15N
t1
t1
0
τr
2τr
3τr
4τr
5τr
6τr
7τr
8τr

Figure 6.2

6.3 Results and Discussion

The result of doubling the apparent N-H dipolar couplings in NAV is shown in Figure 6.3. The $2\Phi_{NH}$-DIPSHIFT spectrum was obtained with the pulse sequence of Figure 6.1a and the normal DIPSHIFT spectrum reflecting the unchanged N-H couplings was taken without the moving 180° pulses[8]. A spinning speed of 2137 Hz was used in both experiments. The left column shows the t_1 modulations of the ^{15}N resonance, which are the sum of the ω_1 cross sections at the various ^{15}N chemical shift sidebands. As expected, the decay of the time signal of the $2\Phi_{NH}$ experiment (Figure 6.3a) is more rapid and greater than that of the normal DIPSHIFT experiment (Figure 6.3d). The single-rotor-period time signals are replicated and Fourier transformed to yield rotational sideband spectra, shown in the middle column. The $2\Phi_{NH}$-DIPSHIFT spectrum (Figure 6.3b) exhibits significant intensities up to the fourth order sidebands, and the sideband envelope has two characteristic singularities reminiscent of the Pake pattern that would be obtained without rotation. In comparison, the sideband pattern of the normal DIPSHIFT spectrum (Figure 6.3e) shows a more featureless envelope dominated by the centerband. Simulations of the two spectra yield an effective dipolar coupling of 10.2±1.0 kHz for the former (Figure 6.3c) and 5.2±0.5 kHz for the latter (Figure 6.3f). These effective couplings are the products of the static one-bond (~ 1.06 Å) N-H dipolar coupling constant and the scaling factor (~ 0.536) of the semi-windowless MREV-8 sequence [23]. Note that the additional sidebands extending to the two edges of the experimental spectra are noise peaks. They are restricted to multiples of $2\pi/\tau_r$ by the periodic replication of the noise in the time signal.

Figure 6.3 Interaction "doubling". (a-c) $2\Phi_{NH}$-DIPSHIFT spectrum and (d-f) normal DIPSHIFT spectrum of NAV. A spinning speed of 2137 Hz was used. Both the t_1 signals and the ω_1 spectra are sums of the cross sections at the ^{15}N chemical shift sidebands. The decay of the time signal in the $2\Phi_{NH}$ experiment (a) is more rapid and greater than in the coupling unchanged experiment (d). Correspondingly, the $2\Phi_{NH}$-DIPSHIFT spectrum (b) displays more rotational sidebands than the normal spectrum (e). Simulations indicate that the effective couplings are 10.2±1.0 kHz (c) and 5.2±0.5 kHz (f), respectively.

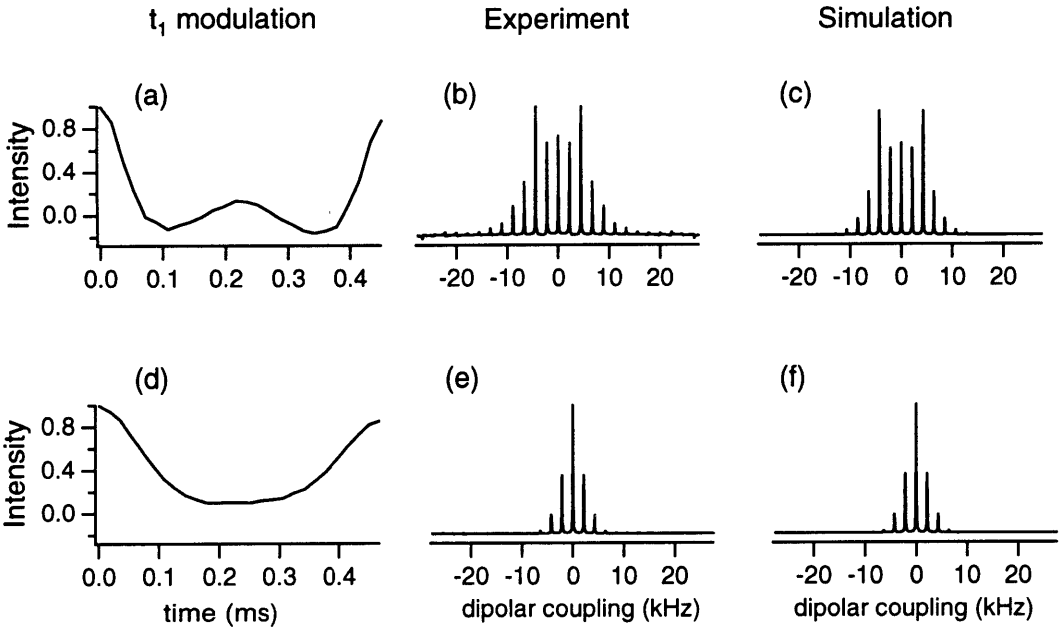
t1 modulation
Experiment
Simulation
(a)
(b)
(c)
(d)
(e)
(f)
Intensity
0.8
0.4
0.0
0.0 0.1 0.2 0.3 0.4
time (ms)
-20 -10 0 10 20
dipolar coupling (kHz)

Figure 6.3

Figure 6.4 compares the $4\Phi_{NH}$- and $2\Phi_{NH}$-DIPSHIFT spectra of NAV. They were taken at $\omega_r/2\pi$ = 2778 Hz with a t_1 dwell time of 9 μs. This short dwell time is necessary for accommodating the increased dipolar coupling in the ω_1 dimension, and was achieved by incrementing a quarter of the semi-windowless MREV-8 cycle per t_1 point, using a ^1H 90° pulse of 3 μs. The best-fit simulations yield effective N-H couplings of 24.0±2.0 kHz and 11.3±1.0 kHz for the $4\Phi_{NH}$ and $2\Phi_{NH}$ spectra, respectively. Small deviations in the center of the spectrum are observed between the experimental and the simulated $4\Phi_{NH}$-DIPSHIFT spectra (Figures 6.4a and 6.4b). They may arise from long-range N-H couplings which are not adequately included in the simulations.

Figure 6.4 Interaction "quadrupling". (a) $4\Phi_{NH}$-DIPSHIFT spectrum of NAV taken at $\omega_r/2\pi$ = 2778 Hz. (b) The best-fit simulation indicates $\omega_{NH} = 24.5 \pm 2.0$ kHz, which is the product of $4b_{NH}$ and the MREV-8 scaling factor. (c-d) The corresponding $2\Phi_{NH}$-DIPSHIFT spectrum and simulation with 11.3±1.0 kHz.

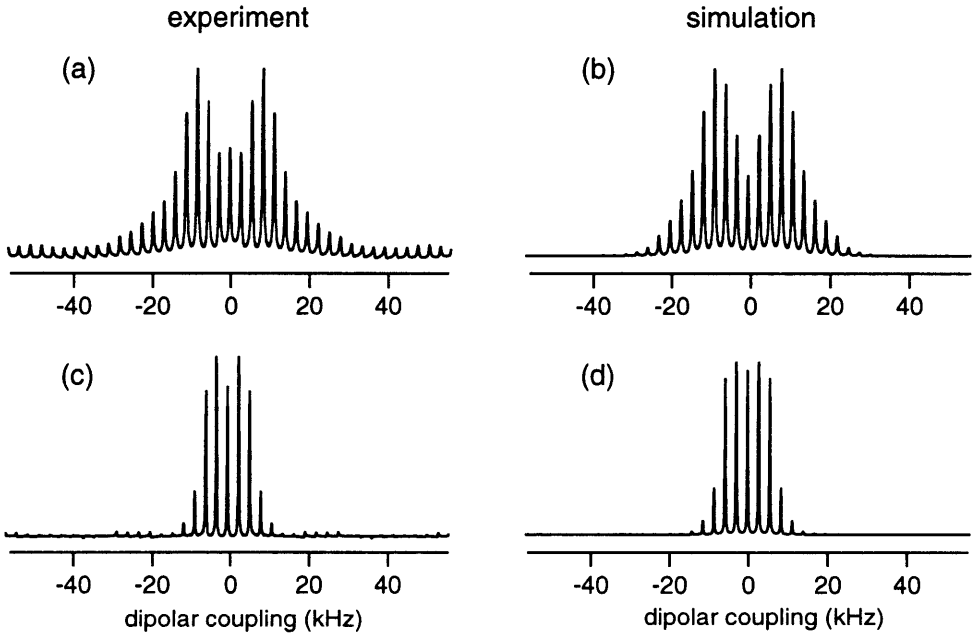
experiment
simulation
(a)
(b)
(c)
(d)
-40
-20
0
20
40
dipolar coupling (kHz)

Figure 6.4

We incorporated the coupling amplification method into the measurement of the peptide torsion angle ϕ. Figure 6.5 displays the $2\Phi_{NH}$-NH/$C^{\alpha}H$ spectrum of NAV. The ω_2 dimension (Figure 6.5a) exhibits only the C^{α} and acetyl carbonyl resonances due to the short N-C dipolar recoupling period used. The t_1 oscillation of the C^{α} resonance (Figure 6.5b) was replicated and Fourier transformed to give a sideband spectrum (Figure 6.5c) that is indicative of the relative orientation of the $N\text{-}H^{N}$ and $C^{\alpha}\text{-}H^{\alpha}$ bonds. Due to the effective doubling of the N-H dipolar coupling, the spectrum shows greater intensities at the first and second-order sidebands compared to the original experiment[8]. The best-fit simulation (Figure 6.5d) was achieved with a torsion angle ϕ=-142°±5°, in fair agreement with the X-ray result of ϕ=-136.5° [28].

Figure 6.5 $2\Phi_{NH}$-NH/$C^{\alpha}H$ spectrum of NAV taken at $\omega_r/2\pi$ = 2778 Hz for determining the torsion angle ϕ. From the C^{α} resonance in the ω_2 spectrum (a), we extracted the t_1 oscillation for one rotor period (b), replicated it and Fourier transformed it to produce a dipolar sideband spectrum (c) that is indicative of the relative orientation of the N-H^N and the C^{α}-H^{α} bonds. Simulation (d) yields ϕ=-142°±5°. The data were acquired with 512 scans for each of the 17 t_1 points. The signal averaging time was 8 hours.

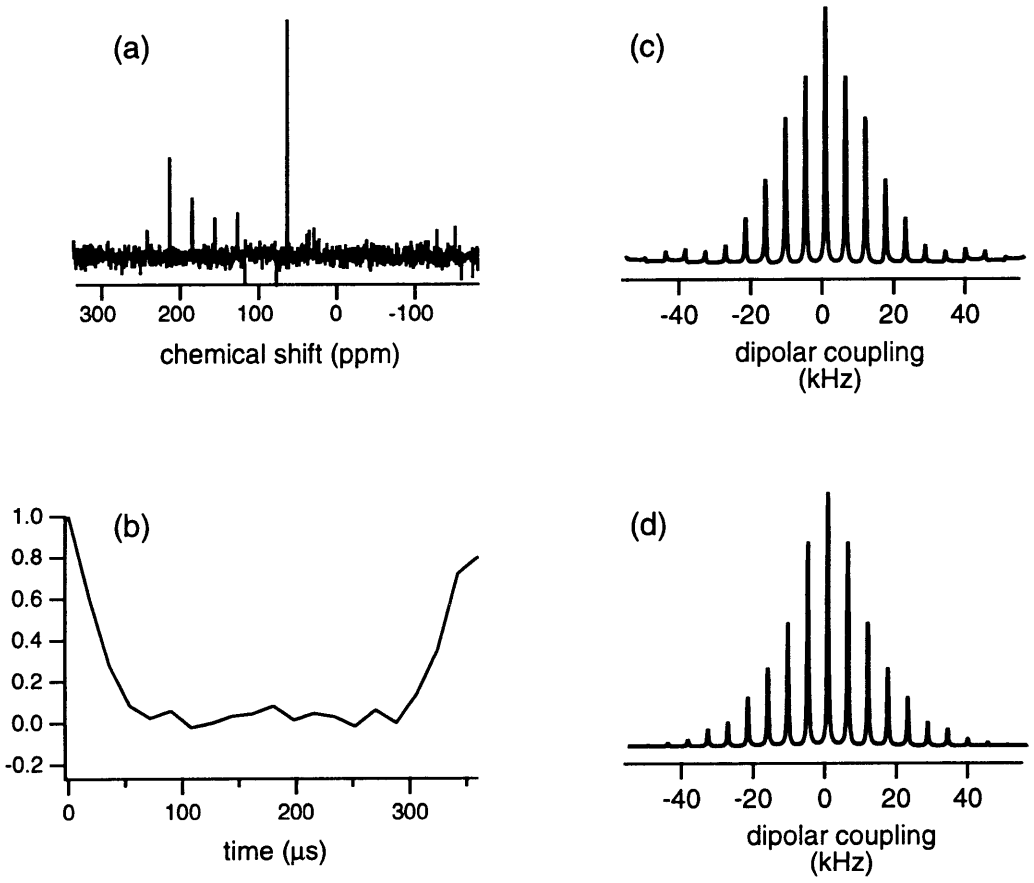
(a)
300
200
100
0
-100
chemical shift (ppm)
(c)
-40
-20
0
20
40
dipolar coupling
(kHz)
(b)
1.0
0.8
0.6
0.4
0.2
0.0
-0.2
0
100
200
300
time (μs)
(d)
-40
-20
0
20
40
dipolar coupling
(kHz)

Figure 6.5

To demonstrate the sensitivity of the $2\Phi_{NH}$-NH/C$^{\alpha}$H experiment to the torsion angle ϕ, we display a series of calculated spectra for ϕ ranging from 60° to -120° in 20° increments (Figure 6.6). The spectral patterns vary more significantly compared to those without the doubled N-H coupling [8], which indicates improved angular resolution. The largest ϕ-dependence is observed in the β-sheet region. As described previously, due to the uniaxiality of the dipolar interaction, each spectrum corresponds to two torsion angles ϕ_1 and ϕ_2 that are related by $(\phi_1+\phi_2)/2=-120°$[8].

To obtain a more quantitative estimate of the angular resolution, we calculated the root-mean-squared deviations (RMSDs) for each pair of spectra and represented them as 2D contour plots, where both axes indicate the torsion angle ϕ (Figure 6.7). The RMSD between spectra $S(\phi_1)$ and $S(\phi_2)$ is defined as

$$\mathrm{rmsd}(\phi_1,\phi_2)=\left\{\frac{1}{N}\sum_{i=1}^{N}\left[S_i(\phi_1)-S_i(\phi_2)\right]^2\right\}^{1/2}, \qquad [5]$$

where $S_i(\phi)$ represents the spectral intensity of the ith sideband, and N is the number of independent sidebands in the spectrum. The RMSDs of both the original NH/C$^{\alpha}$H experiment and the $2\Phi_{NH}$-NH/C$^{\alpha}$H experiment are calculated and compared. The contour levels used in the two plots range from 0 to 100% of the largest value, which occurs in the $2\Phi_{NH}$-NH/C$^{\alpha}$H experiment, at 5% intervals. The contour level of the diagonal is zero, since $S_i(\phi)$-$S_i(\phi)$=0. Away from the diagonal, the contour heights are finite, indicating non-vanishing differences between the spectra. The higher the contour intensity, the larger the spectral difference. The larger the slope, the higher the angular resolution. For both experiments, the highest angular resolution is observed around ϕ=-120°, which corresponds to the extended β-sheet structure, and the lowest resolution occurs near ϕ=60°, corresponding to the rarely occurring left-handed α-helix. Although these qualitative features of the two contour plots are similar, it is important to note that the contour heights for the N-H coupling doubled experiment (Figure 6.7b) are more than a factor of two greater than those of

the original experiment (Figure 6.7a). This indicates an enhancement of the ϕ resolution throughout the whole angular range due to the selective amplification of the N-H coupling. Some cross sections of each contour plot are also displayed in Figure 6.7 to enable better visualization of the 2D plots.

Figure 6.6 Simulated $2\Phi_{NH}$-NH/$C^{\alpha}H$ spectra as a function of the torsion angle ϕ at $\omega_r/2\pi$ = 2778 Hz. Compared with the spectra without the doubled N-H coupling [8], the spectral variation with ϕ is more drastic, indicating higher angular resolution. Each spectrum corresponds to two ϕ angles due to the uniaxial symmetry of the dipolar interaction. Input parameters for the simulation are: ω_{CH}=10.8 kHz, ω_{NH}=-11.3 kHz, $\omega_r/2\pi$=2778 Hz, 5000 crystallite orientations, and various Euler angles $\beta_{PM}^{CH}=109.5°$, $\beta_{PM}^{NH}=60°$, $\gamma_{PM}^{CH}=0°$, $\gamma_{PM}^{NH}=\phi_H=\phi$-60, where the subscript PM indicates rotation from the principle axis frame of the dipolar tensor to the molecular frame. The molecular frame is defined with its z-axis collinear with the N-C^{α} bond,[8] and the β and γ angles are defined according to Spiess' convention [29]

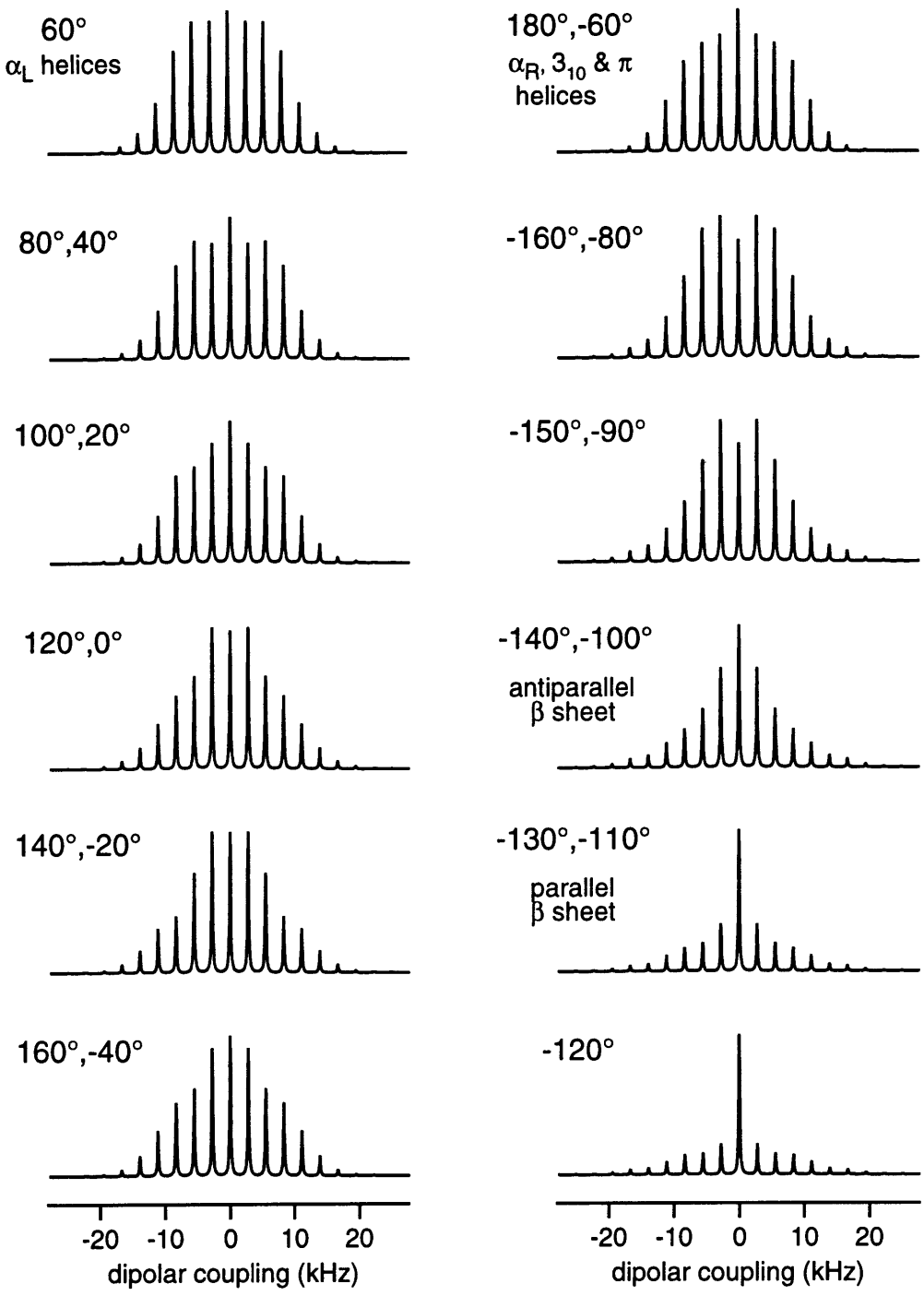
60°
α_L helices
180°,-60°
α_R, 3_{10} & π
helices
80°,40°
-160°,-80°
100°,20°
-150°,-90°
120°,0°
-140°,-100°
antiparallel
β sheet
140°,-20°
-130°,-110°
parallel
β sheet
160°,-40°
-120°
-20 -10 0 10 20
dipolar coupling (kHz)
-20 -10 0 10 20
dipolar coupling (kHz)

Figure 6.6

Figure 6.7 Angular resolution of the NH/C$^{\alpha}$H experiments for the determination of ϕ. Contour levels represent the RMSDs between a pair of simulated spectra $S(\phi_1)$ and $S(\phi_2)$. Contour heights range from 0 to 100% of the highest RMSD value at 5% intervals. (a) Normal NH/C$^{\alpha}$H experiment. (b) $2\Phi_{NH}$-NH/C$^{\alpha}$H experiment. Vanishing RMSDs are obtained along the diagonal of each plot, as required for identical spectra. The largest RMSDs occur around ϕ=-120° in both experiments. The RMSDs of the $2\Phi_{NH}$ experiment are more than twice those of the original experiment, indicating higher ϕ resolution. Some cross sections of each plot are shown, along with the RMSD curve between the experiment and the simulations. The experimental result without doubled N-H coupling is taken from ref.[8].

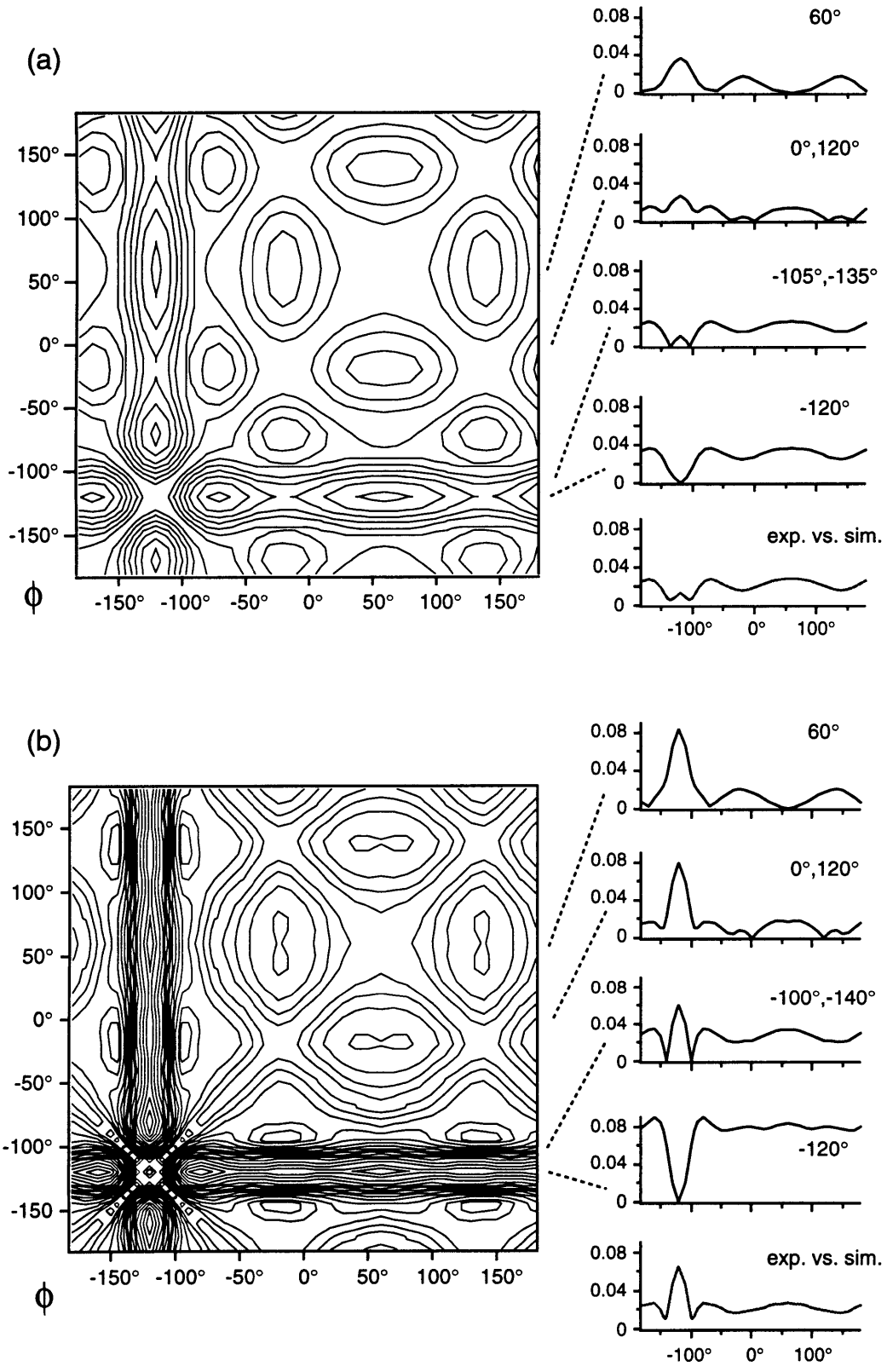
(a)
150°
100°
50°
0°
-50°
-100°
-150°
ϕ
-150° -100° -50° 0° 50° 100° 150°
0.08
0.04
0
60°
0°,120°
-105°,-135°
-120°
exp. vs. sim.
-100° 0° 100°
(b)
150°
100°
50°
0°
-50°
-100°
-150
ϕ
-150° -100° -50° 0° 50° 100° 150°
0.08
0.04
0
60°
0°,120°
-100°,-140°
-120°
exp. vs. sim.
-100° 0° 100°

Figure 6.7

The RMSD calculation can be similarly employed to obtain a more quantitative estimate of the error margin of the experimentally determined ϕ value. Namely, we can calculate the RMSDs between the experimental and the various simulated spectra and plot them in a 1D curve where the x-axis represents ϕ. The minimum of the curve thus corresponds to the best-fit torsion angle, while the breadth of the "valley" defined by the intersection of the experimental RMS noise and the curve indicates the random error of the measurement. The experimental RMS noise can in turn be estimated from the noise sidebands observed at the two edges of the spectra, where no signals are expected from the simulations. In this way, we found the normal NH/$C^{\alpha}H$ experiment to have an uncertainty of $\pm 7^{\circ}$ around -135° or -105°, while the $2\Phi_{NH}$-NH/$C^{\alpha}H$ experiment gave an uncertainty of $\pm 5^{\circ}$ around -142° or -98°. Like other methods of statistical error analysis, the systematic error of the measurement is not taken into account.

6.4 Conclusion

We demonstrated the amplification of the apparent magnitudes of X-^{1}H dipolar interactions in MAS experiments. This was achieved by moving 180° pulses during one or more rotor periods of constant proton homonuclear decoupling. The technique allows dipolar couplings to be determined at relatively high spinning speeds, which are necessary for resolving chemically inequivalent sites in high magnetic fields. Examples of "doubling" and "quadrupling" dipolar couplings are shown for the one-bond N-H coupling in *N*-acetyl-D,L-valine. We also showed a useful application of the technique to the measurement of the peptide backbone torsion angle ϕ through NH/$C^{\alpha}H$ dipolar correlation. Using separate and synchronous evolutions under the C-H and N-H dipolar interactions, we selectively amplified the N-H coupling, thus increasing the ϕ-dependence of the dipolar spectra significantly. An RMSD analysis is employed to quantitate the resolution enhancement of the N-H coupling-doubled NH/$C^{\alpha}H$ experiment compared to the original version.

6.5 Experimental

All experiments were performed on a 9.4 Tesla custom-designed spectrometer equipped with a triple-resonance transmission-line probe with a 4 mm Chemagnetics (Fort Collins, CO) MAS spinning module. The transmission-line design enables high rf powers to be attained on all three channels without arcing. Proton rf fields of about 100 kHz were used for excitation and CW decoupling. CP spin lock was achieved at lower rf fields of about 40 to 55 kHz. The ^{1}H 90° pulse lengths for MREV-8 multiple-pulse decoupling was about 3.0 μs. The semi-windowless version of MREV-8 was used and incremented either in half or in quarter cycles, depending on the required spectral width of the ω_1 dimension. ^{13}C and ^{15}N 90° pulse lengths were typically 4 μs and 6 μs, respectively. The spinning speeds were controlled to ±5 Hz by a Doty (Columbia, SC) spinning speed controller. The recycle delay was 2.5 s. A cross polarization time of 2 ms was used.

Powder ^{15}N-labeled *N*-acetyl-D,L-valine was purchased from Cambridge Isotope Laboratories (Andover, MA) and recrystallized from aqueous solution to reduce chemical shift dispersions due to conformational heterogeneity. Approximately 40 mg of sample was used in the experiments.

Simulations of the various dipolar spectra were performed in the time domain by evaluating the MAS dynamic phases over the course of the evolution period t_1. Powder averaging was carried out by Monte Carlo integration where the Euler angles that transform the molecular frame to the rotor frame are randomly generated according to a powder distribution. Input parameters for the torsion angle simulations include the effective C-H and N-H dipolar couplings, which were obtained from control ^{15}N and ^{13}C DIPSHIFT experiments[8], various Euler angles, the REDOR mixing time, the spinning speed ω_r, the spectral width, and the number of crystallites employed in the powder average. The centerband and twelve sidebands (six on either side) were included in the rmsd fits[30].

Acknowledgments for Chapter 6

This chapter is excerpted from a manuscript that appeared in J. Magn. Reson. 129: (1) 85-92 Nov. 1997. The work was done in collaboration with Mei Hong, Kristin Kumashiro and Klaus Schmidt-Rohr.

References for Chapter 6

[1] J. E. Roberts, G. S. Harbison, M. G. Munowitz, J. Herzfeld and R. G. Griffin, J. Am. Chem. Soc. 109, 4163-4169 (1987).

[2] M. Linder, A. Hoehener and R. R. Ernst, J. Chem. Phys. 73, 4959-4970 (1980).

[3] M. G. Munowitz, R. G. Griffin, G. Bodenhausen and T. H. Huang, J. Am. Chem. Soc. 103, 2529-2533 (1981).

[4] M. Hong, K. Schmidt-Rohr and A. Pines, J. Am. Chem. Soc. 117, 3310-3311 (1995).

[5] J. D. Gross, D. E. Waschawski and R. G. Griffin, J. Am. Chem. Soc. 119, 796-802 (1997).

[6] B. M. Fung, J. Afzal, T. L. Foss and M. Chau, J. Chem. Phys. 85, 4808-4814 (1986).

[7] X. Feng, Y. K. Lee, D. Sandstroem, M. Eden, H. Maisel, A. Sebald and M. H. Levitt, Chem. Phys. Lett. 257, 314-320 (1996).

[8] M. Hong, J. D. Gross and R. G. Griffin, J. Phys. Chem. B 101, 5869-5874 (1997).

[9] X. Feng, P. J. E. Verdegem, Y. K. Lee, D. Sandstrom, M. Eden, P. Bovee-Geurts, W. J. d. Grip, J. Lugtenburg, H. J. M. d. Groot and M. H. Levitt, J. Am. Chem. Soc. 119, 6853-6857 (1997).

[10] W. T. Dixon, J. Chem. Phys. 77, 1800-1809 (1982).

[11] J. Hong and G. S. Harbison, J. Magn. Reson. 105, 128-136 (1993).

[12] Z. Song, O. N. Antzutkin, X. Feng and M. H. Levitt, Solid State NMR 2, 143-146 (1993).

[13] T. Gullion and J. Schaefer, "Advances in Magn. Reson." (W. S. Warren, Ed.), pp. 57-83, Academic Press, San Diego (1989).

[14] V. Bork, T. Gullion, A. Hing and J. Schaefer, J. Magn. Reson. 88, 523-532 (1990).

[15] M. G. Munowitz and R. G. Griffin, J. Chem. Phys. 78, 613-617 (1983).

[16] D. P. Raleigh, A. C. Kolbert, T. G. Oas, M. H. Levitt and R. G. Griffin, J. Chem. Soc. Faraday Trans. 1 84, 3691-3711 (1988).

[17] E. T. Olejniczak, S. Vega and R. G. Griffin, J. Chem. Phys. 81, 4804-4817 (1984).

[18] M. M. Maricq and J. S. Waugh, J. Chem. Phys. 70, 3300-3316 (1979).

[19] A. C. Kolbert, D. P. Raleigh, M. H. Levitt and R. G. Griffin, J. Chem. Phys. 90, 679-689 (1989).

[20] A. C. Kolbert, H. J. M. d. Groot, M. H. Levitt, M. G. Munowitz, J. E. Roberts, G. S. Harbison, J. Herzfeld and R. G. Griffin,"Multinuclear Magnetic Resonance in Liquids and Solids-Chemical Applications" (P. Granger and R. K. Harris, Ed.), pp. 339-354, Kluwer Academic Publishers, Netherlands (1990).

[21] A. C. Kolbert and R. G. Griffin, J. Magn. Reson. 93, 242-255 (1991).

[22] M. E. Merritt, A. M. Christensen, K. J. Kramer, T. L. Hopkins and J. Schaefer, J. Am. Chem. Soc. 118, 11278-11282 (1996).

[23] W.-K. Rhim, D. D. Elleman and R. W. Vaughan, J. Chem. Phys. 59, 1740 (1973).

[24] A. Bielecki, A. C. Kolbert and M. H. Levitt, Chem. Phys. Lett. 155, 341-346 (1989).

[25] M. Lee and W. I. Goldberg, Phys. Rev. 140, A1261-A1271 (1965).

[26] M. Hong, A. Pines and S. Caldarelli, J. Phys. Chem. 100, 14815-14822 (1996).

[27] T. Gullion and J. Schaefer, J. Magn. Reson. 81, 196-200 (1989).

[28] P. J. Carroll, P. L. Stewart and S. J. Opella, Acta Cryst. C46, 243-246 (1990).

[29] H. W. Spiess, "NMR Basic Principles and Progress" (P. Diehl, E. Fluck and E. Kosfeld, Ed.),Springer, Berlin (1978).

[30] Including sidebands further out, where all the simulated spectra show negligible intensity, would change neither the position nor the shape of the minimum in the rmsd curve. Thus the best-fit angle and its error margin would remain unchanged. It would only add an offset to the whole rmsd curve, due to the constant deviation between the experimental noise and the nearly vanishing intensity in the simulated spectra at these outer sidebands.

7. Tilted n-fold symmetric radio frequency pulse sequences. Applications to CSA and heteronuclear dipolar recoupling in homonuclear dipolar coupled spin networks

7.1 Introduction

Solid-state NMR is an invaluable tool for the study of molecular structure and dynamics. Systems which are difficult to characterize by more conventional techniques, such as X-ray crystallography and solution NMR, provide a strong motivation for the application and further development of NMR methods that accurately measure structural features in the solid-state. Furthermore, the anisotropic interactions amongst and between nuclei in rigid solids contain a wealth of information on the bond orientations and interatomic distances. However, in powder samples, these interactions yield broad features and render the spectra of multiple resonances difficult to disentangle.

Special line narrowing techniques such as magic-angle-spinning (MAS)[1,2] and dipolar decoupling[3,4] are capable of producing high resolution spectra rivaling the quality of those obtained in solution NMR, but at the loss of information on anisotropic interactions. There are a number of procedures designed to reintroduce anisotropic interactions within the framework of MAS so that orientation dependent information may be measured with the site resolution provided by the isotropic shift. Specific methods have been designed to recouple the chemical shift anisotropy (CSA)[5-11] in addition to isolated pairs of heteronuclear and homonuclear dipolar coupled spins for quantitative measurements[12]. Ideally, complete isotopic enrichment of molecules with nuclei that are amenable to NMR would provide a route to total structure determination. Unfortunately, the existing methodology is prone to complications arising from strongly homonuclear dipolar coupled spin networks. The dynamics of the recoupled interaction of interest may be influenced or even quenched by incompletely averaged homonuclear dipolar interactions thereby precluding quantitative analysis[13].

The above problems are particularly acute when measuring heteronuclear dipolar interactions between the rare and abundant spins. It is well known that such heteronuclear couplings can be measured with reasonable accuracy if measures are taken to decouple the homonuclear dipolar couplings between abundant spins. Most experiments to date are two-dimensional in nature and employ homonuclear decoupling schemes such as MREV-8[14,15]

during the indirect dimension where rotational sideband manifolds reflect the strength of the heteronuclear dipolar interaction[16]. The use of such multiple pulse sequences is a quite general approach for measuring CH and NH dipolar couplings and has found recent use in correlating these interactions to measure torsion angles across HCCH[17] and HNCH[18] spin topologies. Unfortunately, as the ratio of spinning speed to dipolar coupling is increased, information on the dipolar interaction is lost. In addition, the efficiency of homonuclear decoupling of the abundant spins is compromised as the cycle time of the MAS approaches that of the multiple pulse sequence[19]. A method has been designed to overcome these shortcomings and has been applied in the context of torsion angle measurements[20]. The advantages of fast MAS (defined here to be when $\omega_r > \delta/3$, where δ is mutiple-pulse scaled dipolar coupling or CSA and ω_r is the MAS rate) are clear since both sensitivity and resolution are increased in the directly detected dimension of these experiments. This is due to the fact that under conditions of fast MAS, the intensity of the rotational sidebands is folded into the centerband thereby reducing overlap between sideband manifolds (for the case of multiple sites) while maximizing signal intensities.

A more subtle problem results when attempts are made to measure CSAs in uniformly enriched samples with CSA recoupling schemes developed for non-interacting spin systems. Techniques such as the 4-π pulse sequence[10] or rotary resonance recoupling[11,21-23] work well in a natural abundance environment where the dipolar couplings between neighboring spins may be neglected. The introduction of non-negligible dipolar interactions through uniform labeling poses a problem since most sequences designed to recouple the CSA also recouple both homo and heteronuclear dipolar couplings. The non-commutation between the recoupled CSA and dipolar interactions introduces dipole dependent CSA dynamics which often complicate quantitative measurements.

We introduce a radio frequency pulse sequence that simultaneously recouples the heteronuclear dipolar interaction and/or CSA of the irradiated spin while ensuring that the homonuclear dipolar couplings between the irradiated spins are effectively averaged to zero. The techniques utilize the frequency switched Lee-Goldburg (FSLG)[24-26] scheme for homonuclear

decoupling. Efficient heteronuclear/CSA recoupling is achieved by employing five-fold symmetric phase shifts[27] of the FSLG scheme over one rotor period. The methods proposed here allow measurement of the CSA and heteronuclear dipolar couplings even when the ratio of spinning speed to dipolar couplings is large. Relatively rapid MAS does not compromise the dipolar decoupling due to the short cycle time of the FSLG scheme. We refer to the methods as Tilted Cn (TCn) in analogy with previous sequences proposed by Lee, *et al* [27].

7.2 Physical Picture

The basis of the recoupling schemes presented here is given by the averaging of spin interactions that occurs when a system of spin 1/2 nuclei is exposed to a strong rf field far from resonance. In this case, the rotating frame Hamiltonian may be partitioned:

$$H = H_{Int} + H_{rf,eff} \tag{7.1}$$

with

$$H_{rf,eff} = \Delta\omega\, I_z + \exp[-iI_z\phi]\omega_1 I_x \exp[iI_z\phi] \tag{7.2}$$

where the internal part, H_{Int} , is given by the spin interactions (the conventional secular terms which commute with I_Z) , and the large external part consisting of the effective rf field, $H_{rf,eff}$ containing an offset component parallel to the longitudinal axis of the rotating frame and a rf component in the transverse plane with the phase ϕ. This partitioning of interactions affords a simple physical picture of the effect of the effective field on the spin interactions. The internal Hamiltonian is rotated about the effective rf field at a rate given by the effective field strength. If the effective field is inclined at the magic-angle with respect to the z-axis, the spin operators of H_{Int} rotate at the magic-angle(See Figure 7.1a, left). The homonuclear dipolar coupling, which is characterized as a tensor of rank two with respect to spin rotation, is then averaged to zero (with the proviso that the effective field strength is large relative to the size of the dipolar interactions). This situation of Lee-Goldburg (LG) decoupling[24] can be thought of as magic-angle spinning in "spin space". In contrast, the chemical shift interactions, tensors of rank one, are only scaled in magnitude with the new direction of the interaction along the effective field(Figure 7.1a, right).

Figure 7.1 (a)-left: Direction of the effective rf field in the rotating frame. In a tilted interaction frame defined by the effective rf field, the spin operators are time dependent and rotate about $H_{rf,eff}$, and when θ is chosen equal the magic-angle, the homonuclear dipolar coupling is averaged to zero. (a)-right: Rank one interactions are averaged with new direction along the effective field. (b)-left: MAS modulation of the projection of the residual rank one interaction into the transverse plane. Times t_0, t_1, and t_2 and corresponding vectors correspond to different points in MAS cycle. Dashed arrows correspond to the decomposition of the MAS modulation into counter-rotating components.(b)-right: Result of shifting the azimuthal angle, ϕ, of the basic FSLG cycle in steps of $2\pi/5$ over one rotor period. Change in direction of rf field is coincident with MAS modulation of counter-rotating components and a recoupling is observed.(c) Direction of average Hamiltonian for the complete TCn cycle. The coefficients C and S correspond to $\cos(\theta)$ and $\sin(\theta)$ respectively. The most efficient recoupling occurs when the effective field is completely transverse (when the isotropic parameters are set to zero or negligible in size relative to the recoupled interactions of interest).

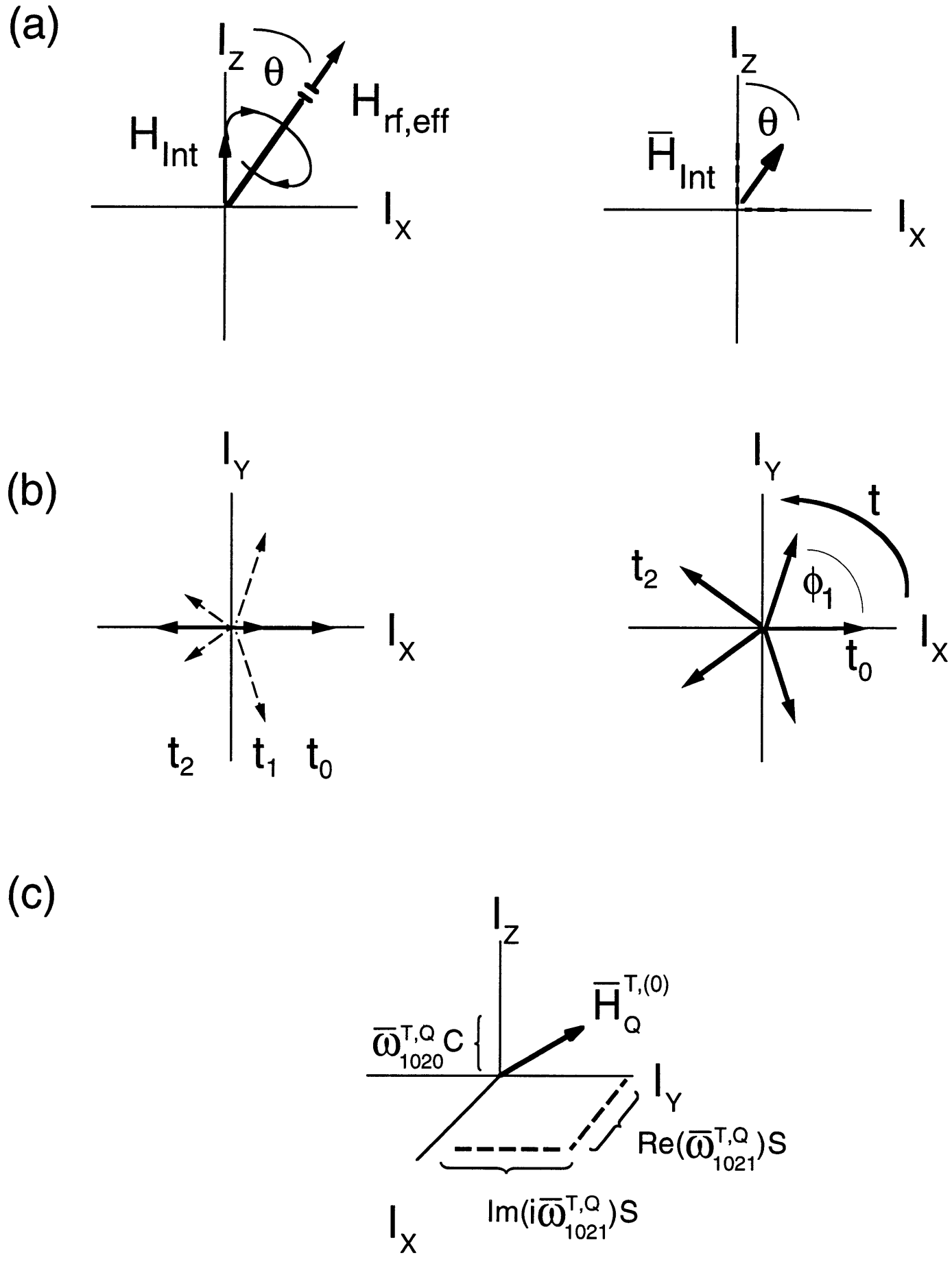
(a)
I_z
θ
$H_{rf,eff}$
H_{Int}
I_x
I_z
θ
$\bar{H}_{Int}$
I_x
(b)
I_Y
I_x
t_2
t_1
t_0
I_Y
t
t_2
ϕ_1
t_0
I_x
(c)
I_z
$\bar{H}_Q^{T,(0)}$
$\bar{\omega}_{1020}^{T,Q}C$
I_Y
$Re(\bar{\omega}_{1021}^{T,Q})S$
$Im(i\bar{\omega}_{1021}^{T,Q})S$
I_x

Figure 7.1

The introduction of magic-angle *sample* spinning does not complicate the above picture provided that the time scales of sample rotation and spin rotation are drastically different. Typically, the size of the effective field may be arranged to be at least an order of magnitude greater than the sample spinning speed so that averaging may be considered separately. Although the spin-part of the chemical shift and heteronuclear dipolar coupling transforms as a tensor of rank one, the spatial part of these interactions transforms as a second rank tensor with respect to sample rotation, and the magnitude of the residual chemical shift (and heteronuclear dipolar coupling) are modulated upon the introduction of MAS. It is illustrative to decompose the residual interaction, depicted in Figure 7.1a, into longitudinal and transverse components. The MAS modulation of the residual transverse spin component is depicted in left panel of Figure 7.1b. During the course of a rotor period the size of the component (symbolized by a bold arrow) is sinusoidally modulcated. (The MAS modulation of the longitudinal component follows a similar trajectory.) The decomposition of the x-component into counter-rotating components (symbolized by dashed arrows) is also depicted. Over one rotor period, the anisotropic interactions are completely averaged leaving behind the unmodulated isotropic components along the x and z-axis of the rotating frame. Improved averaging through sample and spin rotation has been the basis for several techniques aimed at obtaining high-resolution isotropic chemical shift correlation[28] or optimized coherence transfer schemes in which the deleterious effects of homonuclear dipolar couplings are eliminated[29-31].

However, it is also possible to reintroduce anisotropic interactions of interest while decoupling the homonuclear dipolar interaction by imposing a second modulation onto the LG (or FSLG) decoupling scheme. For example, the TCn sequences presented here employ n consecutive $2\pi/n$ phase shifts of the FSLG cycles within one rotor period. In this case, shifts in the radio frequency phase are manifested as phase shifts of the residual rank 1 spin tensors (chemical shift and heteronuclear dipolar coupling terms). The radio frequency phase shift corresponds to a change in the azimuthal angle orienting the transverse component of the residual spin tensor with respect to the rotating frame (See Figure 7.1b, right). In this way, the modulation imposed by

phase shifting the FSLG cycles interferes with the MAS modulation of residual anisotropic interactions and a "recoupling" is observed. Since the rf phase shifts do not modulate the longitudinal spin component, the anisotropic interactions along the z-axis are averaged by MAS. Similarly, the isotropic terms corresponding to the transverse component are averaged by rf phase shifts since they are not modulated by MAS. Therefore, the recoupled Hamiltonian neatly contains information on isotropic interactions along the z-axis and anisotropic interactions in the transverse plane.

7.3 Theory

The general scheme for TCn is outlined in Figure 7.2a. Figures 7.2b-e illustrate three possible implementations for measuring heteronuclear dipolar (IS) couplings and a single implementation of TCn for CSA recoupling in homonuclear dipolar coupled spin networks. For heteronuclear dipolar recoupling the TCn sequence is applied to the abundant I spin, typically ^{1}H, and S spin transverse magnetization is allowed to evolve under the recoupled IS interaction as described below. These experiments may be performed in a one or two dimensional fashion depending on the number of sites to resolve and whether or not refocusing of the S spin CSA is required. The constant-time implementation refocuses the S spin chemical shift and is particularly useful when probing multiple sites over a broad spectral range. The rare spin TCn CSA recoupling sequence is depicted in Figure 7.2e and is strictly two dimensional in nature. The $\pi/2$ pulse after cross-polarization generates longitudinal magnetization which evolves under the recoupled CSA prior to the $\pi/2$ pulse required to monitor evolution.

Figure 7.2 General scheme for TCp subcycle (a) and pulse sequences for TCn recoupling. (b) One dimensional sequence for measuring heteronuclear interactions. (c) Two dimensional implementations, without isotropic chemical shift refocusing and (d) with constant time implementation. (e) Two dimensional implementation for CSA recoupling. Thin and thick black rectangles correspond to $\pi/2$ and π pulses respectively.

(a)

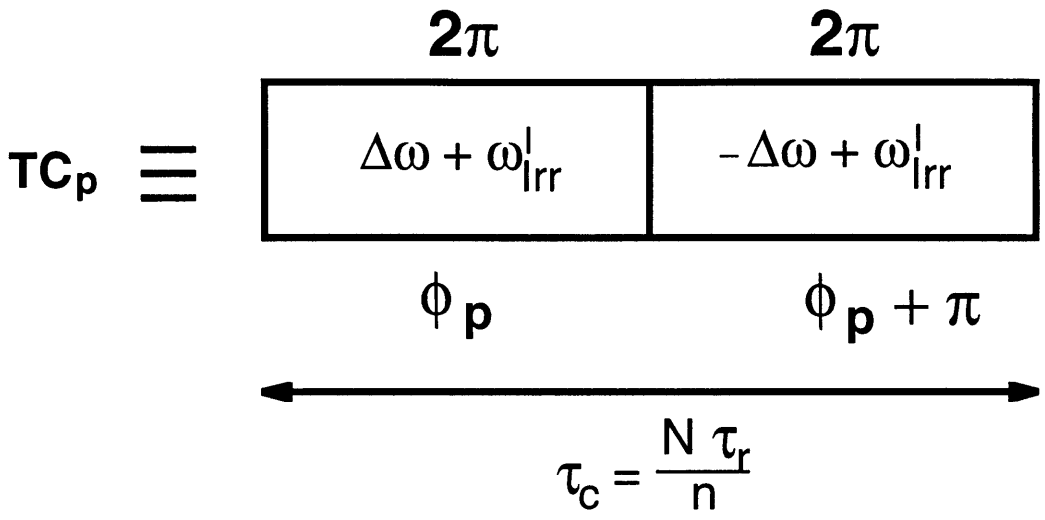
2π
2π
TC_p ≡
Δω + ω|rr
-Δω + ω|rr
ϕ p
ϕ p + π
τc = N τr / n

(b)

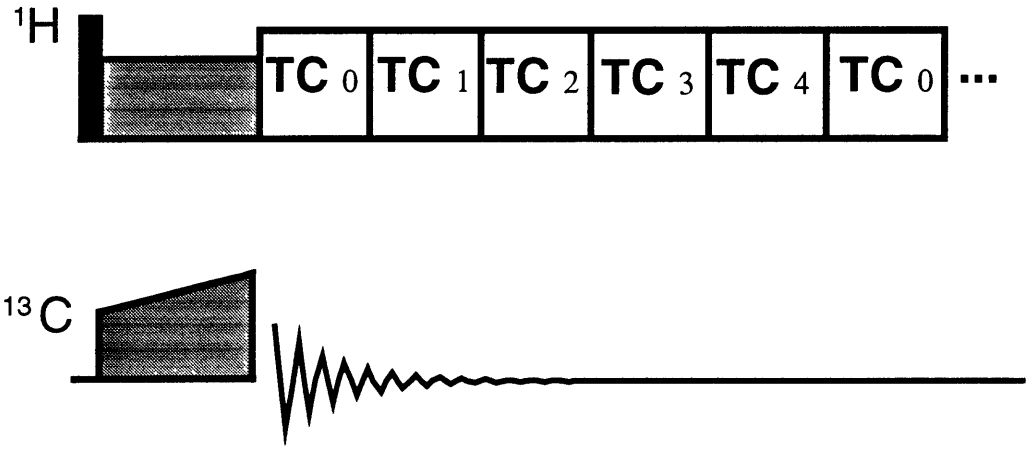
1H
TC 0
TC 1
TC 2
TC 3
TC 4
TC 0
...
13C

Figure 7.2

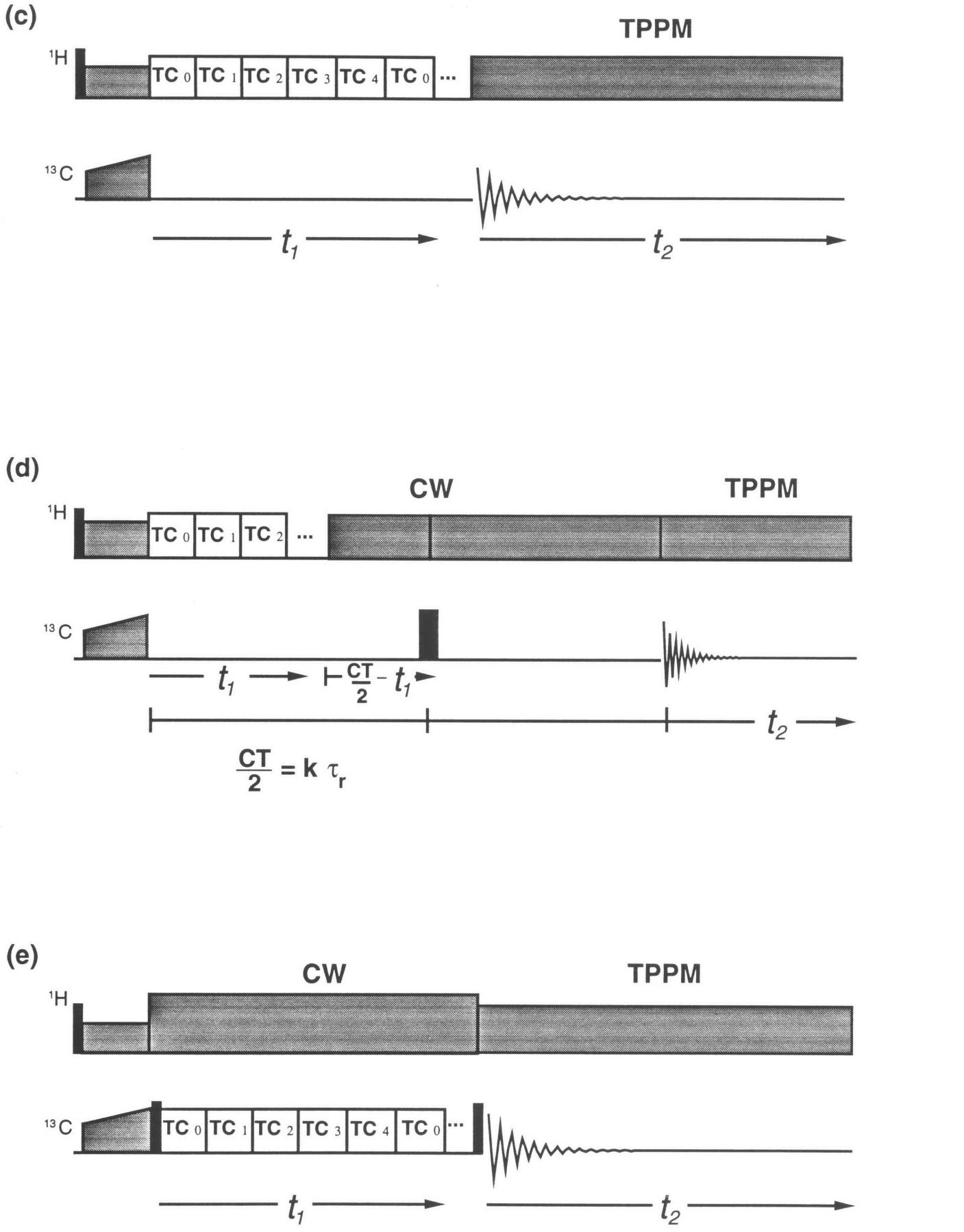
(c)
TPPM
^{1}H
TC 0
TC 1
TC 2
TC 3
TC 4
TC 0
...
^{13}C
t_1
t_2
(d)
CW
TPPM
^{1}H
TC 0
TC 1
TC 2
...
^{13}C
t_1
$\frac{CT}{2} - t_1$
t_2
$\frac{CT}{2} = k\,\tau_r$
(e)
CW
TPPM
^{1}H
^{13}C
TC 0
TC 1
TC 2
TC 3
TC 4
TC 0
...
t_1
t_2

Figure 7.2

In the following treatment only the irradiated spins are considered: the Hamiltonian consists of the chemical shifts, the homonuclear dipolar couplings, and the rf field terms. The results obtained for the recoupled chemical shift will then be extended to cover heteronuclear dipolar interactions. Following the notation in Lee *et al.*[27], the pulse sequences presented here contain n subcycles TCp with p = 0,...,n-1 timed so as to be contained in N rotor periods. The length of each cycle τ_c is $N\tau_r$ /n , the time required for two 2π rotations about the effective rf field, $\omega_e^I = \sqrt{\Delta\omega^2 + \omega_1^2}$, with $\Delta\omega$ as a resonance offset, ω_1 the nutation frequency, and ω_{Irr}^I left as an adjustable parameter where $\omega_{Irr}^I << \Delta\omega$, ω_1 (See Figure 2a). Given the above, the TCn sequences must satisfy the condition $\omega_e^I = 2\,n\,\omega_r / N$. If the TCn sequence is initiated at time t^0 , the pth rf cycle TCp runs between time points t_p^0 and t_{p+1}^0 with $t_p^0 = t^0 + p\,\tau_C$. The relevant Hamiltonian for the pth subcycle, obtained by subsequent transformations where the Hamiltonian is rotated about the y axis of the rotating frame through the angle $\theta = \tan^{-1}\frac{\omega_1}{\Delta\omega}$ followed by transformation to an interaction frame defined by the effective rf field, is:

$$H^T(t) = \sum_Q \sum_{\lambda\mu lm} \sum_{\mu'} \omega_{\lambda\mu lm}^{T,Q}(t - t_p^0)\, d_{\mu',\mu}^{(\lambda)}(\theta) \qquad (7.3)$$

$$\times \exp[\, i\, 2\pi(Nm - \mu')p/n]\, V_{\lambda\mu'}^{T,Q}$$

where

$$V_{\lambda\mu'}^{T,Q} = \exp[il_Y\theta]\, V_{\lambda\mu'}^{Q} \exp[-il_Y\theta] \qquad (7.4)$$

and

$$\omega^{T,Q}_{\lambda\mu lm}(\tau) = \omega^{Q}_{lm}\, d^{(\lambda)}_{\mu 0}(-\theta)\, \exp[i\,(-1)^{S}\mu\omega^{l}_{e}\tau\,] \qquad (7.5)$$

$$\times \exp[im\omega_{r}(\tau + t^{0})]$$

with $d^{(\lambda)}_{\mu\,\mu'}$ as a reduced Wigner function. The exponent S in (5) is zero for the first half of the subcycle and unity for the second half, accounting for the inversion of the effective field which occurs every half subcycle. In equation (7.3), Q references the type of interaction (Q=i for chemical shift and ij for the dipolar interaction) λ characterizes the rank of the interaction with respect to spin rotations, μ' is the spin rotational component ranging from $\mu'=-\lambda \ldots \lambda$, l is the rank of the interaction with respect to sample rotation and m is the spatial rotational component ranging from m=l...-l [27]. The definitions for the irreducible tensor operators of rank one are given by:

$$V^{j}_{10} = I_{jZ} \qquad (7.6)$$

and

$$V^{j}_{1\pm1} = \mp 2^{-1/2} I^{\pm}_{j} \qquad (7.7)$$

while for rank two tensors:

$$V^{jk}_{20} = 6^{-1/2}(3I_{jZ}I_{kZ} - I_{j}\cdot I_{k}) \,, \qquad (7.8)$$

$$V^{jk}_{2\pm1} = \mp 2^{-1}(I^{\pm}_{j}I_{kZ} + I_{jZ}I^{\pm}_{k}) \,, \qquad (7.9)$$

and

$$V^{jk}_{2\pm2} = 2^{-1}\, I^{\pm}_{j}I^{\pm}_{k} \qquad (7.10)$$

with the relevant spatial components defined for the anisotropic chemical shift (assuming axial symmetry for convenience),

$$\omega_{2m}^{j} = \omega_0 \delta_1^j d_{0m}^{(2)}(\beta_{PR}^{j}) d_{m0}^{(2)}(\beta_{RL}) \exp(i\, m\, \gamma_{PR}^{j}) \qquad (7.11)$$

and dipolar coupling

$$\omega_{2m}^{jk} = 6^{1/2} b_{jk} d_{0m}^{(2)}(\beta_{PR}^{jk}) d_{m0}^{(2)}(\beta_{RL}) \exp(i\, m\, \gamma_{PR}^{jk}) \qquad (7.12)$$

where $\delta_1^j\ \omega_0$ is the chemical shift anisotropy of spin j and $b_{jk} = -\left(\frac{\mu_0}{4\pi}\right)\frac{\gamma_j \gamma_k \hbar}{r_{jk}^3}$ is the dipolar coupling constant between spins j and k. The Euler angles β_{PR} and γ_{PR} correspond to the polar and azimuthal angles of the chemical shift or dipolar coupling tensor in the rotor frame while β_{RL} is the inclination of the rotor with respect to the z axis of the laboratory frame.

The dynamics of the irradiated spins are calculated using coherent averaging theory[19]. Using the first level of approximation, the zeroth-order average Hamiltonian is calculated first over the pth subcycle to be:

$$\bar{H}_p^{T\,(0)} = \sum_{Q} \sum_{\lambda\mu m} \sum_{\mu'} \varpi_{\lambda\mu m}^{T,Q} d_{\mu',\mu}^{(\lambda)}(\theta)\ \exp[i2\pi(Nm - \mu')p/n]\ V_{\lambda\mu'}^{T,Q} \qquad (7.13)$$

with the amplitude:

$$\varpi_{\lambda\mu m}^{T,Q} = \tau_c^{-1} \int_0^{\tau c} \omega_{\lambda\mu m}^{T,Q}(\tau)\, d\tau \quad . \qquad (7.14)$$

Equation (7.13) illustrates the response of the spatial and spin rotational components to the phase shifts of the rotor and rf between successive subcycles of the pulse sequence. For the TCn sequences a relationship linking the symmetry numbers of the tilted pulse sequence (N,n) with the rotational components (μ',m) may be derived by calculating the zeroth-order average Hamiltonian over the total cycle through:

$$\bar{H}^{T\,(0)} = n^{-1} \sum_{p=1}^{n-1} \bar{H}_p^{T\,(0)} =$$

$$\sum_{Q} \sum_{\lambda\mu lm} \sum_{\mu'} \varpi_{\lambda\mu lm}^{T,Q} d_{\mu',\mu}^{(\lambda)} (\theta)\, V_{\lambda\mu'}^{T,Q}\; E[(Nm - \mu')/n] \qquad (7.15)$$

where the function E(x) is unity if x is an integer or zero otherwise. The function E(x) in equation (7.15) results from the fact that interactions which survive the average over a subcycle are further modulated by the index, (Nm-μ')/n through equation (7.13). If the index is equal to an integer, a stationary term results, the corresponding interaction survives the final average, and a recoupling is observed.

If $\omega_e^l >> \omega_r$, $\left| d_{\mu 0}^{(\lambda)}(-\theta)\, \omega_{lm}^Q \right|$:

$$\varpi_{\lambda\mu lm}^{T,Q} = \delta_{\mu 0}\, \tau_c^{-1} \int_0^{\tau c} \omega_{\lambda\mu lm}^{T,Q}(\tau)\, d\tau \quad , \qquad (7.16)$$

and in this case, equation (7.13) takes the form:

$$\bar{H}^{T\,(0)} = \sum_{Q} \sum_{\lambda\mu' lm} \varpi_{\lambda 0 lm}^{T,Q} d_{\mu',0}^{(\lambda)} (\theta)\, V_{\lambda\mu'}^{T,Q}\; E[(Nm - \mu')/n] \quad .(7.17)$$

In this limit, if θ is chosen to be the magic-angle, $\varpi_{\lambda 0 lm}^{T,Q} = 0$ for λ = 2, and the homonuclear dipolar interactions are eliminated to zeroth-order over the individual subcycles. This result is expected as each subcycle represents the FSLG sequence applied with a different azimuthal angle, ϕ, of the effective field. The rotational symmetry of the Hamiltonian requires that the FSLG decoupling be invariant to ϕ as is demonstrated here. Equally important is the fact that the amplitude (7.14) corresponding to the chemical shift and heteronuclear dipolar interactions (both λ

= 1) is not drastically reduced for θ = 54.74°. In contrast if θ = 90° the homonuclear dipolar interactions(λ = 2) are scaled by -1/2 while the shifts and heteronuclear interactions are reduced to near zero over a subcycle as in the seven-fold symmetric sequence (C7)[27].

In the C7 sequence the symmetry numbers of the pulse sequence (N,n) are chosen such that N=2 and n=7 so that the residual chemical shift anisotropy is averaged over the total cycle while only the components (μ',m)=2,1 and -2,-1 are selected for efficient double quantum recoupling. In general, the average Hamiltonian may be engineered so that the recoupled interaction contains a reduced orientational dependence if the symmetry numbers, N and n, are chosen such that only terms for which (μ',m) and (-μ',-m) survive the total average through equation (7.15). When the homonuclear dipolar interactions are effectively decoupled the remaining $\mu' = \pm 1$ terms correspond to the CSA and heteronuclear dipolar coupling. The scaling of the recoupled interactions is minimized by choosing the m=1 component. Accordingly, for N=1 rotor period, the (μ',m) = (1,1) and (-1,-1) components are selected if n > 3 (See Table 7.1).

Table 7.1: Symmetry Table for $\mu' = \pm 1$ and N=1 rotor period.

m	$\mu' = \pm 1$	Nm - μ'
2	+	1
	-	3
1	+	0
	-	2
0	+	-1
	-	1
-1	+	-2
	-	0
-2	+	-3
	-	-1

(For N=2 rotor periods, (μ',m)=1,1 and -1,-1 are selected only if n=5.) The final result, expressed in the rotating frame, for N=1,n=5, including both the chemical shift and heteronuclear dipolar coupling is:

$$\bar{H}^{T\,(0)} = [\varpi^{T,I}_{1020} \cos\theta\, I_z + \varpi^{T,I}_{1021} \frac{\sin\theta}{2} I^+ + \varpi^{T,I}_{102-1} \frac{\sin\theta}{2} I^- \,] \quad (7.18)$$

$$+ 2\,[\varpi^{T,IS}_{1020} \cos\theta\, I_z + \varpi^{T,IS}_{1021} \frac{\sin\theta}{2} I^+ + \varpi^{T,IS}_{102-1} \frac{\sin\theta}{2} I^- \,] S_z \quad .$$

The isotropic terms are $\varpi^{T,IS}_{1020} = \pi J_{IS} \cos\theta$, the scaled heteronuclear J coupling, and $\varpi^{T,I}_{1020} = 2\pi\delta^I_0 \cos\theta$, the average offset from resonance (mean offset), where δ^I_0 is defined as the sum of the mean frequency of irradiation, $\varpi^I_{irr}/2\pi$, and the offset of the rf carrier from the I spin resonance (δ^I_0) in the absence of irradiation. The recoupled anisotropic interactions are written:

$$\varpi^{T,Q}_{1021} = \varpi^{T,Q^*}_{102-1} = \qquad (7.19)$$

$$- C^Q \frac{15}{16\pi} \cos\theta \sin 2\beta_{PR} \sin 2\beta_{RL} \{\exp[-i\pi/10] + i\} \exp[i(\omega_r t^0 + \gamma^Q_{PR})\,]$$

with the definitions $C^{IS} = b_{IS}$ and $C^I = \delta^I_i\, \omega_0$. The direction of average Hamiltonian (7.18), defined by the relationship between spin components in the rotating frame, is determined by the isotropic parameters in addition to the angle γ_{PR} (See Figure 7.1c). In general the direction of the effective fields corresponding to the chemical shift and dipolar coupling terms in (7.18) will not be parallel resulting in non-commuting spin interactions. In this case the dynamics would depend on the isotropic parameters in addition to the size and relative orientation of the CSA and dipolar coupling tensors. However, the mean offset may be set to zero and, neglecting the scalar coupling , the outstanding issue is the relative alignment between the principle axis systems of the chemical shift and dipolar tensors since the remaining terms in equation (7.18) do not commute with each

other for different phase angles γ_{PR}. In the case of CSA recoupling, any heteronuclear dipolar couplings that are simultaneously reintroduced may be decoupled. For the case of ^{13}C-^{1}H recoupling where ^{1}H is irradiated, it is safely assumed that the CSA does not effect the dynamics since the magnitude of the ^{13}C-^{1}H dipolar interaction is typically an order of magnitude larger. Thus for the most interesting cases it is possible to arrange matters so that the CSA and dipolar recoupling may be performed independently. For $\theta = \beta_{RL} = \tan^{-1}\sqrt{2}$,

the magnitude of the recoupled interaction is written:

$$\left|\bar{H}_Q^{T(0)}\right| = C^Q \frac{5\sqrt{2}}{24\pi}\sqrt{5-\sqrt{5}}\sin 2\beta_{PR} \qquad (7.20)$$

with Q =I or IS assuming the isotropic parameters, $\varpi_{1020}^{T,Q}$, are zero. The anisotropic interactions are scaled by 0.15 from their static value and the magnitude of the recoupled interaction is independent of γ_{PR}.

7.4 Experimental and Numerical Procedures

All experiments were performed on a 9.4T magnet equipped with a custom built spectrometer console and HCN triple resonance transmission line probe. The spinning rates were either 8 or 10 kHz (controlled to within 2 Hz) and in all cases ramped cross polarization[32] was employed to increase sensitivity and to ensure reproducibility of signal enhancements over long time scales. For the TC5 sequence presented here, the tilt angle was 54.74°. Accordingly, the offset and nutation frequency were chosen to satisfy, $\theta = \tan^{-1}\frac{\omega_1}{\Delta\omega}$, and produce an effective field that is 10 times the spinning speed. The mean frequency of irradiation was varied empirically by adjusting the parameter $\omega_{irr}^{I} / 2\pi$ in steps of 1 kHz, in order to optimize recoupling efficiency (See Discussion below.) The TPPM decoupling scheme was employed during acquisition[4] (where applicable) with rf field strengths of 80 kHz, ϕ = 10 or 15 °, and τ_p = 5.8 μs. CW decoupling was utilized during the t_1 period of the TC5 CSA recoupling sequences with a field strength of 125 kHz to avoid signal losses due to interference between CW decoupling and TC5 mixing. For the 2D experiments, 64 t_1 points where collected by incrementing the evolution period in units one subcycle. The resulting data were zero-filled to 512 points prior to real 2D Fourier transformation. In all cases 10 Hz and 100 Hz of line broadening were added to the direct and indirect dimensions respectively. The nutation frequency employed was measured from a 2π pulse length.

Numerical lineshape simulations were performed using a program written in C that computes the spin dynamics of an IX_2 system of spin 1/2 nuclei exposed to MAS and an arbitrary

rotor synchronized pulse cycle. Numerical integration of the equations of motion[33] are achieved through standard methods and powder averaging was performed using the method of Cheng and Suzukawa[34]. For each crystal orientation, the propagator was calculated over one rotor period. The cyclic nature of the rf pulse sequence and the periodicity of MAS allow the time development of the initial condition to be evaluated by successive application of the propagator. Time domain data corresponding to each crystal orientation were weighted and coadded prior to real Fourier transformation for numerical lineshape analysis.

7.5 Results and Discussion

Results demonstrating the effectiveness of the TC5 recoupling sequence on $^{13}C_{\alpha}$ labeled alanine (obtained from Cambridge Isotope Labs, Woburn MA) are depicted in Figure 7.3.

Figure 7.3 Experimental results for TC5 CH recoupling (N=1) for ^{13}C enriched C_α alanine obtained with sequence depicted in Figure 7.2c. Top trace: FSLG control experiment, obtained with ϕ_p as a constant phase 0. Bottom trace: obtained with $2\pi/5$ phase shifts of basic FSLG subcycle (b). Experimental conditions: $\omega_r / 2\pi$ = 10.0 kHz, δ_0^I < |1| kHz , $\omega_1 / 2\pi$ = 81.65 kHz, $\Delta\omega / 2\pi$ = 57.73 kHz, $\varpi_{Irr}^I / 2\pi$ = 5.0 kHz, B_0 = 9.4 T.

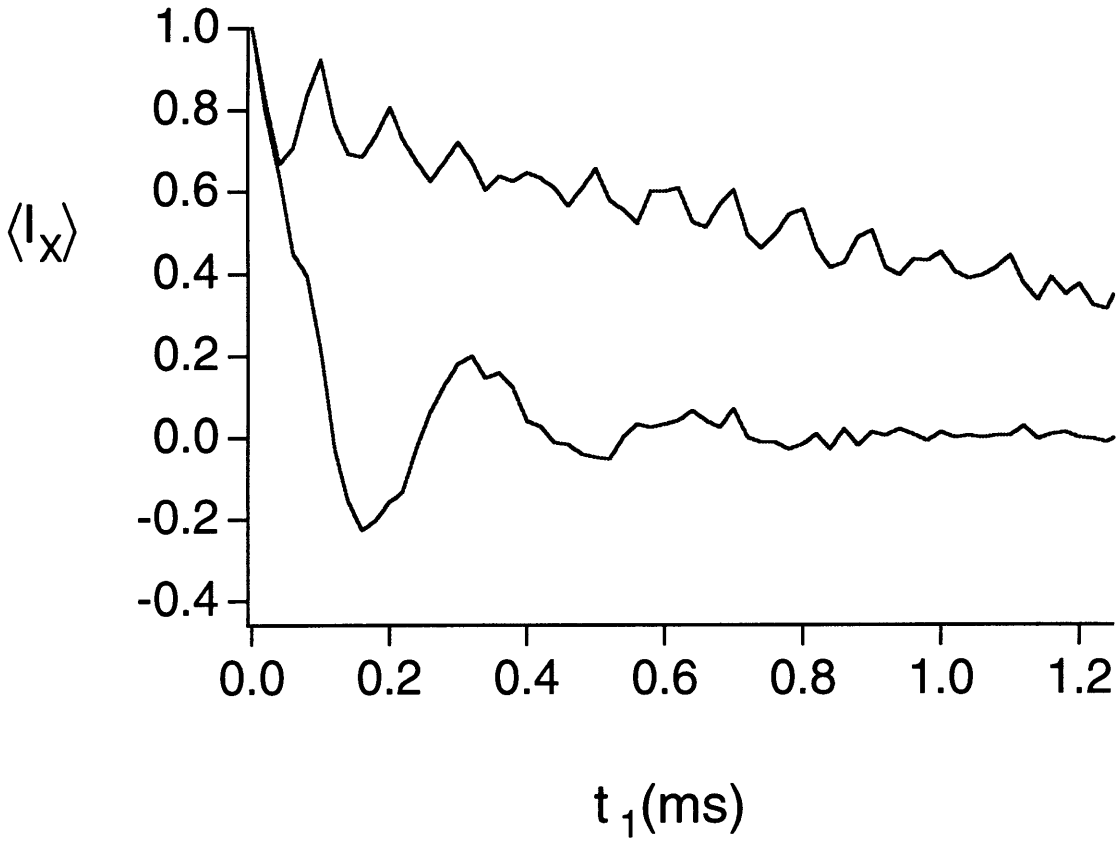

Figure 7.3

These data were acquired with the application of the sequence depicted in Figure 7.2c. The top curve was acquired with FSLG irradiation and serves as a control since minimal decay should be observed in the limit of efficient homonuclear decoupling. As expected, small amplitude rotational echoes are observed since the spinning speed is very near the FSLG scaled dipolar coupling. Upon introduction of the $2\pi/5$ phase shifts between subsequent FSLG subcycles, strong oscillations occur due to the recoupled ^{13}C-^{1}H interaction as depicted in the bottom trace. A real Fourier transformation of the data illustrates the contrast in information content between the low amplitude rotational sidebands produced by free evolution under fast MAS and recoupled powder lineshape obtained upon application of TC5 (See Figure 7.4a,b). The full-width-at-half-height (FWHH) of the spectrum displayed in Figure 7.4a is on the order of several hundred Hz (see below) and places a lower limit on the effectiveness of FSLG decoupling of the ^{1}H-^{1}H dipolar interactions in alanine. Furthermore, numerical lineshape simulations of FSLG decoupling under the conditions presented here indicate that a FWHH well under 1 ppm is obtainable with ^{1}H-^{1}H dipolar couplings as large as 10 kHz (Data not shown). These observations confirm the efficiency of FSLG decoupling when the effective field is ten times the spinning speed and sufficiently larger than the ^{1}H homonuclear dipolar couplings , validating the approximation inherent in equations (7.16-7.17).

Figure 7.4 Comparison of experimental data from Figure 7.3 with numerical lineshape simulations. (a) Real Fourier transform of FSLG control experiment. (b) Real Fourier transform of experimental data from TC5 on ^{13}C enriched Cα alanine and (c) numerical lineshape simulations with (solid line) and without (dashed line) mean offset. Simulation parameters on three spin system CH_a with remote proton H_b: $\omega_r / 2\pi$ = 10.0 kHz, $\delta^I_{0,a}$ = 0 or 1 kHz, $\delta^I_{0,b}$ = 2 kHz , $\varpi^I_{Irr} / 2\pi$ = 0 , $\omega_1 / 2\pi$ = 81.65 kHz, $\Delta\omega / 2\pi$ = 57.73 kHz, b_{ISa} = 20.3 kHz,b_{ISb} = 3 kHz , $\delta^I_{1,a}$ = $\delta^I_{1,b}$ 2.25 ppm with Euler angles $\{ \alpha_{PC}, \beta_{PC}, \gamma_{PC} \}$: {0,109.5,0},{0,60,0),{0,109.5,0},{0,60,0} respectively and B_0 = 9.4 T.

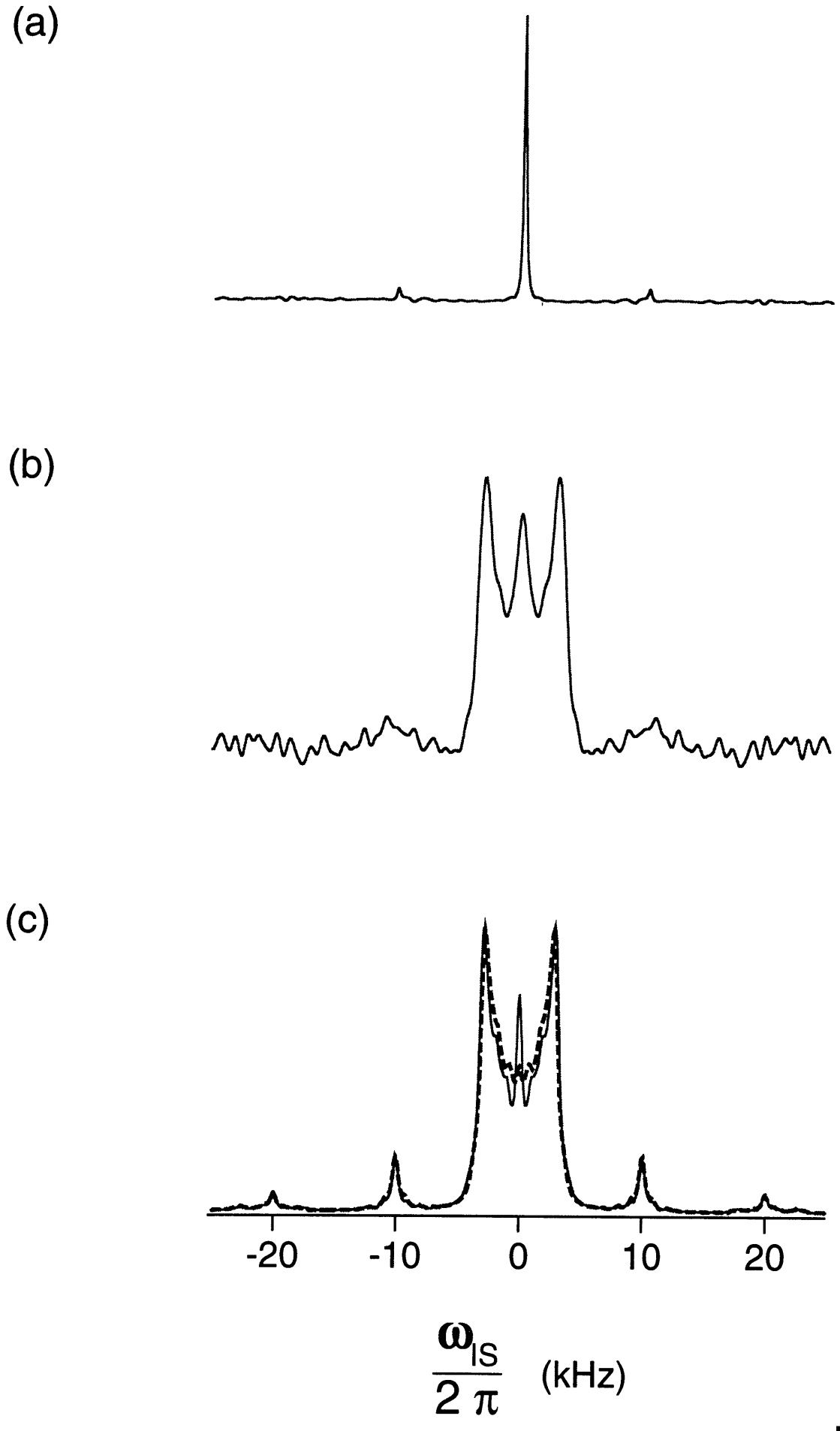

Figure 7.4

Fits of the experimental lineshapes with numerical lineshape simulations are presented in Figure 7.4. The dashed line in Figure 7.4c is a simulation for a model three spin system consisting of a ^{13}C-$^{1}H_a$ group dipolar coupled to a remote proton $^{1}H_b$. There is good agreement between the splitting observed in the experimental data with that given by the idealized simulations. The solid line in Figure 7.4c was taken using the same simulation parameters as the dashed line but with the inclusion of a 1 kHz mean offset. The central peak results from inefficient recoupling of crystallites oriented so as to have weak dipolar couplings where the dynamics are quenched by a finite mean offset. The orthogonality between spin components corresponding to the mean offset and the anisotropic interactions in the effective Hamiltonian (7.18) indicates that the dynamics are dependent on the mean offset and may be quenched entirely in the limit where the scaled mean offset is large relative to the size of the recoupled anisotropic interactions.

Experimentally, the central peak remains even if measures are taken to ensure that the mean offset is zero. Empirical optimization of the recoupling efficiency is achieved by minimizing the central peak through adjustment of the mean frequency of irradiation, ϖ^I_{irr}. Although the resonance offset, δ^I_0, of H_α in alanine was within 1 kHz , optimal recoupling was observed when the frequency switching took place between 62.73 and -52.73 kHz which represents a shift of +5 kHz from the nominal values of ±57.73 (± 1) kHz for $\Delta\omega$. Numerical simulations indicate that a misadjustment of the nutation frequency from its nominal value results in such a central peak.(Data not shown.) Others have observed that displacements of the mean frequency in FSLG decoupling improve the decoupling performance suggesting a second averaging of pulse errors[25,26]. It may be that a slight departure of the mean frequency from the nominal value is necessary to compensate for rf inhomogeneity or phase transients which would be deleterious for both ^{13}C-^{1}H recoupling and ^{1}H-^{1}H decoupling.

The chemical shift anisotropy may be recoupled and measured accurately in the presence of homonuclear dipolar coupled spins using the sequence in Fig 7.2e. Samples of natural abundance and fully ^{13}C, ^{15}N labeled glycine (obtained from CIL) were recrystallized prior to NMR

experiments. Experimental results using the TC5 sequence of Figure 7.2d with a MAS rate of 8 kHz are depicted in Figure 7.5 for the carbonyl group of glycine.

Figure 7.5 Comparison of experimental data corresponding to the carboxylate region for (a) natural abundance glycine and (b) U-^{13}C, ^{15}N glycine under TC5 (N=1) CSA recoupling sequence depicted in Figure 7.2e with numerical lineshape simulations (c). Experimental conditions $\omega_r / 2\pi$ = 8.0 kHz, δ_0^I = 0.5 kHz , $\omega_1 / 2\pi$ = 65.32 kHz, $\Delta\omega / 2\pi$ = 46.18 kHz, $\varpi_{Irr}^I / 2\pi$ = 1.0 kHz and B_0 = 9.4 T. Numerical lineshape simulations performed with (solid line) and without (dashed line) mean offset. Simulation parameters: $\omega_r / 2\pi$ = 8.0 kHz, δ_0^I = 0 or 0.5 kHz , $\omega_1 / 2\pi$ = 65.32 kHz, $\Delta\omega / 2\pi$ = 46.18 kHz, $\varpi_{Irr}^I / 2\pi$ = 0 kHz, δ_1^I = 73 ppm, η^I = 0.93, and B_0 = 9.4 T.

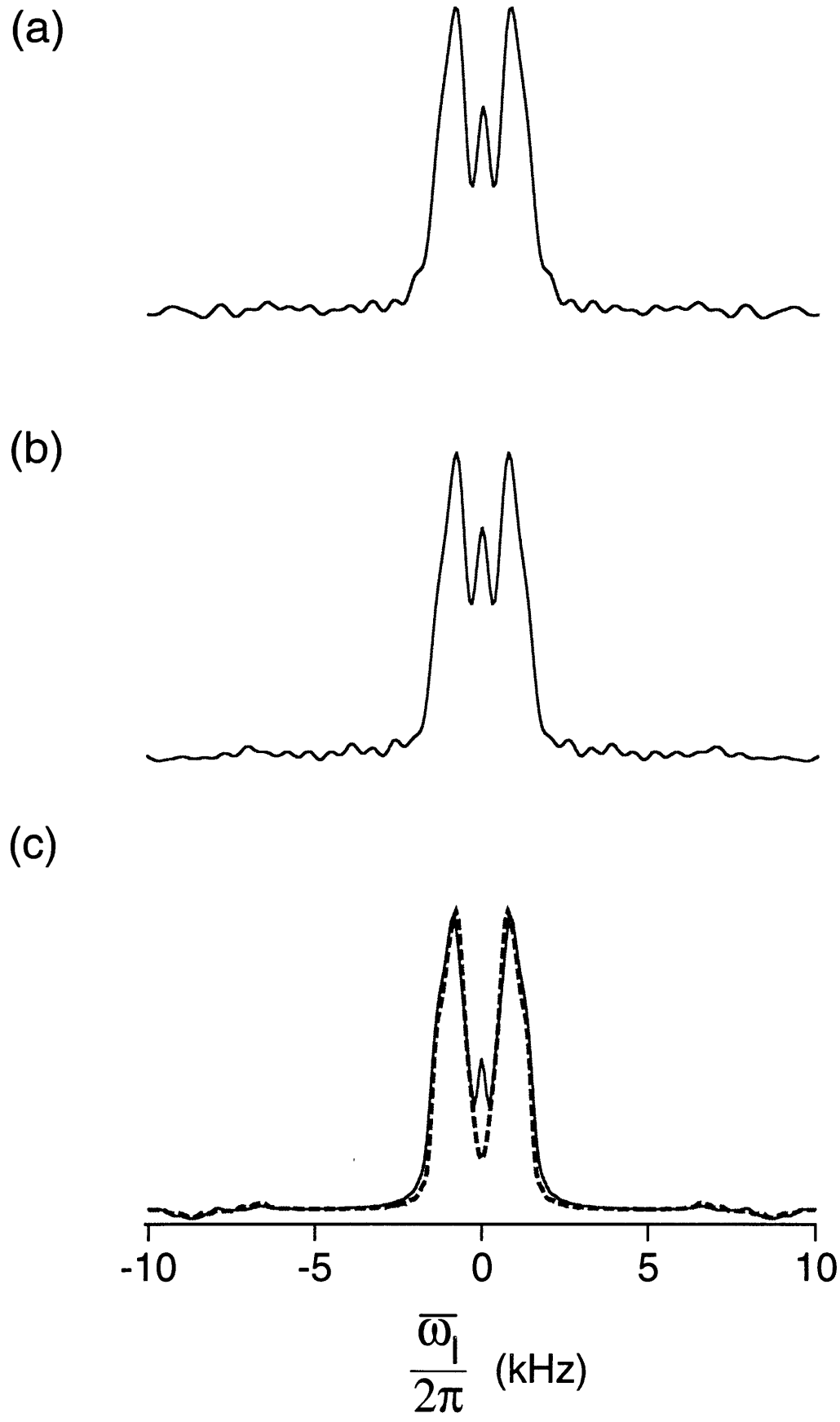

Figure 7.5

Clearly there is good agreement between the recoupled powder lineshape corresponding to natural abundance glycine in Fig. 7.5a with fully labeled glycine in Fig 7.5b. Numerical lineshape simulations using an anisotropy of 73.0 ppm and $\eta = 0.93$[35] show excellent agreement with the experimental data. Again, the experimental recoupling efficiency was optimized empirically by varying the mean frequency of the TC5 irradiation so as to minimize the central peak intensity. The mean frequency employed was approximately 1.0 kHz greater than the nominal value. Although an axially symmetric CSA was assumed during the theoretical treatment for sake of brevity (See eq. 7.11), the lineshapes obtained through the TC5 experiment are sensitive to both the magnitude of the anisotropy and the asymmetry parameter as depicted in Figure 7.6a-f. Unfortunately, the experiment is insensitive to the sign of the anisotropy due the intrinsic symmetry of the recoupled powder lineshapes.

Figure 7.6 Numerical lineshape simulations of TC5 (N=1) CSA recoupling depicting dependence of recoupled powder lineshape on asymmetry parameter, η^I. Simulation parameters: $\omega_r / 2\pi$ =12.5 kHz, δ_0^I = 0 kHz , $\omega_1 / 2\pi$ =102.1 kHz, $\Delta\omega / 2\pi$ = 72.2 kHz, $\varpi_{1rr}^I / 2\pi$ = 0 kHz, δ_1^I = 73 ppm, and B_0 = 9.4 T. In (a)-(f) η^I is equal to 1.0, 0.8, 0.6, 0.4, 0.2, and 0.0 respectively.

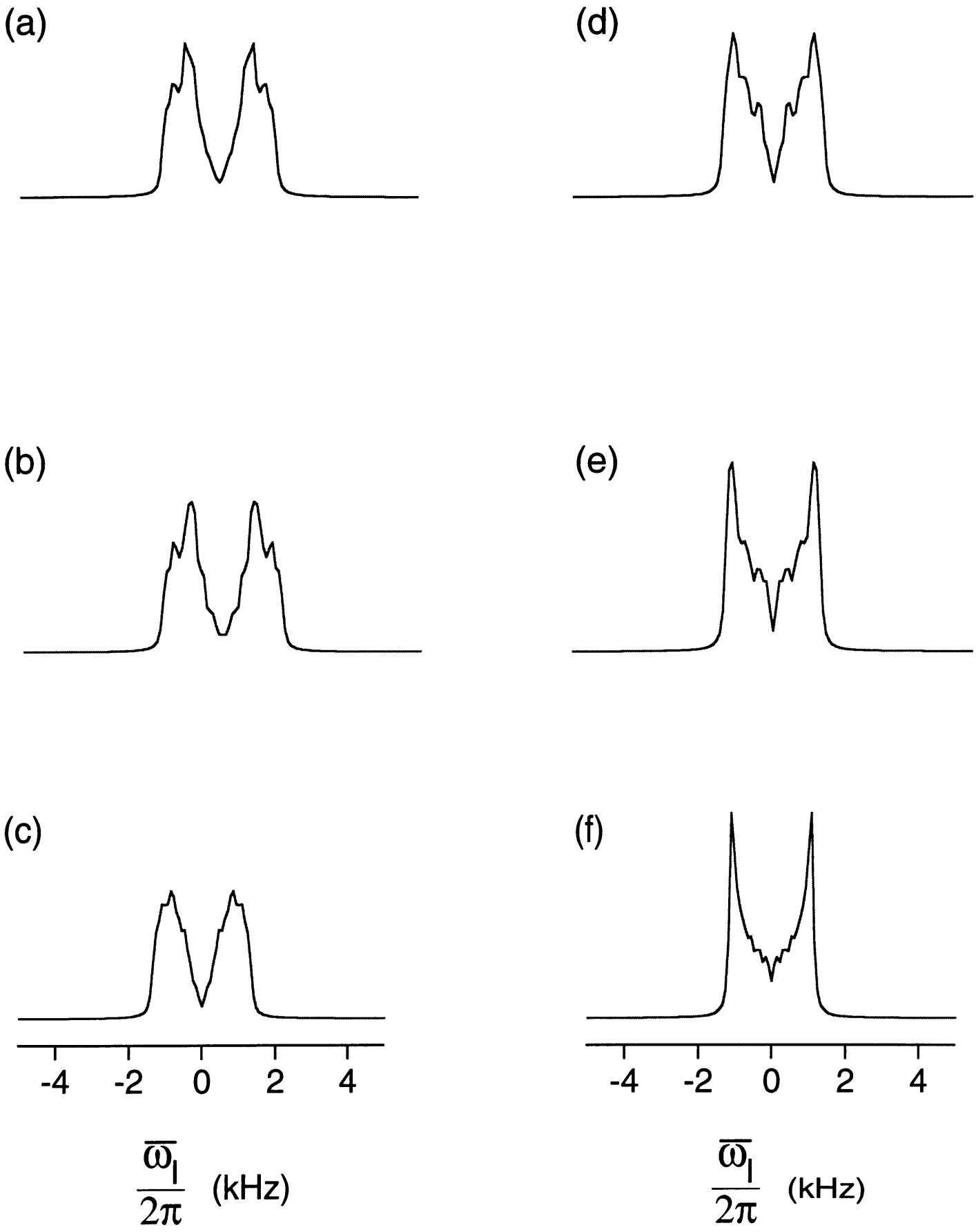
(a)
(d)
(b)
(e)
(c)
(f)
-4
-2
0
2
4
-4
-2
0
2
4
$\frac{\overline{\omega_1}}{2\pi}$ (kHz)
$\frac{\overline{\omega_1}}{2\pi}$ (kHz)

Figure 7.6

Within the framework presented here, where a single irradiation scheme is employed for recoupling of CSA/heteronuclear dipolar interactions, efficient recoupling may take place with the symmetry numbers N=1 and n >3 or N=2 and n=5. These conditions may offer potential advantages because the demands on rf power are smaller. Specifically, for TC4 and TC5 (N=2) the effective field must be either 8 or 5 times the spinning speed, respectively. If the rf power requirement for effective decoupling of the homonuclear interactions is modest, such as in the application of ^{13}C CSA recoupling, then the above conditions would offer an advantage for the measurement of smaller CSAs in the case where efficient ^{1}H decoupling during mixing is required. It is well known that signal loss results during mixing sequences when efforts are not made to avoid a mismatch between the rf power levels of the mixing scheme and CW ^{1}H decoupling[36,37]. Symmetry numbers which result in lower effective field requirements would allow the appropriate mismatch between the ^{1}H decoupling and CSA recoupling sequence that would minimize signal loss from inefficient ^{1}H decoupling. In addition, for the case of a fixed effective field direction, lower effective field strengths correspond to smaller nutation frequencies which would translate into a smaller contribution of rf field inhomogeneity errors, and the increased time required to achieve 2π rotation could potentially reduce the contribution of phase transient errors to the dynamics.

7.6 Conclusion

The proposed methods contain a general scheme for efficient CSA/heteronuclear dipolar recoupling in the presence of homonuclear dipolar coupled spin networks. The magnitude of the anisotropic interactions may be extracted from recoupled powder lineshapes by numerical lineshape simulations, and for the case of CSA recoupling, the lineshape is sensitive to the asymmetry parameter. The methods represent an improvement over previous techniques since the dynamics of the recoupled interaction are completely separated from the homonuclear interactions through efficient dipolar decoupling. An additional advantage is realized since measurements may be made under conditions of fast MAS thereby increasing sensitivity and resolution. Application of TC4 or

TC5 recoupling should allow experiments that measure torsion angles across HCCH[17] or HNCH[18] spin topologies to be implemented at higher spinning rates. In addition, the approaches presented here should allow for the measurement of torsion angles via CSA correlation in uniformly enriched samples. Although the sequences presented here are single irradiation schemes, it is possible to extend the TCn principle to double irradiation schemes which would allow for generation of heteronuclear multiple quantum coherence in a fashion that is independent of HH (or CC) dipolar couplings which would be useful in applications of 2D ^{1}H-^{13}C chemical shift correlation.

Acknowledgments for Chapter 7

This chapter is excerpted from manuscript that appeared in J. Chem. Phys. 108 (17) 1-8, May 1998

References for Chapter 7

[1] Andrew, E. R.; Bradbury, A.; Eades, R. G.; Nature 1958, 182, 1659.

[2] Maricq, M. M.; Waugh, J. S.; J. Chem. Phys. 1979, 70, 3300-3316.

[3] Schaefer, J.; Stejskal, E. O.; J. Am. Chem. Soc. 1976, 98, 1031.

[4] Bennett, A. E.; Rienstra, C. M.; Auger, M.; Lakshmi, K. V.; R.G. Griffin; J. Chem. Phys. 1995, 103, 6951-6958.

[5] Alla, M. A.; Kundla, E. I.; Lippmaa, E. T.; JETP Lett. 1978, 27, 194.

[6] Yarim-Agaev, Y.; Tutjian, P. N.; Waugh, J. S.; J. Magn. Reson. 1982, 47, 51.

[7] Bax, A.; Szeverenyi, N. M.; Maciel, G. E.; J. Magn. Reson. 1983, 55, 494-497.

[8] Aue, W. P.; Ruben, D. J.; Griffin, R. G.; J. Chem. Phys. 1984, 80, 1729.

[9] Olejniczak, E. T.; Vega, S.; Griffin, R. G.; J. Chem. Phys. 1984, 81, 4804.

[10] Tycko, R.; Dabbagh, G.; Mirau, P. A.; J. Magn. Reson. 1989, 85, 265-274.

[11] Gan, Z.; Grant, D. M.; Chem. Phys. Lett. 1990, 168, 304-308.

[12] Bennett, A. E.; Griffin, R. G.; Vega, S.; NMR Basic Principles and Progress 1994, 33, 1.

[13] Costa, P. R.; Sun, B. Q.; Griffin, R. G.; In Preparation

[14] Mansfield, P.; Orchard, M. J.; Stalker, D. C.; Richards, K. H. B.; Phys.. Rev. B 1970, 7, 90-105.

[15] Rhim, W. K.; Elleman, D. D.; Vaughan, R. W.; J. Chem. Phys. B 1973, 59, 3740-3749.

[16] Munowitz, M.; Griffin, R. G.; Bodenhausen, G.; Huang, T. H.; J. Am. Chem. Soc. 1981, 103, 2529.

[17] Feng, X.; Lee, Y. K.; Sandstrom, D.; Eden, M.; Maisel, H.; Sebald, A.; Levitt, M. H.; Chem. Phys. Lett. 1996, 257, 314-320.

[18] Hong, M.; Gross, J. D.; Griffin, R. G.; J. Phys. Chem. 1997, 101, 5869-5874.

[19] Haeberlen, U.; Waugh, J. S.; Phys. Rev. 1968, 175, 453-467.

[20] Ishii, Y.; Terao, T.; Kainosho, M.; Chem. Phys. Lett. 1996, 256, 133-140.

[21] Levitt, M. H.; Oas, T. G.; Griffin, R. G.; Isr. J. Chem. 1988, 28, 271-282.

[22] Oas, T. G.; Griffin, R. G.; Levitt, M. H.; J. Chem. Phys. 1988, 89, 692.

[23] Gan, Z.; Grant, D. M.; Ernst, R. R.; Chem. Phys. Lett. 1996, 254, 349-357.

[24] Lee, M.; Goldburg, W. I.; Phys. Rev. A 1965, 140, 1261.

[25] Bielecki, A.; Kolbert, A. C.; Levitt, M. H.; Chem. Phys. Lett. 1989, 155, 341-346.

[26] Bielecki, A.; Kolbert, A. C.; Groot, H. J. M. D.; Griffin, R. G.; Levitt, M. H.; Adv. Magn. Reson. 1990, 14, 111-124.

[27] Lee, Y. K.; Kurur, N. D.; Helmle, M.; Johannessen, O. G.; Nielsen, N. C.; Levitt, M. H.; Chem. Phys. Lett. 1995, 242, 304-309.

[28] Rossum, B.-J. von ; Forster, H.; de Groot, H. J. M.; J. Magn. Reson. 1997, 124, 516-519.

[29] Wu, C. H.; Ramamoorthy, A.; Opella, S. J.; J. Magn. Reson. Series A 1994, 109, 270

[30] Ramamoorthy, A.; Wu, C. H.; Opella, S. J.; J. Magn. Reson. Series B 1995, 88, 90.

[31] Baldus, M.; Meier, B. H.; J. Magn. Reson. 1997, 128, 122.

[32] Metz, G.; Wu, X.; Smith, S. O.; J. Magn. Reson. 1994, A110, 219-227.

[33] Abragam, A. Principles of Nuclear Magnetism; Clarendon Press: Oxford, 1961; Vol. 32.

[34] Cheng, V. B.; Suzukawa, H. H.; Wolfsberg, M.; J. Chem. Phys. 1073, 59, 3992-3999.

[35] Haberkorn, R. A.; Stark, R. E.; Willigen, H. v.; Griffin, R. G.; J. Am. Chem. Soc. 1981, 103, 2534.

[36] Bennett, A. E. Ph.D. Thesis Thesis, Massachusetts Institute of Technology, 1995.

[37] Ishii, Y.; Ashida, J.; Terao, T.; Chem. Phys. Lett. 1995, 246, 439-445.

8. Solid-State NMR Measurement of Ψ in Peptides. The NCCN 2Q-Heteronuclear Local Field Experiment

8.1 Introduction

In recent years solid-state nuclear magnetic resonance (ssNMR) has proven crucial for investigating the structure of macroscopically disordered biological solids (including lyophilized[1] and membrane[2,3] proteins and peptide aggregates[4,5]). In these systems the details of molecular structure are inaccessible to the more traditional methods of investigation (i.e. X-ray crystallography and liquid-state NMR). The precision of structural models derived using ssNMR techniques does not yet approach the standard that has been set in other areas of structural biology. An intense effort continues to improve both the accuracy and range of the internuclear distance measuring techniques[6-8] which have formed the basis of many ssNMR structural investigations. But alternative experimental approaches which provide complementary data that can increase structural resolution are also of obvious interest.

Feng, *et. al.*, have recently proposed a novel, magic angle spinning (MAS)-based method for measuring torsion angles about ^{13}CH-^{13}CH bonds (denoted 2Q-Heteronuclear Local Field (HLF)) by examining the relative orientation of the two directly-bonded ^{13}C-^{1}H dipolar interactions[9]. A similar proposal has been made for ^{15}NH-^{13}CH torsion angles[10]. These experiments are examples of a general class of measurements which correlate spatially anisotropic spin interactions such as the dipolar coupling and the chemical shift anisotropy (CSA) to extract structural information[11-20]. Because these techniques correlate large spin interactions, they are more easily extended to multiply labeled samples, whereas the weak internuclear dipolar interactions whose magnitudes provide useful distance information may be obscured by strong couplings between directly-bonded nuclei.

The HCCH 2Q-HLF experiment requires creation of ^{13}C-^{13}C double-quantum coherence (DQC), followed by a period of DQC dephasing driven solely by the ^{13}C-^{1}H dipolar interactions. The use of DQC[17] as opposed to sequential periods of single-quantum dephasing[18,19] allows acquisition of a subset of the accessible tensor correlation information and the benefits of a single mixing period and double-quantum filtering. Subsequent evolution of the DQC driven by the ^{13}C-^{1}H dipolar interactions is detected by constant-time division of a single rotor period, τ_r, into CW

heteronuclear and MREV[21,22] homonuclear decoupling periods applied to the ^1H channel. During τ_r the DQC first dephases, and then rephases as the ^{13}C-^1H coupling is refocused by MAS. The manner in which dephasing occurs depends on the relative orientation of the ^{13}C-^1H dipolar tensors, and hence the CC torsion angle. The ease and accuracy with which this experiment allows measurement of certain structural parameters in spinning solids represents a significant technical advance. However the HCCH method, as currently constituted, does have several drawbacks which include the following. In these experiments the condition $\omega_r < \delta_d/3$ must be satisfied, where δ_d is the multiple-pulse scaled ^1H-^{13}C dipolar coupling constant, to achieve significant dephasing (methods for increasing the effective coupling strength during the dephasing period have been devised[23]). Hence these experiments have typically been performed in the slow (3-4 kHz) spinning regime. Furthermore, the time resolution with which data is gathered is limited by the length of the MREV pulse cycle (or subcycle). These two requirements constitute significant limitations of the technique, particularly if extension to uniformly labeled samples is desired.

Here we describe a modification of the 2Q-HLF concept applied to a ^{15}N-^{13}C-^{13}C-^{15}N (NCCN) spin quartet. Creation of $^{13}C_2$ DQC, followed by dephasing solely under the influence of the ^{15}N-^{13}C heteronuclear couplings, will yield a DQC dephasing curve whose shape provides information about the relative orientation of the ^{15}N-^{13}C couplings, and hence the ^{13}C-^{13}C torsion angle. This corresponds to the Ψ angle along a peptide backbone when the ^{13}C nuclei are directly-bonded α- and carbonyl carbons (Fig. (1A)). By recoupling the ^{15}N-^{13}C interactions during the dephasing period, rather than observing their effects during a single rotor cycle at (very) slow spinning speed, we are able to perform the experiment effectively at much higher spinning speeds and with finer time resolution. The result is an experiment that, at least in certain torsion angle regimes, is exquisitely sensitive to conformation. Because the ^{13}C=O lacks a bound ^1H, this represents a unique approach (short of ^{17}O NMR) of applying the 2Q-HLF concept to measuring peptide backbone Ψ angles.

The selection of the appropriate pulse sequence elements for DQ filtering and ^{15}N-^{13}C recoupling is flexible within this framework. The selections used in the implementation presented

here (Fig. (1B)) were guided by the desire for efficient operation at relatively high spinning speeds in uniformly (^{13}C, ^{15}N)-labeled molecules.

8.2 Pulse Sequence and Calculations

The pulse sequence is diagrammed in Fig. (1B), and includes the standard cross-polarization from ^{1}H to ^{13}C nuclei followed by CW decoupling on the ^{1}H channel during mixing and TPPM decoupling[24] during acquisition. We then use the MELODRAMA-4.5[25] (MD) pulse sequence, which requires a rf magnitude 4.5 times the spinning speed, to create DQ coherence. Although other techniques have higher theoretical DQ filter efficiencies, they either require prohibitively high rf powers at high spinning speeds (e.g. C7[26] requires $\omega_{rf}=7*\omega_r$), or have their efficiency compromised by the relatively large chemical shift difference between α- and carbonyl carbons (e.g. 2Q-HORROR[27]), unless very high (>20kHz) spinning speeds can be achieved.

Figure 8.1 (A) Isotope labeling scheme and (B) pulse sequence for NCCN 2Q-HLF Ψ torsion angle measurement.

(A)

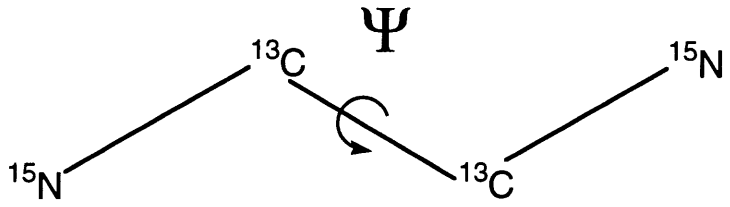
Ψ
13C
15N
15N
13C

(B)

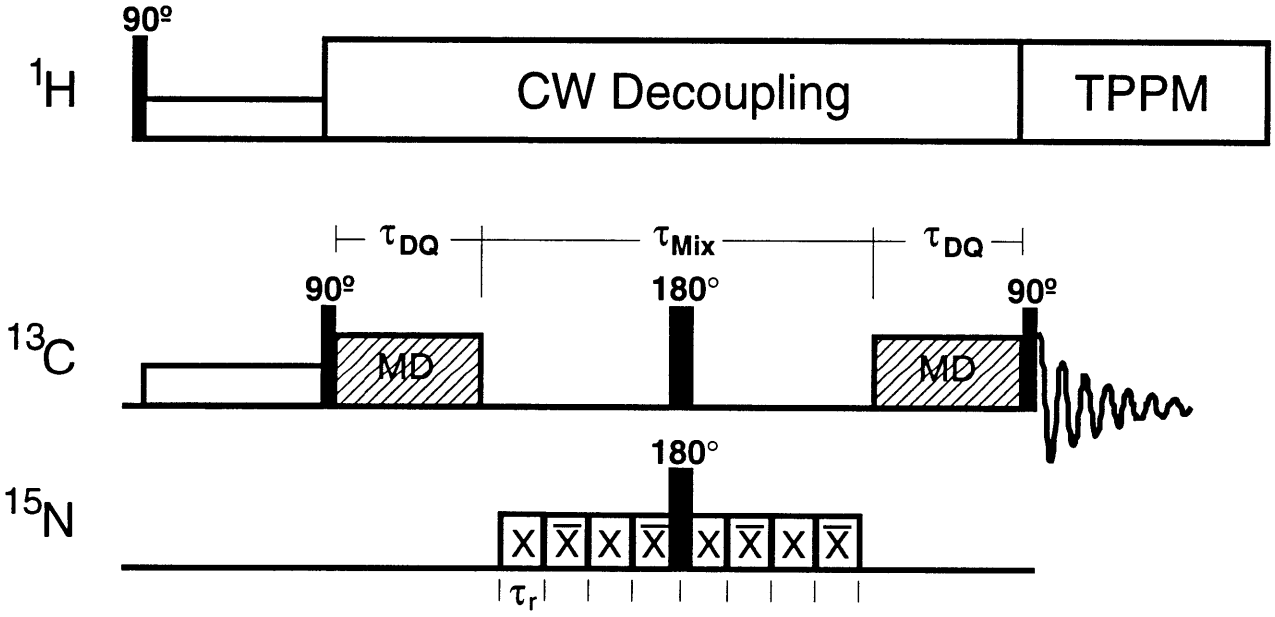
90º
1H
CW Decoupling
TPPM
τDQ
τMix
τDQ
90º
180°
90º
13C
MD
MD
180°
15N
X X X X X X X X
τr

Figure 8.1

The creation of $^{13}C_2$ DQC from longitudinal sum polarization using the MD sequence is straightforward and has been described previously using Average Hamiltonian Theory[25]. The spin part of the recoupled dipolar interaction does not have a rotor phase dependence in the MD experiment, so that the form of the DQ component of the density operator is identical for all crystallites after the first DQ mixing period, and can be written:

$$\rho = C_{1X}C_{2X} - C_{1Y}C_{2Y} \qquad (8.1)$$

where C_1 and C_2 represent the spin operators for the two ^{13}C nuclei.

We apply ^{15}N rf to recouple the ^{13}C-^{15}N dipolar interaction in the period following DQC creation. The ^{15}N rf magnitude is set to match the spinning speed ($\omega_{rf}=\omega_r$) as in the R^3[28] experiment. The rf phase is inverted every rotor cycle (analogous to SPICP[29]). R^3-related techniques allow for recoupling with low rf power even at high spinning speeds without the finite pulse effects associated with pulsed recoupling techniques which increase as the rotor period shrinks. The absence of rf power on the ^{13}C channel, where a strong homonuclear dipolar interaction is present, is also beneficial. Phase inversion has several effects including (i) removal of the ^{15}N CSA dependence of dipolar dynamics induced by unmodified R^3; (ii) compensation for ^{15}N isotropic shift offsets and rf inhomogeneity (demonstrated below). We term the combined technique 'Synchronous Phase Inversion Rotary Resonance Recoupling' (SPI-R^3). Note that 180° pulses in the center of the dephasing period on both ^{13}C and ^{15}N channels refocus ^{13}C chemical shifts while preserving the recoupled dipolar interaction.

The SPI-R^3-induced recoupling effect is illustrated by calculation of the zeroth-order average Hamiltonian[30] for the sequence in the appropriate interaction frame. Given the rotating-frame Hamiltonian for a ^{13}C, ^{15}N spin pair (represented by C and N operators):

$$H = n\omega_r N_X + \omega_D^{NC}(t)2C_Z N_Z \qquad (8.2)$$

(where we have assumed on-resonance irradiation of the ^{15}N nucleus with rf magnitude equal to a multiple n of the spinning speed), transformation to the interaction frame defined by the rf term yields:

$$\tilde{H} = C_Z \sum_{\substack{m=-2 \\ (m\neq 0)}}^{2} \left(\omega_D^{CN(m)} N_+ e^{i(n+m)\omega_r t} + \omega_D^{CN(-m)} N_- e^{-i(n-m)\omega_r t} \right) \qquad (8.3)$$

(where the time-dependence imposed on the coupling by MAS

$$\omega_D^{CN}(t) = \sum_{\substack{m=-2 \\ (m\neq 0)}}^{2} \omega_D^{CN(m)} e^{im\omega_r t} \qquad (8.4)$$

has been explicitly included, and the raising and lowering operators are defined relative to X as the quantization axis). Subsequent averaging over one rotor cycle yields the zero-order average Hamiltonian for the basic R^3 experiment:

$$\bar{\tilde{H}}^{(0)} = C_Z \sum_{\substack{m=-2 \\ (m\neq 0)}}^{2} \left(\omega_D^{CN(m)} N_+ \delta_{n,-m} + \omega_D^{CN(-m)} N_- \delta_{n,m} \right) \qquad (8.5),$$

which for n=1 simplifies to:

$$\bar{\tilde{H}}^{(0)} = C_Z \left(\omega_D^{CN(-1)} N_+ + \omega_D^{CN(1)} N_- \right) = \left| \omega_D^{CN(1)} \right| C_Z \left(N_Z \cos\gamma_D^{CN} + N_Y \sin\gamma_D^{CN} \right) \qquad (8.6)$$

where γ_D^{CN} represents the phase of the CN dipolar axis about the rotor axis. Note that the ^{15}N CSA is similarly recoupled under these conditions - the calculation of the effect proceeds along identical lines but with C_Z dropped. If the ^{15}N CSA and ^{15}N-^{13}C dipolar interactions have different rotor phase angles, their recoupled spin components (evident in eqn. (8.6)) will not commute. This results in ^{13}C-detected dipolar dephasing dynamics that depend upon both the size and orientation of the ^{15}N CSA relative to the heteronuclear dipolar axis.

Rotor-synchronized phase inversions remove the ^{15}N CSA dependence of ^{13}C-detected dephasing dynamics. The average Hamiltonian for the second rotor cycle in the sequence is derived from (8.5) by inverting the sign of n, yielding (as the equivalent of equation (8.6)):

$$\bar{\tilde{H}}^{(0)} = C_Z \left(\omega_D^{CN(1)} N_+ + \omega_D^{CN(-1)} N_- \right) = \left| \omega_D^{CN(1)} \right| C_Z \left(N_Z \cos\gamma_D^{CN} - N_Y \sin\gamma_D^{CN} \right) \qquad (8.7).$$

The zero-order average Hamiltonian for the entire SPI-R^3 sequence can be derived by simply adding the averages for successive rotor cycles:

$$\bar{\tilde{H}}^{(0)} = \left| \omega_D^{CN(1)} \right| C_Z N_Z \cos\gamma_D^{CN} \qquad (8.8).$$

The recoupled ^{15}N CSA has a similar dependence on N_Z. Hence commutation between the two is achieved at the expense of γ_D-dependent recoupled dipolar magnitudes. Simulations (not shown)

indicate that γ-dependent ^{15}N-^{13}C recoupling does not strongly affect the ability to measure torsion angles using DQ dephasing curves, described below.

The rf inhomogeneity compensation of the rotor-synchronized phase inversion follows from a similar cancellation: a positive offset from resonance ($\omega_{rf}=\omega_r+\delta\omega$) during one rotor cycle becomes a negative offset during the next ($\omega_{rf}=-\omega_r-\delta\omega$), so that summing over successive rotor cycles cancels any residual rf component that remains after averaging the nearest-resonant-frame transformed Hamiltonian (of eqn. (8.6)) over a single rotor cycle. Isotropic chemical shift offsets are compensated in a similar manner, as long as the length of each single-phase rf pulse is equivalent to an integer multiple of a 360° rotation. Both compensation effects depend on the fact that the rate at which phase inversion cycles occur ($\omega_r/2$) is much larger than the resonance offset ($\delta\omega$). We demonstrate experimentally below that typical offset and rf inhomogeneity values have no discernible effect on SPI-R^3-induced ^{15}N-^{13}C dephasing dynamics.

In a 4-spin N_1-C_1-C_2-N_2 system, the directly-bonded N-C dipolar interactions drive the evolution of $^{13}C_2$ DQ coherence (from eqn. (8.1)) according to:

$$\rho = \begin{matrix} \left(C_{1X}\cos b_1\tau_{MIX} + C_{1Y}N_{1Z}\sin b_1\tau_{MIX}\right)\left(C_{2X}\cos b_2\tau_{MIX} + C_{2Y}N_{2Z}\sin b_2\tau_{MIX}\right) \\ -\left(C_{1Y}\cos b_1\tau_{MIX} - C_{1X}N_{1Z}\sin b_1\tau_{MIX}\right)\left(C_{2Y}\cos b_2\tau_{MIX} - C_{2X}N_{2Z}\sin b_2\tau_{MIX}\right) \end{matrix} \quad (8.9)$$

where b_1 and b_2 represent the magnitudes of the recoupled interactions and are implicitly orientation dependent. The DQ filtering process completed by the second MD step (phase cycled relative to the first MD period and the receiver phase appropriately[31]) converts only the components of the density matrix that have the form of eqn. (8.1) back to detectable signal, so that the time-dependence of our effective observable during the dephasing period is:

$$\langle O\rangle_{\tau_{MIX}} = \left\langle C_{1X}C_{2X} - C_{1Y}C_{2Y}\right\rangle_{\tau_{MIX}} = \frac{1}{2}\left[\cos\left(b_1\tau_{MIX} + b_2\tau_{MIX}\right) + \cos\left(b_1\tau_{MIX} - b_2\tau_{MIX}\right)\right] \quad (8.10).$$

Calculation of the observed signal as a function of the torsion angle Ψ requires averaging eqn. (8.10) over an isotropic distribution of molecular orientations, with b_1 and b_2 determined in each case by the overall molecular orientation and the peptide backbone geometry. Fig. (8.2A) displays the standard backbone geometry[32], and (8.2B) shows the DQ dephasing curves calculated based on that geometry, with Ψ varying from 0° to 180° in 20° increments. The

calculations in this case (based on numerical integration of the equations of motion derived from the rotating frame Hamiltonian rather than eqn. (8.10)) include only the dephasing effects of the directly-bonded N-C couplings. Although the strength and relative orientation of the longer-range N-C couplings are also fixed by Ψ and hence easily included in calculations, their effect is minimal (shown below), and we do not include them here.

Note that simulations for (Ψ,Ψ') values related by the relation Ψ=360°-Ψ' are identical. In other words, conformations which are equidistant from either *cis* or *trans* configurations (i.e. eclipsed or fully staggered N-to-N orientations, respectively) in the opposite rotational sense about the C-C bond will yield identical simulations. An identical symmetry holds true for the HCCH and related techniques. If the *cis* and *trans* symmetry conformations lie in the center of a highly populated conformational region, structural resolution will be reduced because of the inability to distinguish between conformations on either side of the symmetry. One useful benefit of the NCCN technique is that the symmetry conformations (Ψ=0° and 180°) do not lie near the center of such populated regions.

Figure 8.2 Simulated dephasing curves as a function of the NCCN torsion angle Ψ. (A) diagrams the relevant peptide backbone geometry. (B) shows the calculated dephasing of double-quantum coherence during mixing as a function of Ψ (curves for Ψ varying from 0° to 180° in 20° increments are displayed). For comparison, (C) displays the calculated REDOR curves (single-quantum dephasing) for the N-C_α internuclear distance indicated in (A) as a function of Ψ (again in 20° increments).

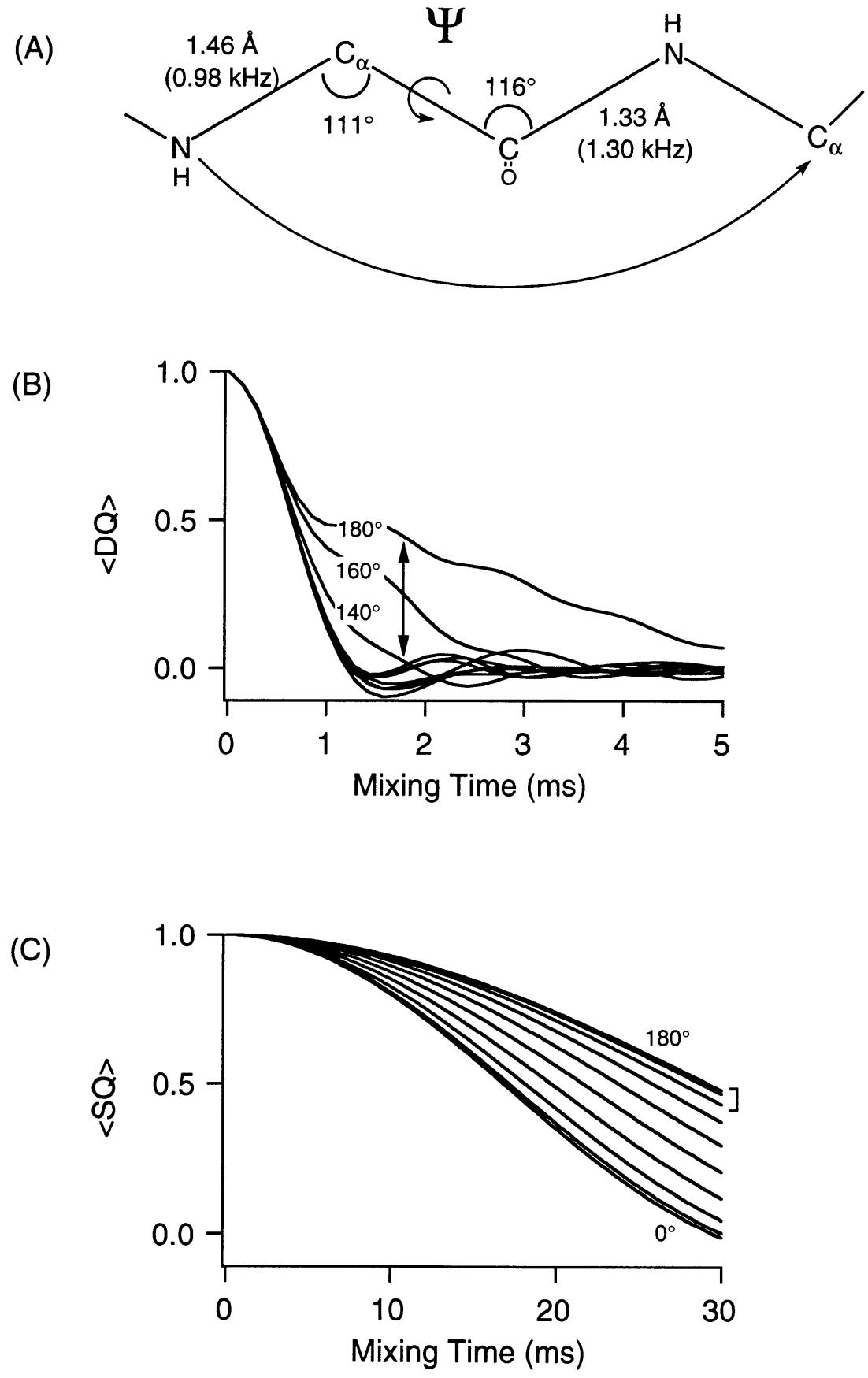
(A)
1.46 Å
(0.98 kHz)
Cα
111°
Ψ
116°
H
N
1.33 Å
(1.30 kHz)
Cα
N
H
C
O
(B)
1.0
0.5
0.0
<DQ>
180°
160°
140°
0
1
2
3
4
5
Mixing Time (ms)
(C)
1.0
0.5
0.0
<SQ>
180°
0°
0
10
20
30
Mixing Time (ms)

Figure 8.2

The DQ dephasing curves are particularly sensitive to variations in Ψ near the *trans* regime (120°-180°). When Ψ=180° the two NC dipolar couplings are most closely aligned, so are recoupled with near identical efficiency for all molecular orientations. Assuming similar coupling constants, this implies that b_1 and b_2 of eqn. (8.10) will be similar for all molecular orientations, and hence that half of the detected signal will decay at a relatively slow rate determined by (b_1-b_2) averaged across the powder. This 'cancellation' effect has been described by Levitt and co-workers[9]. As Ψ deviates from 180°, the recoupling efficiencies begin to differ widely, and both parts of eqn. (10) describe a fast decay.

It is during the transition between these two regimes that the dephasing curves are most sensitive to Ψ - in fact exquisitely so. We can compare them, for example, to a N-C_α REDOR[33] distance measurement. As Ψ varies from 180° to 140°, this internuclear distance varies by <0.1 Å, corresponding to the spread in single-quantum REDOR dephasing curves indicated by the bracket in Fig. (8.2C). The sensitivity of the two techniques to Ψ in this regime differs by an order of magnitude.

8.3 Results and Discussion

Experimental results illustrating the effectiveness of the SPI-R^3 heteronuclear dipolar dephasing sequence in two-spin ^{13}C-^{15}N systems are displayed in Fig. (8.3).

Figure 8.3 Experimental demonstration of the SPI-R^3 heteronuclear dipolar recoupling sequence on ^{15}N, $^{13}C_\alpha$-labeled glycine (diluted 1:10 in natural abundance). (A) displays the single-quantum dephasing curve (filled circles) with ω_1=14kHz rf applied to ^{15}N and ^{13}C detection. The solid line shows the best-fit simulation (b_{IS}=0.90kHz; no correction for rf-inhomogeneity is necessary). The dotted line shows the measured decay of $^{13}C_\alpha$ polarization in the absence of ^{15}N rf (i.e. homogeneous relaxation); the dephasing data (filled circles) is corrected for this decay. (B) displays a series of dephasing curves obtained under identical conditions except for variation of the ^{15}N carrier frequency up to 3 kHz off-resonance. (C) displays a series of curves obtained with ^{15}N rf field strength varying up to 1.5 kHz away from the resonance value (14kHz). Given the width of the rf nutation frequency distribution in our coil (≈7% FWHM), rf inhomogeneity is expected to have a negligible effect on the dephasing dynamics.

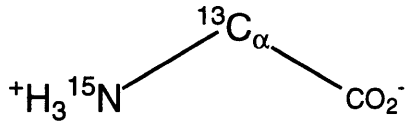
$^{13}C_\alpha$
$^{+}H_3{}^{15}N$
CO_2^-

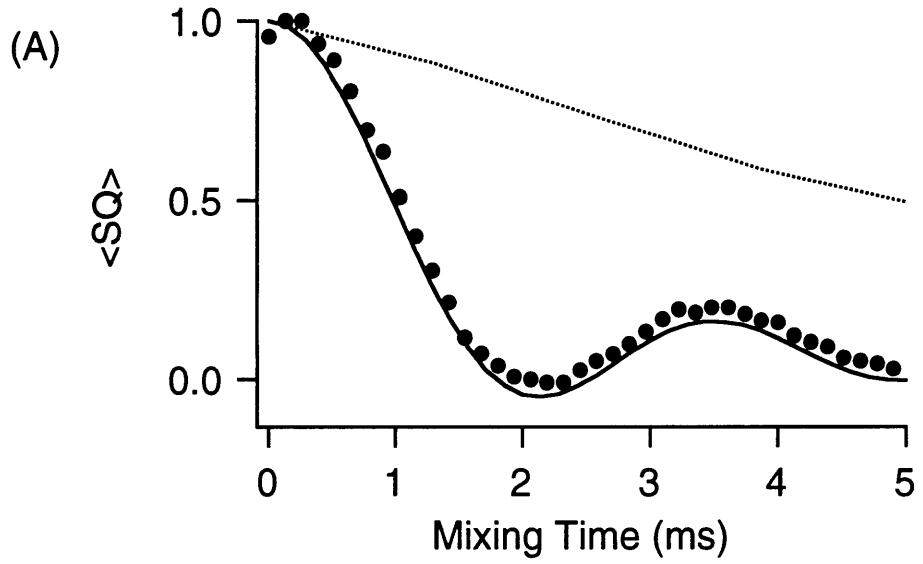
(A)
1.0
0.5
0.0
<SQ>
0
1
2
3
4
5
Mixing Time (ms)

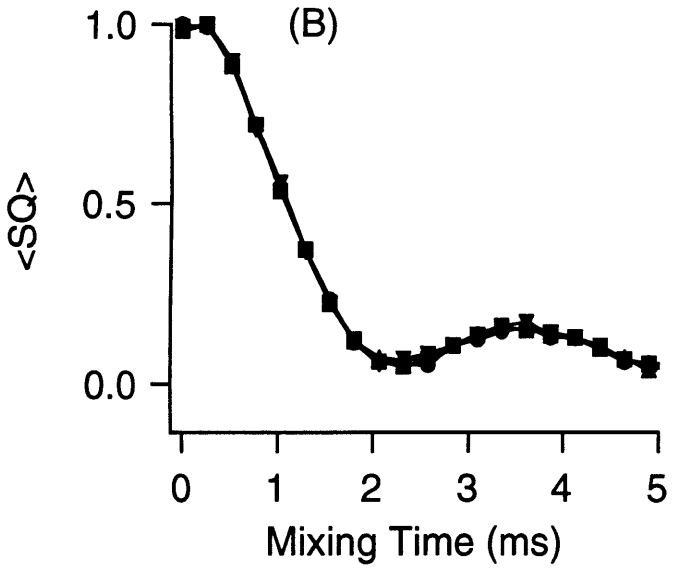
(B)
1.0
0.5
0.0
<SQ>
0
1
2
3
4
5
Mixing Time (ms)

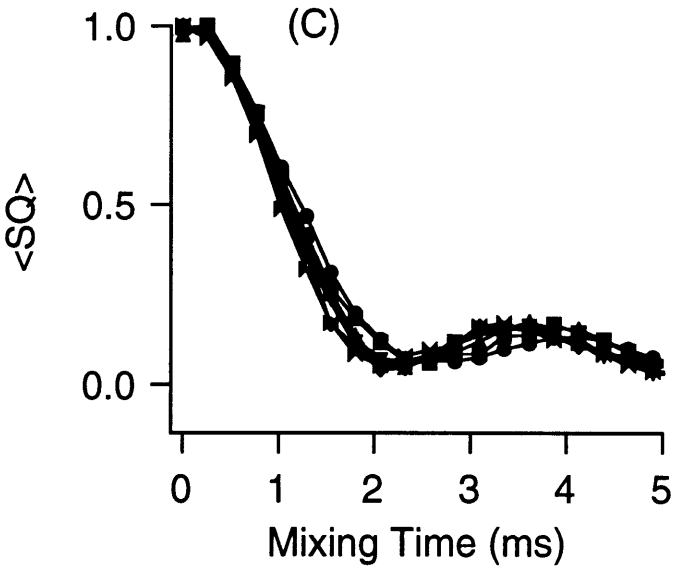
(C)
1.0
0.5
0.0
<SQ>
0
1
2
3
4
5
Mixing Time (ms)

Figure 8.3

The sequence used in these experiments corresponds to that shown in Fig. (8.1) with the 90° pulses and MD evolution periods removed. The spinning speed was set to 14 kHz, and the matching ^{15}N rf field strength was determined using 2D nutation experiments. Applied to a polycrystalline glycine sample in which 10% of the molecules have a (^{15}N,$^{13}C_{\alpha}$) labeling scheme (obtained from Cambridge Isotope Labs, Cambridge, MA), the technique yields the SQ dephasing curve displayed in Fig. (8.3A). The dashed line shows the decay of ^{13}C polarization in the absence of ^{15}N power; the dephasing data (filled circles) has been corrected for this decay as in a typical REDOR experiment[33]. Numerical simulations using a 0.9 kHz coupling constant (solid line) fit the data without the need to include the effects of rf inhomogeneity (measured to be ≈7% FWHM), or ^{15}N CSA.

The phase-inversion compensation for ^{15}N offset and rf inhomogeneity is demonstrated in Figs. (8.3B,C). In Fig. (8.3B) a series of experimental curves are displayed in which the ^{15}N offset was increased from 0 to 3 kHz, and almost no detectable variation in the dephasing curves occurs. In Fig. (8.3C), the ^{15}N rf field strength was varied over a 3 kHz range spanning the resonance field strength (14 kHz); small variations do occur. Over a range corresponding to the measured rf inhomogeneity (≈1 kHz at this field strength) the variation is minimal.

(^{15}N,$^{13}C_2$)-glycyl-(^{15}N)-glycine•HCl provides an appropriate sample to test the full NCCN DQ dephasing torsion angle experiment[34]. The relevant molecular geometry derived from a neutron diffraction study[35] is shown in Fig. (8.4A). In (8.4B) we display the measured DQ dephasing curve (filled circles), which has been corrected for DQ decay without ^{15}N rf (open circles). The spinning speed was 14 kH and the ^{1}H decoupling power throughout the experiment was 100 kHz. We obtained a DQ filtering efficiency of 20-25% with $\tau_{DQ}=8\tau_r$, about half of the maximal efficiency obtainable with MD.

Figure 8.4 Extraction of the NCCN (Ψ) torsion angle in glycylglycine•HCl (diluted 1:40 in natural abundance). (A) displays the relevant molecular geometry. (B) displays the measured DQ dephasing, both with ω_1=14 kHz ^{15}N rf power (filled circles), and without (open circles). Calculated dephasing curves with Ψ=162.1° and ±5° are also displayed. (C) shows (i) the Ψ=162.1° simulation from (B) (thick line), along with simulations in which (ii) C-C, N-N, and longer-range N-C couplings, all chemical shift and J-coupling terms have been ignored (dotted line); and (iii) similar to (ii) but with the generic backbone geometry of Fig. (2A) (dashed line).

Figure 8.4 - Simulations Vs. Experiment

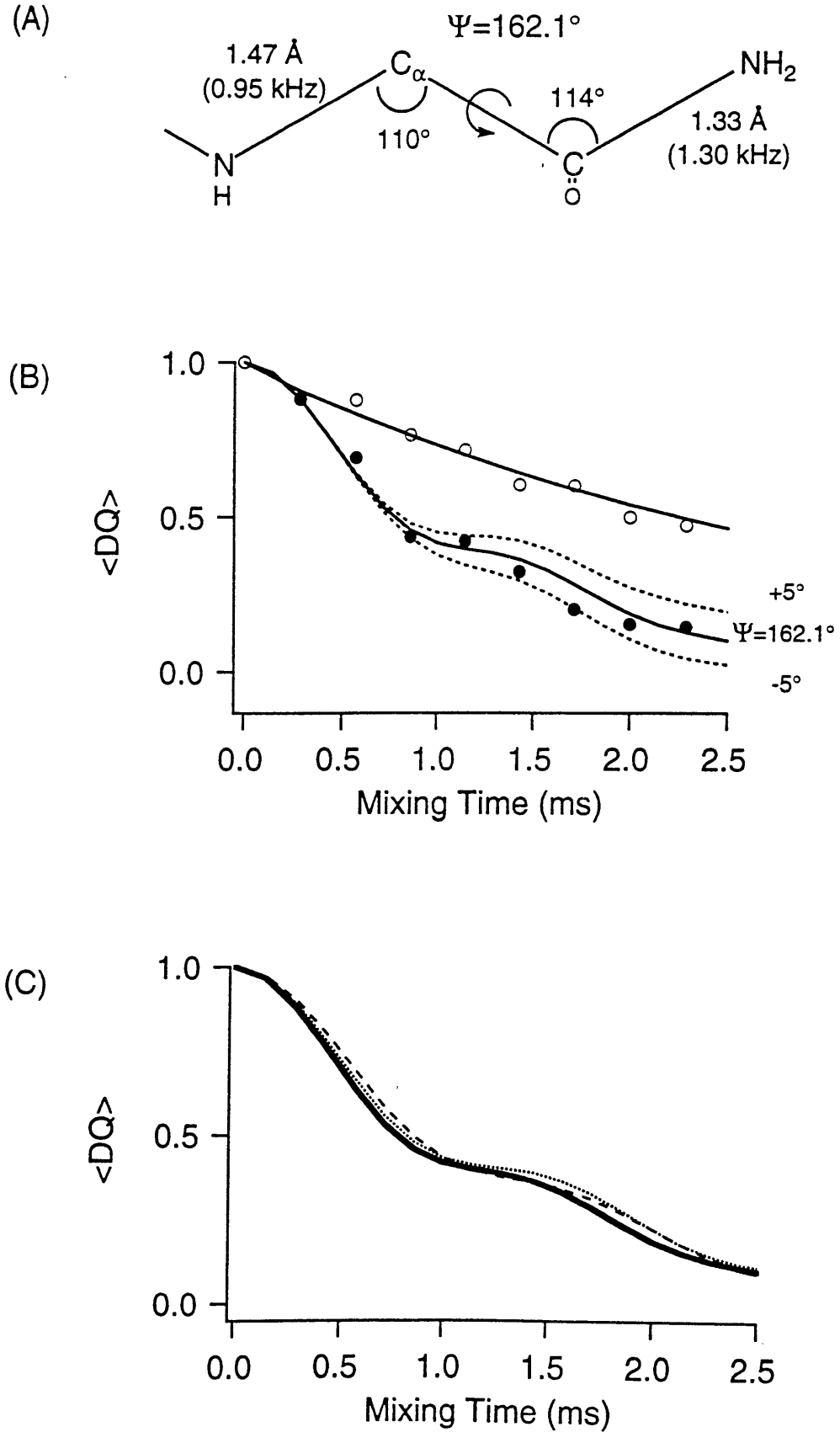

Figure 8.4

Calculation of the DQ dephasing curve based on the geometry of Fig. (8.4A) and including all relevant interactions (long and short range NC, CC, and NN dipolar couplings, estimated NC and CC J-couplings[36], and ^{15}N and ^{13}C CSA tensors[37]) matches the data quite well (lower solid line in (8.4B)). The fluctuations in the data are primarily due to the low S/N obtained from the sample, which contained the labeled material diluted 1:40 in natural abundance material (hence the experiment is roughly equivalent to a measurement in a ca. 40-50 residue peptide). No natural abundance background subtraction is necessary in these experiments, as has been noted, due to the DQ filtering process. The measurement constrains the torsion angle to a relatively small range: simulations where Ψ is varied $\pm 5°$ from the diffraction-determined value essentially bracket all of the data. This is a conservative estimate of the experimental precision.

The accuracy of measurements of this type will also depend on the sensitivity of the DQ dephasing curves to variations in molecular geometry other than that described by Ψ, and to other spin interactions. The calculated curves in Fig. (8.4C) examine this issue. The thick line duplicates the Ψ=162.1 curve from (8.4B), which includes the effects of long- and short- range dipolar and J-interactions and CSA tensors. The dotted line shows the calculation using identical geometric parameters, but with all interactions except the directly-bonded N-C couplings ignored. Even though these interactions are relatively well-fixed by the local geometry as defined by Ψ and the bond lengths and angles, their presence clearly can be ignored to simplify the calculations. The dashed line includes this simplification, and also replaces the geometry of Fig. (8.4A) with that for a generic peptide, shown in Fig. (8.2A). Again, little variation is seen. The overall range of variation corresponds to less than a 5° change in Ψ.

8.4 Conclusion

We have provided a general framework for measuring the peptide backbone torsion angle Ψ in solids that involves ^{13}C-^{15}N dipolar dephasing of $^{13}C_{\alpha}$-$^{13}C_{=O}$ DQ coherence. The specific implementation described here is designed to function effectively at relatively high spinning speeds. To that end we have proposed the SPI-R^3 sequence to induce ^{15}N-^{13}C dipolar dephasing

without the necessity of applying high ^{15}N or ^{13}C rf power or the drawbacks associated with finite pulse effects and sensitivity to rf inhomogeneity. The efficiency of the DQ filtering component of the experiment is limited by the use of the MD sequence, but at high spinning speeds this is the best of few viable options. At slower speeds, the C7 sequence may be substituted for higher efficiency. The SPI-R^3 sequence remains a competitive technique for inducing dipolar dephasing even at slow spinning speeds, but could conceivably be replaced by one of several alternatives including REDOR.

The region of high sensitivity to conformation (Ψ=120°-180°) corresponds roughly to the ß-sheet structural regime[32]. The extended nature of this type of secondary structure has made it difficult to accurately define the structural details of peptides in which it occurs[4,5] using distance measuring techniques with outer ranges of 5-6 Å. Application of the NCCN 2Q-HLF technique to these systems should be particularly useful in delineating the precise nature of their ß-sheet conformation.

Acknowledgements for Chapter 8

This chapter is excerpted from a manuscript that appeared in Chem. Phys. Lett. 280: (1-2) 95-103 Nov 28 1997. The work was done in collaboration with Phil Costa.

References for Chapter 8

[1] McDowell, L. M.; Klug, C. A.; Beusen, D. D.; Schaefer, J.; Biochemistry 1996, 35, 5395-5403.

[2] McDermott, A. E.; Creuzet, F.; Gebhard, R.; van der Hoef, K.; Levitt, M. H.; Herzfeld, J.; Lugtenberg, J.; Griffin, R. G.; Biochemistry 1994, 33, 6129.

[3] Tomita, Y.; O'Connor, E. J.; McDermott, A.; J. Amer. Chem. Soc. 1994, 116, 8766-8771.

[4] Lansbury, P. T. J.; Costa, P. R.; Griffiths, J. M.; Simon, E. J.; Auger, M.; Halverson, K. J.; Kocisko, D. A.; Hendsch, Z. S.; Ashburn, T. T.; Spencer, R. G. S.; Tidor, B.; Griffin, R. G.; Nature Structural Biology 1995, 2, 990-998.

[5] Heller, J.; Kolbert, A. C.; Larsen, R.; Ernst, M.; Bekker, T.; Baldwin, M.; Prusiner, S. B.; Pines, A.; Wemmer, D. E.; Protein Science 1996, 5, 1655.

[6] Bennett, A. E.; Rienstra, C. M.; Lansbury, P. T., Jr.; Griffin, R. G.; J. Chem. Phys. 1996, 105, 10289-10299.

[7] Mehta, M. A.; Gregory, D. M.; Kiihne, S.; Mitchell, D. J.; Hatcher, M. E.; Shiels, J. C.; Drobny, G. P.; Solid State Nuclear Magnetic Resonance 1996, 7, 211-228.

[8] Costa, P. R.; Sun, B. Q.; Griffin, R. G.; J. Amer. Chem. Soc., in press.

[9] Feng, X.; Lee, Y. K.; Sandstrom, D.; Eden, M.; Maisel, H.; Sebald, A.; Levitt, M. H.; Chem. Phys. Lett. 1996, 257, 314-320.

[10] Hong, M.; Gross, J. D.; Griffin, R. G.; J. of Phys. Chem., in press.

[11] Hester, R. K.; Ackermann, J. L.; Neff, B. L.; Waugh, J. S.; Phys. Rev. Lett. 1976, 36, 1081-1085.

[12] Stoll, M. E.; Vega, A. J.; Vaughan, R. W.; J. Chem. Phys. 1976, 65, 4093.

[13] Linder, M.; Hohener, A.; Ernst, R. R.; J. Chem. Phys. 1980, 73, 4959-4970.

[14] Munowitz, M. G.; Griffin, R. G.; J. Chem. Phys. 1982, 76, 2848.

[15] Robyr, P.; Tomaselli, M.; Straka, J.; Grob-Pisano, C.; Suter, U. W.; Meier, B. H.; Ernst, R. R.; Mol. Phys. 1995, 84, 995-1020.

[16] Weliky, D. P.; Tycko, R.; J. Amer. Chem. Soc. 1996, 118, 8487-8488.

[17] Schmidt-Rohr, K.; J. Amer. Chem. Soc. 1996, 118, 7601-7603.

[18] Ishii, Y.; Terao, T.; Kainosho, M.; Chem. Phys. Lett. 1996, 256, 133-140.

[19] Fujiwara, T.; Shimomura, T.; Akutsu, H.; J. Magn. Res. 1997, 124, 147-153.

[20] Henrichs, P. M.; Linder, M.; J. Magn. Res. 1984, 58, 458-461.

[21] Mansfield, P.; J. Phys. C 1971, 4, 1444.

[22] Rhim, W.-K.; Elleman, D. D.; Vaughn, R. W.; J. Chem. Phys. 1973, 59, 3740.

[23] Hong, M.; Gross, J. D.; Rienstra, C. M.; Griffin, R. G.; Kumashiro, K. K.; Schmidt-Rohr, K.; J. Magn. Res. in press.

[24] Bennett, A. E.; Rienstra, C. M.; Auger, M.; Lakshmi, K. V.; Griffin, R. G.; J. Chem. Phys. 1995, 103, 6951-6958.

[25] Sun, B.-Q.; Costa, P. R.; Kocisko, D.; Lansbury, P. T. J.; Griffin, R. G.; J. Chem. Phys. 1995, 102, 702.

[26] Lee, Y. K.; Kurur, N. D.; Helmle, M.; Johannessen, O. G.; Nielsen, N. C.; Levitt, M. H.; Chem. Phys. Lett. 1995, 242, 304-309.

[27] Nielsen, N. C.; Bildsoe, H.; Jakobsen, H. J.; Levitt, M. H.; J. Chem. Phys. 1994, 101, 1805-1812.

[28] Oas, T. G.; Griffin, R. G.; Levitt, M. H.; J. Chem. Phys. 1988, 89, 692-695.

[29] Wu, X.; Zilm, K. W.; J. Magn. Res. A 1993, 104, 154-165.

[30] Waugh, J. S.; Haeberlen, U.; Phys. Rev. 1968, 175, 453-467.

[31] Ernst, R. R.; Bodenhausen, G.; Wokaun, A. Principles of Nuclear Magnetic Resonance in One and Two Dimensions; Oxford University Press: Oxford, 1987.

[32] Voet, D.; Voet, J. G. Biochemistry; John Wiley and Sons: New York, 1990.

[33] Gullion, T.; Schaefer, J.; J. Magn. Res. 1989, 81, 196-200.

[34] (^{15}N)glycyl-(^{15}N,$^{13}C_2$)glycine•HCl was synthesized on Wang resin using standard FMOC techniques. The peptide was purified by RPHPLC and diluted 1:40 in natural abundance glycylglycine•HCl in aqueous solution. Lyophilization yielded the final product.

[35] Koetzle, T. F.; Hamilton, W.; Acta Cryst. 1972, B28, 2083.

[36] Cavanagh, J.; Fairbrother, W. J.; Palmer III, A. G. I.; Skelton, N. J. Protein NMR Spectroscopy: Principles and Practice; Academic Press, Inc.: San Diego, 1996.

[37] Stark, R. E.; Jelinski, L. W.; Ruben, D. J.; Torchia, D. A.; Griffin, R. G.; J. Magn. Res. 1983, 55, 266-273.

9. Preliminary Structural Investigations of Staphlococcal protein G by Solid-State NMR

9.1 Introduction

Solid-state NMR is an invaluable tool for probing details of structure in proteins where conventional methods such as x-ray crystallography or solution NMR fail. For example, membrane proteins are difficult to crystallize and tumble too slowly for solution NMR studies. In addition, solid-state NMR offers an advantage of time-resolved spectroscopy where photo- or enzyme intermediates may be trapped by freeze-quenching along the reaction coordinate so that the details of structural changes elucidated[1, 2]. These types of applications have motivated the development of techniques which allow dipolar couplings, and therefore internuclear distances, to be measured with in the MAS framework[3, 4]. Such dipolar recoupling techniques have been developed to measure distances between pairs of like and unlike spin 1/2 nuclei. Success has been found measuring distances in membrane proteins[5, 6], DNA[7], and enzyme inhibitor complexes in the solid-state[8].

However, an outstanding problem in solid-state NMR is total structure determination. Although specific questions regarding conformation may be addressed by pairwise labeling and dipolar recoupling, a full structural characterization of a protein has yet to be realized. This is in part due to the fact distance measurements between like spins in multiply labeled samples are complicated. Specifically, the non-commutation of the dipolar interaction between spin pairs leads to an attenuation of the weak-and therefore interesting-interactions by the uninformative, strong dipolar interactions between directly bonded nuclei[9]. This dipolar truncation effect has motivated the development of alternative techniques for determining structure. In one approach, correlations between strong heteronuclear dipolar interactions are established as a method of measuring torsion angles in uniformly ^{15}N, ^{13}C labeled samples[10-15]. Dipolar interactions between like spins are kept at bay by either homonuclear decoupling or fast MAS. These methods are a promising means to determine secondary structure in proteins. In addition, both tertiary and secondary structure may be probed by the selective recoupling of weak dipolar interactions between like spins[16]. This approach has found success even in strongly coupled spin networks. Finally, the

methodology is in place for performing full chemical shift assignments through multidimensional correlation spectroscopy[17].

At this point the stage is set for the full structure determination of small protein by solid state NMR. To this end, the B1 domain (Figure 9.1) of Immunoglobulin-Binding Protein G (B1 protein G)is an ideal system to demonstrate the utility of the aforementioned techniques. The full protein, found in *Streptococcus* binds human immunoglobulin G (IgG) and is thought to aid the pathogen in evading the host immune response[18]. In addition, the B1 domain is of interest since the overall fold confers high thermostability (melting temperature at pH 5.4 is 87 °C) which is unusual in the absence of disulfide linkages. The structure of the B1 domain has been determined by solution NMR[19] and x-ray crystallography[20], and these investigations will serve as a basis with which results from solid-state NMR may be compared. The small size (56 amino acids) and high yield of the expression system make the B1 domain of protein G an excellent system for structure characterization by solid-state NMR.

Figure 9.1 (a) Primary sequence of wild-type B1 domain of protein G. Amino acids in bold are in loop regions. Secondary structure and numbering scheme are in left and right columns respectively. (b) Ribbon diagram depicting backbone secondary structure and overall fold of the B1 domain of protein G based on structure determined by solution NMR.

(a)

β MTYKLILN**GK** 10

β **TL**KGETTTE**A** 20

α **VD**AATAEKVFKQYANDN **GVD**

β **G**EWTYD**DAT**K 50

β TFTVTE 56

(b)

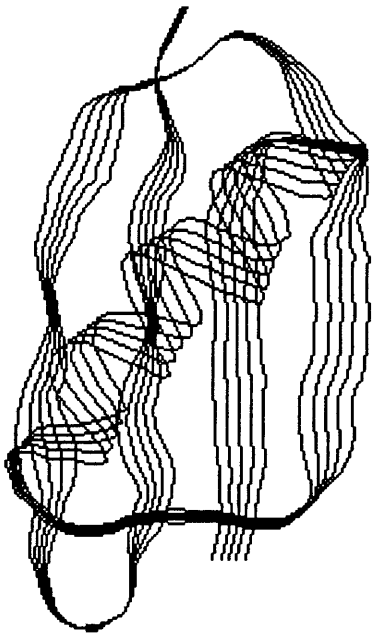

Figure 9.1

9.2 Materials and Methods

9.2.1 Biosynthesis of the B1 domain of Protein G

For the recombinant expression of the B1 domain, a T7 promoter based expression system[21] is used in combination with the *E.coli* strain BL21(DE3), which carries a chromosomal insertion of the T7 Polymerase[22]. The transcription of the T7 polymerase gene is under the control of the lacUV5 promoter, so the heterologous protein expression is IPTG-inducible. Since high yields of recombinant protein are essential for the feasibility of the project, an expression-optimized variant of the B1 domain was used, which carried the mutations E27D/K28R/K31D/Q32K/N35E. For gene expression, a preculture of BL21(DE3) carrying the plasmid PLM1-PG1 was grown in Luria broth for 5-6 hours. The bacteria were then transferred into 1xA minimal medium[23], containing the appropriate isotope label. For N-15 labeling ^{15}N-NH_4Cl was used while fully ^{13}C-labeled glucose was used for C-13 labeling. The bacteria were induced at an OD_{550} of 0.5 and were grown for another 3-4 hours before harvest. The bacterial cell pellet was resuspended in 20 mM Tris-HCl, pH 8.0 and the cells were lysed by threefold passage through a French Pressure Cell. The lysate was centrifuged at 16K in a Sorvall SS34 rotor for 20 minutes. The DNA was precipitated by stepwise addition of polyethyleneimine over a time interval of 20 minutes. After centrifugation of an additional 20 minutes at 16000 K in a Sorvall SS34 rotor the supernatant was diluted 100 fold into Tris-HCl, pH 8.0, and applied to a DEAE-sepharose column at a speed of 5 ml/min. Elution of the protein was achieved by a 0 to 0.5 M NaCl gradient. The B1-domain eluted at 80-100 mM NaCl and was about 95% pure as judged by SDS-PAGE. Typical yields were 30 mg of purified B1 domain / liter and OD_{550}.

9.2.2 Preparation of protein G for Solid State NMR Studies

The purified fractions of protein G were pooled and concentrated by centrifugation with an Amicon filter (3 kDa cutoff) to a final concentration of 10mg/ml. The concentrated sample was then transferred to a 3,000 molecular weight cutoff dialysis bag and dialyzed against two 12-hr changes of phosphate buffer pH 7. The B1 protein G samples were then concentrated to 30 mg/ml

by centrifugation with Amicon 3000 filters prior to introduction to the solid-state which was achieve by either lyophilization or crystallization.

Prior to lyophilization, sample were either quickly frozen by spraying the concentrated protein G solution into liquid isopentane at -140 °C or slowly frozen with liquid nitrogen. Protein crystals were grown by micro-dialysis under conditions of 50% 2-methyl-2,4-pentanediol, 20% isopropanol, 50 mM NaCl, 25 mM NaOAc pH 4.5 which are known cystrallization conditions for the wild-type protein[20].

9.2.3 Solution NMR Spectoscopy

To qualitatively access the incorperation of ^{15}N and ^{13}C labels into protein G and in order to ascertain the effect of lyophilization on protein folding in solution, 2D ^{15}N and ^{13}C HSQC experiments were performed. All experiments were performed on a custom-designed spectrometer operating at 500 MHz for proton with a Nalorac (Martinez, CA) triple resonance probe equiped with pulse field gradients. Experiments were performed at 25 °C on a 2 mM sample of U-^{15}N,^{13}C protein G in H_2O with a 10 mM phosphate buffer at pH 7.0. A gradient enhanced ^{15}N HSQC was performed in addition to a gradient enhanced ^{13}C HSQC which was recorded in constant-time mode[24]. Both experiments employed GARP[25] decoupling during the directly detected dimension. The results are presented in Figures 9.2 and 9.3.

Figure 9.2 2D gradient enhanced ^{15}N HSQC on U-^{15}N, ^{13}C labeled protein G at 25 °C

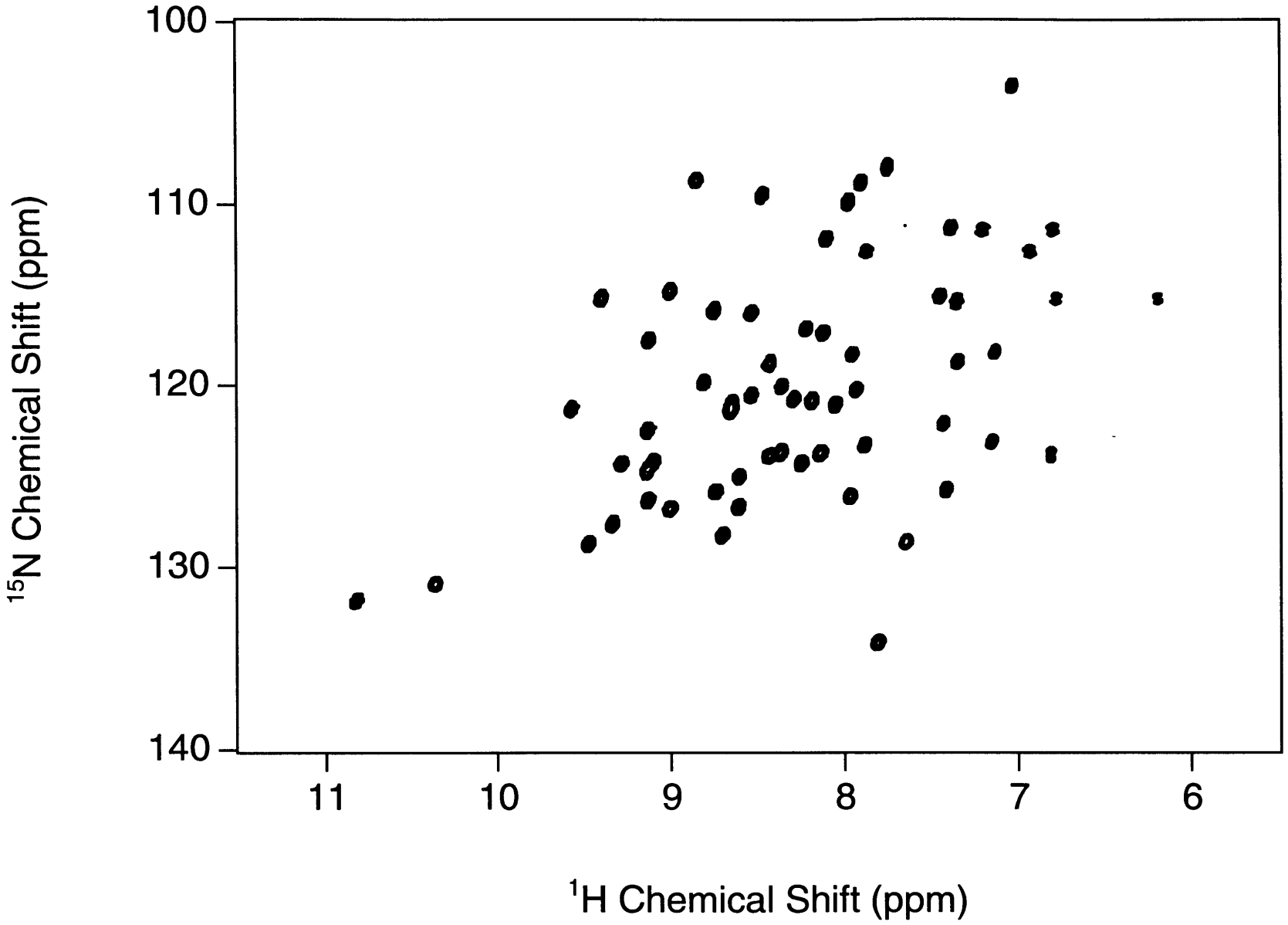
100
110
120
130
140
11
10
9
8
7
6
^{15}N Chemical Shift (ppm)
^{1}H Chemical Shift (ppm)

Figure 9.2

Figure 9.3 2D Gradient Enhanced ^{13}C CT-HSQC on U-^{15}N, ^{13}C labeled protein G at 25 °C

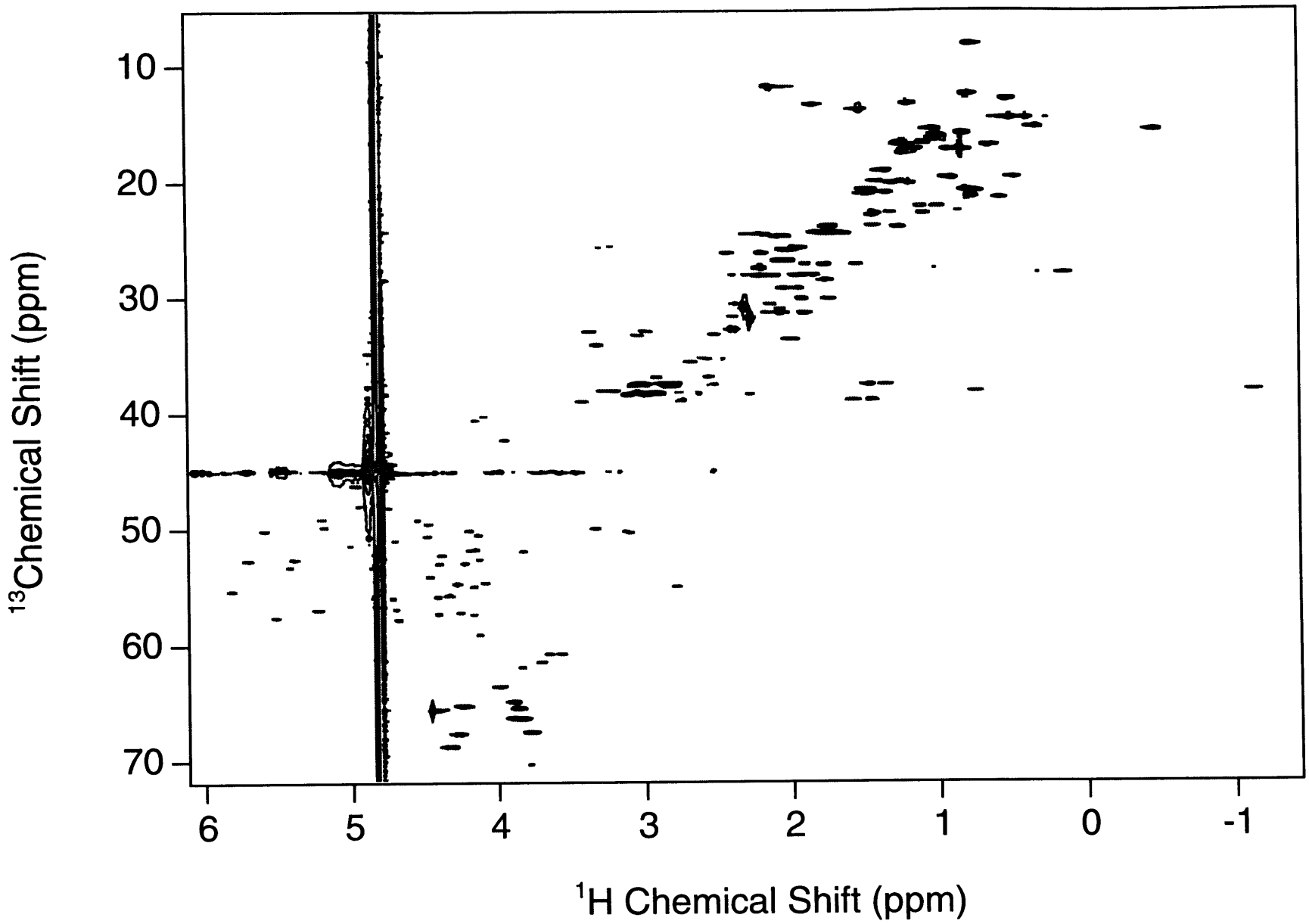
10
20
30
40
50
60
70
^{13}Chemical Shift (ppm)
6
5
4
3
2
1
0
-1
^{1}H Chemical Shift (ppm)

Figure 9.3

9.2.4 Solid-State NMR Spectroscopy

Experiments were performed on either at 9.4T or 11.75T magnets each equipped with a custom built spectrometer console and a HCN triple resonance transmission line probe. The spinning rates were controlled to within 2 Hz and in all cases ramped cross polarization[26] was employed to increase sensitivity and to ensure reproducibility of signal enhancements over long time scales. In all cases experiments were performed on approximately 15 mg of lyophilized sample with CW decoupling at an rf field strength of 125 kHz during the mixing period and TPPM decoupling during acquisition period with an rf field strength of 80 kHz , τ_p=5.8 μs and ϕ = ±10°. The ^{13}C-^{13}C MELODRAMA[27] 4.5 experiment was performed at 11.75T at 12.5 kHz MAS with a mixing time of 1 ms to ensure transfer between directly bonded carbons. The NC correlation spectra were recorded at 9.4T implemented as in Ref. [17] with the first ^{13}C evolution period set to zero and without RFDR mixing. The spinning speed in these experiments was 8.547 kHz while the NC mixing time was 6.25 ms and the ^{13}C rf rield amplitude was ramped over the first Hartmann-Hahn condition. Experimental conditions were identical for all samples.

9.3 Results and Discussion

In order to compare the effects of conformational disorder on resolution, a series of 2D ^{15}N-^{13}C and ^{13}C-^{13}C correlation experiments were performed on U-^{15}N,^{13}C GGV, LMVGGVVIA-where only the central VGG is U-^{15}N,^{13}C labeled, and U-^{15}N,^{13}C protein G. In the top and middle portion of Figure 9.4 are 2D NC correlation spectra of the crystalline peptide GGV and the lyophilized peptide LMVGGVVIA. The only difference between the top two spectra is therefore conformational disorder as the same number and type of sites are labeled. Clearly ,spectral resolution in the regions corresponding to the ^{13}CO and $^{13}C_\alpha$ carbons of the GGV sample is excellent. In contrast, the resolution is severely degraded in the lyophilized LMVGGVVIA. This decrease in resolution results from a dispersion in isotropic shifts that depends on conformational disorder. Even more severe is the crowding in the 2D NC correlation spectrum of lyophilized protein G as depicted in the bottom panel of Figure 9.4. The poor resolution is attributed to conformational disorder in addition to the increase in the number of

labeled sites. For comparison, a series of 2D ^{13}C MELODRAMA spectra on the same set of samples is displayed in Figure 9.5. Only the ^{13}CO,$^{13}C_{\alpha}$ region is displayed. Again, the same trend is followed. There are only 10 resolved ^{13}CO-$^{13}C_{\alpha}$ cross-peaks on the protein G samples which contains 56 amino acids, for example. Clearly, an increase in resolution must be achieved in order to assign the protein.

Figure 9.4 2D ^{15}N-^{13}C correlation spectra of U-^{15}N,^{13}C labeled: GGV, VGG in LMVGGVVIA, and protein G. All experiments were recorded under the same conditions. The GGV sample was recrystallized from a water/isopropanol mixture. All other samples were lyophilized Experimental details are in section 9.2.4.

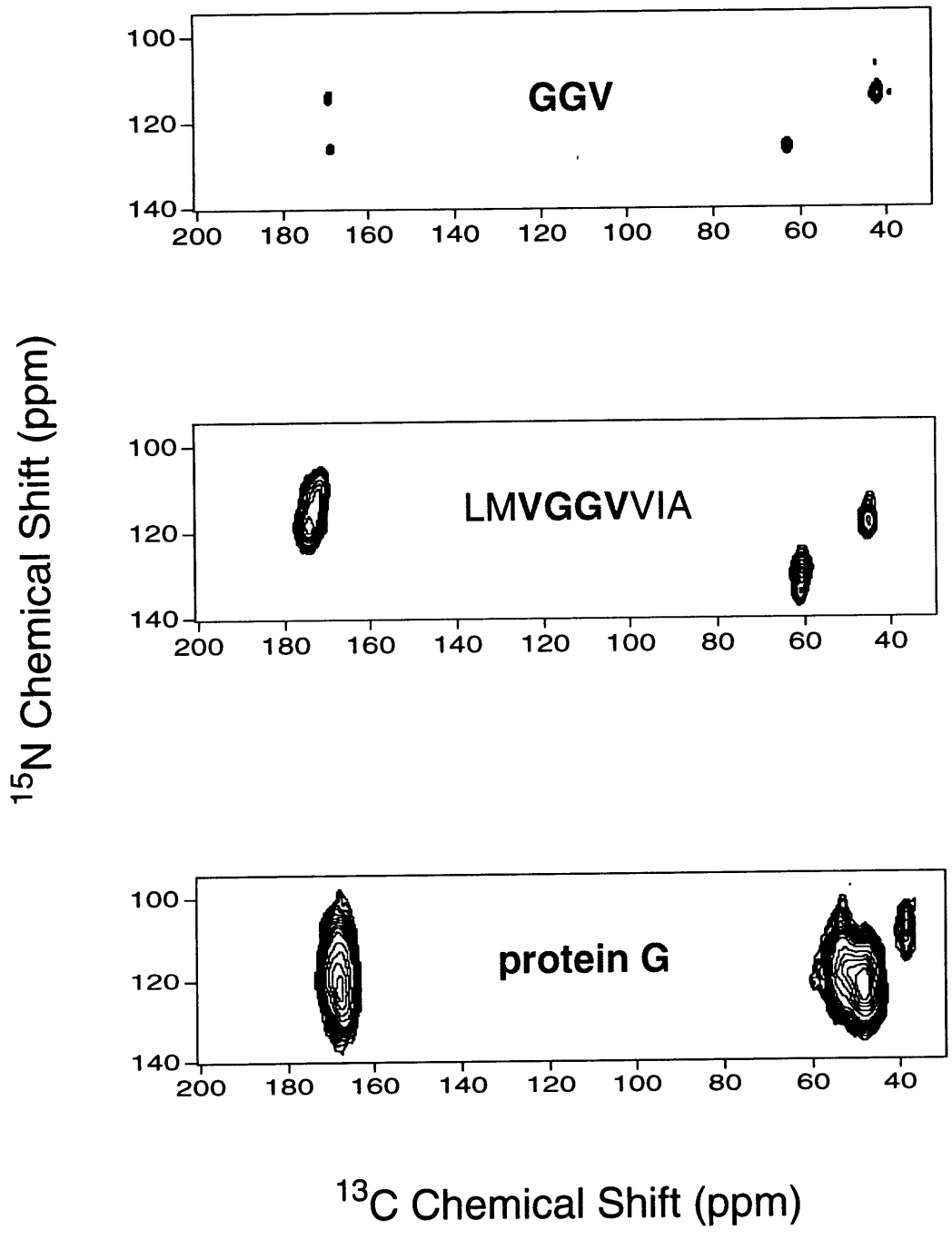
GGV
LMVGGVVIA
protein G
100
120
140
200
180
160
140
120
100
80
60
40
^{15}N Chemical Shift (ppm)
^{13}C Chemical Shift (ppm)

Figure 9.4

Figure 9.5 2D ^{13}C-^{13}C MELODRAMA spectra of U-^{15}N,^{13}C labeled: GGV, VGG in LMVGGVVIA, and protein G. The GGV sample was recrystallized from a water/isopropanol mixture. All other samples were lyophilized Experimental details are in section 9.2.4.

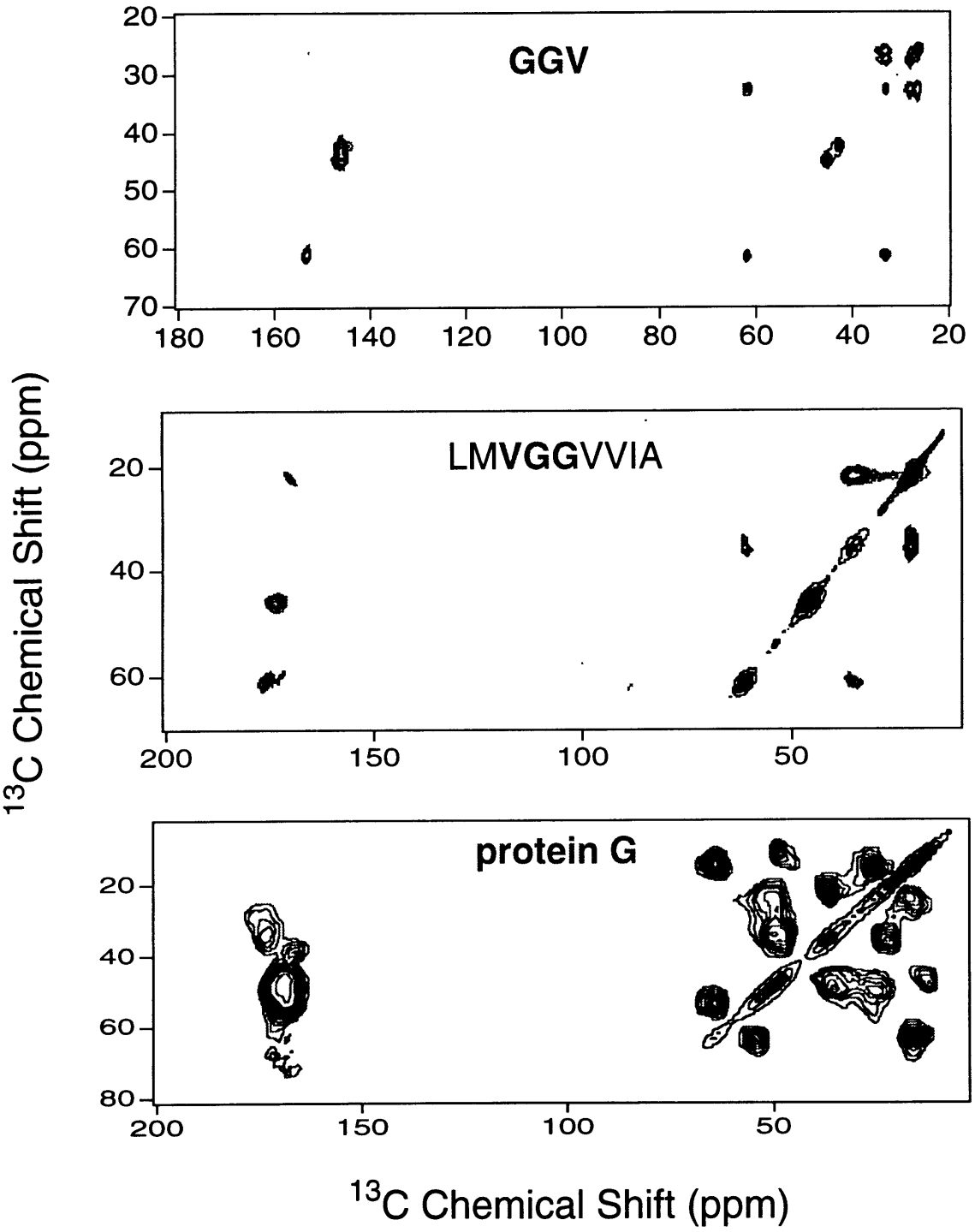
GGV
LMVGGVVIA
protein G
20
30
40
50
60
70
180
160
140
120
100
80
60
40
20
200
150
100
50
80
^{13}C Chemical Shift (ppm)
^{13}C Chemical Shift (ppm)

Figure 9.5

In order to obtain a quantitative estimate of the linebroadening present in the ^{15}N and ^{13}C spectra of protein G, the one dimensional chemical shift spectra in the solid-state are compared with the ^{15}N and ^{13}C (non constant-time) dimensions of the HSQC experiments performed in the liquid state. Depicted in Figure 9.6 is a simulated spectrum with the ^{15}N shifts collected from the indirect dimension of the ^{15}N HSQC where a linebroadening of 10 Hz has been applied. Spectra with additional line broadening of 50 and 200 Hz are also displayed. The ^{15}N spectrum acquired in the solid-state closely resembles the solution spectrum with 200 Hz of linebroadening. Thus, a crude estimate of the linebroadening in the ^{15}N solid-state spectra of protein G to be around 4ppm. At the top of Figure 9.7, the projection of the indirect dimension of the ^{13}C-HSQC with 50 Hz additional linebroadening is presented followed by the same spectrum with additional linebroadening of 50 and 150 Hz respectively. Again, it appears as though the ^{13}C spectrum in the solid state match the solution data with 200 Hz of linebroadening giving an estimate to the solid-state linewidths of greater than 2ppm. The above analysis assumes that each site is broadened by the same amount which is an oversimplification. It is very likely that surface exposed residues contain more conformational disorder, and therefore more broadening due to isotropic shift dispersion, than residues buried deep within the hydrophobic core.

Figure 9.6 Simulated ^{15}N spectra of protein G based on isotropic shifts taken from ^{15}N HSQC recorded in solution with indicated amounts of linebroadening. Bottom spectrum was recorded at 9.4 T on a lyophilized protein G sample with ^{15}N CPMAS. Only the NH region is displayed.

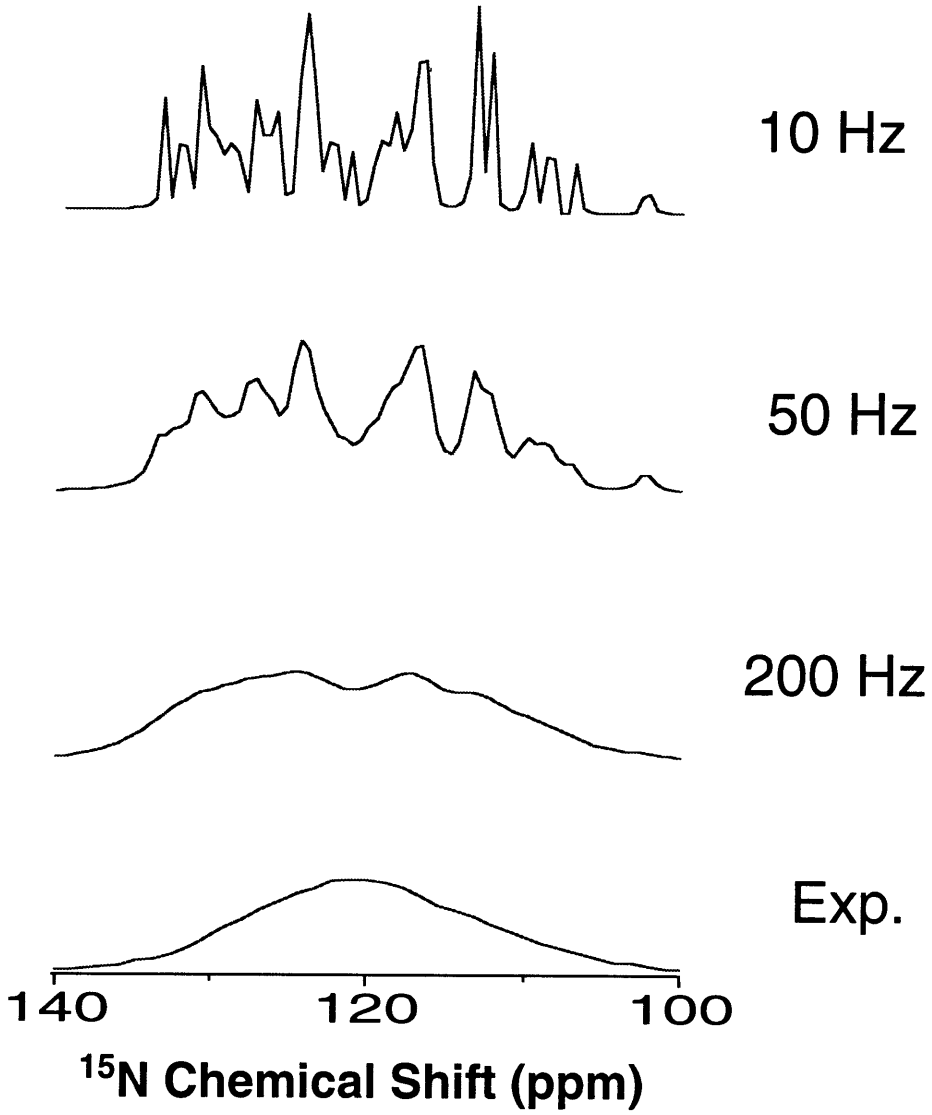

Figure 9.6

Figure 9.7 Projection of the indirect dimension from the 13C HSQC recorded in solution on protein G with indicated amounts of linebroadening. Bottom spectrum recorded on lyophilized protein G with CPMAS. All experimental data were recorded at 11.75 T

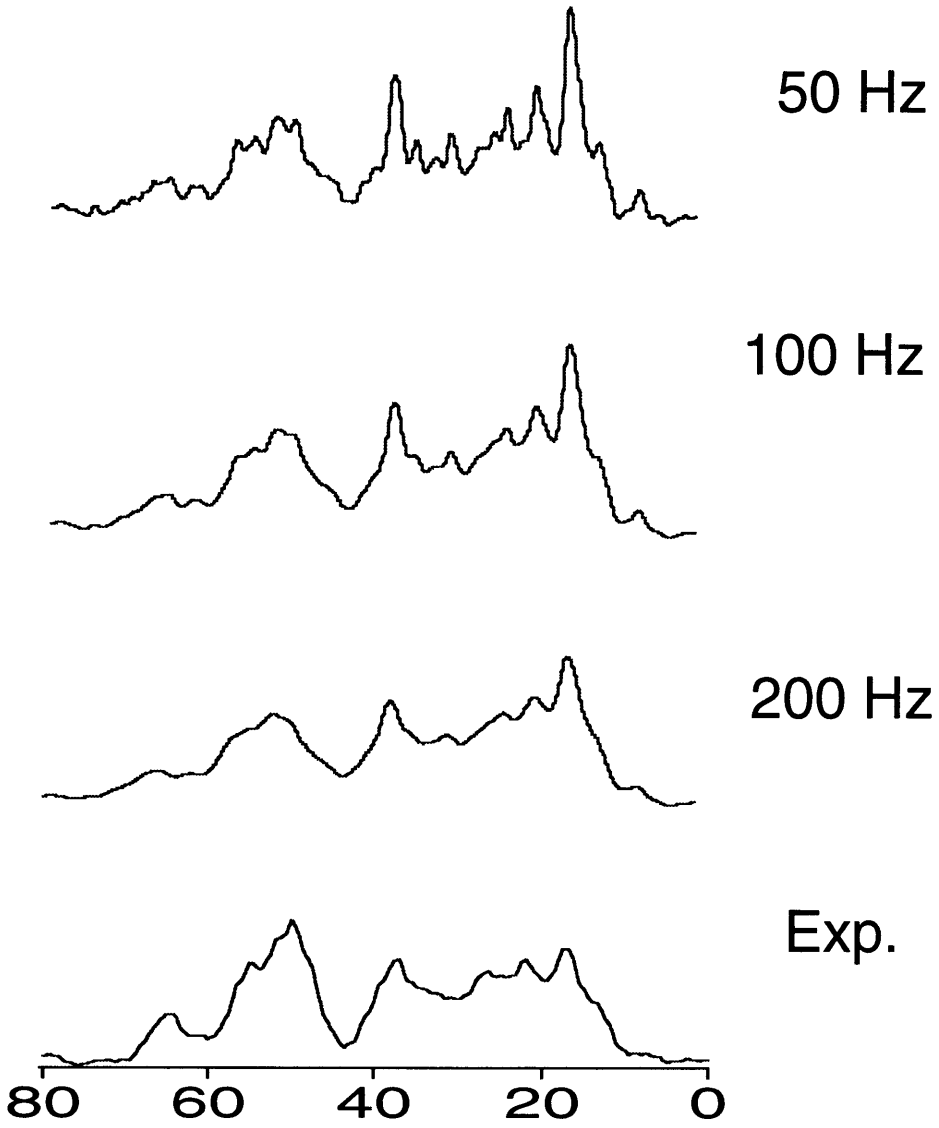

Figure 9.7

Poor resolution is not uncommon of lyophilized proteins in the solid state[28]. Several authors have commented on the effects sample preparation on conformational homogeneity[29-33]. Slowly freezing protein samples in water leads to the formation of crystalline ice domains that are known to exert a shearing force on the protein which may lead to conformational disorder, denaturation, or even disruption of chemical integrity[31, 32]. To avoid this, it is necessary to freeze the solvent rapidly so that a decrease in molecular mobility (an increase in viscosity) outweighs the thermodynamic driving force for crystallization[30, 31]. Alternatively, this may be achieved by the addition of a cryoprotectant which may increase the viscosity and lower the thermodynamic driving force for formation of crystalline domains of ice. A comparison between quick and slow freezing was performed by Christiansen *et. al.* on the ^{31}P resonances of a ternary complex of glyphosate/S3P/EPSP synthase, and the linewidths of the rapidly frozen material are substantially reduced (1.2ppm)[30]. In this study, the sample was quickly frozen by dropping 200 µl alliquots of a protein solution into small (1.5 ml Epindorf tubes) sample containers prior to immersion in liquid nitrogen and lyophilization.

We have attempted slow freezing without cryoprotectants in addition to quick freezing in liquid isopentane prior to lyophilization (See section 9.2.2). Unfortunately, in both cases, the 2D ^{15}N-^{13}C and ^{13}C-^{13}C spectra are identical (Data not shown). In addition, to ensure that sample integrity was not compromised by lyophilization, ^{15}N HSQC were obtained both before and after the procedure and produced identical spectra(Data not shown). These data indicate that the samples are folded (in solution) and that the freezing procedures employed and subsequent lyophilization are not harmful to the sample. Obviously, the data do not address the folding of the protein in the solid-state. In addition to significant conformational disorder, the lyophilized protein may be partially unfolded. It is unclear why our results with quick freezing and lyophilization are different than those obtained by Christiansen *et. al.* although it may be that the effect is system dependent. For example, it has been suggested that there is a differential broadening of surface residues over residues that are buried deep with in the hydrophobic core due to surface disorder induced by intermolecular contacts or solvent disorder. This implies that the broadening for proteins with

small surface area to volume ratios (like protein G) will be larger. EPSP synthase is on the order of 45 kDa and the narrowing observed may be related to the fact that the ^{31}P labels are within the binding sight and not exposed to the surface. In addition, as noted by Tycko[33], the effect of freezing may be thought of as "capturing" the conformational dispersion that is present in the liquid state. It is thought that fluctuations of 10° - 20° are present in the backbone torsion angles ϕ and ψ in liquids. If this fluctuations are frozen out (a non-crystalline solid) then ab initio calculations of conformation-dependent chemical shifts indicate a inhomogeneous broadening of 1 ppm or more[34-37]. This may impose a fundamental limit on resolution in non-crystalline rigid solids.

As an alternative Cole *et. al.* have performed MAS experiments on suspensions of crystals[29]. Not surprisingly, there is a dramatic increase in resolution between lyophilized and crystalline preparations specifically labeled Staphylococcal nuclease. In this case the crystals gave ^{13}C and ^{15}N linewidths of 0.4 and 1.3 ppm respectively. However, this approach is useful only for proteins for which large quantities of crystals are readily available. In a similar vain, Tomita et. al. observed a decrease in ^{13}C linewidths from 5 ppm when the sample was "quickly frozen" to 2 ppm upon precipitation with polyethylene glycol[38] although the present data indicate this level of resolution is insufficient for assigning a 56 residue protein by solid-state NMR[33].

Recent results suggest that the conformational disorder induced by freezing protein solutions followed by lyophilization depend strongly on the identity and relative concentration of buffer and cryoprotectants employed. For example, Evans and coworkers have shown that the ^{31}P linewidths of EPSP synthase complexed with glyphosate depends critically on the concentration and type of buffer and cryoprotectant[39]. For example, after varying the concentration of the buffer Tris-HCL over a 5-50mM range and changing the amount of trehelose in the protein buffer solution it was found that optimal linewidths result with 50mM Tris pH 7, 100 mg protein and 50 mg trehelose. However, it is unclear whether or not the above procedure is general. Nevertheless, the approach, though time consuming, does seem promising even if optimal conditions are unique to protein system.

Linewidths of 0.5-1 ppm are thought to be necessary for fully assigning the backbone for a protein of 30 amino acids using U-^{15}N-^{13}C labeled samples with a standard set of 3D ^{15}N-^{13}C-^{13}C type correlation experiments[33]. However, this requirement may be relaxed somewhat if sidechain resonaces are employed or additional dimensions are provided by the ^{1}H chemical shift[40]. Also, the use of either hetero or homonuclear multiple quantum evolution, may prove useful as a dispersion agent. Futhermore, it is anticipated that alternative labeling schemes such as random fractional or sparse ^{13}C labeling[41] in conjunction with uniform ^{15}N labeling may further increase resolution.

9.4 Conclusion

It is clear that the methodology for determining chemical shifts assignments and secondary structure through torsion angles measurements is in place. However, a method of introducing the protein G sample into the solid-state that produces conformational homogeneity needs to be employed before chemical shift assignments can be obtained. We have shown that 2D ^{15}N-^{13}C and ^{13}C-^{13}C MELODRAMA spectra recorded on either slowly frozen sample or samples which were quickly frozen in liquid isopentane prior to lyophilization are of insufficient resolution to obtain chemical shift assignments. Future prospects in sample preparation include optimization of conditions by varying type and relative concentrations of buffer and cryoprotectant employed. In parallel, it might be worthwhile to initiate structural studies on crystalline protein G to demonstrate how far the NMR methodology may be pushed given high resolution.

Acknowledgments for Chapter 9

This work was done in collaboration with Christian Freund and Professor Gerhard Wagner. Thanks are accorded to Hans Wendt for his advice on protein crystallization and Professor Tom Ellenberger for the use of his laboratory for protein crystallization.

References for Chapter 9

[1] Y. Li, R. J. Appleyard, W. A. Shuttleworth and J. N. S. Evans, J. Am. Chem. Soc. 116 (1994) 10799.

[2] D. R. Studelska, L. M. McDowell, M. P. Espe, C. A. Klug and J. Schaefer, Biochemistry 36 (1997) 15555.

[3] J. M. Griffiths and R. G. Griffin, Anal. Chim. Acta 283 (1993) 1081.

[4] A. E. Bennett, R. G. Griffin and S. Vega, NMR Basic Principles and Progress 33 (1994) 1.

[5] A. E. MacDermott, F. Creuzet, R. Gebhard, K. Vanderhoef, M. H. Levitt, J. Herzfeld, J. Lugtenburg and R. G. Griffin, Biochemistry 33 (1994) 6129.

[6] J. M. Griffiths, K. V. Lakshmi, A. E. Bennett, J. Raap, C. M. Vanderwielen, J. Lugtenburg, J. Herzfeld and R. G. Griffin, J. Am. Chem. Soc. 116 (1994) 10178.

[7] M. A. Mehta, D. M. Gregory, S. Kiihne, D. J. Mitchell, M. E. Hatcher, J. C. Shiels and G. P. Drobny, Solid State Nucl. Mag. Reson. 7 (1996) 211.

[8] L. M. McDowell, C. A. Klug, D. D. Beusen and J. Schaefer, Biochemistry 35 (1996) 5495.

[9] P. R. Costa, Thesis, Ph.D., Massachusetts Institute of Technology (1996).

[10] X. Feng, Y. K. Lee, D. Sandstrom, M. Eden, H. Maisel, A. Sebald and M. H. Levitt, Chem. Phys. Lett. 257 (1996) 314.

[11] M. Hong, J. D. Gross, C. M. Rienstra, R. G. Griffin, K. K. Kumashiro and K. Schmidt-Rohr, J. Magn. Reson. 129 (1997) 85.

[12] M. Hong, J. D. Gross and R. G. Griffin, J. Phys. Chem. 101 (1997) 5869.

[13] P. R. Costa, J. D. Gross, M. Hong and R. G. Griffin, Chem. Phys. Lett 280 (1997) 95.

[14] X. Feng, P. J. E. Verdegem, Y. K. Lee, D. Sandstrom, M. Eden, P. BoveeGeurts, W. J. deGrip, J. Lugtenburg, H. J. M. deGroot and M. H. Levitt, J. Am. Chem. Soc. 119 (1997) 6853.

[15] X. Feng, M. Eden, A. Brinkmann, H. Luthman, L. Eriksson, A. Graslund, O. N. Antzutkin and M. H. Levitt, J. Am. Chem. Soc. 119 (1997) 12006.

[16] P. R. Costa, B. Q. Sun and R. G. Griffin, J. Am. Chem. Soc. 119 (1997) 10821.

[17] B. Q. Sun, C. M. Rienstra, P. R. Costa, J. R. Williamson and R. G. Griffin, J. Am. Chem. Soc. 119 (1997) 8540.

[18] S. R. Fahnestock, P. Alexander, J. Nagle and D. Filpula, J. Bacteriol. 167 (1986) 870.

[19] A. M. Gronenborn, D. R. Filpula, N. Z. Essig, A. Achari, M. Whitlow, P. T. Wingfield and G. M. Clore, Science 253 (1991) 657.

[20] T. Gallagher, P. Alexander, P. Bryan and G. L. Gilliland, Biochemistry 33 (1994) 4721.

[21] M. Sodeoka, C. J. Larson, L. Chen, W. S. Laue and G. L. Verdine, BioMed. Chem. Lett. 3 (1993) 1095.

[22] F. W. Studier and B. A. Moffat, J. Mol. Biol. (1986) 113.

[23] J. H. Miller, Cold Spring Harbor Laboratory (1972) 356.

[24] L. E. Kay, P. Kiefer and T. Saarinen, J. Am. Chem. Soc. 114 (1992) 10633.

[25] A. J. Shaka, P. B. Barker and R. Freeman, J. Magn. Reson. 64 (1985) 547.

[26] G. Metz, X. Wu and S. O. Smith, J. Magn. Reson. A110 (1994) 219.

[27] B. Q. Sun, P. R. Costa, D. Kocisko, P. T. Lansbury and R. G. Griffin, J. Chem. Phys. 102 (1995) 702.

[28] D. L. VanderHart, W. L. Earl and A. N. Garroway, J. Magn. Reson. 44 (1981) 361.

[29] H. B. R. Cole, S. W. Sparks and D. A. Torchia, Proc. Natl. Acad. Sci. USA 85 (1988) 6362.

[30] A. M. Christensen and J. Schaefer, Biochemistry 32 (1993) 2868.

[31] R. J. Appleyard and J. N. S. Evans, J. Magn. Reson. Series B 102 (1993) 245.

[32] R. J. Appleyard, W. A. Shuttleworth and J. N. S. Evans, Biochemistry 33 (1994) 6812.

[33] R. Tycko, J. Biomol. NMR 8 (1996) 239.

[34] I. Ando, H. Saito, R. Tabeta, A. Shoji and T. Ozaki, Macromolecules 17 (1984) 457.

[35] A. C. de Dios, J. G. Pearson and E. Oldfield, J. Am. Chem. Soc. 115 (1993) 9768.

[36] A. C. de Dios and E. Oldfield, J. Am. Chem. Soc. 116 (1994) 5307.

[37] H.-B. Le, J. G. Pearson, A. C. de Dios and E. Oldfield, J. Am. Chem. Soc. 108 (1995) 2215.

[38] Y. Tomita, E. J. O'Conner and A. McDermott, J. Am. Chem. Soc. 116 (1994) 8766.

[39] D. Jakeman, W. Shuttleworth, D. Mitchell and J. N. S. Evans, 39th Experimental NMR Conference, Asilomar M/T Poster 050 (1998)

[40] B.-J. van Rossum, H. Forster and H. J. M. D. Groot, J. Magn. Reson. 124 (1997) 516.

[41] D. M. LeMaster and D. M. Kushlan, J. Am. Chem. Soc. 118 (1996) 9255.

Appendices

Appendix A- RF Interaction Frames

A1- The Toggling Frame

In order to analyze the effects of a radio frequency irradiation on the internal dynamics of a nuclear spin system, it is convenient to write the Hamiltonian:

$$H(t) = H_{Int}(t) + H_{rf}(t) \qquad \text{(A1.1)}$$

where $H_{Int}(t)$ is the high-field truncated Hamiltonian consisting of the internal nuclear spin interactions under MAS (See Eq 1.32 and 1.34) while $H_{rf}(t)$ radiofrequency field given by:

$$H_{rf}(t) = R_Z[\phi(t)]\ \omega_1(t) I_X R_Z^{+}[\phi(t)] \qquad \text{(A1.2)}$$

In this case, an interaction frame defined by the rf field where V(t) = Hrf(t) using the notation in Eq. 1.19 leads to the result

$$U(t,0) = U_{rf}(t,0)\ U_{Int}(t,0) \qquad \text{(A1.3)}$$

for the evolution operator.

with

$$U_{rf}(t,0) = \hat{T}\ \exp\{-i\int_0^t dt'\ H_{rf}(t')\} \quad , \qquad \text{(A1.4)}$$

$$U_{Int}(t,0) = \hat{T}\ \exp\{-i\int_0^t dt'\ \tilde{H}_{Int}(t')\} \qquad \text{(A1.5)}$$

and

$$\tilde{H}_{Int}(t) = U_{rf}^{-1}(t,0)\ H_{Int}\ U_{rf}(t,0). \qquad \text{(A1.6)}$$

The name "Toggling Frame" is suitable for this interaction representation since the effect of the rf field is to manipulate the spin operators. If the irradiation is periodic with τ_c and satisfies the cyclic condition Eq. X becomes:

$$U(n\tau_c,0) = U_{Int}(n\tau_c,0) \qquad \text{(A1.7)}$$

which is suitable for Average Hamiltonian Analysis.

Appendix B- Effects of Fast limit Axial diffusion on ^1H MAS Spectra

As mentioned in Chapter 1, the ^1H spin dynamics are homogeneous in the Maricq and Waug sense due to the fact that the Hamiltonian, $H(t) = H_I(t) + H_{II}(t)$ is such that $[H(t),H(t')] \neq 0$. Howeve it can be shown that under fast limit axial diffusion-as discussed in section 1.5.1- th $[\langle H_{II}(t)\rangle^{AD}, \langle H_{II}(t')\rangle^{AD}] = 0$. In this case, the spins may be treated as isolated pairs. This impli that MAS may effectively narrow the ^1H dipolar linewidth provided that the spinning rate is well-off rotational resonance as indicated by equation 1.37b. Under fast limit axial diffusion the dipol Hamiltonian between a system of like spins may be written:

$$\langle H_{II}(t)\rangle^{AD} = \sum_{i<j} \langle \omega^{ij}(t)\rangle^{AD}(3I_{iZ}I_{jZ} - I_i\cdot I_j) \qquad \text{(B1)}$$

$$= F(t) \sum_{i<j} \langle \tilde{\rho}^{ij}_{20}\rangle (3I_{iZ}I_{jZ} - I_i\cdot I_j)$$

with

$$F(t) = \sum_{m=-2}^{2} D^{(2)}_{0,-m}(\Omega_{PD}) D^{(2)}_{-m,0}(\omega_r t, \beta_{RL}, 0) \qquad \text{(B2)}$$

where Eqs. 1.32,1.33,1.44 and 1.45 have been employed.

Clearly, in this case:

$$[\langle H_{II}(t)\rangle^{AD}, \langle H_{II}(t')\rangle^{AD}] =$$

$$F(t)F(t')\,[\sum_{i<j} \langle \tilde{\rho}^{ij}_{20}\rangle (3I_{iZ}I_{jZ} - I_i\cdot I_j)\,,\, \langle \tilde{\rho}^{ij}_{20}\rangle (3I_{iZ}I_{jZ} - I_i\cdot I_j)\,] = 0 \quad . \qquad \text{(B3)}$$

Physically, the effect of the fast axial motion is to project the dipolar coupling on to the motional axis, a the motionally averaged dipolar interactions are all colinear with the unique direction parallel to t diffusion axis and the magnetude scaled by $P_2(\cos(\beta_{PD}))$. Therefore, the motionally averaged couplin behave as a linear chain of spins as discussed by Maricq and Waugh.

Using the same argument, it can be shown that the "n=0" rotational resonance is forbidden. F the case of a geminal ^1H-^1H pair found in a CH_2 group, this follows trivially since, without motion, t magnitudes of the CSA are the same but the orientation of the ^1H CSA is along the CH bond. With fa limit axial diffusion, the CSAs are projected onto the motional axis and have the same orientation. T "n=0" resonance is quenched in this case as the motionally averaged CSAs are coaxial. More generall for two spins with *identical isotropic shifts*, the "n=0" resonance results from the fact that the Hamiltonia

$$H^{23}(t) = \omega_{\Delta}(t)I_z^{23} - \omega^{II}(t)I_x^{23} \qquad \text{(B4)}$$

with

$$I_z^{23} = \frac{1}{2}(I_{jz} - I_{iz}) \qquad \text{(B5)}$$

and

$$I_x^{23} = \frac{1}{2}(I_j^+ I_i^- + I_j^- I_i^+) \qquad \text{(B6)}$$

where wd(t) is the time-dependent difference the Ij and Ii spin chemical shifts as defined by Eq. 1.32 is such that $[H^{23}(t),H^{23}(t')] \neq 0$. However, for the case of fast limit axial diffusion, a similar factorization as in Eq. B1 may be performed such that:

$$\langle H^{23}(t) \rangle^{AD} = F(t)\{\langle \tilde{\rho}_{20}^{j} \rangle - \langle \tilde{\rho}_{20}^{i} \rangle\} I_z^{23} - \langle \tilde{\rho}_{20}^{ij} \rangle I_x^{23} \qquad \text{(B6)}$$

which is clearly follows:

$$[\langle H^{23}(t) \rangle^{AD}, \langle H^{23}(t') \rangle^{AD}] = 0 \qquad \text{(B7)}$$

The result does not hold for a finite isotropic shift difference: "n>0" rotational resonances may be observed under fast limit axial diffusion. Futhermore, it should be noted that the results in this appendix are specific to axial diffusion or any other fast limit motion with three-fold symmetry. (ie-a three site hop with equal conformational probabilities).